



City Research Online

City, University of London Institutional Repository

Citation: Le, Binh (2017). The effect of forepole reinforcement on tunnelling-induced movements in clay. (Unpublished Doctoral thesis, City, University of London)

This is the accepted version of the paper.

This version of the publication may differ from the final published version.

Permanent repository link: <https://openaccess.city.ac.uk/id/eprint/17331/>

Link to published version:

Copyright: City Research Online aims to make research outputs of City, University of London available to a wider audience. Copyright and Moral Rights remain with the author(s) and/or copyright holders. URLs from City Research Online may be freely distributed and linked to.

Reuse: Copies of full items can be used for personal research or study, educational, or not-for-profit purposes without prior permission or charge. Provided that the authors, title and full bibliographic details are credited, a hyperlink and/or URL is given for the original metadata page and the content is not changed in any way.

**THE EFFECT OF FOREPOLE REINFORCEMENT ON
TUNNELLING-INDUCED MOVEMENTS IN CLAY**

by

Binh Thanh Le

A dissertation submitted for the Degree of
Doctor of Philosophy

City, University of London
Research Centre for Multi-scale Geotechnical Engineering
School of Mathematics, Computer Sciences & Engineering

February 2017

CONTENTS

LIST OF TABLES	i
LIST OF FIGURES	ii
ACKNOWLEDGEMENT	x
ABSTRACT	xi
NOTATION	xii
ABBREVIATIONS	xv
CHAPTER 1 INTRODUCTION	1
1.1 Preface	1
1.2 Background	1
1.2.1 Prediction of tunnelling induced ground settlement	2
1.2.2 Soil reinforcement measures in tunnelling	3
1.2.3 Introduction to Forepoling Umbrella System	3
1.3 Objectives & methodology	4
1.4 Outline of report	5
CHAPTER 2 BACKGROUND AND PREVIOUS WORK	7
2.1 Introduction	7
2.2 Tunnel construction techniques	7
2.3 Sources of ground deformation due to tunnelling	9
2.4 Tunnel heading stability	10
2.5 Prediction of ground movements due to tunnelling	13
2.5.1 Field measurements	14
2.5.2 Centrifuge modelling	16
2.5.3 Empirical method	19
2.5.4 Numerical modelling	29
2.5.5 Plasticity theorems	30
2.6 Soil reinforcement measures	32
2.6.1 Overview of protective measures for tunnelling	32

2.6.2	Spile reinforcement at tunnel face	33
2.7	Forepoling Umbrella System	35
2.7.1	Introduction	35
2.7.2	Steel pipes installation	36
2.7.3	Current understanding on Forepoling Umbrella System	36
2.8	Summary	40
CHAPTER 3 CENTRIFUGE MODEL TESTING		43
3.1	Introduction	43
3.2	A brief history of centrifuge modelling technique	43
3.3	Background to centrifuge model testing	44
3.3.1	Principles of centrifuge modelling	44
3.3.2	Scaling laws	45
3.3.3	Errors and error control in centrifuge modelling	47
3.4	The London Geotechnical Centrifuge Testing Facility	49
3.4.1	The Acutronic 661 geotechnical centrifuge	49
3.4.2	Data acquisition	50
3.5	Measurement instrumentation	51
3.5.1	Displacement transducer	52
3.5.2	Pressure transducer	52
3.6	2D Image processing - Visimet	53
3.7	2D Image processing – GeoPIV_RG	54
3.8	Image processing - 3D Imaging System	56
3.8.1	Available 3D Topography techniques	57
3.8.2	Principles of SfM- MVS technique	57
3.8.3	Review on SfM-MVS technique and MicMac software	59
3.8.4	Development of 3D Imaging System	60
3.8.5	Quantification of system performance	62
3.8.6	3D displacement vectors	64
3.9	The suitability of the measurement systems	64
3.10	Summary	65

CHAPTER 4 EXPERIMENTAL APPARATUS DEVELOPMENT	66
4.1 Introduction	66
4.2 Test series	66
4.3 Testing apparatus	67
4.3.1 The model container (strong-box)	68
4.3.2 Model tunnel	68
4.3.3 Potential boundary effects	69
4.3.4 Model Forepoling Umbrella System	69
4.3.5 Ground water supply	71
4.3.6 Location and fixing of instrumentation	71
4.4 Soil model	72
4.5 Experimental procedure	74
4.5.1 Clay preparation	74
4.5.2 Preparation of the model	75
4.5.3 Centrifuge test procedure	76
4.5.4 Summary of model stress history	77
4.6 Summary	78
CHAPTER 5 CENTRIFUGE TEST RESULTS	79
5.1 Introduction	79
5.2 Performance of the measurement systems	79
5.2.1 Performance of Visimet compared with LVDT	79
5.2.2 Performance of GeoPIV_RG and 3D Imaging system	81
5.2.3 Summary	83
5.3 Soil deformations in reference tests	83
5.3.1 Transverse soil surface settlement	83
5.3.2 Horizontal displacement in transverse direction	85
5.3.3 Longitudinal soil surface settlement	86
5.3.4 Soil displacement with depth	87
5.3.5 Summary	88

5.4	Assessment on the amendments of the testing apparatus	89
5.4.1	Change in measurement system - comparison on reference tests	89
5.4.2	Change in stiffness of tunnel lining	91
5.5	Illustrative results of the FUS reinforcing effect	92
5.5.1	Effect of using FUS	92
5.5.2	Effect of filling angle α	94
5.5.3	Effect of forepole stiffness	96
5.5.4	Effect of embedded length	96
5.6	Summary	97
CHAPTER 6 DISCUSSION		98
6.1	Introduction	98
6.2	The general effect of using the FUS on soil deformations	98
6.2.1	Reduction on the maximum vertical surface settlement	98
6.2.2	Reduction in horizontal soil displacement in the transverse direction	100
6.3	Tunnel stability	100
6.3.1.	Estimation of model clay undrained shear strength	101
6.3.2	Determination of tunnel support pressure at collapse	103
6.3.3	Effect of the FUS on tunnel stability	105
6.4	Soil stiffening effect offered by FUS	106
6.5	Relative effects of the parameters of the FUS	107
6.5.1	The effect of tunnel depth	108
6.5.2	The effect of the forepole stiffness	108
6.5.3	The effect of the filling angle in different tunnel depths	110
6.5.4	Effect of the embedded length with tunnel depth	110
6.6	An assessment on the prediction of V_L using Load Factor approach	112
6.7	Summary	114
6.7.1	The test results within the current frame work	114
6.7.2	The relative effects of the parameters of the FUS	115

CHAPTER 7 CONCLUSION	117
7.1 Introduction	117
7.2 Development of the 3D measurement system	117
7.3 The centrifuge tests	117
7.4 The merit of appropriate simplification approaches in this research	118
7.5 The reinforcing effectiveness of the FUS	118
7.6 Limitations of the result and recommendation for further work	120
7.6.1 Coverage of filling angle and number of forepoles	120
7.6.2 Friction between clay model and Perspex windows	120
7.6.3 Use of finite element analysis	121
7.6.4 Improvement in 3D Imaging System	121
7.7 Implications of results	121

REFERENCE

TABLES

FIGURES

APPENDIX 1

LIST OF TABLES

- Table 1.1:** Typical parameters of a FUS (Volkman & Schubert, 2007).
- Table 2.1:** θ_1 and θ_2 calculated by **Equation 2.2** proposed by Davis *et al.*, (1980).
- Table 2.2:** Typical values of volume loss, V_L .
- Table 3.1:** Centrifuge scaling laws (Marshall, 2009).
- Table 4.1:** Undertaken centrifuge tests.
- Table 4.2:** Speswhite kaolin clay properties.
- Table 6.1:** Average of reduction of maximum surface settlement SR offered by FUS.
- Table 6.2:** Undrained shear strength of model clay post test.
- Table 6.3:** Tunnel stability ratio at collapse N_{TC} and stability increase SI .
- Table 6.4:** Effectiveness of the FUS for different ratios C/D .
- Table 6.5:** Relative effect of filling angle α to increase in stiffness of the forepole.
- Table 6.6:** Relative effect of filling angle α in different ratios C/D .
- Table 6.7:** Relative effect of embedded length EL/D in different ratios C/D .

LIST OF FIGURES

- Figure 1.1:** Congestion in underground space (courtesy Keller).
- Figure 1.2:** Forepoling Umbrella System (after Carrieri *et al.*, 2002).
- Figure 1.3:** Forepoling Umbrella System schematic diagram.
- Figure 2.1:** Idealised 3D tunnel advance and related soil deformations.
- Figure 2.2:** An idealisation of shield tunnelling (after Davis *et al.*, 1980).
- Figure 2.3:** Cases of tunnel heading (after Davis *et al.*, 1980).
- Figure 2.4:** Four upper bound collapse mechanisms for the transverse plane strain section of a circular tunnel (After Davis *et al.*, 1980).
- Figure 2.5:** Upper bound mechanisms for a plane strain heading (after Davis *et al.*, 1980).
- Figure 2.6:** Influence of heading geometry on stability ratio at failure (after Kimura & Mair, 1981).
- Figure 2.7:** Surface settlement at a British coal mine tunnel project (after Schmidt, 1969).
- Figure 2.8:** Bruxelles Metro tunnel, 1968 (after Schmidt, 1969).
- Figure 2.9:** Instrumentation layout plan at St James' Park (Nyren, 1998).
- Figure 2.10:** Time line of the surveys in relation to the advance of the tunnel (Nyren, 1998).
- Figure 2.11:** Comparison of final displacement profiles determined from independent measurements immediately after westbound tunnel construction (After Nyren, 1998).
- Figure 2.12:** Vertical subsurface settlement with westbound tunnel face position for extensometer (positions of the extensometers are depicted in **Figure 2.9**) (after Nyren, 1998).
- Figure 2.13:** Vertical profile of horizontal displacements from electrolevel inclinometers (after Nyren, 1998).

- Figure 2.14:** Parallel profiles of normalised centreline settlement and surface trough volume with tunnel face position for both tunnels at St. James's Park, and comparisons with other field data (Nyren, 1998).
- Figure 2.15:** Usage of Gaussian curve to represent settlement trough (after O'Reilly & New, 1982).
- Figure 2.16:** Relationship between volume loss and load factor (after Macklin, 1999).
- Figure 2.17:** Variation of subsurface settlement trough width parameter with depth for tunnels in clays (after Mair *et al.*, 1993).
- Figure 2.18:** Variation of K with depth for subsurface settlement profiles above tunnels in clays. (Mair *et al.*, 1993).
- Figure 2.19:** Variation of trough width parameter K with depth in different soil types (Grant, 1998).
- Figure 2.20:** The variation of trough width with depth for NATM/SCL tunnelling in clay (Dimmock, 2003).
- Figure 2.21:** Variation of trough width with depth for open-face shield tunnelling in clay (Dimmock, 2003).
- Figure 2.22:** Distribution of horizontal ground surface displacement above a tunnel (after Hong & Bae, 1995).
- Figure 2.23:** Predicted and observed tunnel support pressure at collapse (after Kimura & Mair, 1981).
- Figure 2.24:** Idealisation of tunnel heading and ground behaviours around tunnel heading (after Mair & Taylor, 1993).
- Figure 2.25:** Radial deformation associated with unloading a cavity in an elastic-perfectly plastic continuum (after Mair & Taylor, 1993).
- Figure 2.26:** Non-dimensional plot of Tartaguille tunnel axial movements (Mair, 2008).
- Figure 2.27:** Schematic of tunnel reinforced by spiles (After Harris, 2001).
- Figure 2.28:** Testing arrangement of spiles in centrifuge modelling (after Calvelo & Taylor, 1999).

- Figure 2.29:** The arrangement patterns of bolts (Date *et al.*, 2008).
- Figure 2.30:** Tunnel failure patterns on the longitudinal section (Date *et al.*, 2008).
- Figure 2.31:** Installation of steel pipes into tunnel crown (DSI website).
- Figure 2.32:** Testing arrangement of forepoling roof in centrifuge modelling (Vrba & Bartak, 2007).
- Figure 2.33:** Surface settlement contours after tunnel excavation (Juneja *et al.*, 2010).
- Figure 2.34:** Model heading configuration (Yeo, 2011).
- Figure 2.35:** Model forepoles after testing (Yeo, 2011).
- Figure 2.36:** Deflection curve diagrams displaying measured settlement values from the Trojane tunnel (Volkman & Schubert, 2007).
- Figure 2.37:** Foundation model for pipe roof (Carrieri *et al.*, 2002).
- Figure 2.38:** Centrifuge test conducted by Divall *et al.*, (2016).
- Figure 2.39:** Tunnel support pressure against maximum vertical surface settlement for all forepoling arrangements (Divall *et al.*, 2016).
- Figure 2.40:** Stability ratio against forepoling position (Divall *et al.*, 2016).
- Figure 3.1:** Comparison of stress variation with depth in a centrifuge model and its corresponding prototype (after Taylor, 1995).
- Figure 3.2:** Lateral acceleration component a_L created within the model during spinning.
- Figure 3.3:** General arrangement of the Acutronic 661 at City University London.
- Figure 3.4:** Flow chart for Visimet image processing procedure (after Grant, 1998).
- Figure 3.5:** Image manipulation during PIV analysis (White, 2002).
- Figure 3.6:** Workflow of Structure from Motion and Multi-View Stereo.
- Figure 3.7:** Feature detection and correspondence of SfM (after Le *et al.*, 2016).
- Figure 3.8:** Complete 3D Imaging system apparatus (after Le *et al.*, 2016).
- Figure 3.9:** Details on camera and housing.
- Figure 3.10:** Details of reference plate.

- Figure 3.11:** Determination of vertical displacement accuracy on reconstructed 3DPC of measured surfaces when $U_z = 0\text{mm}$ (reference surface) and $U_z = 15.24\text{mm}$ (after Le *et al.*, 2016).
- Figure 3.12:** Accuracy histograms in four elevation increments. The total number of cells is 390 (after Le *et al.*, 2016).
- Figure 3.13:** Experiment set up to quantify horizontal displacement measurement accuracy (after Le *et al.*, 2016).
- Figure 3.14:** Schematic of horizontal tracking procedure.
- Figure 3.15:** Accuracy histograms in four horizontal displacements. The total number of cells is 336. (after Le *et al.*, 2016).
- Figure 3.16:** Typical strain levels for reliable measurement in geotechnical events (after Mair, 1993).
- Figure 4.1:** Schematic of Forepoling Umbrella System arrangements.
- Figure 4.2:** The complete model apparatus illustration.
- Figure 4.3:** Spacing S of the model forepoles.
- Figure 4.4:** Guide produced by high-resolution 3D printer for precise installation of rods.
- Figure 4.5:** Locations and fixing details of instrumentation.
- Figure 4.6:** Relationship of the undrained shear strength with OCR and consolidation pressure (after Mair, 1979).
- Figure 4.7:** Create semi-circular tunnel cavity.
- Figure 4.8:** Model ready to load on to the centrifuge swing.
- Figure 4.9:** Model on swing before spin-up.
- Figure 4.10:** Pressure transducers responses from spin up to spin down in test 5BL.
- Figure 4.11:** Stress history of model clay in $C/D=3$ tests.
- Figure 5.1:** Comparison on the measurements on surface settlement made by LVDT and Visimet when σ_T reduced from 368kPa (Test 5BL).
- Figure 5.2:** Top surface of the model captured by the middle camera during the test.

- Figure 5.3:** Three-dimensional centrifuge model simulating tunnel construction.
- Figure 5.4:** Comparison of the vertical surface settlement above the tunnel face measured by 3D imaging system and 2D PIV.
- Figure 5.5:** Comparison of horizontal displacements measured by 3D imaging system and 2D PIV when σ_T reduced from 206 to 106kPa.
- Figure 5.6:** A typical 3D Settlement trough in test 18BL ($\sigma_T=60\text{kPa}$).
- Figure 5.7:** Transverse surface settlement profile above tunnel face in test 18BL.
- Figure 5.8:** The fitting of the measured settlement trough with Gaussian curve ($\sigma_T=80\text{kPa}$).
- Figure 5.9:** Horizontal displacement at the surface in test 18BL when σ_T reduced to 60kPa.
- Figure 5.10:** Trend of horizontal soil displacement.
- Figure 5.11:** Illustration of parameters in Equation 5.5.
- Figure 5.12:** The trend of longitudinal settlement above tunnel centreline in reference tests.
- Figure 5.13:** Subsurface settlement with depth in test 18BL at $\sigma_T=150\text{kPa}$ and 120kPa.
- Figure 5.14:** Typical profiles of subsurface settlement with depth in reference tests.
- Figure 5.15:** Typical longitudinal horizontal soil displacements ahead of the tunnel face in test 18BL.
- Figure 5.16:** Comparison on the crown and surface settlements in reference tests 5BL and 18BL.
- Figure 5.17:** Shear box apparatus for friction determination.
- Figure 5.18:** Shear box experiments results.
- Figure 5.19:** Comparison on the subsurface soil deformations in tests 5BL ($\sigma_T=80\text{kPa}$) and 18BL ($\sigma_T=68.5\text{kPa}$).
- Figure 5.20:** Subsurface soil displacements in test 3BL when σ_T reduced from 381kPa to 200kPa.

- Figure 5.21:** Subsurface soil displacements in test 5BL when σ_T reduced from 365kPa to 200kPa.
- Figure 5.22:** Vertical settlement of a point above the tunnel lining in $C/D=3$ tests.
- Figure 5.23:** Vertical settlement of a point above the tunnel lining in $C/D =1$ tests.
- Figure 5.24:** Typical data set from centrifuge tests (From test 18BL).
- Figure 5.25:** Subsurface soil deformations in test 8BL & 9BL when σ_T reduced from 55kPa to 40kPa.
- Figure 5.26:** Subsurface soil deformations in test 8BL & 9BL when σ_T reduced from 55kPa to 20kPa.
- Figure 5.27:** Subsurface soil deformations in tests 2BL and 5BL when σ_T reduced from 180kPa to 140kPa.
- Figure 5.28:** Subsurface soil deformations in tests 2BL and 5BL when σ_T reduced from 180kPa to 100kPa.
- Figure 5.29:** Subsurface soil deformations in tests 18BL and 20BL when σ_T reduced from 180kPa to 80kPa.
- Figure. 5.30:** Model post-test in reference test 9BL.
- Figure. 5.31:** Model post-test in reinforced test 8BL.
- Figure 5.32:** $C/D=3$ models post tests.
- Figure 5.33:** Soil displacements in tests 18BL and 20BL when σ_T reduced from 180 to 80kPa.
- Figure 5.34:** Effect of filling angle - Subsurface soil deformations in tests 8BL and 10BL when σ_T reduced from 55kPa to 20kPa.
- Figure 5.35:** Effect of filling angle - Subsurface soil deformations in tests 2BL and 4BL when σ_T reduced from 180kPa to 80kPa.
- Figure 5.36:** Effect of filling angle - Subsurface soil deformations in tests 19BL and 20BL when σ_T reduced from 180kPa to 60kPa.
- Figure 5.37:** Effect of filling angle - Soil displacement in tests 19BL and 20BL when σ_T reduced from 180 to 60kPa.

- Figure 5.38:** The tunnel headings and the model forepoles post-test.
- Figure 5.39:** Effect of FUS stiffness - Subsurface soil deformations in tests 10BL and 13BL when σ_T reduced from 55kPa to 20kPa.
- Figure 5.40:** Effect of FUS stiffness - Subsurface soil deformations in tests 3BL and 12BL when σ_T reduced from 180kPa to 60kPa.
- Figure 5.41:** Effect of EL - Subsurface soil deformations in tests 10BL and 11BL when σ_T reduced from 55kPa to 20kPa.
- Figure 5.42:** Effect of EL - Subsurface soil deformations in tests 3BL and 4BL when σ_T reduced from 180kPa to 60kPa.
- Figure 5.43:** Schematic representation of rod post-test.
- Figure 6.1:** Maximum surface settlement above tunnel face.
- Figure 6.2:** Settlement reduction delivered by the FUS.
- Figure 6.3:** Horizontal displacement in transverse direction when σ_T reduced from 180kPa to 72kPa ($0.2\sigma_{ob}$).
- Figure 6.4:** Horizontal displacement in transverse direction when σ_T reduced from 180kPa to 72kPa ($0.2\sigma_{ob}$).
- Figure 6.5:** Undrained shear strength and water content of centrifuge model clay post-test at various depth.
- Figure 6.6:** Soil displacements in test 5BL.
- Figure 6.7:** Soil displacements in test 12BL.
- Figure 6.8:** Gradient of soil displacement in test 5BL.
- Figure 6.9:** Gradient of soil displacement in test 12BL.
- Figure 6.10:** Engineering shear strains in soil in test 5BL at $\sigma_{TC}=126\text{kPa}$.
- Figure 6.11:** Engineering shear strains in soil in test 12BL at $\sigma_{TC}=88\text{kPa}$.
- Figure 6.12:** Longitudinal horizontal soil displacement ahead of the tunnel face in tests 18BL, 19BL and 20BL ($\sigma_T=90\text{kPa}$).
- Figure 6.13:** Change in stiffness of soil during the centrifuge tests.

Figure 6.14: Relative locations of the shear planes and the FUS with $EL/D=1$ in the reference tests and reinforced tests.

Figure 6.15: Comparison of the shear planes for the reinforced and reference tests.

Figure 6.16: The measured volume loss when σ_T reduced.

Figure 6.17: Comparison of the Load Factor-Volume loss relationship with Macklin (1999).

Figure 7.1: Recommended embedded length EL/D for different tunnel depth C/D .

Figure 7.2: Relationship between settlement reduction SR and EL/D for different tunnel depths C/D .

**THE FOLLOWING PARTS OF THIS THESIS HAVE BEEN REDACTED
FOR COPYRIGHT REASONS:**

Figure 1: Congestion in underground space (Keller)

Figure 2.31: Photo

ACKNOWLEDGEMENT

I have been fortunate to be a member of Research Centre for Multi-scale Geotechnical Engineering in which I have had the privilege of working closely with highly skilled people who have been willing to offer help and advice.

Firstly, I wish to acknowledge with many thanks the help and guidance provided to me by my first supervisor Professor Neil Taylor. He has been so generous with his time and has been an unending source of wisdom which has played a huge part in my development. Without his patience, commitment, inspiration and care, even before my arrival to the UK, I could have not completed this thesis. I also would like to thank my second supervisor Dr Richard Goodey whose practical knowledge and advice were extremely appreciated.

Huge thanks also go to the people in the Group who have always created an atmosphere filled with not only a source of valuable discussions about technical problems but also with warm friendship and good humour. That made my supposedly challenging time in the UK an enjoyable experience from which I learnt a lot about life, research and tackling problems.

I wish to thank Professor Sarah Stallebrass for her rigorous and constructive comments on the test results in the early time of the research along with Dr Andrew McNamara for his practical input.

I am particularly grateful to Dr Sam Divall, Hitesh Halai, Dr Neil Phillips, Sadegh Nadimi, Jignasha Panchal, Dr Rohit Gorasia, Dr Joana Fonseca for their stimulating discussions about the research and the support they gave me. Thanks are also due to Dr Deqiong Kong and Tianqi Zhang for the help during their time at City.

My research was funded by the Ministry of Education and Training of Vietnam Government. That enabled me to pursue the research and I gratefully acknowledge their support.

I would like to thank Neil Moss, TfL for showing me the Bond Street Station Upgrade project and engineers from DSI for expressing their interests in my research and insightful discussions.

Centrifuge model testing required a considerable input from technical staff. Therefore, thanks are due to Jim Hookers, Melvyn Hayes and Keith Pamment for their assistance in fabricating the testing apparatus.

Finally, special thank to my parents for their love, financial support and for the belief they always have in me.

ABSTRACT

The research concerns the effects of a Forepoling Umbrella System (FUS) that comprises steel pipes installed in a canopy shape above a tunnel heading to reduce ground movements induced by tunnelling. As an in-tunnel reinforcement measure, FUS is known to be beneficial in reducing soil deformations at source and has been used in a number of projects. An extensive literature review was provided covering the framework of tunnelling-induced soil movements and current understanding of the FUS. That highlighted deficiencies in how key parameters of a FUS can be combined to produce effective support. The aim of the research was to investigate the relative effect of the system parameters to gain a clearer insight into achieving an optimal design of a FUS.

Twenty centrifuge tests were carried out. Tunnels at two depths $C/D=1$ and $C/D=3$ were tested (C : cover above tunnel crown, D : tunnel diameter). In those tests, effect of a FUS with various filling angles (coverage of the forepoles in a tunnel cross section), embedded lengths EL (distance from the face to the end of the forepoles in front of the tunnel) and forepoles stiffnesses was investigated. The experiments were conducted at $125g$. The non-axisymmetric characterises of a forepoles supported tunnel heading required a 3D model. A novel image-based measurement system was developed to measure soil surface displacements in 3D to a high precision that widened the coverage of the measured data and allowed more detailed analysis to be performed. The tunnel was modelled by a 50mm diameter semi-circular cavity cut into the clay model which was partly supported by a stiff lining. The unlined tunnel heading was supported by a thin rubber bag supplied with air pressure. The steel pipes were modelled by 1mm diameter brass or steel rods. The tunnel excavation process was simulated by gradually reducing tunnel air support pressure. The induced surface and subsurface ground movements were measured using a combination of displacement transducers and 2D & 3D image analysis.

Soil deformations in the centrifuge tests were shown to be similar to tunnelling-induced soil movement in practice. That enabled confidence that the experiment study revealed realistic effects of a FUS. Significant benefits of using a FUS were reflected by the marked reduction in magnitude and extent of soil displacements at surface and subsurface. The reinforcing effectiveness of using a FUS was quantified by assessing the reduction in maximum settlement and increase in tunnel stability. A wide range of reduction of 35÷75% in maximum settlement was achieved by using FUS arranged in different settings. The results showed that the relative influence of the FUS parameters vary with the tunnel depth. For a shallow tunnel, arranging the forepoles into the area around the tunnel spring line was found less effective than concentrating the forepoles near the tunnel crown. In contrast, for a deeper tunnel, having the forepoles near the tunnel spring line delivered a higher reinforcing effect. Using an appropriate filling angle yielded an increase of approximately 10% in settlement reduction compared with a non-optimal filling angle. The support provided by the tunnel lining and the surrounding ground to the forepoles has a large influence to the effectiveness of the FUS. It is important to maximise this support by ensuring a minimum deformation of the tunnel lining and maintain an adequate embedded length of the forepoles. For example, for a $C/D=1$ tunnel, an embedded length $EL = 1D$ is deemed sufficient. Increasing the forepoles stiffness delivered a considerable reinforcing effect which can be opted to reduce the required EL . The influence of each parameter of the FUS to its reinforcing effectiveness at different tunnel depths was analysed. From there, an optimum combination of essential parameters of the FUS and their effect on the system performance is suggested.

Keywords: Centrifuge; Ground movements; Soil improvement; Tunnel & Tunnelling

NOTATION

a	Radial acceleration or radius of tunnel cavity ($D=2a$)
AAE	Average of absolute error
C	Cover above tunnel crown
C_v	Coefficient of consolidation
D	Tunnel diameter
e	Voids ratio
E	Young's modulus of model forepoles
EI	Bending stiffness
EL	Embedded length
E_u	Undrained Young's modulus
g	Acceleration due to gravity (9.81m/s^2)
G	Soil stiffness
$G()$	Function of normal probability curve
H	Distance over which the excess pore pressures are dissipated or drainage path length
i_x	Settlement trough length parameter
i_y	Settlement trough width parameter
K	Dimensionless trough width parameter for Gaussian settlement trough
L	Length of forepoles
LF	Load factor
M	Stress ratio at critical state ($q':p'$)
n	Gravity scaling factor
N	Tunnel stability ratio or specific volume on INCL when $p'=1\text{kPa}$
N_{TC}	Tunnel stability at collapse
OCR	Overconsolidation ratio

p	Mean normal stress $(\sigma_1 + \sigma_2 + \sigma_3)/3$
p'	Mean normal effective stress $(\sigma'_1 + \sigma'_2 + \sigma'_3)/3$
P	Unlined portion of tunnel heading
q	Deviator stress $(\sigma_1 - \sigma_3)$
r	Radius in the elastic perfectly plastic spherical/cylindrical model
S	Centre-to-centre spacing between forepoles
SAE	Sum of absolute error
SR	Settlement reduction
SI	Stability increase
S_u	Undrained shear strength of clay
t	Time
T_V	Dimensionless time factor
u	Horizontal displacement in X direction
v	Specific volume or horizontal displacement in Y direction
V_L	Volume loss
V_S	Volume of settlement trough
V_{ex}	Volume of excavation
w	Vertical displacement in Z direction
z_0	Depth to tunnel axis level
α	Filling angle in Forepoling Umbrella System
β	Insertion angle in Forepoling Umbrella System
Γ	Specific volume at critical state when $p' = 1\text{kPa}$
γ	Unit weight of soil
γ_w	Unit weight of water
δ	Displacement used in the elastic perfectly plastic spherical/cylindrical model
κ	Gradient of swelling line in $v - \ln p'$ place

λ	Gradient of normal compression line in $v - \ln p'$ plane
ω	Angular velocity
σ_{ob}	Overburden stress at tunnel centreline
σ_s	Surface surcharge (if any)
σ_T	Tunnel support pressure
σ_{TC}	Tunnel support pressure at collapse
σ'_{v0}	Maximum vertical effective stress
ϕ'_c	Critical state angle of shearing resistance

Subscripts

m	Model
max	Maximum
p	Prototype

ABBREVIATIONS

3D	Three-dimensional
3DIS	Three-dimensional imaging system
CCD	Charged Coupled Device (camera for Visimet)
CL	Centreline
CNC	Computer numerical control machine
DPI	Digital Pressure Indicator
LVDT	Linear Variable Differential Transducer
NATM	New Austrian Tunnelling Method
SCL	Sprayed Concrete Lining
PPT	Pore Pressure Transducer
FUS	Forepoling Umbrella System
PIV	Particle Image Velocity
FOV	Field of view
TBM	Tunnel boring machine
ROI	Region of interest
SfM	Structure from Motion
MVS	Multi-view Stereo

CHAPTER 1 INTRODUCTION

1.1 Preface

The research project concerns the effects of a Forepoling Umbrella System (FUS) as a soil reinforcement measure placed at the tunnel heading in soft clay. Ground deformations and tunnel stability are analysed to assess the performance of the Forepoling Umbrella System. The variables are the tunnel depth, the arrangements and materials of the Forepoling Umbrella System. The background, objectives and research methodology are presented in this introductory chapter.

1.2 Background

Transportation is a major life line for every country. In many urban environments the available over ground space is no longer adequate to sustain construction of new transportation systems to serve the growing traffic and congestion. This pressure on space has led to an increase in the number of tunnelling projects for services and mass transit projects all over the world. The London Underground is known as the world's first underground railway and was opened in 1863. This is a vivid example of underground space usage within a dense network of overground space.

Tunnelling in soft ground inevitably induces ground deformations. This is obviously a critical issue relating to the safety of people and nearby buildings and services especially in congested urban areas with congested underground space (**Figure 1.1**). In fact, damage to existing buildings due to tunnelling-induced ground deformations has been encountered on many projects all over the world. Therefore, the demands on understanding ground movements due to tunnelling and soil reinforcement measures to reduce its effect have been continuously attracting researchers.

1.2.1 Prediction of tunnelling induced ground settlement

Several methods have been developed by previous researchers and applied to predict the tunnelling induced ground displacements.

The empirical method is a conventional approach to estimate ground deformation due to tunnelling using data and experience learnt from previous tunnel constructions. Every tunnelling project is an opportunity to study the soil response to tunnelling. It is worth noting that measurements of the soil displacements at the ground surface are more straightforward than that of the subsurface ground movements. Therefore, more data relating to the surface settlements are available hence most of the empirical equations were developed for prediction of the soil surface displacements. These equations have been proved to be capable of producing good agreement with site data (O'Reilly & New, 1982; Attewell & Woodman, 1982; Mair & Taylor, 1997). Limited data are available on the patterns on the relationships of soil displacements with depth. So, fewer empirical equations have been suggested for their prediction (Attetwell & Woodman, 1982; Mair *et al.*, 1993; Mair & Taylor, 1997).

The centrifuge modelling technique, with its capabilities in replicating soil behaviour in physical events, has contributed to the understanding of ground deformation mechanisms caused by tunnel construction (Mair, 1979; Taylor, 1995). By the means of high quality measurement instrumentation and appropriate testing apparatus, the centrifuge modelling technique has revealed two-dimensional (2D) subsurface soil displacements and vertical settlements at the model surface in plane strain (Mair, 1979; Taylor, 1984; Grant, 1998; Divall, 2013) and three-dimensional experiments (Calvello & Taylor 1999; Date *et al.*, 2008; Yeo, 2011) by taking advantage of the model symmetry. In this project, a new imaging measurement system was developed to measure 3D soil deformations at the model surface which enlarged the coverage of the measured area and aided the understanding to the soil response to tunnelling (Le *et al.*, 2016).

The last decades have witnessed the development of numerical modelling and soil constitutive models that can represent soil behaviour. Together with the recent advances in computing power, numerical methods have been used to investigate the complex tunnelling induced ground displacements.

These above methods are presented in detail and discussed in Chapter 2.

One of the aims of estimating tunnelling induced ground movements is to aid in designing suitable reinforcement methods to minimise the negative effects of settlement damage on adjacent structures and to ensure safety in tunnel construction.

1.2.2 Soil reinforcement measures in tunnelling

Congested urban environments in both overground and underground spaces have led to a requirement to minimise tunnelling induced deformations. Tunnel heading stability is of critical concern in every tunnel construction especially in urban areas where tunnelling takes place underneath important buildings and next to underground services. Therefore, ground movements need to be minimised to mitigate negative effects to adjacent structures. To cope with these demands, ground reinforcement measures have been developed and utilised in practice. Many case studies that were reported from the Jubilee Line Extension Project in London showed the success of using reinforcement measures to ensure the safety of existing buildings such as Big Ben and the Palace of Westminster from the tunnel construction.

Ground reinforcement measures are chosen based on tunnelling technology, soil properties and allowable ground deformations. Common ground improvements such as Forepoling Umbrella System, soil nailing, facebolts, forepoling board, jet grouting, ground freezing and compensation grouting are nowadays frequently applied to minimise tunnelling induced ground movements. Each of these methods has its own application and could be used in conjunction with others to achieve the net effect of improving soil conditions and minimising ground movements.

1.2.3 Introduction to Forepoling Umbrella System

A Forepoling Umbrella System consists of steel pipes (forepoles) in a canopy shape ahead of the advancing tunnel face, as illustrated in **Figure 1.2**. This is typically undertaken to provide structural support to the surrounding soils. As an in-tunnel measure, one of the noticeable advantages of the FUS is the immediate support from the steel pipes to reduce soil deformations at source. In some cases, grout is injected via

inserted perforated steel pipes to form a closed canopy above the tunnel heading to prevent water and soil ingress into the tunnel.

A schematic diagram of a Forepoling Umbrella System is presented in **Figure 1.3**. Where D is tunnel diameter, C is the cover above the tunnel crown and S is centre to centre spacing between the steel pipes. The Forepoling Umbrella System steel pipes with the length, L , are installed from within the tunnel heading at an insertion angle, β . The soil beneath the embedded length of the forepoles acts like a foundation to support the steel pipes as they bridge over the unlined tunnel heading and this is known as the foundation effect. In order to remain a sufficient support to the tunnel heading, a minimum embedded/overlap length, EL , of the Forepoling Umbrella System is required ahead of the tunnel face. After the excavation of a tunnel section of length $L\cos(\beta)-EL$, the next Forepoling Umbrella System is installed. This leaves an overlap of EL between the two Forepoling Umbrella System sections.

Typical parameters of a FUS are presented in **Table 1.1**. Generally, the steel pipes used in a Forepoling Umbrella System are 70mm to 200mm diameter with a wall thickness of 4mm to 8mm (Volkman & Schubert, 2007). The lengths of steel pipes vary from 12m to 15m and do not normally exceed 15m due to drilling guidance considerations (Leca & New, 2007). The insertion angle, β , and filling angle, α , vary from 5° to 7° and 60° to 75° , respectively. The minimum EL is usually between 3m and 6m. The spacing, S , is from 300mm to 600mm (centre to centre).

1.3 Objectives & methodology

When a void is created by tunnelling, it is crucial to maintain adequate tunnel heading stability. Insufficient support will lead to ground movements potentially causing damage to existing structures. In weak or unstable ground, movement could be controlled by providing a Forepoling Umbrella System ahead of the tunnel face.

The following points highlight the deficiencies in the current design guidance of a Forepoling Umbrella System and are therefore the areas for investigation in this research project:

- Effect of tunnel depth to arrangement of steel pipes,
- Appropriate filling angle α ,
- Influence of forepole stiffness,
- Effect of overlap/embedded length.

This research aims to obtain a better understanding of the effects of the aforementioned parameters in Forepoling Umbrella System design and implementation by the means of centrifuge modelling. To this end, the key elements are:

- Develop new centrifuge modelling apparatus to model a three-dimensional (3D) tunnel heading reinforced by a Forepoling Umbrella System;
- Use centrifuge model testing to investigate the relative effects of the model forepoles with the tunnel depth, the materials and arrangement of the forepoles as varied parameters;
- Develop an image measurement system to measure the 3D deformations of the soil surface in centrifuge tests to gain a broader insight into the soil displacements and the effects of FUS parameters.

1.4 Outline of report

The dissertation comprises seven chapters:

Chapter 1 is an introductory chapter and provides a background on tunnelling including the needs of soil improvement in soft ground. Research objectives, methodology and research outlines are also presented.

Chapter 2 reviews available methods and work undertaken by previous authors regarding the estimation of tunnelling induced ground deformations, the general in-tunnel soil reinforcement measures and the Forepoling Umbrella System.

Chapter 3 covers the principles of centrifuge technology and the facilities used to implement the research. Development of the novel 3D imaging measurement system is described. Discussion on the precision of the instrumentation and its suitability to the research objectives is presented.

Chapter 4 describes the developments of apparatus designed specifically to achieve the research objectives. The procedure, experimental variables and series of tests undertaken are also described.

Chapter 5 reports the results obtained from the centrifuge tests conducted to present the key features of the tests and the quality of the data obtained. Firstly, the performance of the measurement systems and the testing apparatus are assessed. Then the measured soil displacements at the subsurface and surface of the model are presented to illustrate the reinforcement effects of FUS and its parameters.

Chapter 6 draws the experimental results together and analyses the trends observed. The influence of the FUS parameters and the system reinforcement effectiveness are quantified based on the reduction on the soil displacements and increase in tunnel stability achieved.

Chapter 7 summarises the works done and the limitations of the research. An optimum reinforcement arrangement of the essential FUS parameters and their effect on the patterns of tunnelling-induced ground deformations is suggested. From there, implications derived from the analysis for practical use and suggestion for further work is discussed.

2.1 Introduction

In this chapter, typical tunnel construction techniques and relevant sources of ground movement are presented. Then current understanding on the ground deformations due to tunnelling developed from field measurements, physical modelling, empirical solutions, numerical methods and plasticity theorems are reviewed. These will serve as a framework to assess the pattern and the trend of soil movements observed in the centrifuge tests in the later chapters.

This is followed by a discussion on studies related to the effect of the Forepoling Umbrella System for tunnelling in clay and the present limitation on the understanding of the influence of the system parameters to its effectiveness. From there, key requirements that need to be addressed for this research to gain a clearer insight into the reinforcing effect of the Forepoling Umbrella System are proposed.

2.2 Tunnel construction techniques

Mair & Taylor (1997) categorised tunnel construction techniques in terms of open face and closed face tunnelling. Access to the tunnel face in open face tunnelling is easy as opposed to closed face tunnelling.

Closed face tunnelling

Closed face tunnelling involves using tunnel boring machines (TBM) which is usually in a cylindrical steel shield form. The TBM is pushed forward along the tunnel axis as the soil is excavated. The steel shield provides support for the excavated cavity until a temporary or final lining is installed behind the TBM (Maidl *et al.*, 2013).

Closed face tunnelling is particularly suited to long circular tunnels without significant change in soil conditions along the excavation length. This method is not appropriate for

short tunnels due to the high cost. Unusual large settlements were observed in tunnelling projects using TBM within mixed soil conditions (Shirlaw, 2003). Key advantages of this technique are the minimisation of the effects to adjacent buildings, high advance rates and safety for miners.

Open face tunnelling

In contrast to closed face tunnelling, open face tunnelling, sometimes referred to as the New Austrian Tunnelling Method (NATM) uses sprayed concrete to form temporary and final linings. The principle of Sprayed Concrete Linings (SCL) is to spray concrete on the excavated tunnel annulus to provide temporary support before the final lining is installed. Recent developments have introduced composite sprayed concrete (normally concrete mixed with steel fibres) to improve the structural capacity and deliver a better reinforcing effect. Sprayed concrete is particularly suitable for tunnels which are short, non-circular sections such as an enlargement at a station and for large diameter tunnel constructions by dividing the face into smaller sections.

An ideal example of the application for SCL is the Bond Street Station Upgrade in London which involves construction of new short connecting tunnels between the London Underground network and Crossrail. Steel fibre SCL was used as the major reinforcement measure in this project.

The flexibility offered by NATM enables the miners to change tunnel direction and inclination and it also provides easy access for construction of joints between tunnels. Besides direct access to the tunnel face, the SCL technique also allows soil improvement methods such as spile and a Forepoling Umbrella System to be added when required.

Tunnel support air pressure

Compressed air is one of the earliest measures to provide face support in tunnelling especially in difficult ground conditions with a high water table level and weak soil. The principle behind using compressed air is to provide a pressure to counteract the soil stresses and water pressure in order to maintain the stability of the tunnel heading and prevent water from ingress into the cavity.

A constant air pressure is applied to the tunnel heading. However the pressure of soil and water increases from the top to the bottom of the tunnel heading due to the self-weight effect. This results in a larger pressure required for the bottom of the tunnel than for the top to maintain equilibrium. Choosing an air pressure to balance the soil and water pressure at the bottom of the tunnel will cause the upper part of the tunnel to be over pressurised and a blow-out is possible especially for a shallow tunnel. Moreover, working in a high pressure environment is not ideal for the miners. These issues necessitate an optimal support air pressure to be determined which can maintain the stability of the tunnel without creating the hazards.

This research is concerned with tunnel construction using NATM in which soil improvements to the tunnel heading are normally required. The Forepoling Umbrella System is one of the reinforcing measures in tunnelling used to provide structural support that controls ground deformation, prevents soil ingress and reduces the additional support pressure required.

2.3 Sources of ground deformation due to tunnelling

Basically, tunnelling is used to create space for underground services by removing soil and replacing it by tunnels. **Figure 2.1** shows a typical settlement trough caused by tunnelling and defines the coordinates system, notations for soil displacement used in this research and relevant parameters.

The main sources of ground deformation in open face tunnelling are illustrated in **Figure 2.1** and summarised below (Mair & Taylor, 1997):

- 1) Stress relief due to excavation that leads to ground deformation toward the tunnel heading including face intrusion and radial displacement which are depicted as (1-a) and (1-b) respectively,
- 2) Tunnel lining deformation induced by surrounding soil and water pressure depicted as (2), and

3) Consolidation: as pore water pressures revert to their long-term equilibrium conditions (following excavation), the resulting changes in effective stresses leads to further ground deformations depicted as (3).

Among the three main components stated above, settlement caused by consolidation tends to cause less damage to nearby structures compared to the first component but requires monitoring over a long period of time (Mair & Taylor, 1997; Leca & New, 2007). The relief of ground stress is considered as the major contributor to ground deformations and is the key focus of prediction methods for tunnelling induced ground movement.

2.4 Tunnel heading stability

The unlined tunnel heading is the major source of ground deformation due to tunnelling. Therefore, the stability of the tunnel heading is of primary concern in every tunnel construction. The need to understand tunnel heading stability has consequently attracted much research.

Broms & Bennermark (1967) quantified tunnel heading stability ratio N , equal to the difference between the overburden stress at the tunnel axis level and the tunnel support pressure divided by the undrained shear strength of soil, S_u , given in **Equation 2.1**.

$$N = \frac{\sigma_{ob} - \sigma_T}{S_u} = \frac{\gamma \left(C + \frac{D}{2} \right) + \sigma_s - \sigma_T}{S_u} \quad (2.1)$$

where γ is the unit weight of the soil,

D is the tunnel diameter,

C is the soil cover above tunnel,

σ_{ob} is the overburden stress at the tunnel axis level,

σ_s is the surface surcharge pressure (if any),

σ_T is the tunnel support pressure (if any), and

S_u is the undrained shear strength of soil at the tunnel axis level.

The physical meanings of the above parameters are illustrated in **Figure 2.2**. In undrained conditions, the parameters in **Equation 2.1** are assumed to be constant except for tunnel support pressure σ_T . Therefore, the value of N depends on the tunnel support pressure σ_T . If the tunnel support pressure is equal the overburden stress then the tunnel heading is in a fully stable condition and the corresponding stability $N = 0$.

However, in practice when soil is being excavated and replaced by the tunnel lining the difference between the overburden stress and tunnel support pressure is expected. As the difference between the tunnel support pressure and the overburden stress increases so the tunnel heading becomes less stable which is reflected in a higher value of stability ratio N . The induced difference in the tunnel support pressure and the overburden stress ($\sigma_{ob} - \sigma_T$) is supported by the soil surrounding the tunnel heading and reinforcement measures (if any) to maintain the stability of the tunnel heading.

When the pressure difference exceeds the ability of the soil to maintain a stable condition, the tunnel fails or collapses. Broms & Bennermark (1967) stated that the tunnel heading is stable provided $N < 6$. Therefore, the concept of a safe operational stability ratio is beneficial in determining an adequate tunnel support pressure that ensures a stable tunnel heading and provides construction safety.

Consistent results on tunnel stability obtained from two-dimensional (2D) circular tunnel and three-dimensional (3D) circular tunnel heading centrifuge model tests and numerical analyses were reported by Mair (1979). The author distinguished two modes of ground movement due to tunnelling: face movement (three-dimensional behaviour - component 1-a in **Section 2.3**) and inward radial movement (two-dimensional behaviour - component 1-b in **Section 2.3**). Mair (1979) suggested that the tunnel geometry is as an important factor to determine the pattern of ground movement. Larger P/D ratios result in more two-dimensional ground deformation behaviour whereas shorter P/D ratios lead to more three-dimensional ground deformation behaviour (P is the unlined length and D is the tunnel diameter, see **Figure 2.2**). The observations from the field showed that ground

displacement due to tunnelling was a combination of the two modes. Mair (1979) demonstrated that tunnel stability is affected significantly by the P/D ratio.

Davis *et al.*, (1980) investigated the tunnel stability of three cases of tunnel heading in clay soils using plasticity theorems (**Section 2.5.5**). An idealisation of shield tunnelling is presented in **Figure 2.2** and cases of tunnel headings are shown in **Figure 2.3**. **Figure 2.3-a** shows the plane strain case of an unlined circular tunnel (Case 1) and is equivalent to the case illustrated in **Figure 2.2-b** when P/D is large. **Figure 2.3-b** represents the second case of a plane strain tunnel heading with the assumption the excavation is not cylindrical but similar to a long wall mining excavation. In that assumption, D is not the diameter but is instead the height of the tunnel. Case 3 is the plane strain tunnel heading shown in **Figure 2.3-b** but now with the assumption the excavation is cylindrical and D is the tunnel diameter. Case 3 is identical to the geometry that Broms & Bennermark (1967) used to examine the stability ratio of a tunnel heading.

Four upper bound collapse mechanisms for the transverse plane strain section of a circular tunnel (Case 1) proposed by Davis *et al.* (1979) are shown in **Figure 2.4**. Mechanisms A and B have ground movement concentrated at the “roof” and “roof and invert”. Mechanism C is the mechanism which combines mechanisms A and B. Mechanism D has ground movements from “roof, sides and bottom”. The authors suggested that mechanisms A, B and C are more dominant for low values of C/D and is replaced by mechanism D for high values of C/D .

Figure 2.5 presents the upper bound mechanism for a plane strain heading which was optimised with respect to the three variable angles θ_1 , θ_2 and θ_3 where;

$$\tan \theta_1 = \tan \theta_2 = 2\sqrt{C/D + 1/4} \quad (2.2)$$

$$\theta_3 = \pi/2 \quad (2.3)$$

The angles θ_1 and θ_2 are tabulated in **Table 2.1** which imply that for a deeper tunnel, the soil mobilisation area in front of the tunnel face is larger than that for a shallower tunnel.

Kimura & Mair (1981) made use of the results gained from centrifuge tests from Mair (1979) and plasticity theory to assess the stability ratio at failure under different tunnel heading geometries. The stability ratio at failure is defined as;

$$N_{TC} = (\sigma_{ob} - \sigma_{TC}) / S_u \quad (2.4)$$

where σ_{TC} is the tunnel support pressure at collapse.

Mair (1979) defined the tunnel support pressure at collapse, σ_{TC} as the pressure at which the increase in the ground settlement is the most rapid. The results obtained from Kimura & Mair (1981) showed the influence of heading geometry C/D and P/D on stability ratio at failure (**Figure 2.6**). The chart suggested by Kimura & Mair (1981) has been used by previous researchers as a quick reference to determine the tunnel geometry for a stable tunnel heading.

For the same soil (undrained shear strength S_u) and same tunnel depth (constant C), a shorter unsupported length P can lead to a higher N_{TC} which means the tunnel requires smaller tunnel support pressure to remain stable compared with those having a longer unsupported length P . Hence, a maximum allowable P can be estimated by the means of the chart. Other uses of this chart include the stability ratio at collapse using the known parameters C/D and P/D of a particular tunnel heading. This will assist other analysis, for example estimation of the tunnelling-induced ground settlement (**Section 2.5.3**).

2.5 Prediction of ground movements due to tunnelling

Common values used in prediction of tunnelling-induced soil deformations and their physical meanings are illustrated in **Figure 2.1**. These values are:

- Volume of excavation, V_{ex} . The author is unaware of cases where the actual volume of soil excavated during tunnel construction has been reported though there is some anecdotal evidence of measurements being made. This value is commonly assumed and stated as volume per length of tunnel advance. For a circular tunnel, the volume of excavation per unit length is as below;

$$V_{ex} = \pi D^2 / 4 \quad (2.5)$$

- Volume of settlement trough, V_S , (depicted in **Figure 2.1**) is also generally stated as volume per length of advance (m^3/m).
- Volume loss, V_L , is caused by the volume of the finished tunnel being less than the excavated soil. This is because of the overcut during excavation, the passage of the tunnel shield and the gap between the tunnel shield and the tunnel lining. This ground loss is considered as one of the major sources of the ground deformations due to tunnelling. Most of the prediction methods are for the undrained situation which is immediately after the tunnel construction (components 1 and 2 in **Section 2.3**). Therefore, the volume of the settlement trough is assumed to be equal to the volume of the ground loss (Schmidt, 1969; Sugiyama *et al.*, 1999). Volume loss is commonly expressed as the percentage of V_S compared to V_{ex} i.e.

$$V_L = \frac{V_S}{V_{ex}} (\%) \quad (2.6)$$

Most of the prediction methods have been established from back analysis of on site measurements. This section presents several typical field measurement data to illustrate the patterns of ground movement due to tunnelling. Then other methods are described to discuss their prediction capabilities.

2.5.1 Field measurements

From early field measurements by Schmidt (1969)

In the early days of tunnelling, most of the field measurements were only on the transverse soil settlement at the ground surface. One of the first works that reported various field measurements on soil surface settlement due to tunnelling was made by Schmidt (1969). Those projects were undertaken in many places in the world including America, Asia and Europe with different soil conditions from sand to clay using different excavation techniques.

Typical tunnelling projects with sufficient measurement data on surface settlement reported by Schmidt (1969) are replotted in this research. Other useful data such as

volume of excavation, V_{ex} , volume of settlement trough, V_S , and maximum surface settlement, S_{max} , were also estimated and presented. **Figure 2.7** presents the transverse surface settlement profile at a coal mine in Britain after the passage of the tunnel shield. Soil settlement in Bruxelles metro tunnel is presented in **Figure 2.8** where the magnitude of the transverse settlement profiles increases with the advance of the tunnel shield. It can be seen that the maximum surface settlement occurred above the tunnel centreline and the magnitude of soil settlement reduced when the offset to tunnel centreline increased.

To extensive field measurements by Nyren (1998)

Nyren (1998) reported extensive, high quality and detailed field measurements of three-dimensional soil displacements from the Jubilee Line Extension project at St. James's Park site, London. The project consisted of twin tunnels constructed sequentially. For consideration of the measured data independently from the effect of the other tunnel construction, only field measurement data immediately after the completion of the first tunnel construction, the westbound tunnel, is presented here. The tunnel diameter $D = 4.85\text{m}$ and was at depth $z_0=31\text{m}$.

The map of the locations of the instrumentation in relation to the position of the tunnel is given in **Figure 2.9**. Details of the instrumentation can be found in Nyren (1998). The time line of the survey and position of the extensometer instrumentation in relation to the tunnel advance is presented in **Figure 2.10**.

The final 3D surface displacements profile immediately after the construction of the westbound tunnel measured by four different methods showed consistent results with a difference generally within $\pm 1\text{mm}$ (**Figure 2.11**). The longitudinal surface horizontal displacement, u , along the tunnel centreline was very small. The maximum transverse surface horizontal displacement, v , was observed at 15m (approximately $z_0/2$) from the tunnel centreline. The vertical surface settlement, w , was similar to that observed in other projects, with the maximum occurring above the tunnel centreline.

Subsurface settlements and horizontal displacements were measured by extensometers and electrolevel inclinometers respectively. Measurement lines A and C were positioned near the two sides of the tunnel and B positioned above the tunnel centreline (depicted in **Figure 2.9**). **Figure 2.12** presents the development of the subsurface settlement measured

by those three extensometers in relation to the advance of the tunnel face. For extensometer Bx, the instrumentation was only available up to the depth of 28m to avoid obstructing the tunnel excavation.

It can be seen that magnitude of the soil settlement increased as the tunnel advanced. The subsurface settlement profile with depth showed a constant magnitude (vertical line) before the tunnel face went past the measurement line. After the passage of the tunnel face, the subsurface displacement increased with depth. Interestingly, the profile of the subsurface settlement with depth appeared to maintain an analogous trend as the tunnel continued to advance despite the increase in the magnitude of settlement. Nyren (1998) observed that as the distance from the tunnel face to the measurement line (after shield passage) increased from 20m to 45m, the additional settlement was less than 0.5mm.

Figure 2.13 illustrates the development of subsurface horizontal displacements measured by electrolevel inclinometers in relation to the advance of the tunnel. The vertical profile of horizontal displacement measured by electrolevel inclinometers Ai and Ci showed the maximum magnitude near the tunnel spring line. **Figure 2.14** illustrates the comparisons on the development of the surface settlement $w_{surface}/w_{max}$ with the volume of settlement trough V_S/V_{Smax} during the construction of the two tunnels in the project.

It is evident that the development of the surface settlement above the tunnel centreline is analogous to that for the volume of settlement trough. The short-term settlement at a measurement point reached its maximum value when the tunnel face went past the measurement line by a distance of more than z_0 .

2.5.2 Centrifuge modelling

Brief introduction to centrifuge modelling

In centrifuge modelling, the geotechnical events are investigated using small scale models subjected to acceleration fields of magnitudes many times Earth's gravity (Taylor, 1995). As a consequence, gravity dependent factors including dimensions and soil stresses in the prototype and processes are correctly reproduced. Well established centrifuge scaling laws enable the researchers to design representative models and interpret observations from small scale models that relate to full scale prototypes.

Most geotechnical events involve the interaction between soils and structures. With centrifuge modelling techniques the behaviour of soil, structures (such as foundations, retaining walls and tunnels) and construction events (e.g. excavation, tunnelling) can be replicated. Consequently, the interaction between the soil and the structure can be modelled as a real time event and observed closely.

With recent developments in instrumentation, desired data such as surface and subsurface ground deformations and pore water pressures can be obtained and stored for further analysis. Another advantage of centrifuge modelling is it allows a parametric study to be carried out with high repeatability and hence reliable results are expected (Taylor, 1984). Therefore, centrifuge modelling has been used to investigate soil behaviour in a wide range of geotechnical engineering including tunnelling.

Application of new technology in centrifuge modelling technique

Tunnelling is a 3D event and it is very complicated to conduct full 3D modelling. Efforts have been made to replicate the principal characteristics of the tunnelling event in centrifuge modelling (Hisatake & Ohno, 2007; da Silva, 2016). Recent developments in technology have allowed the centrifuge modeller to fabricate sophisticated equipment to serve research purposes.

One of the interesting applications of technology into centrifuge modelling is the development of a small scale Tunnel Boring Machine for centrifuge modelling reported by Hisatake & Ohno (2007). By utilising the model TBM in centrifuge modelling, Hisatake & Ohno (2007) were able to investigate soil displacements caused by an advancing tunnel reinforced by pipe roofs.

However, fabricating a model TBM robot and incorporating it into a centrifuge facility was not a straightforward task. Hisatake & Ohno (2007) could only measure the displacement at the model surface and subsurface soil deformations were not recorded. The presence of the model TBM might have prevented other measurement systems being used hence the limitation in the recorded data. Thus, simplification in modelling procedure and technique is usually needed while a representative outcome is also required.

The last decade has witnessed the application of new technologies to centrifuge modelling in various ways which extend the capability of the technique in studying the soil behaviour including the use of imaging analysis for high quality soil deformation measurements, 3D printing for fabricating delicate and precise equipment, fibre optics for measuring strains in soil etc. Some of these are used in this research and described in detailed in Chapter 3.

Simplifications in centrifuge modelling

Observations from field measurements showed that the settlement troughs for single tunnel projects were nearly symmetric and the increase in the magnitude of settlement after the tunnel face had passed the measurement line by a distance of z_0 was negligible (Attewell & Woodman, 1982; Nyren, 1998). Therefore, 3D models can be simplified into 2D models for the purpose of modelling the soil deformations behind the tunnel shield.

Previous research using 2D centrifuge modelling has enabled the investigation of soil response to tunnelling (Mair, 1979; Taylor, 1984; Grant, 1998; Divall, 2013). One drawback of this simplification is that the 2D model does not take into account the ground movement into the tunnel face (component 1-a in **Section 2.3**), and only movements in the plane perpendicular to the tunnel centreline are simulated. To some extent, this may affect the distribution of the soil movements.

3D centrifuge modelling

In studies where non-axisymmetric soil behaviours to tunnelling are the main objects of the study then a 3D modelling approach must be considered.

Mair (1979) carried out a series of 3D centrifuge tests to investigate the effect of the unsupported length P on the soil deformation mechanisms and tunnel heading stability and those results were presented in **Section 2.4**.

A series of 3D centrifuge tests was carried out by Boonyarak & Ng (2015) to investigate the effect of tunnel construction sequence and cover depth on crossing-tunnel interaction. The tunnels were modelled by a set of rings containing heavy fluid which had the same density as the soil model. The tests were carried out by consequently draining heavy fluid

out of the rings to simulate the volume loss as a result of tunnel excavation sequence. That allowed the complicated crossing-tunnelling interaction to be modelled and useful data was obtained.

Calvello & Taylor (1999), Hisatake & Ohno (2007), Date *et al.*, (2008) and Yeo (2011) made use of 3D centrifuge modelling to carry out sophisticated studies into the effects of non-axisymmetric soil reinforcement systems in tunnelling events which are presented in **Sections 2.6** and **2.7**.

Indeed, important contributions to the current understanding of tunnelling have been made using the centrifuge modelling techniques, and they have been used to solve practical problems, some of which are reported in the following sections.

2.5.3 Empirical method

Most of the empirical methods for predicting the surface settlement trough after tunnel construction has been completed, i.e. when the settlement is at its maximum value, were developed using a plane strain approach. From the several field measurements reported in **Section 2.5.1**, it is evident that the transverse settlement troughs have a similar shape regardless of the soil condition, excavation technique, tunnel size and depth. This pattern has been recognised by previous researchers based on a substantial number of case studies. Many authors (Martos, 1958; Peck, 1969; O'Reilly and New, 1982) demonstrated that the transverse surface settlement trough caused by tunnelling can be well described by an inverse Gaussian function as below and shown in **Figure 2.15**;

$$w = w_{max} \exp\left(\frac{-y^2}{2i_y^2}\right) \quad (2.7)$$

where w is surface settlement,

y is the distance from the tunnel centreline to the settlement point in the transverse direction (along the Y direction in **Figure 2.1**),

w_{max} is the maximum settlement (usually corresponding to $y = 0$), and

i_y is the distance from the centreline to the point of inflexion in transverse direction (along the Y direction in **Figure 2.1**).

It can be seen that the width of the settlement trough (**Figure 2.15**) extends up to $3i_y$. Therefore, a good prediction on i_y can help in estimating the width of the settlement trough and the area affected by ground settlement.

The above equation was first proposed by Martos (1958) regarding the settlements above mine openings and it has been used extensively to predict ground surface settlement due to single tunnel construction in practice. Good agreement between this method and the measured data has been reported (Schmidt, 1969; Nyren, 1998; Dimmock, 2003).

By integrating **Equation 2.7** with respect to y , the relationship between the area of the settlement trough, or normally termed as volume per unit length, V_S with w_{max} can be derived as;

$$w_{max} = V_S / \sqrt{2\pi} i_y; \quad (2.8)$$

Estimation of volume loss

In tunnelling, the maximum settlement is of great interest as it is indicative of how much damage the induced ground deformations could cause to nearby buildings and structures. By estimating V_S , w_{max} can be predicted. The volume of the settlement trough V_S , normally expressed as volume loss, V_L , depends on many factors; namely soil condition, tunnelling technique, tunnel geometry and quality of workmanship. Therefore, it is difficult to predict volume loss V_L . As a consequence, V_S is commonly estimated based on engineering judgement and case studies of similar projects. Typical volume losses from different case studies are presented in **Table 2.2**.

Another approach to estimate the volume loss was proposed by Mair *et al.*, (1981). In their method, centrifuge test data were analysed to establish the relationship between tunnel stability ratio, load factor and volume loss. The concept of load factor in tunnelling was introduced by Mair (1979) as a ratio between tunnel stability ratio with tunnel stability ratio at collapse;

$$LF = \frac{N}{N_{TC}} \quad (2.9)$$

Macklin (1999) reassessed the relationship between load factor and volume loss proposed by Mair *et al.*, (1981) using 22 case history data in stiff overconsolidated clay and produced the chart presented in **Figure 2.16**. Despite the variety in soil conditions, tunnel construction techniques and tunnel geometries the majority of the data points lie within a range enclosed by the thick dashed lines on the plot. The upper bound and lower bound lines are parallel to the linear regression line expressed by the equation;

$$V_L = 0.23e^{4.4(LF)}; \text{ for } LF \geq 0.2 \quad (2.10)$$

By applying load factor into **Equation 2.10**, the value of volume loss can be estimated. However, the calculation of load factor LF requires both the tunnel stability ratio and stability ratio at collapse. It is somewhat unpractical and dangerous to have the tunnel close to a collapse state and hence the tunnel stability at collapse can be studied by centrifuge modelling (**Figure 2.6**) or estimated by the mean of plasticity theorems (Davis *et al.*, 1980). The tunnel stability ratio can be calculated using **Equation 2.1** with the tunnel support pressure as the air support pressure or the pressure in the chamber of the TBM depending on the tunnelling technique.

In centrifuge modelling, the tunnel support pressure can be measured easily by a pressure transducer. However, for some cases, the tunnel support pressure was not measured. For such a case, Dimmock (2003) used the stability ratio from a reference site (Westminster) to estimate the tunnel stability ratio for the St. James's Park site and the results were compared well with Macklin (1999). Divall (2013) reported the volume loss estimated using the Macklin (1999) method was close to the measured volume loss in plane strain centrifuge tests.

Dimmock (2003) and Burland *et al.*, (2004) noted that a drawback in the Macklin (1999) approach was the assumption for the unsupported length P . Macklin (1999) assumed the unsupported length to extend to the tail of the shield which is not universally applicable. To deal with this difficulty, Dimmock (2003) divided the volume loss into four components for open face shield tunnelling:

- (i) In front of the shield volume loss is caused by:
 - a. soil movement towards the unsupported excavated face, and
 - b. movement associated with the unsupported tunnel heading.
- (ii) Behind the front of the shield volume loss caused by:
 - a. the passage of the shield, and
 - b. over cut and tunnel lining deformation.

By assuming the excavation procedure does not result in instability at the tunnel heading, the Load Factor approach can be used to predict the volume loss in component (i) for any actual unsupported heading ahead of the edge of the tunnel shield (Dimmock, 2003). The volume loss caused by component (ii) can be determined by estimating the size of the overcut around the shield, the gap between the shield and the tunnel lining and the tunnel lining deformation.

In centrifuge modelling, by using appropriate testing apparatus, the volume loss components can be studied separately and the difficulty in determining the unsupported length can be overcome.

If V_S and i_y are known then the transverse settlement profile can be determined using **Equation 2.7**.

Estimation of settlement trough width parameter i_y

While V_S dictates S_{max} (**Equation 2.8**), i_y governs the width of the settlement trough. Following the analysis of field data, O'Reilly & New (1982) proposed the relationship between i_y and z_0 as below;

For tunnels in clay;

$$i_y = 0.43z_0 + 1.1 \quad (2.11)$$

For tunnels in sand;

$$i_y = 0.28z_0 - 0.1 \quad (2.12)$$

For practical purposes, i_y is often determined by;

$$i_y = K(z_0 - z) \quad (2.13)$$

where K is a dimensionless trough width parameter and depends on the soil properties.

It is suggested that $K = 0.5$ for clay and 0.25 for granular soils are suitable. Later studies have shown that K varies from 0.4 to 0.7 for stiff clay to soft silty clay.

Clough & Schmidt (1981) suggested another commonly used equation for i_y in clay as:

$$i_y = \frac{D}{2} \left(\frac{z_0}{D} \right)^{0.8} \quad (2.14)$$

Combining **Equations 2.5, 2.6, 2.8** and **2.13** gives;

$$w_{max} = 0.313 \frac{V_L D^2}{K(z_0 - z)} \quad (2.15)$$

From **Equation 2.15** it can be deduced that for a given tunnel diameter and volume loss in the same soil condition (constant K) then the maximum surface settlement is inversely proportionally to the depth of the tunnel (Mair *et al.*, 1993). Therefore, one of the methods to reduce the maximum settlement is to increase the tunnel depth.

Field measurements reported by Tadashi *et al.*, (1999) showed that the value of i_y at the surface remained constant during the tunnel construction. Constant values of i_y were observed at different stages in centrifuge tests reported by Mair (1979) and Grant & Taylor (2000). A detailed study on the variation of i_y during the tunnel construction was conducted by Nyren (1998) who showed that the value of i_y decreased by 2 to 4m as the

tunnel approached closer to the measurement line. Once the tunnel face moved past the measurement line then the estimated i_y stayed constant.

Most of the prediction methods on tunnelling-induced ground deformations were concerned with ground surface settlement. Nowadays, tunnels are often constructed in crowded underground spaces consisting of underground utilities such as water supply, sewer systems, deep foundations and basements. This makes the understanding of subsurface ground deformations increasingly important. However, limited field data are available on the subsurface soil movements due to the difficulties and the cost of field measurement. Relatively few methods are available for the prediction of subsurface soil settlement and a commonly used approach is that developed by Mair *et al.*, (1993) which has proved to produce good predictions.

Mair *et al.* (1993) investigated subsurface ground deformations induced by tunnelling by using site data obtained from previous projects and centrifuge tests results. It was found that the Gaussian distribution curve well represents the subsurface troughs with the parameter K increasing and i_y decreasing with depth. This means the maximum soil settlement increases and the width of the settlement trough decreases with depth. Detailed field measurements from Nyren (1998) and Dimmock (2003) confirmed this observation. The relationship of i_y and K with depth suggested by Mair *et al.* (1993) is described below;

$$\frac{i_y}{z_0} = 0.175 + 0.325 \left(1 - \frac{z}{z_0} \right) \quad (2.16)$$

$$K = \frac{0.175 + 0.325 \left(1 - \frac{z}{z_0} \right)}{1 - \frac{z}{z_0}} \quad (2.17)$$

Figure 2.17 shows the distribution of i_y with depth (both normalised by z_0) using **Equation 2.16** in comparison with case history data of tunnelling projects in clay. Using **Equation 2.16** shows better correspondence with the case history data compared to **Equation 2.13** with the assumption $K=0.5$ (dashed line in **Figure 2.17**). This can be further assessed in **Figure 2.18** where the prediction of K with depth using **Equation 2.17**

is compared with case history data. As there was no measurement close to the tunnel crown, caution should be applied when predicting K in that area.

It is evident that the width of the subsurface settlement troughs was underestimated (smaller i_y) when K was assumed to be constant and equal to 0.5 (dashed line in **Figure 2.17**). This underestimation may lead to unpredicted damages to nearby underground services which would have been determined as being out of the affected zone of the subsurface settlement troughs using the assumption of constant K with depth.

The underestimation of the width of the subsurface settlement troughs when using **Equations 2.13** and **2.14** proposed by O'Reilly and New (1982) and Clough and Schmidt (1981) was further upheld by Moh *et al.*, (1996) and Dyer *et al.*, (1996). Grant (1998) observed that by applying **Equation 2.18** to the field data from Moh *et al.*, (1996) and Dyer *et al.*, (1996), the profile of K with depth of these two projects are comparable to the distribution of K calculated in Mair *et al.*, (1993) as shown in **Figure 2.19**.

Dimmock (2003) observed that the profiles of the inferred trough width parameter K with depth in the two projects Elizabeth House site and Heathrow Express Trial Tunnel used SCL/NATM methods were below the curve suggested by Mair *et al.*, (1993) (**Figure 2.20**). That implies SCL/NATM tunnelling method resulted in narrower settlement troughs than open-face shield tunnelling. Similar narrower settlement trough width was also observed in Green Park tunnelling project using an Earth Pressure Balance Machine (**Figure 2.21**). Thus, Dimmock (2003) suggested that the relationship between K and depth also depends on the tunnelling method. By assessing field measurement data of projects using open face shield tunnelling, Dimmock (2003) modified the Mair *et al.*, (1993) equation for London clay;

$$K = \frac{0.225 + 0.275 \left(1 - \frac{z}{z_0}\right)}{1 - \frac{z}{z_0}} \quad (2.18)$$

This modification offered a slightly better fit with the measured soil settlement induced by open face tunnelling in westbound tunnel at St. James's Park site (**Figure 2.21**). However, the universality of this equation is not yet confirmed and more field data and

physical experiments are needed to enable more confidence in using this equation to predict the settlement trough width parameter K with depth.

Estimation of parameters of settlement trough profile

When surface settlement measurements are available, a Gaussian curve may be fitted which allows estimation of the trough width parameters at the surface and with depth and calculation of volume loss. It is a common practice that the ground settlement induced by tunnelling can be very small and the distance between the measurement points are relatively large compared to the width of the settlement trough. That makes the fitting of the Gaussian curve more difficult.

Jones & Clayton (2013) proposed a nonlinear regression method to estimate parameters i_y and V_L . The procedure involves varying the two parameters i_y and V_L and calculating the corresponding sum of absolute errors (SAE). The “best-fit” is defined as the combination of i_y and V_L that results in the smallest SAE . The SAE is calculated as the difference between the measured data and the Gaussian curve data;

$$SAE = \sum_{m=1}^n \left| \frac{V_s}{\sqrt{2\pi}i_y} \exp\left(\frac{-y_m^2}{2i_y^2}\right) - w_m \right| \quad (2.19)$$

where n is the total number of measurement points,

w_m is the measured data.

The advantage of this method is it is straightforward and involves only a simple spreadsheet to obtain an objective estimation of i_y and V_L .

Horizontal soil displacement

Horizontal soil movement can lead to damage of nearby structures. Horizontal movements are more difficult to measure and relatively few data from case histories have been published. O’Reilly & New (1982) proposed the relationship between vertical and horizontal soil displacement at a point at depth z and y offset from the tunnel centreline as below;

$$v_{(y,z)} = \frac{yW_{(y,z)}}{z_0 - z} \quad (2.20)$$

With $w_{(y,z)}$ as;

$$w_{(y,z)} = w_{max}^z \exp\left(\frac{-y^2}{2i_y^z}\right) \quad (2.21)$$

where i_y^z is the settlement trough width parameter at the depth z .

At the surface **Equation 2.20** is simplified to;

$$v_{(y,0)} = \frac{yW_{(y,0)}}{z_0} \quad (2.22)$$

It is worth noting that **Equations 2.20** and **2.21** are for soil displacement prediction for a plane strain situation i.e. the tunnel face has passed the area of consideration by a sufficient distance which is more than z_0 . Hong & Bae (1995) compared the measured horizontal displacement in a tunnelling project in Korea with prediction using **Equation 2.22 (Figure 2.22)**. In general, the prediction fits favourably with the field measurement except the far field data. However, soil displacements in the far field area are very small and this underestimation is negligible.

Longitudinal soil settlement

Prediction of soil settlement in the longitudinal direction of the tunnel is also of interest when a three-dimensional scenario is considered. Attewell & Woodman (1982) showed that the cumulative probability curve fits reasonably well with the longitudinal settlement curve. Attewell & Woodman (1982) observed from several field data that the surface settlement above an unsupported tunnel face w_{face} in a stiff clay is approximately equal to half of the maximum final settlement w_{max} . In contrast, for tunnels constructed in soft clays with the face supported by compressed air, the surface settlement above the tunnel face is smaller than $0.5w_{max}$. Nyren (1998) and Dimmock (2003) reported the ratio between the surface settlement above the tunnel face and the maximum surface settlement w_{face}/w_{max} varies from 0.25 to 0.5. Attewell & Woodman suggested the following equation for the longitudinal settlement trough;

$$w_{(x,y,z)} = w_{final} \exp \left[\frac{-y^2}{2(i_y^z)^2} \right] \left\{ G \left(\frac{x - x_i}{i_x^z} \right) - G \left(\frac{x - x_f}{i_x^z} \right) \right\} \quad (2.23)$$

where x, y, z are the Cartesian coordinates of any point in the ground deformation field as shown in **Figure 2.1**;

w_{final} is the final surface settlement above the tunnel centreline;

i_x is the settlement trough length parameter;

x_i is the initial or tunnel start point ($y = 0$);

x_f is the tunnel face position ($y = 0$);

$G()$ is the function of normal probability curve;

There has been not much information on the relationship between the longitudinal settlement trough length parameter i_x , and transverse settlement trough width parameter i_y (Dimmock, 2003). Nyren (1998) observed that the ratio i_x/i_y varies from 0.7 to 0.8 based on field measurements at St James's Park green field site on the Jubilee Line Extension project. A smaller i_x means the longitudinal settlement trough is relatively shorter. Interestingly, Dimmock (2003) reported that the longitudinal surface settlement trough given by the above equation with the assumption $i_x = i_y$ showed good agreement with field data from the Southwark Park green field and Elizabeth House sites at the Jubilee Line Extension project.

Summary

With sufficient reference data from similar projects, empirical methods can be performed by simple calculations to predict the ground displacements due to tunnelling. In the early stages of tunnel design, the prediction results will aid the tunnel designers to choose suitable tunnelling methods and reinforcement measures if required. Monitoring data from the field during the construction stage can be used to calibrate the parameters for improved prediction in the latter stages of the project.

2.5.4 Numerical modelling

Numerical modelling has been widely used in the recent decades and provided considerable contributions for settlement prediction due to tunnelling. One of the methods in numerical modelling is the Finite Element Method (FEM).

There have been several approaches to model the ground movements due to tunnelling in FEM. One of the methods involves reducing the radial stresses in the ground at the tunnel boundary. The magnitude of the reduction of the radial stress is related to the desired volume loss. Another method is to replace the soil in the tunnel with a constant radial support stress then reduce the stress to generate the ground movement. This approach is comparable to the mechanism of reducing the tunnel air pressure in centrifuge modelling which will be described later in **Section 4.5.3**.

Essential information that needs to be taken into account in FEM modelling includes the boundary conditions, constitutive soil model, and construction procedure. Boundary conditions play an essential role in the FEM to model the behaviour of the entire soil mass. Choosing a suitable constitutive soil model is critical to any FEM. One of the utmost requirements for a soil model is the ability to model correctly the non-linear behaviour of soil. Nowadays, numerical modelling software programs allow users to utilise a variety of constitutive pre-programmed models to meet the investigation aims.

The development of computer technology has enabled numerical methods to be able to perform four-dimensional modelling where time is the fourth dimension. This advancement offers a more sophisticated modelling than in two-dimensions which can only investigate plane strain conditions. Initial conditions are vital input factors that heavily affect the output of numerical modelling. Essential initial conditions that need to be taken into account are, for example, stress history, and soil deformations prior to commencement of excavation. Therefore, a good understanding of the properties of and stress paths followed by the soil and the construction sequence will improve the quality of the prediction.

In practice, tunnelling requires continuous monitoring of the soil response to excavation to be used as the basis for the following construction procedure and adjustments if required (due to changes in soil conditions). With its capabilities, numerical modelling is

able to update the changes into its simulation and provides a better prediction to the soil response to tunnelling.

One of advantages of FEM is it can include structures such as buildings, foundations, retaining walls and soil reinforcement components such as FUS into the model together with the tunnel so that the interaction between soil and structure in tunnelling event can be investigated. Several researchers used FEM to study the effect of FUS in tunnelling and positive results have been obtained (**Section 2.7.3**).

2.5.5 Plasticity theorems

Prediction of the maximum load that can be applied to a structure is important to ensure safety for every construction. In theory, this problem could be solved by simultaneously satisfying conditions of equilibrium and compatibility in which the properties of materials are taken into account (Atkinson, 1981). However, this type of calculation is not always easy hence an alternative approach was proposed to estimate the collapse load. An upper bound to the collapse load could be calculated by ignoring the equilibrium condition. Therefore, if the structure is loaded to this value, it must collapse. Similarly, by ignoring the compatibility conditions, it is possible to set a lower bound to the collapse load. Hence, if the structure is loaded to this value, it cannot collapse. Consequently, the true collapse load lies between the upper and lower bounds.

With regards to stability analysis using the theorems of plasticity, the soil is idealised as an elastic, perfectly plastic material with a strength equal to the undrained shear strength S_u , Davis *et al.*, (1980) addressed that this assumption is reasonable for many clays. **Figure 2.23** showed the predicted upper bounds and lower bounds were corroborated by the tunnel support pressures at collapse obtained from centrifuge tests conducted by Mair (1979). Using the bounds theorem in tunnel heading stability analysis provides a procedure for linking tunnel geometry and potential reinforcement support required.

Another usage of plasticity solutions in predicting the soil deformation due to tunnelling was proposed by Mair & Taylor (1993). In their method, the tunnel was idealised as in **Figure 2.24-a** with the clay assumed to behave as a linear elastic-perfectly plastic soil. The induced ground deformations around a tunnel heading were idealised as the unloading of a spherical cavity (**Figure 2.24-b**) or the unloading of a plane strain

cylindrical cavity (**Figure 2.24-c**). The displacement in the spherical cavity contraction is given by;

$$\frac{\delta}{a} = \frac{S_u}{3G} \left(\frac{a}{r}\right)^2 \exp(0.75N^* - 1) \quad (2.24)$$

where δ is the longitudinal displacement at radius r ,

a is the inner radius of the cavity (tunnel),

N^* is the stability ratio. For a deep tunnel, N^* is equivalent to the usual definition of the tunnel stability N in tunnelling (**Section 2.4**).

G is the elastic shear modulus (for isotropic conditions, the undrained Young's modulus $E_u = 3G$).

Soil movements due to tunnelling in clay can also be considered in term of contraction of a cylindrical cavity which is expressed as;

$$\frac{\delta}{a} = \frac{S_u}{2G} \left(\frac{a}{r}\right) \exp(N^* - 1) \quad (2.25)$$

Equations 2.24 and **2.25** show that (δ/a) is proportional to $(a/r)^2$ and (a/r) in spherical cavity and cylindrical cavity respectively which are depicted in **Figures 2.25**. The gradient of the lines in **Figures 2.25** increase exponentially with increasing tunnel stability ratio N as expressed in **Equations 2.24** and **2.25**.

Subsurface soil displacements around an advancing tunnel face obtained from field measurements were shown to be well predicted using this method (Mair & Taylor, 1993; Dimmock, 2003; Mair, 2006). One of the detailed field measurements of the longitudinal soil displacement in front of a tunnel face reported by Mair (2006) is presented in **Figure 2.26**. The tunnel depth was 110m and the soil displacement was measured by horizontal multiple-point extensometers installed in the centre of the tunnel face at two separate locations. It can be seen that the predictions were in line with the measured data. The inferred undrained Young's modulus from the slope of the line $E_u=469\text{MPa}$ which was close to the assumed design value $E_u=400\text{MPa}$ based on in-situ measurements.

2.6 Soil reinforcement measures

This section reviews the available protective measures for reducing the effects of tunnelling-induced ground deformations.

2.6.1 Overview of protective measures for tunnelling

Harris (2001) categorised protective measures for tunnelling as;

- Structural measure: increasing the capacity of the buildings and the structures to reduce the impact of the tunnelling-induced ground deformations;
- Ground treatment measure: improving the engineering response of the ground by imposing changes to the ground structure such as compensation grouting or ground freezing.
- In-tunnel measure: comprising of all the methods that are undertaken from within the tunnel heading during the excavation to control the induced ground movements at source.

In case an in-tunnel measure cannot be undertaken or the protective effects it provides are deemed inadequate, the first two types can be introduced as alternative or additional measures. In practice, two or three methods are used in combination to yield adequate protective effects in order to mitigate the damage to the surrounding building and structures caused by tunnelling-induced ground movements.

It is beneficial to provide the support effects to the ground as early as possible in the excavation cycles to minimise the induced ground deformations. For in-tunnel movement mitigation measures the reinforcements are introduced at the tunnel heading i.e. the source of ground deformations. Therefore, the reinforcing effect offered by in-tunnel measures can be expected to act immediately which minimises further development of tunnelling-induced soil deformations. This makes the in-tunnel measures favourable.

Two common in-tunnel measures are spiles and Forepoling Umbrella System that deliver similar reinforcing effects and are reviewed in the following sections.

2.6.2 Spile reinforcement at tunnel face

Figure 2.27 illustrates a tunnel reinforced by spiles (or also termed as facebolts). The principle of the spiles reinforcement measure is to improve the stiffness of the ground hence reduce soil deformations. The spiles are inserted to the tunnel face in the direction parallel with the tunnel axis from within the tunnel heading through the pre-drilled holes. The insertion of the spiles is followed by immediate injection of cement mortar (Lunardi, 2008).

The use of cement mortar is to fill the void between the holes and the fibre glass and thus increase the friction between the spiles and the ground. Fibre glass is normally chosen as material of spiles because of its high stiffness (compared to soft soil) which is necessary for reinforcement effect and its fragility that makes it easy to break during the excavation as the tunnel advances.

Lunardi (2008) suggested that fibre glass spiles are normally distributed evenly over the tunnel face and the embedded length is required to be longer than one diameter of the tunnel to provide adequate support. There have been several research projects undertaken to study the spiles reinforcement effects which are summarised below.

Parametric study of spiles by Calvello & Taylor (1999)

A series of centrifuge tests of a spile-reinforced tunnel face were carried out by Calvello & Taylor (1999). The length, quantity and distribution of spiles were the variables. The arrangements in the test series are shown in **Figure 2.28**. Plastic rods were used to model the spiles.

It was found that long spiles (beyond the zone of significant ground movement ahead of the tunnel face) concentrated near the tunnel periphery delivered significant reduction in ground movement.

Study on FUS and spiles by Date et al., (2008)

The combination of the two reinforcing measures spile and Forepoling Umbrella System (FUS) have been reported by Volkmann & Schubert (2007) and Lunardi (2008).

However, recommendations on selecting the parameters for the two systems were not provided.

Date *et al.*, (2008) conducted a series of centrifuge tests and numerical analyses on the reinforcing effects of forepoling and facebolts in shallow sandy ground tunnelling and the results showed the resemblance between the methods.

The model bolts were made of aluminium. The face bolts were installed perpendicularly to the tunnel face while the forepoling bolts were glued to the outside of the stiff lining which are illustrated in **Figure 2.29** together with the testing parameters.

The results can be seen in **Figure 2.30**. Both face and forepoling bolts showed their efficiency by reducing the ground settlement above the tunnel crown when compared with the unreinforced test. Similar to observations made by Calvello & Taylor (1999) on the effect of using spiles, the presence of face bolts reduced the affected area in front of the tunnel excavation and the face extrusion. On the other hand, the effect of forepoling rods in reducing the affected zone ahead of the tunnel face was not as apparent as observed in tests using face bolts tests (**Figure 2.30**).

Summary on spiles reinforcement

A drawback of pile reinforcement is that the excavation needs to cut the fibre glass as well as the soil. This requires more work to be done than that for excavation of ground only. More importantly, the excavated soil in tunnel using spiles is contaminated by the fibre glass and must be processed. This is arguably not environmentally friendly. In contrast, the use of the Forepoling Umbrella System does not generate contamination and the forepoles are not in the way of the tunnel advance. Moreover, the immediate support of the FUS provided by the steel forepoles make this method more attractive.

2.7 Forepoling Umbrella System

2.7.1 Introduction

The Forepoling Umbrella System comprises steel pipes in a canopy shape and works as a roof over the tunnel heading that shares the vertical load induced by the ground above. Therefore, the Forepoling Umbrella System contributes to decreasing the deformations caused by excavation and increasing stability in the working area.

This system is sometimes referred to as a pipe roof support, Steel Pipe Umbrella Arch, Pipe Fore-Pole Umbrella or Steel Pipe Canopy (Volkman & Schubert, 2007). A summary of the terminology of Forepoling Umbrella System and other relating reinforcement measures can be found in Oke (2016).

Oke (2016) investigated the effects of soil reinforcement measures including the Forepoling Umbrella System in tunnel construction in rock. The results showed that the Forepole Umbrella System, combined with other soil reinforcement measures, delivered a reduction of surface settlement from 20% to 76% compared with unreinforced sections. These studies included data from field measurement in some tunnelling projects (Ocak, 2008; Aksoy & Onargan, 2010). It is worth noting that in these projects, the Forepoling Umbrella System was used in conjunction with other reinforcement measures (e.g. spiles, soil nailing) hence the exact contribution from the Forepoling Umbrella System cannot be clearly identified.

Gall & Zeidler (2008) reported applications of the Forepoling Umbrella System to control ground movements due to tunnelling in clay in urban areas where allowable settlements are very limited. Small ground settlements were observed as an achievement in some major projects which applied the Forepoling Umbrella System such as Victoria Station Upgrade and King Cross Station Redevelopment (Gall & Zeidler, 2008). Shirlaw *et al.*, (2003) reported the use of the pipe roof system to ensure the safety of the construction of a new tunnel in which the crown was only approximately 4m beneath the inverts of the two existing tunnels in operation.

2.7.2 Steel pipes installation

The installation of a new row of Forepoling Umbrella System requires a local widening of the tunnel profile to provide space for drilling and insertion of steel pipes. **Figure 2.31** shows the installation of steel pipes into the tunnel crown. Volkmann & Schubert (2007) summarised two different methods for Forepoling Umbrella System installation which are the pre-drilling system and the cased-drilling system.

In the pre-drilling system, the holes for installation are drilled first then the steel pipes are inserted into the holes after the withdrawal of the drill bit. Before the insertion of the steel pipes, drilled holes are unsupported and the closure of these holes might occur especially in soft soils.

In the cased-drilling system, the steel pipes are inserted immediately behind the drilling bit and provide instant support for the installation holes. In weak ground, a pre-drilling system may result in a higher ground settlement than a cased-drilling system (Volkmann & Schubert, 2007).

2.7.3 Current understanding on Forepoling Umbrella System

Despite the increase in Forepoling Umbrella System use, guidelines on Forepoling Umbrella System design is still limited (Volkmann & Schubert, 2007; Yeo, 2011; Oke, 2016). The specification for tunnelling Third edition (2012) issued by the British Tunnelling Society (BTS) and Institution of Civil Engineers (ICE) refers to forepoling but gives no guidance on the factors that affect the proficiency of forepoling in controlling ground movements. As a consequence, this subject has attracted research and the findings are reported below.

Centrifuge tests and FE analysis on FUS by Vrba & Barták (2007)

Vrba & Barták (2007) conducted analysis on the effect of forepoling in tunnel construction in clay. Centrifuge modelling and numerical analysis were implemented and well-matched results were obtained. Steel strips were used to model the forepoling roof. The testing arrangement is shown in **Figure 2.32**. Significant effects of the pre-lining structure on the stability of the tunnel were observed. The test results implied that

increasing the embedded length EL of the forepoles into the ground delivered increased stability to the tunnel face. Similarly, results from centrifuge tests conducted by Hisatake & Ohno (2007) showed the benefit of having FUS in reducing the maximum surface settlement.

Centrifuge test by Juneja et al., (2010)

Juneja *et al.* (2010) used centrifuge modelling to investigate the effect of forepoling reinforcement on a tunnel face. The brass rods were used to model the forepoles. Speswhite kaolin was used for the clay model. The variables were the lengths of the unlined portion P and the Forepoling Umbrella System. Surface settlements were measured by LVDTs. In agreement with Vrba & Barták (2007), Juneja *et al.*, (2010) found that that the use of forepoles reduced the extent of the settlement trough ahead of the tunnel face while the width of the settlement trough remained unaffected (**Figure 2.33**).

Results from centrifuge tests and FE analysis from Zeidler & Yeo (2007)

Zeidler & Yeo (2007) conducted 2D and 3D FE analysis on the performance of the FUS in the Fort Canning Tunnel, Singapore. The tunnel was constructed in residual soil. The effects of the FUS was reflected in the reductions on the surface settlement. However, when compared with field measurements both 2D & 3D FEA overestimated the actual surface settlement.

The reasons were explained as the use of a simple soil model that does not consider the nonlinear behaviour of soil and the difficulties in realising the construction sequence into the FEA model. Zeidler & Yeo (2007) also suggested that using centrifuge modelling will be beneficial to further assess the stability of a tunnel heading reinforced by FUS.

Centrifuge test results by Yeo (2011)

A comprehensive series of centrifuge tests on the effects of the canopy arch to the tunnel stability were conducted by Yeo (2011). The test arrangement modelling a 3D tunnel heading is shown in **Figure 2.34**. The variables in the testing series were P/D , L/D and

the number of forepoles. The cover depth was constant at $C/D = 1$. The clay model was consolidated to 100kPa by hydraulic consolidometer powered by oil pressure.

This oil pressure source was also used to actuate the apparatuses on the centrifuge. However, because the centrifuge system was in regular use, the oil pressure to the consolidometer was often interrupted. This resulted in the inconsistent consolidating pressure applied to the clay sample, hence different stress path histories and undrained shear strengths in the model. Therefore, most of interpretations from Yeo (2011) focused on the trend and mechanisms of the soil deformations and the tunnel stability, not the soil displacement magnitude. Nevertheless, some effects of the tunnel geometry variables, FUS and their parameters have been observed.

The collapse mechanisms of the unreinforced tests with three different unsupported lengths $P/D = 0, 0.5$ and 1 were analysed first to form the reference basis for comparison with the reinforced tests. Three different collapse mechanisms were observed with different P/D ratios. The dominant collapse mechanism in tests featured the unsupported lengths $P=0$ and $P=D$ were the face-mechanism and the roof-mechanism respectively. While the unsupported length $P=0.5D$ led to a combination of face and roof mechanism. These observations confirm the association between the unsupported length with the corresponding soil deformation mechanisms suggested by Mair (1979) (**Section 2.4**).

The introduction of a FUS with short embedded length did not change the collapse mechanism compared with the reference test. Very long forepoles enabled the heading to remain stable with a very low support pressure. One of the interesting observations was the formation of a void within the soil mass above the FUS as a result of the movement of soil and water through the gap between the model forepoles into the tunnel heading. Deformations of the rods post-test are shown in **Figure 2.35**.

It is noted that the deformation magnitude of the rods increases from the lower to the higher elevation rods. This denotes the soil mobilisation at the upper part of the tunnel was more significant than the lower portion of the tunnel. By comparing this observation with the four upper bound collapse mechanisms proposed by Davis *et al.* (1980), it implies that the collapse mechanism was relevant to mechanism A (**Figure 2.4**). This comparison is relevant to the suggestion made by Davis *et al.*, (1980) that shallow tunnels are likely to have mechanism A.

Field measurement from Volkmann & Schubert (2007)

Volkmann & Schubert (2007) reported the results obtained from a site measurement of a tunnel construction in rock using a pipe roof. The rock mass consisted of mainly faulted mudstones, claystone and sandstone (Volkmann *et al.*, 2006). The diameter of the tunnel was 10m. The cover depth at the measured section was approximately 15m. The tunnel was constructed in 2m rounds using NATM. Displacements of the top most steel pipe were measured by an inclinometer chain system which is provided in **Figure 2.36**. The development of displacement of the steel pipe was examined with the advance of the tunnel.

Figure 2.36 shows the settlement induced from the excavation of the first three rounds after the installation of the pipe roof was small and the settlement increased as the later rounds were excavated. Volkmann & Schubert (2007) explained that as the tunnel face advanced, the extent of the soil beneath the steel pipe reduced. That led to the support from the soil to the steel decreased hence the increase in the settlement of the steel pipe. This confirmed the similar findings reported by Vrba & Barták (2007) and Juneja *et al.*, (2010) about the influence of the long embedded length. A new row of pipe roof is required before the ground settlements reach the maximum allowable value. Volkmann & Schubert (2007) suggested that new rows of pipes are not affected by previous activities but the construction process after the installation activates the support function of the pipes.

Volkmann & Schubert (2007) suggested that the stiff shotcrete arch and the soil in front of the tunnel face which lies beneath the pipe roof created foundations for the longitudinal arching effect to counteract the load that the pipe roof was bearing. A similar assumption was made by Carrieri (2002) in which ground in front of tunnel face was considered as an elastic foundation and the back end as a spring support for the pipe roof (**Figure 2.37**). Therefore, the strength and stiffness of the pipe roof are dependent not only on the pipe material but also on the properties of the ground and the tunnel lining.

Plane strain centrifuge tests by Divall et al., (2016)

Divall *et al.*, (2016) carried out a series of eight 2D plane strain centrifuge tests to investigate the effect of the positions of a steel pipe canopy on tunnel stability and the

induced ground deformations in a Speswhite kaolin clay model. The tunnel was at the depth of $C/D = 2$ and was reinforced by the model pipe canopy with the variables presented in **Figure 2.38**. The effect of the different arrangements of the FUS was assessed by comparing the maximum settlement and the tunnel heading stability in the tests which are presented in **Figures 2.39** and **2.40** respectively.

The results showed the positioning of the FUS that interferes directly with the formation of a plastic collapse mechanism (Davis *et al.*, 1980) offers both significant increase in stability and widening the settlement trough. Divall *et al.*, (2016) reported that little overall benefit was gained by only having FUS to protect tunnel crown and invert zones alone.

They recommended the inclusions of forepoles should extend to at least the spring line and preferably beyond. By adopting a 2D modelling approach, this work was able to determine the effect of different arrangements of the forepoles independently from the unsupported length P , the embedded length EL and the foundation effect from the tunnel lining.

2.8 Summary

The tunnelling technique, corresponding sources of ground movements and the available methods for prediction of the soil displacements have been discussed. Current understanding on the performance of Forepoling Umbrella System contributed by previous research obtained from field measurement, centrifuge modelling and numerical analysis have been reviewed.

Case histories highlight the benefits of the Forepoling Umbrella System in reducing soil movements and mitigating the risks towards nearby buildings and subsurface structures such as existing tunnels in operation. An increase in the number of publications reported the use of Forepoling Umbrella Systems in tunnelling projects has been observed over the last decades. From there, insight into the effects of a Forepoling Umbrella System on tunnel stability and the relationship of the system parameters to its performance has been studied. Despite the research conducted to investigate the effects of a Forepoling Umbrella System, the understanding in the following aspects are still limited hence being the main focus of this research.

The literature review showed that the tunnel geometry including the cover depth C/D and the unsupported length P/D dictate the soil deformation mechanisms (Davis *et al.*, 1980). Previous studies of the Forepoling Umbrella System only conducted their experiments and analyses with constant C/D (**Section 2.7.3**). The reinforcement effectiveness of the Forepoling Umbrella System at different C/D ratios (i.e. different soil deformation mechanisms) is expected to be different and this influence needs to be investigated.

The bending stiffness of forepoles is an important feature of the performance of the Forepoling Umbrella System. The use of different materials for the model forepoles have been reported by different researchers but it is difficult to make comparisons that quantify the effect of forepoles bending stiffness. Hence, having bending stiffness of forepoles as a variable for a parametric study is valuable.

Detailed soil displacement measurement in case histories of tunnelling projects using the Forepoling Umbrella System were few and the level of details in the soil displacements was found to be limited (Volkman & Schubert 2006; Gall & Zeilder, 2008).

Previous studies were able to observe the subsurface soil settlements either in plane strain (Volkman & Schubert, 2006; Divall, 2016) or a single plane through the centre line of a 3D heading (Calvello & Taylor 1999; Yeo, 2011; Juneja *et al.*, 2010) and limited data on horizontal soil displacements were reported. These are attributed to the limitations of the testing apparatus, available measurement instrumentation in physical modelling or the complexity of the model used in numerical analysis to replicate both small-strain behaviour of soils and the interaction between soil and forepoles.

Using a measurement system that is capable of accurately recording subsurface soil displacements and 3D soil deformations at the surface will offer greater details into the behaviour of soil reinforced by the Forepoling Umbrella System in tunnelling. Moreover, this will enable the changes in the settlement trough width at the surface to be determined and subsurface to be estimated which are important to buildings and underground services respectively.

In order to investigate the effects of a Forepoling Umbrella System in relation to the above mentioned factors, the behaviour of both soil and steel pipes need to be modelled appropriately and simultaneously. These issues could not be solved by available empirical

methods as no structural aspects are taken into account. The centrifuge modelling technique was chosen as the methodology for this research due to its advantageous capabilities in modelling soil-pipe behaviour.

CHAPTER 3 CENTRIFUGE MODEL TESTING

3.1 Introduction

A background to centrifuge modelling technique and its principles are presented to highlight the capabilities of the method for geotechnical engineering. Following this, the facilities available at the centrifuge testing centre at City, University of London are discussed including instrumentation and the development of a new 3D Topography Imaging technique that allows more data on ground movements to be obtained from centrifuge tests.

3.2 A brief history of centrifuge modelling technique

The idea of using a centrifuge for model tests in engineering problems was probably first suggested by E. Phillips in 1869 (Craig, 1995). Phillips proposed the exploitation of centrifugal acceleration to create self-weight effects in small scale models to study the behaviour of a corresponding prototype.

Early research using centrifugal model testing for the construction industry was conducted in the U.S.S.R in 1930's but was largely unpublished. The research included investigations of slope stability, behaviour of buried pipes, problems regarding earth dams and underground explosions which were reported later by Pokrovsky & Fyodorov (1968, 1969).

The Proceedings of the Seventh Conference of the International Society for Soil Mechanics and Foundation Engineering, Mexico 1969, introduced papers related to centrifuge testing. The centrifuge modelling technique had gained considerable interest outside the U.S.S.R after S. Mikasa in Japan and A.N. Schofield at Cambridge realised the potential of centrifugal acceleration in solving geotechnical problems. Then, in the early 1970's the first geotechnical centrifuges were established in the UK and Japan. From this debut, centrifuge modelling has developed rapidly and made major

contributions in geotechnical engineering. An in-depth history of centrifuge modelling technique in geotechnics can be found in Craig (1995).

3.3 Background to centrifuge model testing

In situ stresses within the soil mass are a key factor in determining ground deformation behaviour. The stresses within a soil body increase with depth from zero at the ground surface due to self-weight effects. Thus, physical modelling studies generally require the reproduction of a representative self-weight stress regime (Mair, 1979).

3.3.1 Principles of centrifuge modelling

Taylor (1995) states that centrifuge modelling techniques, by means of the applied inertial radial acceleration, can create a proper self-weight effect in a small scale model representative of a full scale prototype. Hence, the soil behaviour at a prototype scale can be replicated in a model of $1/n$ scale. Moreover, small scale models enable researchers to investigate geotechnical problems while full scale investigations are not always easy to implement or can be very costly. With careful selection of dimensions and materials the structural behaviour of components present in a soil-structure interaction problem can also be modelled. With these benefits, centrifuge model tests can deliver valuable insights into the effect of a Forepoling Umbrella System on tunnel face stability in clay.

The inertial radial acceleration is a function of the angular velocity and radius from the centre of rotation;

$$a = \omega r^2 \tag{3.1}$$

where a is the radial acceleration (m/s^2),

ω is the angular velocity (rad/s), and

r is the radius from the centre of rotation (m).

n is defined as a gravity scaling factor as previously described and given by **Equation 3.2**;

$$n = \frac{a}{g} \quad (3.2)$$

where g is the Earth's gravity (9.81 m/s²).

Scaling laws and potential scaling errors are issues that need to be appreciated in centrifuge modelling. Scaling laws were established to aid centrifuge modellers in designing appropriate models to ensure stress similarity with a corresponding prototype. Scaling errors are induced by the artificial gravity field generated by the centrifuge. Discussions on these two issues are presented in the following sections.

3.3.2 *Scaling laws*

The key advantage of centrifuge modelling is the reproduction in a model of the stress distribution in the prototype in its simplest form, stress similarity requires;

$$\sigma_{vp} = \sigma_{vm} \quad (3.3)$$

where σ_{vp} denotes vertical total stress.

p denotes "prototype",

m denotes "model".

The vertical total stress in the prototype is given as;

$$\sigma_{vp} = \rho g h_p \quad (3.4)$$

where ρ is the soil density, and

h is the depth.

If in a corresponding model, the soil is subjected to a field of acceleration of n times greater than the Earth's gravity, the vertical total stress in the soil model is;

$$\sigma_{vm} = \rho n g h_m \quad (3.5)$$

If density of soil in the model is identical to that in the prototype then from **Equations 3.3, 3.4 and 3.5** the scale factor for length in the model is;

$$h_m = \left(\frac{1}{n}\right) h_p \quad (3.6)$$

The scaling law also affects other geometrical properties of components used in the model. Specifically in this research, the bending stiffness of the Forepoling Umbrella System is dominated by the equation given below;

$$E_m I_m / E_p I_p = 1/n^4 \quad (3.7)$$

where E is the Young's modulus,

I is the second moment of area.

Another scaling law applying to small scale modelling is concerned with consolidation. The dimensionless time factor T_v represents the degree of consolidation;

$$T_v = c_v \frac{t}{H^2} \quad (3.8)$$

where c_v is the coefficient of consolidation,

t is time, and

H is the drainage path length.

For the dimensionless time factor T_v to be equivalent in both model and prototype, ie;

$$T_{vm} = T_{vp} \quad (3.9)$$

then;

$$c_{vm} \frac{t_m}{H_m^2} = c_{vp} \frac{t_p}{H_p^2} \quad (3.10)$$

which leads to;

$$t_m = t_p \frac{c_{vp} H_m^2}{c_{vm} H_p^2} \quad (3.11)$$

using **Equation 3.6**;

$$\frac{H_m^2}{H_p^2} = \frac{1}{n^2} \quad (3.12)$$

so;

$$t_m = t_p \frac{1}{n^2} \frac{c_{vp}}{c_{vm}} \quad (3.13)$$

Assuming c_v of soils in model and prototype are the same then the scaling factor for consolidation time is $1/n^2$. In other words, this scaling law delivers a huge advantage in model preparation i.e. one hour of consolidation in a centrifuge at 125g equates to 651 days at prototype scale.

Other important scaling laws to geotechnical engineering are summarised in **Table 3.1** (Marshall, 2009).

3.3.3 Errors and error control in centrifuge modelling

In general, errors in modelling studies are almost inevitable and centrifuge modelling is not an exception. It is important to recognise errors that would occur in centrifuge

modelling and then use appropriate solutions to deal with them. Moreover, understanding those errors is beneficial to data analysis which is essential for correct interpretation.

This section addresses typical errors that centrifuge modellers need to be aware of, namely boundary effects, non-uniform acceleration field created in centrifuge models, lateral acceleration and particle size effects. Particularly in this research, there are other errors or lack of similitude e.g. non advancing tunnel, no actual face excavation, use of compressed air, modelling of forepoles and installation processes.

The errors associated with boundary effects pertaining to this research are discussed further in **Section 4.3.3**.

While the Earth's gravity is assumed uniform for the soil depths encountered in civil engineering, the artificial acceleration generated by the centrifuge is slightly variable throughout the depth of the model (Taylor, 1995). This is because there is variation in radius over the height of the model which results in variation in the acceleration from **Equation 3.1**. As a consequence, the stress profiles of model soils are not identical to those in the prototype. Comparison on distributions of vertical stress in the model and corresponding prototype are shown in **Figure 3.1**. Taylor (1995) argued that the effective radius should be measured from the central axis to one-third the depth of the model. Consequently, the amount of under-stress and over-stress are minimised and the least variation is obtained (Taylor, 1995). At two-thirds model depth the vertical stress in the model and prototype are then equal. For most geotechnical centrifuges, the maximum error in the stress profile is minor and normally less than 3% of the prototype stresses (Taylor, 1995).

During the operation of the centrifuge to generate the inertial acceleration field which is directed away from the centre of rotation, there is a lateral acceleration component, a_L , created within the model and is presented in **Figure 3.2**. This horizontal component of acceleration increases as the distance from the centre line increases and is given by;

$$a_L = \frac{a \cdot d}{r} \quad (3.14)$$

where a is the radial acceleration,

d is the distance from the centre line, and

r is the radial distance measured in direction perpendicular to centrifuge swing.

Therefore, the greatest lateral acceleration a_L is at the furthest offset from the model centreline (a_L is linear to d as in **Equation 3.14**) and $a_L = 0$ at the model centreline (if the model positioned at the middle of the swing). In order to minimise the errors caused by this lateral acceleration, the model container should be positioned in the way that the corresponding maximum d to be smallest to minimise the induced a_L . And, major events that need to be investigated should occur near the central region of the model.

The other error of concern for centrifuge modellers is the particle size effect. The scaling laws in the centrifuge apply equally to dimensions of model and grain size. This can lead to problems of compatibility between grain size and scaling. In some situations, the ratio of the grain size to some dimensions or zone of shearing may be important. In other situations, interests are on the soil behaviour as a continuum displaying the same characteristics as the soil in prototype. This research is primarily concerned with the pre-failure deformations of soil (clay) under the change of tunnel support pressure causing on volume loss, hence it is critical to replicate the stress-strain response of the prototype soil.

3.4 The London Geotechnical Centrifuge Testing Facility

The London Geotechnical Centrifuge Testing Facility located at City, University of London. The Centre was established in 1989 and the facility has been continuously developed to tackle complex geotechnical problems. The research described here benefits from the enriched facility of the London Geotechnical Centrifuge Testing Facility which is described in detail below.

3.4.1 The Acutronic 661 geotechnical centrifuge

The Acutronic 661 beam centrifuge is a 40g/tonne machine which is capable of accommodating a package weight of 400kg at 100g. This capacity reduces linearly with

acceleration to give a maximum 200kg at 200*g*. The general arrangement of the Acutronic 661 is shown in **Figure 3.3**. A model package with dimensions of up to 500mmx700mm in plan and 970mm in height can be placed on the swing platform at one end of the beam. In order to balance the package, there is 1.45 tonne counterweight that can be moved radially along the centrifuge arm by a screw mechanism. The radius of the swing bed is 1.8m resulting in an effective radius in a soil model typically between 1.5m and 1.6m.

The mass of the rotating arm of the centrifuge is about 3.5 tonnes and it has considerable stored energy when rotating to generate the high acceleration field for a centrifuge. Consequently, the centrifuge machine is located within a reinforced room to ensure a safe working environment. In order to avoid undue stress on the bearing due to centrifuge imbalance and to allow safe overnight operation, sensors are built into the centrifuge mounting to detect any out-of-balance forces. The machine is automatically shut down if the out-of-balance load exceeds the maximum pre-set of 15kN.

There is a slip ring stack located above the central rotating shaft including four fluid rings, sixteen electrical rings and one fibre optic. The four fluid rings provide capability to feed compressed air and water to a maximum pressure of 10 bar to the model package. The sixteen electrical rings are used to provide power to on-board control systems, instrumentation, cameras, data acquisition (DAQ), motors, lighting and solenoids. The fibre optic cable with optical slip ring facilitates two-way communication between the control room and on-board centrifuge computer. This gives access to feedback and output signals from the DAQ, camera and motor control system and allows control of electronic actuators on the centrifuge.

3.4.2 Data acquisition

Signals from instrumentation on the centrifuge swing are collected by permanently mounted junction boxes. These signals are then passed on to an onboard signal conditioning unit for filtering and amplification. Amplification gains of 1, 10, 100, 500 and 1000 are available allowing a wide range of sensitive, low output voltage instruments to be used such as strain gauges and pressure transducers.

An inflight PXI Computer mounted on the centrifuge swing, supplied by National Instruments, captures and stores real time data using a Labview program. The data is available to inspect during the test via a remote desktop computer in the control room connected to the PXI computer via a LAN connection which interfaces with the fibre optic switch located in the control room.

3.5 Measurement instrumentation

One of the criteria to quantify the effect of the Forepoling Umbrella System is the magnitude of ground deformation due to tunnelling which resulted from the reduction of the tunnel pressure. Hence, instrumentation needs to be sufficiently precise to record the sensitive changes in ground settlements and tunnel support pressure.

The tunnel support pressure and the pore water pressure throughout the centrifuge tests were measured by the pressure transducers. Their specification and precision are described in **Section 3.5.2**.

During the research period, improvements were made to not only increase the precision of the measuring data but also the extent of the ground surface area at which movements were measured.

In the first thirteen centrifuge tests, the longitudinal surface ground settlement above the tunnel centre line and the subsurface ground deformations were measured by a row of displacement transducer (Linearly Variable Differential Transformers type) (**Section 3.5.1**) and an imaging processing software Visimet (**Section 3.6**) respectively.

In later tests, a newer imaging processing software, GeoPIV-RG, was incorporated into the centrifuge testing facility providing improved quality. Therefore, GeoPIV-RG (**Section 3.7**) was used to replace Visimet to measure subsurface ground deformations in later centrifuge tests. A new 3D topography apparatus (**Section 3.8**) was also developed to measure movements of the whole model ground surface which significantly enlarges the measured area compared to a single line of surface settlement provided by a row of LVDTs.

3.5.1 Displacement transducer

Vertical surface settlements of the soil were accurately measured by displacement transducers using the principles of Linearly Variable Differential Transformers (LVDTs) manufactured by Schlumberger and supplied by RS Components Limited, Northants. The range of travel of the LVDTs is $\pm 15\text{mm}$ with an output limit of $\pm 5\text{V}$. These LVDTs were calibrated individually within this range using a screw micrometer. After obtaining the calibration factor, the LVDTs measurement was checked against the micrometer and the accuracy found to be within $\pm 5\mu\text{m}$. With this high accuracy, LVDTs were used as a benchmark to assess the performance of imaging measurement Visimet (**Section 3.6**).

3.5.2 Pressure transducer

Changes in pore-water pressure within the clay model during the consolidation stage in flight and testing process were measured by miniature Pore Pressure Transducers (PPTs) model PDCR81 supplied by Druck Limited, Leicester. A porous stone at the front of the PPT supports the effective stress while allowing the pore water to reach the pressure-sensitive diaphragm. These PPTs were always deaired before being calibrated and used to ensure precise measurement of the pressure.

Another PPT without a porous stone was used to monitor the water head in the standpipe. Calibration was carried out with a 101 Digital Pressure Indicator (DPI) also supplied by Druck. The calibration factors were checked again by comparing the reading from PPTs with the reading of the DPI and the accuracy was found to be within 0.2kPa. These PPTs were positioned in the clay through the rear wall of the strong-box.

During the pre-flight consolidation process, a sub-miniature flush diaphragm pressure transducer, model PX600-200GV series and supplied by Omega Engineering Ltd, was used to measure the air pressure in the tunnel bag at the tunnel axis level. This pressure transducer was calibrated with a DPI 104 supplied by Druck. An accuracy within 0.5kPa was also observed when the tunnel pressure transducer checked against the DPI 104.

These transducers were calibrated before every test to ensure accurate and repeatable measurements. Location and fixing details of these transducers to the model are described in Chapter 4.

3.6 2D Image processing - Visimet

A small Charge Coupled Device (CCD) camera was mounted on the swing of the centrifuge to observe the subsurface ground movement of the model, in-flight, through a Perspex window. During model preparation (see **Section 4.5.2**) an array of 3mm diameter by 5mm long black delrin marker beads were inserted into the front face of the model clay in a 10mm centre-centre square cell. The subsurface ground deformations were observed by tracking the movement of the targets relative to fixed targets machined into the Perspex window. Movement of these targets could then be quantified using techniques of close range photogrammetry and image analysis software.

The mathematics behind the close range photogrammetry used within the image processing system are beyond the scope of this dissertation. Details on the background of photogrammetry and the image analysis system for the geotechnical centrifuge are given by Taylor *et al.*, (1998). The flow chart for the image processing procedure is illustrated in **Figure 3.4** and the general methodology is described below.

The image processing could be split into two stages. The first involves recording and tracking the target in the image space (on the pixel board of the CCD camera) and the second is the calibration from image space to object space (a coordinate system in the soil plane). The fixed control targets on the Perspex window were required for the calibration procedure. The program Visimet for Geotechnics was used to process the captured images and determine the targets coordinates. The calibrated positions show the true locations of the targets in the object space. During the testing period, inflight images were captured and stored at a rate of approximately one per second. Therefore, the real time subsurface ground deformations were obtained by the means of CCD camera and image processing program.

The quality of measurement firstly depends on the precision in determining the target positions and the calibration procedure. In digitised form, an image is a two-dimensional matrix of intensities recorded at each pixel on the camera sensor. The indexes of the matrix are the horizontal and vertical coordinates of the pixel on the image plane. The colour of a pixel is defined by three values of intensity.

In this research, a target of 3mm diameter in the object space occupies 6 to 7 pixels of the image space in vertical and horizontal directions giving a total of 36 to 49 pixels. The CCD camera used is a monochrome camera so these three intensity values are identical. By plotting the intensity of pixels across the target, a three-dimensional intensity distribution can be established. Tracking a target in sequential images is achieved by tracking the movement of the intensity distribution. Lighting conditions, clearness of the target and the coverage area are all important factors for the precise determination of the positions of targets.

Transforming the target positions from image space (pixel unit) to object space (e.g. mm unit) requires the parameters of the cameras and lens including focal point, focal length, distortion factors, camera position and orientation, etc. These parameters are derived in respect of the control point targets. Having an adequate number of control point targets is essential to evaluating the aforementioned parameters and hence the precision of the method.

Grant (1998) reported that the precision of measuring the movements of a targets is within the range of 50 to 80 μ m.

3.7 2D Image processing - GeoPIV_RG

White *et al.*, (2003) introduced the use of Particle Image Velocimetry (PIV) and close-range photogrammetry for measuring soil deformation. PIV is the technique used to measure the velocity which was originally developed for the field of experimental fluid mechanics. The PIV requires textures so that the image processing can operate. In the geotechnical field, natural sand has its own texture as the grains have, for example, different colours. However clay is almost textureless hence texture need to be created by adding ‘flock’ material or dyed sand on the observed plane (White *et al.*, 2003). This technique delivers an order-of-magnitude increase in accuracy and precision compared to previous image-based methods (White *et al.*, 2003). Recently, improvement in the PIV technique in centrifuge applications has been made to increase the precision, accuracy and robustness (Stanier *et al.*, 2015; Stanier *et al.*, 2016).

The principle of PIV to measure the displacement between two consecutive images 1 and 2 is illustrated in **Figure 3.5**. Initially, the reference image is divided into test patches which are collections of pixels with intensity values. The tracking of a patch is achieved by searching for that test patch within a bigger area which is called search patch in the next image (**Figure 3.5**). The size of this search patch needs to be sufficiently large to ensure the test patch can be found within it but not too large to avoid lengthening the searching times. This procedure is similar to tracking the intensity of targets in Visimet. The search is deemed successful when a threshold ‘degree of match’ (or cross-correlation) of test patch in the reference and target images is achieved. In most of the analysis conducted in this research, a degree of match of 0.9 (maximum 1) was set to ensure high precision data.

The difference in the positions of the test patch in the pair of images is the displacement in image space (pixel unit). The transformation from image space displacement to object space displacement uses close-range photogrammetry and this process is similar to Visimet. The searching mechanism used in PIV can achieve a sub-pixel resolution which offers high precision measurement.

The performance of the PIV technique relies on the tracking of patches between image pairs. Therefore, stable lighting conditions, quality of texture in the observed surface and high resolution images are the key factors in obtaining good results. Glass ballotini of 1mm diameter and dyed black were used to create texture and good contrast on the clay surface in front of the soil model (**Section 4.5.2**) to aid the PIV tracking process. Distortion in the patch shape (due to large soil deformations) and change in lighting conditions tend to downgrade the ‘degree of match’ and hence reduces the precision of the measurements. A LED light strip was used to illuminate the front face of the model to ensure good lighting condition. New GeoPIV-RG (Stainer *et al.*, 2015) takes into account the deformation of the patch hence improves the precision over the previous version of GeoPIV. A quantification experiment on the precision of the PIV system at City, University of London showed the difference in measurements by GeoPIV-RG and LVDTs were within 5 μ m (Nadimi *et al.*, 2016). This project used GeoPIV-RG to replace Visimet in measuring the soil subsurface deformations in later test series.

3.8 Image processing - 3D Imaging System

At the beginning of the research, a 3D Imaging System for centrifuge modelling was not available. Instead, LVDTs were used to measure surface settlements at several discrete points and subsurface displacements were determined from images using Visimet. Due to the relatively large size of the LVDTs compared to the model container and the limited number of LVDTs available, the whole model ground surface was not measured. After finishing a number of centrifuge tests it was felt that the need to understand the effect of FUS on the whole ground surface would give greater insight into the effects of FUS. Therefore, a decision was made to develop a 3D Imaging System (3DIS) to measure the ground surface deformation during the modelling of tunnel construction. The overall requirements to this 3DIS are to be:

- capable of measuring 3D deformations in the region of interest to a precision of at least 50 μ m to provide useful and useable data;
- adaptable within the current centrifuge facility and model container in which space is limited;
- sufficiently stiff and robust so as to function under high gravity;
- synchronised with the data logger system and GeoPIV_RG;
- economical in term of cost and time needed to develop the system.

The following sections review the available 3D imaging techniques and go on to describe the development of the 3D imaging system (3DIS) and the experiments undertaken to quantify the precision and accuracy of the 3DIS. A common term for quoting the accuracy of a measurement system is accuracy over the area of field of view. It is worth differentiating the field of view (FOV) and the region of interest (ROI). FOV is the area of the view captured by the camera whereas, ROI is the area where the main events occur within the FOV.

3.8.1 Available 3D Topography techniques

There were several options available for 3D Topography mapping including: X-ray scanner, laser Scanner and structure from motion (SfM) with Multi-view Stereo (MVS). Robinson *et al.*,(2016) reported the use of laser scanner in centrifuge modelling to measure a static soil model surface (post-test) to an accuracy of 1/758 of the FOV (0.5mm over a FOV of 384mm wide). The advantage of this method is the fairly simple setup. However, this system cannot measure the deformations of a mobile surface nor can be adapted to an inflight centrifuge model. X-ray scanners were ruled out due to the expensive cost, the space needed to house the scanner into the current system were not available and more importantly the lack of capability to measure the moving ROI. SfM-MVS was chosen because of its robustness, high quality data and available open source software which can be edited to suit the needs of the research.

3.8.2 Principles of SfM-MVS technique

SfM-MVS originates from computer vision and photogrammetry which can produce a high quality 3D point cloud while not requiring expensive equipment and specialist expertise. Smith *et al.*, (2015) reported that SfM has been used in a wide range of applications such as 3D topographic surveys, monitoring glacier movements, observing and tracking lava movements and landslide displacements. The SfM algorithm is described in detail by Robertson & Cipolla (2009). The general work flow structure of SfM-MVS is illustrated in **Figure 3.6** and explained in the following sections.

Feature detection and correspondence

The first step in the work flow is to find the features known as keypoints in each image and assign them with a unique identifier. A feature is defined as sets of pixels that are invariant to changes in scale and orientation and which are likely to be identifiable in other images (**Figure 3.7**). In this research, the feature detection is realised by the means of the Scale Invariant Feature Transform (SIFT) algorithm (Lowe, 2004). SIFT allows corresponding features to be matched even with large variations in scale induced by the change of the viewpoint up to 40°. Once the features are detected and matched in multiple images, the distance between features in image planes can be calculated.

Bundle adjustment

By using the locations of the features in multiple images, the parameters of the scene including individual positions of the cameras, orientation of the cameras, intrinsic camera parameters (e.g. skew, focal length, principal point and radial distortion parameters) and relative locations of the features in object space can be estimated in a process called bundle adjustment. Bundle means a collection of features are used to estimate the parameters through iterations. In each iteration, the parameters and the features that are simultaneously adjusted to minimise the measurement error until a desired precision is achieved. Poorly matched features (outliers) that exceed the error threshold are then removed. The term Structures from Motion is derived from this process. Structure is referred to as the parameters estimated by the data obtained from different positions of the viewing angle (motion or position of camera). Images taken from different positions add more data to the bundle to improve the precision of the parameters estimated (Triggs *et al.*, 1999). Therefore, the more images available the better quality of the reconstructed model. A minimum number of images required by SfM is two but a larger number of images is recommended.

Multi-View Stereo Image Matching

In the previous steps, only keypoints (features) were detected and used for the bundle adjustment process hence the 3D point cloud has a coarse density. A further step named Multi-View Stereo (MVS) matching algorithm increases the density of the 3D point cloud by at least two orders of magnitude (Furukawa & Ponce, 2010; James & Robson, 2012; Smith *et al.*, 2015).

3D model reconstruction and Georeferencing

After the bundle adjustment process, the camera parameters and the relative positions of features are estimated; a 3D point cloud is then produced. This 3D point cloud is in image space units (pixel) and needs to be transformed into physical space units (e.g. mm) in a process named georeferencing. A set of reference targets with known coordinates usually referred as Ground Control Points (GCP) is used to transform the 3D point cloud from image space (pixel) into object space (mm). It is essential to have these GCP visible in at least two images to improve the precision of the transformation process. Therefore, the

precision in the coordinates of the GCPs is critical to the precision of the 3D point cloud in physical space.

3.8.3 Review on SfM-MVS technique and MicMac software

Structure from Motion & Multi-View Stereo

James & Robson (2012) assess the precision of SfM-MVS by comparing a 3D model produced by an open source SfM-MVS software named Bundler with data obtained by a laser scanner. The calculated precision varied from 69-110 μ m for an average imaging distance of 0.7m. That suggests the ratio of precision to imaging distance was determined as approximately 1:6400 and thus the precision could be improved by reducing the distance between the camera and FOV.

Smith *et al.*, (2015) suggested that SfM-MVS is not suitable for measuring mobile objects as the moving features cannot be matched in multiple images. Most of the applications of SfM-MVS involve measuring static FOV for example a 3D topography survey or features with relatively slow movement (e.g. landslide, lava displacement etc.). In those applications, normally only one camera is used to capture the FOV from multiple viewpoints so as to cover the whole area. During the image acquisition progress, the displacement of the field of view is deemed negligible and the surface can be modelled with low reprojection error.

The open source SfM-MVS software MicMac

Several available SfM-MVS software exist such as commercial software Agisoft Photoscan and open source software Bundler, VisualSfM and MicMac. One of the drawbacks of MicMac is the software is not as user friendly as Agisoft Photoscan and VisualSfM. Smith *et al.*, (2015) reported that MicMac outperformed Agisoft Photoscan and VisualSfM due its sophisticated self-calibration camera models. Galland *et al.*, (2016) reported that a precision of 1/10 000th of the FOV was achieved by using MicMac. In Galland *et al.*, (2016), the input images were taken by four 24 megapixel (MP) cameras and only 4 GCPs were used. MicMac also allows the user to amend image processing procedure (open source) to meet the processing purposes. As a consequence, MicMac was chosen here for 3D Topography in centrifuge models.

Limitation and requirements

In order to maximise the quantity and quality of features detected in this step, the requirements that need to be achieved are:

- The FOV should be visible in all images or at least two thirds of the FOV must overlap;
- The images should be of high quality so as to give high quality output;
- The FOV must be static in a set of images to enable the features to be matched between images;
- The interval between sets of image acquisition should be minimised as change in lighting condition does affect the detection and matching of features;
- Shiny, reflective or textureless surfaces should be avoided as those surfaces are indistinguishable by the feature detection algorithm;

The solutions to tackle the aforementioned requirements and limitations are described in more detail in the next section.

3.8.4 Development of 3D Imaging System

Figure 3.8 presents the complete 3D Imaging System. Details of the components are described in the following sections.

Cameras and lenses

Three 2MP cameras UI-5360CP-M-GL (supplied by Imaging Development Systems (IDS) GmbH) were used in this research (**Figure 3.9**). The key features of these cameras are the use of a global shutter sensor and the capability to use a time sync signal. Rolling shutter sensors are not recommended as not all parts of the FOV are captured at the same moment which increases reprojection error. Equally, the delay between image acquisition in the three cameras needs to be minimised. This was realised by using an electrical signal to trigger the cameras at the same instant which minimises any potential delay to

nanoseconds. A program InstIm (Instant Imaging) was written to send the electrical trigger signal to the cameras to capture images and save them into the computer for later analysis.

The lenses used in this research are 8mm fixed focal length Kowa LM8JCM which have a low level of distortion and are specifically designed for machine vision purposes. These short focal length lenses allow the FOV to be captured at the imaging distance of approximately 330mm.

As the lenses and cameras were not designed to work in high gravitational environment, strong housings were designed to support the cameras and lenses and ensure their functionality in flight. Details of the housings are provided in **Figure 3.9**.

GCP Reference plate

For transformation purposes, more GCPs result in a more robust solution and less sensitivity to error from any one point (Smith *et al.*, 2015). Therefore, a set of 59 GCPs were provided on a reference plate despite the fact that only minimum of 3 GPCs is required. These GCPs are arranged towards the edge of the FOV so that the coordinate transformations are not being extrapolated. The reference plate is made of aluminium which is suitable for machining and adequately stiff so as its deformation due to self-weight effect under high gravity is negligible. This reference plate was fabricated by a CNC machine to an accuracy of 5 μ m. Details of the reference plate is provided in **Figure 3.10**.

The gantry

The cameras and the reference plate were securely fixed to the gantry ensuring they were stable in the high gravity field. This arrangement enables the whole FOV (500x250mm) and all 59 GCPs to be visible in the three images which is beneficial for the SfM-MVS and georeferencing processes (**Figure 3.8**).

Lighting conditions

Two strips of light-emitting diode (LED) lights were used to provide good brightness on the FOV which is important to maximising the number of features to be reconstructed hence the quality of the 3D model.

3.8.5 Quantification of system performance

Two sets of experiments were carried out to assess the performance of the 3DIS in measuring displacements in the vertical and horizontal directions.

Vertical direction

The setup used to quantify the performance of the measurement system in the vertical direction is shown in **Figure 3.8** by comparing the change in elevation measured by 3DIS with the actual value.

The measured ROI is a surface plate which has texture created by spraying fraction E Leighton Buzzard Sand on a previously applied plastic coating. The ROI elevation was determined relatively to the reference plate. The actual change in the elevation of the ROI, U_z , is realised by placing slip gauges of thickness U_z between the reference and surface plates. The FOV were reconstructed representing the changes in vertical direction U_z of 0mm (reference 3D point cloud (3DPC)), 2.540mm, 5.105mm, 10.160mm, 15.240mm and 25.400mm.

The 3DPCs were rather dense and contained nearly 200,000 data points over the ROI of 300x130mm (about 4÷5 data points/mm²). Using the software CloudCompare or Matlab, these 3DPCs can be viewed and exported, en masse, into text files that store the coordinates and intensities of data points. Due to the large data set, a program was written in C++ to automatically process these text files. Typical 3DPCs and accuracy calculation is illustrated in **Figure 3.11**. The reconstructed 3D surfaces were divided into 10mm cells. The elevation of cell i , Z_i , is the average of the elevations of all the points within that cell. The measurement accuracy is calculated in every cell which was used to compile the accuracy histograms of the whole ROI.

Figure 3.12 shows accuracy histograms in the first four experiments. The bell shape of the histogram with the peak near 0 of the horizontal axis denotes that most of the data points have an error close to 0. The standard deviation for each increment was found to be less than $50\mu\text{m}$ for changes in elevations below 15.240mm. For the large change in elevation $U_z = 25.400\text{mm}$, some parts of the ROI were out of the cameras focus, which may explain the reduction in accuracy and the results are not presented here.

The maximum ground displacement in most of the centrifuge tests is expected to be smaller than 10mm (see **Section 6.2.1**). Therefore, a threshold of 10.16mm is sufficient to ensure the measurement of any displacement on the model ground surface has a precision of $50\mu\text{m}$. Consequently, in centrifuge tests, the bottom of the reference plate was placed close to the model surface.

Horizontal directions

Four experiments have been conducted using the controlled movement of a sliding bed (**Figure 3.13**) to realise horizontal displacements. In each experiment, the sliding bed was moved by 1mm in either the X or Y direction. The measurement accuracy was determined by comparing the displacement measured by the 2D PIV analysis and the actual movement realised by the micrometer over whole extent of the ROI (300x112mm).

The ‘*master image*’ (image taken by the central camera) has been undistorted and transformed to Cartesian coordinates. Then, conventional 2D PIV was carried out on the new set of images. The flow chart of this process is illustrated in **Figure 3.14**. Details on 2D PIV principles and applications in centrifuge modelling can be found in White *et al.*, (2003) and Nadimi *et al.*, (2016). 2D PIV analysis on the rectified Master images show standard deviations of less than $35\mu\text{m}$. The accuracy histograms in these experiments are shown in **Figure 3.15**.

The reliability and repeatability of the 3D imaging system is confirmed by the consistent accuracy and precision achieved in two sets of performance quantification experiments. The achieved accuracy was proved to be $1/10\,000^{\text{th}}$ and $1/14\,200^{\text{th}}$ of the FOV in vertical and horizontal directions respectively.

3.8.6 3D displacement vectors

By combining the vertical and horizontal displacement determined from 3DPCs and 2D PIV analysis, using the procedure illustrated in **Figure 3.14**, the 3D displacement vectors can be determined (later shown in **Figure 5.24**).

3.9 The suitability of the measurement systems

Every measurement has its own purpose and its precision must meet the requirement to ensure the stress-strain response of soil can be measured to a level that the obtained data is useable to gain the insight into soil behaviour. The satisfactory nature of the measurement system to the research purpose is discussed below.

The main interests of this research are the reinforcement effects of the FUS which is reflected in the soil deformations induced by the reduction of the tunnel support pressure. Hence precise measurements of these two components are critical to gain the insight into the effect of FUS parameters. The pressure transducer used in this research has a precision of 0.5kPa and is deemed to be capable of providing reliable measurement of the change of the tunnel support pressure in a range of 155kPa (for $C/D = 1$ tests) or 360kPa (for $C/D = 3$ tests).

Figure 3.16 illustrates typical strain levels in geotechnical events which suggests the resolutions to which strains should be measured to obtain a good understanding of the soil behaviour (Mair, 1993). Taking tunnelling events as example, if the measurement purpose is to study collapse mechanisms then the measurement instrumentation must be capable of measuring strains of approximately 2÷25%. However, the collapse state alone of the soil model might not be adequate to reveal the progressive development of the collapse mechanism. That leads to the need to investigate pre-failure deformations and strains of the order of 0.1÷1% need to be measured to obtain reliable data. In small scale physical modelling, this requirement becomes more challenging as the measurement resolution must be reduced by at least an order of magnitude.

Typically, the centrifuge models in this research have ROI of approximately 400x200mm. If this ROI is divided into cells of 10x10mm then the measurement system must be capable of measuring to a precision of $10\div 100\mu\text{m}$ (0.1÷1% of 10mm). The achieved precision of GeoPIV_RG at the City, University of London facility meets this requirement. Both the Visimet imaging analysis and the newly developed 3DIS have a precision of typically $50\mu\text{m}$ which falls within the suggested limits. Increasing the cell size (in PIV and 3DIS) leads to an increase in measurement precision however the number of data points will be reduced. Cells of 10x10mm were chosen as they deliver a balance between the desired precision and adequate data points being obtained and these have been used in analysis of the results.

In Chapter 5 and Chapter 6, the precision delivered by the described measurement system are shown to be adequate in distinguishing the effects of the FUS in different arrangements.

3.10 Summary

The background to centrifuge modelling techniques was presented and its suitability to this research was discussed. The scaling laws and inherent errors relevant to the work have been addressed which was shown to be negligible and can be overcome by appropriate selections of model dimensions and soil model.

Full descriptions of the instrumentation have been given including pressure transducers, LVDTs, 2D imaging analysis technique and the new 3D imaging system to measure 3D deformations of the ground surface. The capabilities of the measurement system was also examined and shown to be sufficient for the measurement purposes.

CHAPTER 4 EXPERIMENTAL APPARATUS DEVELOPMENT

4.1 Introduction

This chapter describes the variables of the centrifuge tests to tackle the deficiencies in the understanding of the influence of the parameters of the Forepoling Umbrella System (FUS). This is followed by the development of testing apparatus and the experimental procedure to meet the research objectives. Principal features of the model clay sample including stress history and estimation of undrained shear strength are also discussed.

4.2 Test series

The limitations in the understanding of the effects of the FUS (**Section 2.8**) are the main aspects to design the test series so that a clearer insight into achieving an optimal design of the FUS can be gained. In order to accomplish those objectives, the significance of the effect of the following parameters needs to be investigated:

- The influence of the tunnel depth to the reinforcing effects of the FUS. Davis *et al.*, (1980) suggested that soil deformation mechanisms vary with tunnel depth. Acknowledging the significance of the effect of the tunnel depths is beneficial in FUS design. Therefore, $C/D = 1$ and $C/D = 3$ have been used for the model tunnel tests because these two are likely to result in considerably different soil deformation mechanisms.
- The review of the projects using the FUS showed that the filling angle normally lies in a narrow range of $\alpha=60^\circ$ to $\alpha=75^\circ$. A larger filling angle is worth studying to assess the effect of the filling angle. Therefore, $\alpha=75^\circ$ and $\alpha=90^\circ$ are chosen to be the variables in the test series.

- The increase in the stiffness of the forepoles and the embedded length were expected to offer greater reinforcing effects. However, information on those effects have not been reported elsewhere. Therefore, the forepoles are modelled by two different materials, brass and steel, with two different embedded lengths $EL/D=0.5$ and $EL/D=1$.

These objectives have been realised within the test series described in **Table 4.1**. The variables are defined in **Figure 4.1**. Test series CD3B and CD1B were used to investigate the effects of the forepole arrangement (α and EL) at two different tunnel depths $C/D=1$ and $C/D=3$. In these series, the forepoles were modelled by brass rods. The effect of the forepole stiffness to the FUS reinforcement effectiveness was studied in Series S and CD3S where steel rods were used. The other tests 1BL, 14BL, 15BL, 16BL and 17BL were conducted to check the functionalities of the testing apparatus and measurement system including the model tunnel, new GeoPIV-RG system and 3D imaging system (3DIS).

Having the aforementioned variables allows not only the effect of a single parameter to be studied but also the relative influence of these variables. The approach is to examine the influence of the FUS with different variables on the soil deformations induced by the simulated tunnelling event in a centrifuge test. Therefore, the intention was to replicate not only soil behaviour but also the properties of the FUS in terms of its geometry and structure.

The following sections describe the development of the testing apparatus to realise the centrifuge tests.

4.3 Testing apparatus

A typical centrifuge model is illustrated in **Figure 4.2** and the key aspects are described in the following.

4.3.1 The model container (strong-box)

A duraluminium strong-box was used to contain the model clay, tunnel, Forepoling Umbrella System and instrumentation. A Perspex window was used for the front face of the strong-box which allowed the model to be observed by cameras and from which images would be stored for later processing. The base plate of the strong-box has a machined herring-bone pattern to provide a drainage path for water to exit or enter the model clay during the consolidation and testing phases.

The inside dimensions of the strong-box are 550mm (L) x 200mm (W) x 375mm (H). The strong-box allows centrifuge tests with the tunnel depth up to $C/D=3$ to be undertaken which is deemed adequate to cover different soil deformation mechanisms.

4.3.2 Model tunnel

The tunnel heading was simulated by a semi-circular cavity cut into the clay model which could be viewed through the front Perspex window of the centrifuge strong-box that formed the vertical plane of symmetry of the tunnel heading (**Figure 4.2**). Therefore, the soil deformations in this plane, which are expected as the largest in the soil mass, can be measured by means of image analysis.

The total length of the tunnel was 190mm. The stiff tunnel lining was 165mm long and modelled by a 50mm diameter semi-circular brass tube. That left the unlined tunnel heading to be $P=25$ mm which was supported by a thin rubber bag supplied with air pressure. In later tests, this brass tube was replaced by a semi-circular stainless steel tube. The reasons and effects of this amendment are discussed in **Section 5.4.2**.

The ratio of the unlined portion of the tunnel heading with the diameter $P/D=0.5$ was chosen because it is within the range of $P/D=0.1\div 1$ which was observed in many case studies (Macklin, 1999; Dimmock, 2003).

All the tests were conducted at 125g. At this acceleration, the model tunnel represented a corresponding tunnel at equivalent prototype scale with diameter of 6.25m located at depths of approximately $z_0=9.5$ m and $z_0=22$ m for $C/D=1$ and $C/D=3$ tests respectively.

These corresponding diameter and depths are common in tunnelling practice in urban areas.

4.3.3 Potential boundary effects

Results from centrifuge tests reported by Kimura & Mair (1981) suggested that the soil boundary of $3D$ from the tunnel centre-line was sufficient for centrifuge tests investigating mechanisms of ground deformation due to tunnelling. Calvello & Taylor (1999) conducted a series of 3D tunnel heading tests with the same size strong-box to this research which delivered valuable results.

Modelling half of the tunnel heading led to the distance from the tunnel centre line to the side of strong-box to be $200\text{mm}/50\text{mm}=4D$ (**Figure 4.2**). This was larger than the value of $3D$. The depth of the model clay below the tunnel invert was greater than one tunnel diameter so minimising any potential boundary effect (Taylor, 1995). The minimum longitudinal distance from the tunnel heading to the sides of the strong-box was 165mm (the length of the model tunnel lining) which was larger than $3D$ and minor disturbance to the soil displacements in this direction can be expected.

Therefore, with the strong-box and the model dimensions used in this research, the boundary effect is considered to be negligible.

4.3.4 Model Forepoling Umbrella System

Model forepoles

It was decided to examine the effect of the forepoles arranged in two different filling angles: $\alpha=75^\circ$ and $\alpha=90^\circ$ (**Section 4.2**). With these two filling angles, a number of fourteen 1mm rods (brass/steel) was considered appropriate so that the gap between the model forepoles was small enough to prevent the soil from slipping through and causing a piping effect as observed by Yeo (2011) (**Section 2.7.3**) which is not desired in tunnelling practice. The length of the rods, L , was 100mm . According to centrifuge scaling laws, the 1mm diameter brass and steel rods under 125g have a bending stiffness equivalent to steel pipes of respectively 135mm and 165mm outer diameter with 8mm wall thickness at prototype scale (See **Appendix 1**). The corresponding length of the

forepoles at the equivalent prototype scale is 12.5m. These sizes of the forepoles are common in projects using a Forepoling Umbrella System (**Section 1.2.3**).

Arrangement of the forepoles

In tests 2BL, 8BL and 20BL the distribution of the brass rods were concentrated around the tunnel crown in the filling angle $\alpha=75^\circ$ (the spacing between the eight upper rods was 1.7mm but the six lower rods had a spacing of 3.4mm) (**Figure 4.3-a**). In other reinforced tests, the rods were evenly spaced at 3mm in the filling angle $\alpha=90^\circ$ (**Figure 4.3-b**). In the reference tests 5BL, 9BL and 18BL there was no reinforcement. The schematics of the Forepoling Umbrella System arrangements used in the tests are illustrated in **Figure 4.1**.

The model forepoles, via a guiding device (**Figure 4.4**), were inserted in the model at an insertion angle of 5° . This guiding device was produced by a high-resolution 3D printer for precise installation of the rods.

The effect of difference in density of the forepoles materials

The forepoles were modelled either with brass or steel rods of the same dimensions. Hence there are differences in density and stiffness of each material. The density of brass is only 8% greater than steel and the rods were supported by the surrounding soil and the tunnel lining. Therefore, the induced effect of this discrepancy is negligible. That allows the influence of the forepole stiffness to be studied independent of material density.

Effect of lateral acceleration component to the model forepoles

The lateral acceleration component a_L , given in **Equation 3.14**, was created during the operation of the centrifuge (**Section 3.3.3**) and its effect to the model forepoles needs to be considered. The greatest distance from the model forepoles to the model centreline $d \approx 0.07\text{m}$ and the radial distance from the centre of rotation to the model forepole $r \approx 1.66\text{m}$. Using these values of d and r to **Equation 3.14** gives the maximum value of the lateral acceleration equal to approximately 0.042 times the ‘vertical’ acceleration. In addition, this lateral acceleration applied equally to the clay model and the forepoles in all the centrifuge tests hence its effect is deemed negligible.

4.3.5 Ground water supply

The ground water level within the model was maintained by the standpipe system which was fixed next to the strong-box on the swing platform. The water table was set to 20mm below the model surface in $C/D=3$ and 25mm in $C/D=1$ tests. The overflow pipe level inside a standpipe was set to discharge excess water and provide the desired water table level.

Typically, the standpipe was offset from the model centreline by approximately 240mm and consequently the overflow level was set approximately 19mm higher than the height of the water table (measured from the swing bed) due to the radial acceleration field effect (**Figure 4.5**).

Water passed through the fluid slip rings and was fed into the standpipe which in turn was connected to the model via the base drainage system.

4.3.6 Location and fixing of instrumentation

In test series CD3B, CD1B and S, the LVDTs were used to measure the top surface settlement. In series CD3S, the LVDTs were replaced by the 3D Imaging system (3DIS) (**Section 3.8**) to measure the whole surface deformations. **Figure 4.5** gives details on positions and fixings of all the instrumentation.

Eight LVDTs, arranged in a row close to the tunnel centreline, were used to measure the ground surface settlement. The LVDTs were clamped to a gantry frame which was fixed to the strong-box. The frame was designed to allow reasonably flexible positioning of the LVDTs horizontally as needed and to be secured firmly during the test. The ends of the LVDT probes were fitted with plastic feet to prevent self-weight induced penetration into the clay under the high g field. These feet were in contact with the top of the clay which resulted in identical movements between LVDTs rods and the surface settlement. **Figure 4.5** shows the arrangement of the LVDTs used to provide surface settlement data.

The miniature Pore Pressure Transducers (PPTs) were installed into the model via ports on the back wall of the strong-box to measure the pore water pressure and check when

equilibrium conditions had been reached. Another pressure transducer was installed inside the stand-pipe to double check the water table level.

It was necessary to monitor real time tunnel support pressure in the model tunnel to balance the overburden pressure throughout the full duration of centrifuge flight. In order to cope with that requirement, a pressure transducer was connected to the tunnel fitting to monitor the tunnel pressure (**Figure 4.5**). A tunnel fitting unit was secured to the latex bag which sealed the bag against the wall and allowed for the supply of compressed air through the wall.

4.4 Soil model

With relatively high permeability and inert nature, Speswhite kaolin clay has been widely used in laboratory and centrifuge testing (Grant, 1998). Properties of Speswhite kaolin are presented in **Table 4.2**.

As this research is focused on the pre-failure mechanisms of ground deformations due to tunnelling in undrained conditions, the undrained shear strength, S_u , of clay is of interest. Several authors have proposed empirical solutions to estimate the undrained shear strength of soil in centrifuge models based on the effective stress level and the overconsolidation ratio (OCR) as expressed below;

$$S_u = a\sigma'_v OCR^b \quad (4.1)$$

where a, b are empirically derived constants, and

OCR is overconsolidation ratio.

For Speswhite kaolin clay as the sample used in centrifuge model, Garnier (2002) proposed $a=0.19$ and $b=0.59$ and Springman (1989) suggested $a=0.19$ and $b=0.71$.

Another method to determine the undrained shear strength of clay in centrifuge models is to conduct hand shear vane tests on the unloaded sample (i.e. immediately after stoppage of the centrifuge). Consistent results of undrained shear strength of model clay obtained by hand shear vanes on unloaded centrifuge models have been reported by Grant (1998), Divall (2013) and Gorasia (2013). The Speswhite kaolin clay used in these researches were consolidated to relatively high pressure $\sigma'_{v0}=500\text{kPa}$.

However, for clay models subjected to a low consolidation pressure ($\sigma'_{v0}<180\text{kPa}$), Mair (1979) and Le & Taylor (2017) reported unrepresentative undrained shear strength S_u obtained by hand shear vane on centrifuge models post test. The development of cavitation when the model was unloaded was determined to be responsible for the reduction of the undrained shear strength of the unloaded samples (Mair, 1979).

Removing total stress from a fully saturated clay sample (the same as stopping the centrifuge for a centrifuge model) results in negative pore pressure that is expected to be equal to the mean normal total stress that the clay experienced so that the mean normal effective stress remains unchanged. However, the pore pressure cannot become more negative than a threshold. Once the pore pressure reaches this threshold on unloading the sample, a certain portion of the water vaporises and cavitation takes place.

Mair (1979) conducted a set of triaxial tests to investigate the effect of cavitation in reducing the undrained shear strength of an unloaded sample. The tests were carried out immediately once the cell pressure was reduced to zero. One of the variables was the consolidation pressure and details of the tests can be found in Mair (1979). The results showed that specimens subjected to a lower consolidation pressure were more susceptible to the cavitation phenomenon which resulted in a higher reduction in the undrained shear strength.

Mair (1979) suggested that most of the elements of clay around and above the tunnel in three-dimensional heading tests experience extension stress path during the reduction of tunnel support pressure. Therefore, undrained shear strength of clay in a three-dimensional heading test is relevant to the strength of one-dimensionally consolidated kaolin in triaxial extension. For estimation of undrained shear strength S_u in centrifuge tunnel tests, Mair (1979) used the relationship between the *OCR* and the consolidation pressure σ'_{v0} , derived from triaxial extension tests shown in **Figure 4.6**.

4.5 Experimental procedure

4.5.1 Clay preparation

The model soil was prepared by mixing Speswhite kaolin clay with distilled water in an industrial ribbon mixer until a uniform mixed slurry of moisture content at approximately 120% was achieved. Speswhite kaolin slurry is normally mixed at this moisture content (e.g. roughly twice the liquid limit of clay) since then the particles are free to develop their own structure under a given system of applied stresses (Mair, 1979).

The slurry was poured into the model container (the strong-box). In terms of time saving in model preparation, it is important to minimise the time required for the model clay to reach fully drained equilibrium. A 3mm porous plastic sheet and filter paper were placed on the bottom of the model container to allow the passage of water between the model and the drainage system on the strong-box but prevent the loss of clay. Water-pump grease was applied to the walls of strong-box to minimise the friction between the clay and the strong-box wall (Mair, 1979). Care was taken when the slurry was placed into the strong-box to ensure no air voids were formed. When the required volume of clay was placed into the strong-box, a filter paper and porous plastic sheet were placed on the top of the sample to enable dual drainage paths. This reduces the drainage path length and shortens the time required for consolidation.

The strong-box was then placed under a hydraulic press where the model clay was one-dimensionally consolidated. The piston was lowered to the sample and the initial consolidation pressure was set to approximately $\sigma'_{v0}=60$ kPa. The consolidation pressure was subsequently increased over the following day to $\sigma'_{v0}=175$ kPa. The consolidation pressure was held at $\sigma'_{v0}=175$ kPa (final consolidation pressure) for around another five days after which vertical movements were observed to be negligible.

Before the test day, the PPTs were installed into the clay model through holes in the backwall of the strongbox. This was done by fixing a guide into the holes to direct an auger which then bored a clay core to create space for the PPTs. The PPTs were located remotely from the model tunnel to minimise any potential effects to the induced soil deformations. Once the PPTs were placed into the bored holes, de-aired kaolin slurry was used to fill up the cavities. This was followed by installing special fittings to seal the holes

while allowing the cables of the PPTs to thread through for connection with the junction box later.

4.5.2 Preparation of the model

On the day of the test, the model was removed from the consolidation press for the model preparation. In order to prevent the model from swelling, drainage ports were closed prior to pressure removal.

The front plate of the strong-box was removed to provide access to the clay model. A cutting jig was clamped on to the front of the strong-box to guide a sharpened box cutter to trim the model clay to the required height. In order to prevent moisture loss, the top surface and the front face of the model was coated with ‘plastidip’ and silicone fluid respectively.

In the first test series CD3B, CD1B, and S, the target marking beads were inserted into the front face of the model clay to be used as targets in 2D image processing Visimet (**Section 3.6**) for subsurface displacements analysis. In the test series CD3S, GeoPIV-RG replaced Visimet in measuring subsurface displacements hence glass ballotini were inserted into the front surface to create texture instead of target marking beads (**Figure 4.7**). The effect of changing from target marking beads to glass ballotini is discussed in **Section 5.4.1**.

A tunnel cutting guide and tunnel cutter were then used to cut the semi-circular tunnel cavity (**Figure 4.7**). The brass rods used to model the Forepoling Umbrella System were inserted into the clay sample. The stiff lining and rubber bag were then placed into the model respectively. A tunnel fitting was used to ensure an air-tight seal between the rubber bag and strong-box wall.

The front Perspex window was coated by high viscosity silicone fluid to minimise friction with the clay sample before being firmly bolted into place.

The LVDTs gantry or 3DIS was then mounted onto the strong-box to record the surface deformation data during the test. **Figure 4.8** shows model ready to load onto the centrifuge swing.

4.5.3 Centrifuge test procedure

The centrifuge strong-box containing the tunnel model was weighed for the counter weight calculation and then loaded on the centrifuge swing. A number of tasks were then undertaken including: stand-pipe setup, pressure transducer installation in the stand-pipe, air-pressure supply connection to the tunnel fitting, adjusting the cameras and lighting for image processing, connection of all instrumentation into the junction boxes, checking on amplification gains and data logging, counter weight positioning and vertical positioning of LVDTs. Final safety checks were completed and the model was then ready to spin-up (**Figure 4.9**).

The models were accelerated to $125g$ and left running overnight until the clay model reached an equilibrium state and hydrostatic pore pressures were achieved. During the spin up phase, the tunnel support pressure was increased to balance the overburden pressure at tunnel axis level. The overburden stress at tunnel axis level was calculated using the following equation:

$$\sigma_{ob} = \left(C + \frac{D}{2} \right) \times \gamma \quad (4.2)$$

where σ_{ob} is the overburden stress at the tunnel centreline,

$\gamma = 16.5kN/m^3$ is the unit weight of the soil,

C is the cover depth above the tunnel,

$D=50mm$ is the tunnel diameter.

The calculated overburden stresses in $C/D=3$ and $C/D=1$ tests were 360kPa and 155kPa respectively.

The water supply to the model was turned on. Data during this phase were recorded every minute and typical results are presented in **Figure 4.10**. As an example the tunnel pressure in test 5BL was increased from approximately zero to 368kPa and kept constant until the next phase of the test (tunnel pressure reduction) took place (**Figure 4.10**). The inclined

slope part of tunnel pressure represents the increase in centrifuge acceleration and the approximately horizontal part of the graph represents the inflight consolidation phase.

After the clay model reached equilibrium, the tunnel pressure was gradually reduced to simulate the ground movement due to tunnelling. This technique has been shown to be successful in simulating tunnelling induced ground movements (e.g. Mair, 1979).

Readings from the LVDTs, PPTs, Tunnel Pressure Transducer (TPT) and images from cameras during tests were recorded at one second intervals for later analysis.

4.5.4 Summary of model stress history

It is essential to understand the stress history of the model clay for correct interpretation of the soil behaviour. The stress history described herein is based on the actual centrifuge test procedure.

The sample was consolidated to a maximum vertical effective stress $\sigma'_{v0}=175\text{kPa}$. After the consolidation was complete at 175kPa, the pore water pressure would be close to zero giving a vertical effective stress of 175kPa throughout the sample (the self-weight effect of 300mm high sample at 1g is deemed negligible).

On the test day, the drainage valves were closed before removing the model from the consolidation press to prevent the model from swelling. The model was unloaded to zero vertical total stress very rapidly. As a consequence, a suction should develop in the pores of the soil and the vertical effective stress then remains at a magnitude corresponding to the negative pore pressure.

During the model making time, the negative pore pressure continued to dissipate and the model clay swelled back. The negative pore pressures measured by the fully de-aired PPT were shown in **Figure 4.10**. Then, the model was accelerated to 125g and the water was fed into the soil model from the standpipe via the drainage system at the bottom of the strong-box.

Pore water pressure during the equilibrium stage of the model in-flight can be seen in **Figure 4.10**. It is evident that the pore water pressure was negative at the initial stage and

gradually increased to hydrostatic conditions relative to the base aquifer at the end of the equilibrium period. Consequently, the model clay had reached effective stress equilibrium. **Figure 4.11** presents the stress history of the clay in the model from preconsolidation to immediately before the reduction of tunnel pressure.

4.6 Summary

Full details of the centrifuge modelling conducted for this research are presented in this chapter. The requirements for the model to achieve the research purposes have been introduced and the development of the testing apparatus to cope with these requirements was described.

The dimensions of the model tunnel, the model forepoles and the centrifuge acceleration were chosen to give a realistic equivalent prototype. With the available model container, the inherent boundary effects with respect to the chosen size of the model tunnel were considered negligible. The broad variables of the tunnel geometries (C/D , P/D) and the parameters of the FUS (α , EL/D and forepole stiffness) allow their relative effects to be studied.

Improvements made to the testing apparatus and the measurement instrumentation during the progression of the research project were presented. The properties and stress history of the model clay were described which will be used for later analysis.

CHAPTER 5 CENTRIFUGE TEST RESULTS

5.1 Introduction

The essential data obtained from the centrifuge tests described in Chapter 4 are presented in this chapter. Firstly, the performance of the measurement systems of the centrifuge tests are examined. The newly developed 3D Imaging System provided valuable additional information that widened the scope of measured soil displacements and enabled greater insight into the soil deformations and the effect of the FUS.

The existing framework on the soil deformations due to tunnelling reviewed in Chapter 2 are used to assess the tests results. The soil deformations in the reference tests show the consistency with the current framework.

Next, the influence of the amendments made to the testing apparatus is studied. Then the results are presented to illustrate the reinforcing effect of the FUS for different tunnel depths and arrangements and stiffnesses of the model rods.

5.2 Performance of the measurement systems

5.2.1 *Performance of Visimet compared with LVDT*

The image processing technique Visimet has been utilised within the Geotechnical Centrifuge facility at City, University of London and reliable results have been reported by previous researchers (Grant, 1998; McNamara, 2001; Divall, 2013). Their experiments were plane strain in which the LVDTs were placed in a row along the central plane of the model at the surface to measure the soil settlement. In contrast, Visimet was used to record the soil displacements of the front face of the model which was monitored through a Perspex window.

In the previous research, there was a lag in the soil movements measured by Visimet and those recorded by LVDTs. The reason for the discrepancy was explained as being due to

friction at the interface between the Perspex window and the clay of the model. As the test progressed, LVDTs along the central plane of the model detected settlements due to the simulated tunnel construction. However, friction between the clay and Perspex window resulted in a delay to the onset of the deformations at this interface. This created an initial offset between the LVDTs and Visimet measurements. Once the soil at that interface moved, it continued to displace at the same rate with the rest of the model (Grant, 1998) which showed the identical trend in soil displacements measured by LVDTs.

The centrifuge experiments conducted by Grant (1998) had the similar testing procedure with the tests in this project which involved using compressed air to support the tunnel cavity ($\sigma_T=360\text{kPa}$ at the beginning of the test for $C/D = 3$) and reduction of air pressure to simulate the tunnel excavation process. The delay between Visimet and LVDTs in Grant (1998) caused by the friction was consistent throughout the centrifuge tests and was determined being equivalent to approximately 15kPa in terms of tunnel support pressure reduction.

The centrifuge tests in this project used the same procedure and lubrication between the clay and Perspex window as in Grant (1998), McNamara (2001) and Divall (2013). **Figure 5.1** presents typical measurements of an LVDT (located approximately 10mm from the Perspex window) and a nearby target (positioned approximately 8mm below the soil surface) when the tunnel support pressure was reduced. **Figure 5.1.a** shows good agreement between the measurements made by LVDT and Visimet. **Figure 5.1.b** plots the same data but focuses on the early stage of the test with the displacement scale magnified by ten.

It can be seen that the target started to move at the same time as the LVDT and any offset between the two measurements existed only for a very short range of tunnel support pressure reduction from 200 to 150kPa. The latter data showed very good match between the two measurements. Evidently, the delay between LVDT and Visimet measurements was not as pronounced as observed in Grant (1998). A possible explanation for this is that the row of LVDTs in this project was positioned close the Perspex window, hence close to the target. Also, the clay had a lower preconsolidation stress, compared with $\sigma'_{v0}=500\text{kPa}$ in Grant (1998), though it is unclear what the relative effects of this might have been.

In this project, some difficulties were encountered in the usage of the Visimet image processing system for recording soil deformations. The maximum noise level of Visimet data was approximately 20 μ m and was deemed acceptable as it is less than 10% of the maximum soil displacement observed in the centrifuge tests. Visimet measurements rely on tracking of the density distribution of the targets in sequential images (**Section 3.6**). As a consequence, some targets near the tunnel face and heading could not be tracked at the late stage of the tests due to the large change in the target density distribution caused by rapid displacements and some targets becoming partially covered by clay.

The synchronisation of the image acquisition and the other electronic transducers was conducted manually as they were logged on two separate computers. The reason was the compatibility issue of the image recording hardware and software for Visimet with the data logger PXI computer. The maximum error due to the manual synchronisation is deemed to correspond to around ± 5 kPa. Having images and the electrical transducers recorded on the same computer would minimise this tunnel pressure reduction discrepancy. In later tests, Visimet was replaced by GeoPIV_RG to measure the soil deformation at the front face of the model. The reason being was GeoPIV_RG offers improved measurement precision as well as automatic synchronisation with electronic transducers and 3DIS (all the data were then recorded using one computer).

5.2.2 Performance of GeoPIV_RG and 3D Imaging system

Even though the 3DIS was shown to achieve a precision of 35 μ m and 50 μ m for horizontal and vertical movements respectively (**Section 3.8**), it is also necessary to examine its performance under the high acceleration centrifuge condition and with restricted lighting conditions to identify its limitations.

Having two imaging systems GeoPIV_RG and 3DIS to measure the model on the front face and the top surface introduces difficulties in achieving optimal lighting on both fields of view (FOV). The area that had the most adverse effect (poor contrast) was at the top edge of the model where the front face and top surface meet and the light from the front and the top of the model tended to interfere. As a consequence, the quality of texture in the images was reduced. After four centrifuge tests (14BL, 15BL, 16BL and 17BL), a good arrangement for positions of the light strips had been determined. It was found beneficial to have a black tape covering the part of the Perspex window above the model

surface (indicated in **Figure 5.2**) to prevent the light source at the front from affecting the measurements at the top and vice versa.

The GeoPIV_RG system used by the Geotechnical Centrifuge Research Group was reported as giving comparable measurement precision with LVDTs (Nadimi *et al.*, 2016). Hence, GeoPIV_RG is used to evaluate the quality of the measurement made by 3DIS in the centrifuge tests. The assessment of the performance of the two systems can be made by comparing their measurements of soil movements at the interface between the top surface and the front face of the model as illustrated in **Figure 5.3**. These comparisons are presented in **Figures 5.4** and **5.5** which show the maximum difference of the measurements recorded by the two systems was about 35 μm and the average discrepancy was about 20 μm .

It was also observed that the silicone oil (described in **Section 4.5.2**) between the window and the clay was squeezed vertically upwards as the contact pressure between the clay and the window increased during the test. This tended to spill over onto the top of the model as the model surface settled down (depicted in **Figure 5.2**). Consequently, the silicone oil covered the texture on the upper surface which resulted in the reduction on the measurement precision in this area as 3DIS relies on the texture for image processing. Therefore, the measurements of the top of the model near the Perspex window in the later stage of the tests was taken from GeoPIV_RG to complete the data set for the whole model surface.

Tracking the displacement of a cell at the top surface of the model involved searching that cell in consecutive images. If there are significant surface deformations between successive images, there will be significant distortion in the shapes of a cell. Large changes in the shape of the cell results in the decrease in the “degree of match” and the precision of the measurements (**Section 3.7**). At the latter stages of the centrifuge tests, rapid ground deformations of the model surface were observed (e.g. after the tunnel support pressure was lower than 60kPa in test 18BL) and the degree of match decreased hence the horizontal displacements data are not reliable.

One possible solution to tackle this problem is to increase the frequency of the image capture so that the change in the cell shape between the consecutive images is small, so improving the “degree of match”. However, the ethernet bandwidth of the data logging

PC was not large enough to have more than 3 high quality images to be taken at the interval of 1 second. Nevertheless, the data from the beginning of the test until the tunnel support pressure reduced to 60kPa is deemed adequate to gain the insight into the effects of FUS.

5.2.3 Summary

The performance of the measurement systems has been examined and shown to provide reliable results in the centrifuge tests. Using two separate measurement systems, either LVDTs + Visimet or 3DIS + GeoPIV-RG, for measuring the soil displacements enabled the recorded data to be cross-checked which enabled confidence in the results obtained.

5.3 Soil deformations in reference tests

5.3.1 Transverse soil surface settlement

Previous studies showed that the transverse surface settlement trough caused by tunnel construction is well described by the Gaussian curve (**Section 2.5.3**).

$$w = w_{max} \exp\left(\frac{-y^2}{2i_y^2}\right) \quad (2.7 \text{ bis}) \quad (5.1)$$

The transverse soil settlement trough can be plotted if the two parameters i_y and V_L are known. Jones & Clayton (2013) proposed a linear regression approach to estimate these two parameters. In their method, i_y and V_L are varied to find the best fit with the measured data and the best fit is indicated by the minimum sum of absolute error (*SAE*). In this research, for the centrifuge tests using 3D Imaging System the volume of the settlement trough was measured accurately and V_L does not need to be estimated. The remaining parameter i_y is varied to find the “*best fit*” with the measurements.

A typical 3D settlement trough obtained from the reference test 18BL is presented in **Figure 5.6**. As expected, the maximum settlement occurred in the area above the tunnel face and along the tunnel centreline. The fit of the settlement trough in the centrifuge test

(depicted in **Figure 5.6**) to the Gaussian curve can be checked by comparing the measured and the predicted settlement profiles. For this purpose, the transverse settlement troughs above the tunnel face at three different tunnel support pressures $\sigma_T=120\text{kPa}$, 100kPa and 80kPa were considered. The Gaussian curves were estimated using the values of the measured volume loss V_L and i_y estimated using the linear regression method proposed by Jones & Clayton (2013). The sum of the absolute error was calculated by **Equation 2.19** which is presented again in **Equation 5.2**; the average of the absolute error (*AAE*) was calculated by **Equation 5.3**.

$$SAE = \sum_{m=1}^n \left| \frac{V_S}{\sqrt{2\pi}i_y} \exp\left(\frac{-y_m^2}{2i_y^2}\right) - w_m \right| \quad (2.19 \text{ bis}) \quad (5.2)$$

$$AAE = \frac{1}{n} SAE \quad (5.3)$$

where n is the total number of measurement points,

w_m is the measured settlement value.

The total number of the measured points at the model surface for each tunnel support pressure was 14 points and the sum of absolute error $SAE=0.45\text{mm}$ ($AAE =0.03\text{mm}$) at $\sigma_T=120\text{kPa}$, $SAE=0.58\text{mm}$ ($AAE=0.04\text{mm}$) at $\sigma_T=100\text{kPa}$ and $SAE=1.02\text{mm}$ ($AAE=0.07\text{mm}$) at $\sigma_T=80\text{kPa}$. The estimated best fit i_y for the measured settlement troughs at these three tunnel support pressures showed negligible variation with calculated values of $i_y=84.8\text{mm}$, 82mm and 83.1mm respectively.

This observation is in agreement with the relatively constant i_y observed in previous research (**Section 2.5.3**). The equivalent factor K for $i_y=82\div 84.8\text{mm}$ is $K = i_y/z_0=0.47\div 0.48$ which falls within the range of the typical $K=0.4\div 0.7$ for many reported case histories of tunnelling in clay (**Section 2.5.3**). The average of absolute error $AAE=0.03\div 0.07\text{mm}$ is considered very good. This is reflected in the good agreement between the measured settlement trough with the best fit Gaussian curve in **Figure 5.7** apart from the data point above the tunnel centreline ($y=0$) at the later stage of the test (i.e. when σ_T was reduced lower than 80kPa).

A possible explanation for the relatively large discrepancy between the measured and predicted settlement was the rise of the silicone oil from the interface between the model clay and the Perspex window as the model surface settled (**Section 5.2.2**). The oil flooding onto the model surface acted as a small surcharge in the area above the tunnel centreline and may have caused larger local settlement.

Another method to test the fit of the settlement trough with the Gaussian curve is to plot $\ln(w/w_{max})$ versus the square of the offset from the tunnel centreline y^2 and a perfect fit would give a straight line (deduced from **Equation 2.4.3**). The line in **Figure 5.8** appears to have some noise but most of the data points lie close to the best fit straight line. When σ_T reduced below 80kPa, it was noticed that i_y continuously decreased considerably.

5.3.2 Horizontal displacement in transverse direction

Figure 5.9 compares typical measured and the predicted (empirical) horizontal displacement profiles at the model surface in test 18BL when the tunnel support pressure σ_T reduced to 60kPa. In the empirical curve, the horizontal surface displacement v at a distance y from the tunnel centreline was determined using **Equation 2.22** which is presented again in **Equation 5.4**.

$$v_y = \frac{yw_y}{z_0} \quad (2.22 \text{ bis}) \quad (5.4)$$

where w_y is the surface settlement at a distance y from the tunnel centreline (calculated using the procedure described in **Section 5.3.1**).

The measured horizontal displacements were very small especially in the area near the tunnel centreline. It can be seen that the empirical horizontal displacement curve overpredicted the actual magnitude of the horizontal soil displacement. **Figure 5.10** compares the trend of horizontal displacements in test 18BL with **Equation 5.4** and field measurement from Hong & Bae (1995). The distance from tunnel centreline y is normalised against i_y and horizontal displacement v normalised against the maximum value v_{max} . The experimental data appeared to have an offset from the tunnel centreline.

This suggests that near the ground surface, there was a separation from the Perspex window which altered the focus of horizontal movement when the soil surface settled.

Another empirical line (dashed line) is shown in **Figure 5.10** which has an offset from the tunnel line to examine the fit with the measured data. It is evident that the fit between the empirical line with the measured line was fairly reasonable except the offset.

5.3.3 Longitudinal soil surface settlement

Previous authors (Attewell & Woodman, 1982; Nyren, 1998; Dimmock, 2003) demonstrated that the measured longitudinal soil settlement was well represented by the cumulative probability function (**Equation 2.23**) proposed by Attewell & Woodman (1982). For the surface settlement developed above the tunnel centreline ($y = 0$ and $z = 0$), **Equation 2.23** simplifies to;

$$w_x = w_{final} \left\{ G \left(\frac{x - x_i}{i_x} \right) - G \left(\frac{x - x_f}{i_x} \right) \right\} \quad (5.5)$$

With the model tunnel heading in this research, the starting point of the tunnel (x_i) can be considered as the edge of the tunnel lining and the tunnel face (x_f) considered to be the end of the unlined section (as shown in **Figure 5.11**). The required variables to define the longitudinal surface settlement profile above the tunnel centreline are the final surface settlement above tunnel centreline w_{final} and settlement trough length parameter i_x .

The tunnel heading model in the centrifuge test did not simulate an advancing tunnel face hence the maximum final settlement w_{final} could not be obtained. However, it is reasonable to consider the final surface settlement w_{final} as a constant. By doing so, the dimensionless profile of the longitudinal surface settlement above the tunnel centreline can be determined by normalising w_x against w_{face} . The value $i_x = 80\text{mm}$, derived by using a best fit method similar to the procedure described in **Section 5.3.1**, was used for this empirical line.

Figure 5.12 shows the good fit between the empirical and the measured longitudinal settlement profiles in the reference tests. For both tunnel depths, the settlement is very small at a horizontal distance corresponding to z_0 from the tunnel face.

5.3.4 Soil displacement with depth

Settlement with depth

Typical profiles of soil settlement with depth in the vertical plane through the tunnel centreline from test 18BL (from PIV measurement) are presented in **Figure 5.13** together with the corresponding empirical profiles. The empirical profiles of settlement with depth were determined using **Equation 2.21** with $y=0$ which is simplified to **Equation 5.6**;

$$w_z = w_{(max,z)} \quad (2.21 \text{ bis}) \quad (5.6)$$

where $w_{(max,z)}$ is the maximum soil settlement at the depth z and is calculated by **Equation 2.15** which is represented in **Equation 5.7**;

$$w_{(max,z)} = 0.313V_L D^2 / [K(z_0 - z)] = 0.313V_L D^2 / i_y^z; \quad (2.15 \text{ bis}) \quad (5.7)$$

The value of i_y with depth is determined using the equation proposed by Mair *et al.*, (1993);

$$\frac{i_y^z}{z_0} = 0.175 + 0.325 \left(1 - \frac{z}{z_0} \right) \quad (2.16 \text{ bis}) \quad (5.8)$$

At the surface, $i_y=87.5\text{mm}$ (determined using **Equation 5.8** with $z=0$) is consistent with the estimated $i_y=82\div 84.8\text{mm}$ based on the measured transverse settlement trough (**Section 5.3.1**). It can be seen that the fit between the measured and the corresponding empirical settlement with depth profile is very good except for the settlement near the depth $z/z_0=0.8$. Mair *et al.*, (1993) also suggested that their equation was established based on many field measurements but only a few data points were available in the area near the tunnel centreline (i.e. when $z/z_0 \geq 0.8$) and caution should be exercised with the prediction at this depth.

In the later stage of the test when tunnel support pressure reduced below 100kPa, the fit between the measured and empirical profiles was no longer observed and collapse of the tunnel occurred. The profiles of the settlement with depth in other reference tests 5BL ($C/D=3$) and 9BL ($C/D=1$) are also presented in **Figure 5.14** which demonstrate the good

agreement with the empirical line. This also confirms the soil behaviour in test 5BL was similar to that in test 18BL despite the change in the measurement system used.

Longitudinal horizontal soil displacement at tunnel axis level

Field measurements from relatively few cases history showed that the maximum horizontal displacement in the longitudinal direction occurred at the tunnel axis level. This was also observed in the centrifuge tests conducted in this research. Subsurface horizontal displacements at the tunnel axis can be predicted using the simple linear elastic-perfectly plastic model proposed by Mair & Taylor (1993) which provided a good fit with some case history data (**Section 2.5.5**). Mair & Taylor (1993) suggested that the modelled 3D tunnel heading in this research can be idealised as the unloading of a spherical cavity.

Figure 5.15 presents the measured longitudinal horizontal displacement in test 18BL when the tunnel support pressure was reduced from the beginning of the test to 200kPa, 150kPa and 100kPa. The idealisation to unloading of a spherical cavity predicts that the longitudinal horizontal soil displacement ahead of the tunnel face (u/a) is proportional to $(a/r)^2$ which is demonstrated in **Figure 5.15**. Also, the gradient of the lines increases as the tunnel support pressure decreases (i.e. increase in tunnel stability ratio N) which is consistent with the framework of the linear elastic-perfectly plastic model.

5.3.5 Summary

Although the tunnel heading in the centrifuge testing apparatus did not model an advancing tunnel face, the observed soil response to the simulated tunnel excavation process was found to have similar tunnelling-induced soil deformations including the settlement trough in the longitudinal and transverse directions and the settlement with depth. This gives confidence that the experiment study will reveal realistic effects of forepoles on tunnelling induced ground movements.

5.4 Assessment on the amendments of the testing apparatus

5.4.1 Change in measurement system - comparison on reference tests

In the later tests, 3DIS replaced LVDTs to measure the deformations of the model surface and GeoPIV_RG replaced Visimet to measure the subsurface displacements which offered improved measurement precision and also introduced changes to the model. The changes includes the usage of glass ballotini for GeoPIV_RG instead of targets for Visimet, texturing sand at the model surface for 3DIS instead of the row of LVDTs. To some extent, this inevitably affected the test results in the later tests when compared with the earlier tests. Successful reference tests were essential to establish a reliable datum to compare with the other reinforced tests. Therefore, the reference test 5BL (using LVDTs and Visimet) was repeated in test 18BL (using 3DIS and PIV) to assess the discrepancies caused by the change in measurement systems and to establish the datum for the tests using 3DIS and PIV.

Figure 5.16 compares the surface and crown settlements above the tunnel face in tests 5BL and 18BL. The data for the tunnel crown in test 5BL was available only when the tunnel support pressure $\sigma_T \geq 80\text{kPa}$ as Visimet lost tracking of this point at lower support pressure (**Section 5.2.1**). The magnitude of the settlements in test 18BL were smaller than those that in test 5BL especially in the early stage of the tests. When large displacements developed in test 18BL ($\sigma_T < 125\text{kPa}$), the shape of the settlement curves at both the surface and tunnel crown show a similar trend and gradient with those in test 5BL.

A possible explanation for this discrepancy was the friction between the Perspex window against the clay textured by glass ballotini (for GeoPIV_RG in test 18BL) was higher than that between the Perspex window against the clay with targets (for Visimet in test 5BL). To examine this, a set of shear box experiments were carried out to measure the friction between the Perspex with the clay model.

Three different surfaces of clay model were examined: blank surface (no texture or target), target (as in Visimet), and glass ballotini (as in GeoPIV_RG). The model clay was consolidated to 100kPa in a consolidometer. After consolidation, the clay block was trimmed to 100x100x20mm sample that fitted into half of a sample container of the shear box apparatus and a Perspex plate (same material as Perspex window) was inserted into

the other half to model the interface between the Perspex window and the front face of the model in the centrifuge tests. **Figure 5.17** illustrates the experimental setup.

The procedure of applying the lubrication, the arrangement of the targets and glass ballotini in the centrifuge test were replicated at the clay interface in the shear box test. The clay samples were tested at a total vertical stress of 100kPa which is comparable to the total horizontal stress in the centrifuge tests. The test was conducted by applying horizontal displacement to the lower half of the model container. The horizontal displacement was measured by an LVDT and the resistance horizontal load was measured by a load cell (**Figure 5.17**).

The results of the experiments are presented in **Figure 5.18** which show no displacement developed until the horizontal load reached a certain value that was adequate to overcome the static friction. The frictional resistance then tended to increase until a horizontal displacement of about 6mm had been reached. This relatively simple experiment demonstrated the greater friction developed (by about 20%) when using glass ballotini for the image texture which could explain the “lag” in measured settlement when using PIV (with glass ballotini) compared with Visimet (using plastic target). The gradients of the load-displacement curves in the three experiments (**Figure 5.18**) are similar which is relevant to the similar soil displacement trend in tests 5BL and 18BL (**Figure 5.16**).

This reason resulted in the offset in the settlement development in test 18BL when compared with test 5BL (**Figure 5.16**). The magnitude of this offset at the surface and the tunnel crown in these two tests appeared to be similar in the later period. It is essential to ensure the soil deformation mechanisms in the two tests were the same. This could be checked by comparing the subsurface soil deformations. The soil displacement at the tunnel crown in test 5BL at 80kPa was similar to that in test 18BL at 68.5kPa hence these two tunnel support pressures were used for comparison purpose. Contours of ground displacements and shear strain in test 5BL when $\sigma_T=80\text{kPa}$ and 18BL when $\sigma_T=68.5\text{kPa}$ are compared in **Figure 5.19**.

The magnitude and extent of the contours in the two tests were closely comparable. Therefore, it can be argued that the mechanism of soil deformations were consistent in the two tests despite the different measurement systems used. Therefore, the comparison

of the soil deformations will be made between tests that used the same measurement systems to exclude the discrepancies caused by the different target or texture material.

5.4.2 Change in stiffness of tunnel lining

In the first two tests 2BL and 3BL, a semi-circular brass tube was used to model the tunnel lining. Inflight images showed considerable deflection of the tunnel lining when the tunnel support pressure reduced to 180kPa. As a consequence, the ground above the tunnel lining settled which can be seen in the subsurface ground movements presented in **Figure 5.20**. The tunnel support pressure in tests 2BL and 3BL at the start of the test was set at 381kPa to balance the overburden stress at the tunnel centre-line. Therefore, the upper part of the tunnel was over pressurised (as discussed in **Section 2.2**). As a consequence, the brass lining initially elongated on its vertical diameter when the tunnel pressure was increased and then sprang back elastically to its normal shape when the support pressure was reduced. This was attributed to a lack of hoop stiffness of the brass lining.

To overcome this, stiffeners were added to the brass lining and the tunnel support pressure during the equilibrium phase was reduced to 368kPa for subsequent tests 4BL and 5BL. These changes reduced the settlement immediately above the lining as well as the ground surface prior to tunnel collapse which can be seen in **Figure 5.21**. In later tests, a semi-circular stainless steel tube was used to model the tunnel lining.

FUS reinforcing capability depends on the foundation effect (**Section 2.7.3**) which largely results from having the forepoles resting on the tunnel lining. Therefore, the FUS only delivers reinforcing effects when the support to one end of the model rods is provided by the tunnel lining i.e. when the tunnel lining deflection becomes negligible. **Figures 5.22** and **5.23** illustrate the settlement of a point immediately above the tunnel stiff lining to examine the magnitude of the tunnel lining deflection in the $C/D=3$ and $C/D=1$ tests. It can be seen that the increase of tunnel lining deflection becomes negligible when the tunnel support pressure $\sigma_T \leq 180\text{kPa}$ in $C/D=3$ tests and $\sigma_T \leq 55\text{kPa}$ in $C/D=1$ tests.

Therefore, in order to study the effect of FUS independently from deflection of and the change to the stiff lining the results will be examined from the tunnel support pressure $\sigma_T=180\text{kPa}$ for $C/D=3$ and $\sigma_T=55\text{kPa}$ for $C/D=1$ tests.

5.5 Illustrative results of the FUS reinforcing effect

Figure 5.24 presents typical data from a centrifuge test and shows the coordinate system and displacement convention used in this research. The effects of the FUS variables (filling angle α , the embedded length EL/D , the model FUS stiffness) will be investigated by examining soil deformations as a result of the tunnel support pressure reduction.

The data at the front face of the models (available in all tests) are presented first. For each comparison, the movement data are presented as horizontal displacement, with the convention of positive in the direction of tunnel “advance” i.e. a horizontal movement from in front of the tunnel towards the tunnel face is negative. This is followed by vertical movements with settlement shown as positive. These deformations are then combined to give the magnitude of resultant movement. Also, the movements are shown in the form of contours. Finally, contours of engineering shear strain are presented.

Then, surface displacement obtained by the 3DIS (only available in tests 18BL, 19BL and 20BL) are shown to complete the general picture of soil deformations in different tests using different FUS arrangements.

Following this order, the effects of having FUS are studied by comparing a reference test with a typical reinforced test. Then, in turn, the effects of the filling angle α , the embedded length EL/D and the stiffness of the model FUS are investigated.

5.5.1 Effect of using FUS

Three pairs of tests are examined to assess the effect of using FUS presence [9BL & 8BL] for $C/D=1$, [5BL & 2BL] and [18BL & 20BL] for $C/D=3$. The details of the FUS for all tests are given in **Table 4.1** and illustrated in **Figure 4.1**.

The progressive development of soil deformations is presented by plotting displacement and strain contours from high tunnel support pressure to lower support pressures. For $C/D=1$ tests, **Figures 5.25** and **5.26** present the soil deformations in tests [8BL & 9BL] when the tunnel support pressure σ_T reduced from 55kPa to 40kPa and 20kPa respectively. For $C/D=3$ tests, **Figures 5.27**, **5.28** and **5.29** present the soil deformations

in tests [2BL & 5BL] and [18BL & 20BL] when tunnel support pressure reduced from 180kPa to 140kPa, 100kPa and 80kPa.

As expected, the magnitude and extent of the soil deformations increased as the tunnel support pressure decreased. In the reference tests for both $C/D=1$ and $C/D=3$, shear strains developed at the tunnel invert first due to the large displacement in front of the tunnel face. Then, shear strain started to occur and increase at above the tunnel heading near the stiff lining following the increase in soil displacements when the tunnel support pressure σ_T reduced.

In **Figures 5.25** and **5.26** (for $C/D=1$ tunnels) and **Figures 5.27**, **5.28** and **5.29** (for $C/D=3$ tunnels), it is evident that the presence of FUS delivered a reduction in the magnitude and extent of the soil displacements and shear strains. The area that benefitted the most from the FUS was above the tunnel heading where the model rods were installed to reinforce the surrounding soil. In other areas that are far from the tunnel face or below the FUS, the effect of the FUS was less pronounced. In tests with the FUS, large engineering shear strains ($\geq 4\%$) did not developed at the tunnel heading as observed in the reference tests and only occurred in the invert of the tunnel (**Figures 5.26-d**, **5.28-d**, **5.29-d**). This is because the soil near the tunnel heading was reinforced by the FUS.

Figures 5.30 and **5.31** present the photos of the model post-test and the corresponding engineering shear strains in shallow tunnel $C/D=1$ tunnels. There were two visible shearing planes in front of the tunnel face and behind tunnel heading (**Figure 5.30-a**) which reflected in the corresponding strain fields (**Figure 5.30-b**). By contrast, in the reinforced test (8BL), the slip plane was only evident in front of the tunnel face and there was no slip plane developed behind the tunnel face (**Figure 5.31**).

In $C/D=3$ tunnels, there was no clear distinction between the extent of the slip planes in front of the tunnel face in the two tests (**Figure 5.32**). The slip plane above the tunnel heading in the reinforced test was shorter compared with that in the unreinforced test which implies smaller soil mass was sheared.

The upper bound mechanisms for $C/D=1$ and $C/D=3$ tunnels proposed by Davis *et al.*, (1980) are also presented in **Figure 5.30-a** and **5.32-a**. The dimensions of these failure zones are defined in **Figure 2.5** and provided in **Table 2.1**. It is evident that the upper

bound mechanisms over predicted the extent of the collapse zones in front of the tunnel face for both C/D ratios. However, the differences between the predicted and experimental zones of failure are small and their shapes are comparable. This observation further supports the upper bound mechanisms proposed by Davis *et al.*, (1980).

The soil displacements on the ground surface in the two tests 18BL and 20BL when the tunnel support pressure reduced from 180kPa to 80kPa are compared in **Figure 5.33**. Similar to subsurface ground deformations, the effect of FUS are most pronounced in the area above the model forepoles and in front of the tunnel face. The area behind the tunnel face and far from the FUS showed negligible distinction between soil displacements in reinforced and unreinforced tests.

In the early stage of the tests, the soil displacements were very small especially in the horizontal direction. Therefore, the data presented in the next sections are chosen for the purpose of illustrating the effects of FUS variables in a visual manner.

5.5.2 Effect of filling angle α

In this section, the effects of the filling angle $\alpha=90^\circ$ and $\alpha=75^\circ$ are compared for two different tunnel depths $C/D=1$ and $C/D=3$. Three pairs of tests are examined: [8BL vs 10BL – brass rods] for $C/D=1$, [2BL vs 4BL – brass rods] and [19BL vs 20BL – steel rods] for $C/D=3$.

For the $C/D=1$ tests, **Figure 5.34** illustrates the subsurface ground displacements in two tests 8BL ($\alpha=75^\circ$) and 10BL ($\alpha=90^\circ$) when the tunnel support pressure reduced from 55kPa to 20kPa. The area that reflected the effect of α was close to the tunnel heading and there is no clear distinction in movements or strains in the areas that far away from the FUS. The horizontal soil displacements in the two tests were similar. In contrast, the vertical soil displacements in 8BL ($\alpha=75^\circ$) were considerably smaller than those in test 10BL ($\alpha=90^\circ$). The extent of the area that had large shear strains ($\geq 8\%$) occurred near the tunnel invert in test 10BL was larger than that in test 8BL (**Figure 5.34-d**). These observations imply that for a relatively shallow cover, arranging the model rods in small filling angle $\alpha=75^\circ$ outperformed $\alpha=90^\circ$.

Figures 5.35 and **5.36** compare the subsurface soil displacements in two pairs of tests [2BL vs 4BL - brass rods] and [19BL vs 20BL - steel rods] to investigate the effects of $\alpha=75^\circ$ and $\alpha=90^\circ$ for a deeper tunnel ($C/D=3$). The soil displacements on the top surface in tests 19BL and 20BL are presented in **Figure 5.37**. Contrary to observations made in the $C/D=1$ tests, soil displacements and shear strains in the $C/D=3$ tests that had forepoles arranged in filling angle ($\alpha=90^\circ$) were smaller compared to those in tests with $\alpha=75^\circ$. Hence, for the deeper $C/D=3$ tunnels, arranging the forepoles in filling angle $\alpha=90^\circ$ outperformed filling angle $\alpha=75^\circ$. This observation suggests the soil mobilisation mechanisms around deeper tunnels (in this case $C/D=3$) is different to shallower tunnels (in this case $C/D=1$).

Figures 5.38-a and **5.38-c** present the tunnel heading post-test with the deformed forepoles in test 10BL ($C/D=1$) and 4BL ($C/D=3$) respectively. Note that in these two tests, the forepoles were distributed to the tunnel spring line i.e. filling angle $\alpha=90^\circ$.

In test 10BL ($C/D = 1$), it is evident that the deformations of the upper rods were large while the deformations of the bottom rods were negligible (**Figure 5.38-a**). This suggests that for the shallow tunnel large soil movements occurred mainly in the vicinity of the tunnel crown and small soil movements occurred near the tunnel spring line. This is consistent with the collapse mechanism A suggested by Davis *et al.*, (1980) (**Section 2.4** and **Figure 5.38-b**). Therefore, having more forepoles concentrated at the tunnel crown to reduce the majority of large soil deformations induced by tunnel excavation delivers a better reinforcement effect. This is confirmed in the comparison between 8BL ($\alpha=75^\circ$) and 10BL ($\alpha=90^\circ$) (**Figure 5.34**).

Figure 5.38-c demonstrates that all the model rods in test 4BL ($C/D = 3$) had large deformations. This observation denotes large soil displacements occurred at both the tunnel crown and near the tunnel spring line. This is relevant to the tunnel collapse mechanism D suggested by Davis *et al.*, (1980) (**Section 2.4** and **Figure 5.40-d**). The indication is that having forepoles near the tunnel spring line added to reduce lateral soil displacements which resulted in a better reinforcement effect and is confirmed by the smaller soil movements associated with FUS arranged with $\alpha=90^\circ$ compared to $\alpha=75^\circ$ (**Figures 5.35, 5.36** and **5.37**).

Also, the difference in the magnitude and extent of soil displacements between the tests with steel rods is more significant compared to those for the tests with brass rods. This implies the increase in stiffness of rods amplifies the effects of the filling angle.

5.5.3 Effect of forepole stiffness

As would be expected, the use of steel rods delivered a better reinforcement effect than brass rods as reflected in smaller soil deformations in **Figures 5.39** and **5.40**. The improvement delivered by the increase in the stiffness of forepoles appears to be considerable.

5.5.4 Effect of embedded length

The comparison of soil deformations and shear strains for tests with $EL/D=0.5$ and $EL/D=1$ at two different depths $C/D=1$ and $C/D=3$ are shown in **Figures 5.41** and **5.42** respectively. Evidently, the longer embedded length EL/D delivered a better reinforcement effect which was reflected in smaller soil displacements and shear strains.

A schematic representation of a typical forepole at the end of tests with $EL/D=0.5$ and $EL/D=1$ are presented in **Figures 5.43-a** and **5.43-b** respectively. The model rods for the $EL/D=0.5$ tests showed one inflexion point while the rod for the $EL/D=1$ test showed two inflexion points. This implies there was difference between the support mechanisms for the two arrangements.

As discussed in **Section 2.7.3** the FUS reinforcement capabilities rely on the foundation effect provided by the tunnel lining and the surrounding soil underneath the FUS. With a short embedded length $EL/D=0.5$, the foundation effect provided by the surrounding soil was relatively small and the system worked mainly as a cantilever beam with one end supported by the tunnel lining. Therefore, when the tunnel support pressure reduced, the soil moved down and so did the front part of the FUS which caused the inflexion point in the FUS near the tunnel lining edge. In contrast, the longer embedded length $EL/D=1$ benefits from the greater foundation effect provided by the larger area of the soil underneath the FUS. As a consequence, there were two inflexion points in the rods in $EL/D=1$ tests. This observation supports the foundation effect proposed by Volkmann & Schubert (2007) and Carrieri *et al.*, (2002).

5.6 Summary

The key results from the centrifuge tests have been presented to demonstrate and examine the quality of the data obtained. The capabilities and limitations of the testing apparatus and the measurement systems have been discussed which defined the range of data that can be analysed. The following summarises the main findings from the centrifuge tests presented in this chapter.

- The use of two independent measurement systems recording the surface and subsurface soil displacements not only offered greater confidence in the quality of the data obtained but also widened the coverage of the measured area and enabled the effects of the FUS variables to be studied in more detail.
- The data obtained from the centrifuge tests have been assessed and the results show that the soil response observed was similar to the tunnelling-induced soil movements. This is important to have confidence in the findings of the effects of the FUS parameters using the centrifuge modelling technique.
- The effect of having FUS was evident and was reflected via the reduction in the magnitude and extent of the soil deformations. Those effects became more pronounced at lower tunnel support pressures. The FUS had the most significant effects at the tunnel crown where the rods were installed. In the areas remote from or below the FUS the reinforcing effects were not apparent.
- The effect of the filling angle α proved to be dependent on the tunnel depths. For a shallow tunnel ($C/D=1$ in this project), FUS arranged in filling angle $\alpha=75^\circ$ delivered a better reinforcement effect than $\alpha=90^\circ$. In contrast, for the deep tunnels ($C/D=3$ in this project), $\alpha=90^\circ$ offered a larger reduction on the soil deformations. These observations are consistent with the form of tunnel collapse mechanisms suggested by Davis *et al.*, (1980).
- The longer embedded length EL/D delivered better reinforcement effects because of the better foundation effects provided by the larger soil area beneath the FUS. The increase in the FUS stiffness improved its reinforcement effect.

6.1 Introduction

This chapter draws together the key findings obtained from the centrifuge tests. Analysis on these findings are carried out and the results further substantiate the current frame work in soil response to tunnelling and underline the influence of the FUS parameters to the reinforcing effects of the system.

Two key factors including the reduction on the soil settlement and the increase in the tunnel stability are used to weigh the significance of the effect of the FUS parameters. This allows the quantifications on their effects to be made which enable a clearer understanding into the effectiveness of the system to be gained.

6.2 The general effect of using the FUS on soil deformations

6.2.1 Reduction on the maximum vertical surface settlement

The maximum surface settlement is of great interest as it indicates the potential damage to near surface structures. **Figure 6.1** presents the maximum surface settlement above the tunnel face (measured by LVDTs or GeoPIV_RG) in the centrifuge tests. Previous research has demonstrated that a FUS can reduce significantly the maximum settlement but the degree of reduction was not quantified. Being able to quantify the reduction of settlement will be valuable in decision making in selecting the FUS parameters. It would allow relative benefits offered by the FUS parameters such as bending stiffness or longer embedded length EL and the corresponding cost in term of construction time and economy to be taken into account.

The accurate measurements of the tunnel support pressure and the corresponding soil deformations observed in centrifuge tests allowed the settlement reduction offered by the FUS to be quantified. The settlement reduction delivered by FUS is defined as;

$$SR = [(w_0 - w_r)/w_0] \times 100\% \quad (6.1)$$

where w_0 , w_r are respectively the maximum surface settlement in the reference and reinforced test with the same geometry and having the same tunnel support pressure.

SR is the settlement reduction (%), based on a comparison of the maximum surface settlement between reinforced and reference tests,

Figure 6.2 illustrates the reduction on the maximum surface settlement delivered by the FUS. The presence of the FUS reduced the surface settlement by approximately 5%-85% at different tunnel support pressures. Initially, the overburden pressure, σ_{ob} , was supported by the tunnel support pressure σ_T . When σ_T reduced, the induced stress difference ($\sigma_{ob} - \sigma_T$) was supported by the surrounding soil and the FUS. Thus, the effects of the FUS became more significant as the stress difference ($\sigma_{ob} - \sigma_T$) increased as a result of the reduction of tunnel support pressure σ_T . It is also noted from **Figure 6.2** that the difference between the settlement reduction offered by different variables (α , EL and forepoles stiffness) decreased towards the end of the test. It may be that the structural capacity of the forepoles had been exceeded which led to the effects of the variables being diminished.

Generally, the stronger forepoles (steel compared with brass) delivered a higher reduction in settlement. However, there is a data point in **Figure 6.2-b** which suggests the steel rods delivered lower settlement reduction compared with that in a test with brass rods (Test 20BL compared with 2BL). This data point could be an anomaly due to noise in the measurement system. In tests 8BL and 3BL, the settlement reduction was lower than expected in the earlier stage of the tests (**Figures 6.2-a, b**). This can be explained by the extra deflection of the tunnel lining in tests 8BL and 3BL compared to the other tests (**Section 5.4.2**) hence the delay in the FUS becoming effective.

Therefore, the average of the settlement reduction will be used to assess the effectiveness of the FUS in general as the average value will be less sensitive to anomalies and the inconsistency in the deflection of tunnel lining experienced in tests 3BL and 8BL. The average values of the reductions in settlement offered by FUS in different arrangements

are tabulated in **Table 6.1** which will be used in later sections for more detailed assessments.

6.2.2 Reduction in horizontal soil displacement in the transverse direction

Horizontal displacements of the model surface in the transverse direction were only available in tests using 3DIS including 18BL, 19BL and 20BL. The horizontal displacements developed in the tests were very small in comparison with the corresponding vertical displacements.

Therefore, the horizontal displacement was only investigated when the tunnel support pressure reduced to 72kPa ($0.2\sigma_{ob}$) at which the displacement profile had been established and the magnitude was above the measurement error level (**Figure 6.3**). At this tunnel support pressure, the reduction in the maximum horizontal displacements were 53% and 35% which were delivered by the FUS in tests 19BL ($\alpha=90^\circ$) and 20BL ($\alpha=75^\circ$) respectively. The ratio between these reduction percentage was $53/35=1.5$ which is similar to the ratio of the corresponding settlement reduction $62/47=1.3$ (**Table 6.1**).

Figure 6.4 presents the normalised horizontal displacement with the maximum horizontal displacement plotted against the offset from the tunnel centreline. The change to the shape of the profile of the horizontal displacement due to the presence of the FUS appears to be negligible.

6.3 Tunnel stability

The tunnel heading stability calculation involves the overburden stress σ_{ob} , tunnel support pressure at collapse σ_{TC} and the undrained shear strength of clay S_u as shown in **Equation 6.2**;

$$N_{TC} = \frac{\sigma_{ob} - \sigma_{TC}}{S_u} \quad (6.2)$$

The overburden stress at the tunnel centreline σ_{ob} in the $C/D=1$ and $C/D=3$ tunnels were 360kPa and 155kPa respectively. The following sections in turn determine S_u and σ_{TC} for tunnel stability calculation.

6.3.1 Estimation of model clay undrained shear strength

Undrained strength determined from shear vane tests

The undrained shear strength S_u of the model clay after the tests was measured by hand shear vane at several locations of the model immediately after stopping the centrifuge. The purpose of conducting shear vane tests at three to four locations of the model was to obtain a representative undrained shear strength which was less sensitive to error compared to that measured at just one location. The average values of the measured undrained shear strength are presented in **Table 6.2**. **Figure 6.5-a** illustrates typical undrained shear strength profiles and fairly consistent values of S_u were observed.

These values of S_u appeared low and arguably unrepresentative of the true strength. Several attempts were made to use the T-bar penetrometer (Gorasia, 2013) to measure the undrained shear strength of clay in flight in a number of tests. However the equipment failed to operate successfully and no useable results were obtained. Time constraints and the use of the 3D imaging system in the later tests prevented the T-bar penetrometer being utilised in the research.

Undrained strength calculated using Critical State Soil Mechanics

In the later tests, the water content of the clay was also measured which show fairly consistent values among the tests (**Figure 6.5-b**). Using Critical State Soil Mechanics (Schofield & Wroth, 1968), the undrained shear strength of clay can be estimated using the equation;

$$S_u = \frac{M}{2} \exp\left(\frac{\Gamma - v}{\lambda}\right) \quad (6.3)$$

The parameters M , Γ and λ of Speswhite kaolin are presented in **Table 4.2**. Specific volume v was calculated using the water content measured at the tunnel centreline in the model post-test. The average water contents at the tunnel centreline in $C/D=1$ and $C/D=3$

tests were 54.5% and 53.5% respectively. These led to the corresponding undrained shear strength $S_u=30.3\text{kPa}$ and $S_u=34.8\text{kPa}$ for tests with $C/D=1$ and $C/D=3$ respectively.

Undrained strength estimated using Mair (1979) approach

Low values of the order of up to 50% of the expected strength obtained from shear vane tests on unloaded clay models conducted by various researchers were also reported by Mair (1979). It was suggested that the low undrained shear strength obtained in unloaded models were because of the cavitation in the clay at the region of the vane which resulted in the reduction of the effective stress over the shearing surface. The cavitation phenomenon was described in **Section 4.4**.

Therefore, Mair (1979) used the relationship between *OCR* and undrained shear strength to estimate S_u of the clay model for tunnel stability calculation (**Section 4.4**). The Speswhite kaolin clay in this project is the same with the clay used in 3D heading tests conducted by Mair (1979). The *OCR* of the clay at the tunnel centreline for tests at $C/D=1$ and $C/D=3$ were 1.87 and 1.02. According to **Figure 4.6**, the undrained shear strengths of the clay at the tunnel centrelines for the $C/D=1$ and $C/D=3$ tests are determined as follow;

$$S_u = 0.16\sigma'_{v0} = 0.16 \times 175 = 28(\text{kPa}); \text{ for } C/D=1 \text{ tests} \quad (6.4)$$

$$S_u = 0.18\sigma'_{v0} = 0.18 \times 175 = 31.5(\text{kPa}); \text{ for } C/D=3 \text{ tests} \quad (6.5)$$

The undrained shear strengths determined from **Equations 6.4** and **6.5** are in line with the estimate using Critical State Soil Mechanics (**Equation 6.3**) as opposed to the measured values obtained from hand shear vane tests on the unloaded sample in which the undrained shear strengths were possibly affected by cavitation.

As a result, for consistency with the framework for tunnel stability calculation proposed by Mair (1979) and Kimura & Mair (1981), the undrained shear strength of the clay model in this project was estimated using the relationship between undrained shear strength and *OCR* (**Equations 6.4** and **6.5**).

6.3.2 Determination of tunnel support pressure at collapse

Traditional method proposed by Mair (1979)

For a 3D tunnel heading, Mair (1979) defined the tunnel support pressure at collapse σ_{TC} as the pressure at which the displacements increased most rapidly. The estimation of σ_{TC} is achieved by examining the shape of the curves (u vs σ_T) and (w vs σ_T) to find the support pressure at which significant increase in soil displacements occurred (u and w are respectively horizontal displacement at the tunnel face and surface settlement above the tunnel face). Drawing tangents to these curves gives various possible choices of σ_{TC} .

Examples of using this method are given in **Figures 6.6** and **6.7** for the two tests 5BL and 12BL. Typical tangents (black lines) were drawn to the displacement curves in reference test 5BL and reinforced test 12BL (steel rods, long embedded length $EL/D=1$). The intersections of the tangents are the possible tunnel support pressure at which the collapse of the tunnel could be said to occur.

One difficulty in using the tangent method is in tests with small soil displacements, the tangents might not give clear indications at which the soil displacements rapidly increase. More importantly, determination of σ_{TC} needs to be reasonably consistent among the tests so that the effect of the FUS on tunnel stability can be studied objectively. That in turn requires a quantifiable method in estimating σ_{TC} . Thus, an approach has been developed to aid the determination of the tunnel support pressure at collapse. The detailed procedure is described in the following.

New method

First of all, the idea of using the tunnel support pressure at collapse σ_{TC} in assessing tunnel stability is that the magnitude of soil movement is not the only factor under consideration. Another important factor is the rate of soil movement with respect to the reduction of tunnel support pressure. For example, relatively large displacement for large reduction of tunnel support pressure is deemed more favourable (or stable) than the same amount of soil displacement occurring for a small reduction of tunnel support. Therefore, it is important to consider the gradient of the displacement vs. tunnel pressure curves in assessing the stability of the tunnel.

The gradient curves of the displacement development are presented in **Figures 6.8** and **6.9**. The gradient calculation was performed over a range of changes in tunnel support pressures of between 10 to 15kPa (illustrated in **Figure 6.6**) to avoid problem caused by noise in the measurement system. A larger gradient indicates a more significant increase in displacement for a given reduction in tunnel support pressure and is a valuable indicator to detect the tunnel support pressure at collapse. More importantly, gradients of the curves of $(\Delta u/\Delta\sigma_T$ vs σ_T) and $(\Delta w/\Delta\sigma_T$ vs σ_T) are quantifiable which allows consistent assessment of the tunnel stability between the tests to be undertaken.

Demonstration of using the new method

For test 5BL, the intersections of the tangents to the three displacement curves showed similar values of tunnel support pressures of approximately 126kPa and 109kPa (**Figure 6.6**) which are reflected in the considerable increases in the gradients depicted in **Figure 6.8**. That implies the tunnel collapse stage might have started from $\sigma_T=126$ kPa which can be checked by examining the corresponding shear strains developed in the soil mass at this σ_T .

According to Mair (1993) and Grant (1998), the range of shear strain at collapse in the tunnelling event typically varies from 2% to 20% (**Figure 3.16**). Therefore, if shear strains in the soil mass fell within this range then the tunnel was at collapse stage. **Figure 6.10** presents the engineering shear strains in the soil mass for test 5BL at the tunnel support pressure $\sigma_{TC}=126$ kPa (the engineering shear strain is twice the shear strain). Shear strains of 4% (or 8% engineering shear strains) which is in the typical strains range of tunnel collapse event, developed near the tunnel face and above the tunnel crown (**Figure 6.10**). Combining the indicators including the intersections of tangents, noticeable change in the gradients and the large shear strains developed in the soil mass, the tunnel support pressure at collapse in test 5BL was estimated as $\sigma_{TC}=126$ kPa.

For test 12BL, the significant increases in the gradient curves (**Figure 6.9**) corresponding to the intersections of the tangents (**Figure 6.7**) suggested that the collapse might have started at $\sigma_T=102$ kPa or $\sigma_T=88$ kPa. At $\sigma_T=102$ kPa, the magnitudes of the gradients of $\Delta u/\Delta\sigma_T$ vs σ_T and $\Delta w/\Delta\sigma_T$ vs σ_T are much smaller than those for test 5BL at $\sigma_{TC}=126$ kPa (**Figures 6.8** and **6.9**) and it can be argued that the tunnel for test 12BL did not collapse at $\sigma_T=102$ kPa. It is then necessary to examine the magnitudes of those gradients

for test 12BL at $\sigma_T = 88\text{kPa}$. It is evident that the magnitudes of the gradients at $\sigma_T = 88\text{kPa}$ are comparable to those for test 5BL at $\sigma_{TC} = 126\text{kPa}$ (**Figures 6.8** and **6.9**). Therefore, a consistent approach is to consider that the collapse of the tunnel for test 12BL occurred at $\sigma_{TC} = 88\text{kPa}$. This is confirmed by the fact that shear strains of 4% developed in front of the tunnel face in test 12BL at the tunnel support pressure $\sigma_{TC} = 88\text{kPa}$ (**Figure 6.11**). It is also noticed that, in the tunnel crown where the FUS were installed, the shear strains were small relative to those in front of the tunnel face.

The quantifiable gradients of $\Delta u/\Delta\sigma_T$ vs σ_T and $\Delta w/\Delta\sigma_T$ vs σ_T in the new method allows a consistent determination of the tunnel support pressure at collapse to be performed. This is beneficial to investigate the effect of the FUS to tunnel stability.

6.3.3 Effect of the FUS on tunnel stability

From **Figure 6.8**, it is evident that in test 5BL when the tunnel support pressure $\sigma_T=172\text{kPa}\div 165\text{kPa}$, the gradients of $(\Delta u/\Delta\sigma_T)$ and $(\Delta w/\Delta\sigma_T)$ were approximately constant indicating a linear relationship between displacement and tunnel support pressure reduction. That implies the soil response was essentially elastic. In test 12BL, the constant section of the gradient curve was observed for the range of tunnel support pressure $\sigma_T=172\text{kPa}\div 150\text{kPa}$ suggesting a greater range of elastic response (**Figure 6.9**). This increased range of elastic response reflects the stiffer structural support offered by the steel rods. This means that the presence of FUS delivered a more controlled soil displacement and improved stability compared with the reference test.

The procedure described in **Section 6.3.2** was used to determine the tunnel support pressure at collapse in the other tests. **Table 6.3** tabulates the tunnel stability ratio at collapse calculated using **Equation 6.2** and values of S_u determined by **Equations 6.4** and **6.5**. The estimated tunnel support pressure at collapses σ_{TC} for these tests are in line with the corresponding values determined from the chart in **Figure 2.6** proposed by Kimura & Mair (1981) which suggests $N\approx 5$ and $N\approx 8$ for $C/D=1$ and $C/D=3$ tests respectively (for $P/D=0.5$). The increase in the tunnel stability delivered by the FUS is calculated by **Equation 6.6** and the results are presented in **Table 6.3**;

$$SI = (N_{TCr} - N_{TC0})/N_{TC0} \times 100\% \quad (6.6)$$

where SI is the stability increase delivered by the FUS,

N_{TCr} is the tunnel stability ratio at collapse in reinforced test,

N_{TC0} is the tunnel stability ratio at collapse in unreinforced test.

Similar to the observations made for settlement reduction offered by the FUS, an increase in the stability ratio was observed for the stiffer forepoles and longer embedded length EL . Details on the significance of these parameters will be discussed in **Section 6.5**.

6.4 Soil stiffening effect offered by FUS

The purpose of using a FUS is to increase the stiffness of the soil in the areas that are subjected to change in effective stress as a result of stress relief due to tunnel excavation. It would be of interest to determine the effective soil stiffness and to quantify the increase in soil stiffness delivered by the FUS. One problem is that the determination of soil stiffness within the centrifuge model is not a straight-forward process due to various reasons including the variation of stress path of the model from consolidation stage to testing stage, different parts of the model being subjected to different stress paths and different changes in stress and the effect of friction between the clay and the Perspex window. Moreover, the introduction of the FUS installed in the soil further complicates this problem.

Nevertheless, the trend of the change in soil shearing stiffness can be obtained using the simple linear elastic-perfectly plastic model proposed by Mair & Taylor (1993) which was shown to provide reasonable estimation of soil stiffness (Mair & Taylor, 1993; Mair, 2008). As discussed in **Section 5.3.4**, the 3D tunnel heading in this research can be idealised as a spherical cavity contraction. Therefore, the gradient of the longitudinal horizontal soil displacement (plotted in the non-dimensional manner as in **Figures 2.26** and **6.12**) is proportional to the product of shear stiffness, undrained shear strength and the stability ratio N based on **Equation 2.24** (represented below);

$$\frac{u}{a} = \frac{S_u}{3G} \left(\frac{a}{r}\right)^2 \exp(0.75N - 1) \quad (2.24 \text{ bis}) (6.7)$$

Figure 6.12 compares the longitudinal soil horizontal displacements ahead of the tunnel face in three tests 18BL, 19BL and 20BL when the tunnel support pressure reduced to 90kPa. It can be seen that the gradient of the line for test 18BL was the largest among the three lines. That suggests the stiffness of soil in test 19BL and 20BL was higher than that for test 18BL for the same tunnel support pressure (stiffness G is inversely proportional to the gradient of the line, **Equation 6.7**). The gradient of the lines can be estimated using a best-fit method. Having the gradient of the line estimated, the stiffness G then can be determined using **Equation 6.8** (derived from **Equation 6.7**);

$$G = \frac{S_u}{3 \text{gradient}} \exp(0.75N - 1) \quad (6.8)$$

The values of S_u and N calculated in **Section 6.3** are used to calculate the corresponding stiffness in tests 18BL, 19BL and 20BL when the tunnel support pressure reduced. The results are illustrated in **Figure 6.13**. As would be expected, in the reference test 18BL where there was no FUS, the soil stiffness decreases as the tunnel support decreases (i.e. shear stress within the soil mass increases). However, the stiffness of soil model appears to increase in tests 19BL and 20BL in the early stages reflecting the reinforcement effect of the steel rods. This observation is consistent with the foundation effect to the steel rods when the tunnel lining stopped deflecting. In the later stages, the soil stiffness decreases implying the influence of the FUS gradually diminished. The observed change in soil stiffness when the tunnel support pressure reduced suggests that a nonlinear elastic perfectly plastic approach would improve the prediction of the soil displacement compared with that in linear elastic perfectly plastic.

6.5 Relative effects of the parameters of the FUS

It is worth noting that the same consolidation pressure was used for the clay model for all the tests hence all the models had similar strength and stiffness characteristics. Therefore, any significant differences in the reinforcement effectiveness of the FUS were the result of the variation of the arrangement and material of the forepoles and the ratio C/D . The

effects of these factors are studied by weighing the reduction of the soil settlement SR and increase in tunnel stability SI delivered by the FUS.

The values of SR and SI are derived from **Tables 6.1** and **6.3** respectively. It can be seen that the influences of the FUS parameters are reflected clearly via the considerable reductions in settlement ($SR=35\div75\%$) which is more evident than the modest increase in the tunnel stability ($SI=6\div20\%$). Therefore, in the following sections, the settlement reduction SR delivered by the FUS will be used as the main factor to assess the effectiveness of the FUS. This is considered reasonable because the maximum surface settlement is of great concern and the reduction in settlement is important when considering potential damage to nearby infrastructure. The increase in tunnel stability will be assessed to see if it is consistent with the trend observed in the settlement reduction.

6.5.1 The effect of tunnel depth

Table 6.4 compares the effectiveness of the FUS using the same arrangement and material of the forepoles at two different tunnel depths $C/D=1$ and $C/D=3$. The results show that the FUS offers greater benefit for the tunnel with $C/D=1$ reflected via the higher settlement reduction and increase in the tunnel stability. A possible explanation for this is that the overburden stress in $C/D=1$ test was relatively small and could be supported by the structural capacity of the FUS so that its effectiveness was considerable. For the deep tunnels, $C/D=3$, this overburden stress was $360/155 \approx 2$ times larger than that for the $C/D=1$ tunnels and exceeded the support capacity of the FUS. That probably led to the effect of the FUS for $C/D=3$ tunnels being less significant than that for $C/D=1$ tunnels.

6.5.2 The effect of the forepole stiffness

If the forepoles are considered as cantilever beams or beams supported at two ends then the deflection of the beam is inversely linear to the beam bending stiffness or Young's modulus E . The relationship between the deflections of brass and steel rods Δ_b and Δ_s that have identical geometry but different Young's moduli E_b and E_s is expressed as;

$$\frac{\Delta_b}{\Delta_s} = \frac{E_s}{E_b} \quad (6.9)$$

The Young's modulus of the brass rods and steel rods were $E_b=110\text{GPa}$ and $E_s=210\text{GPa}$ respectively. Using these Young's moduli in **Equation 6.9**, the relationship between the deflection of the brass rods and steel rods for the same loading condition can be derived as $\Delta_b/\Delta_s = 210/110 = 1.9$ or $\Delta_s=0.52\Delta_b$. That means the increase in bending stiffness of steel relative to brass forepoles leads to a reduction in their deflection as a beam of approximately 50%. It is reasonable to assume the FUS and the soil immediately above it settled together as a single unit since the gap between the rods was very small. Hence, the overall reduction in soil settlement might be expected to correspond to the beam deflection.

Table 6.5 tabulates the increase in the settlement reductions offered by using steel rods to replace brass rods for different filling angles and different EL/D . For $C/D=3$ tunnels, the results showed that using steel rods to replace brass rods, for the same arrangement of the forepoles, only yielded an increase in reduction of soil settlement of approximately 10% in tests with filling angle $\alpha=75^\circ$ (2BL vs 20BL) and approximately 20% in tests with filling angle $\alpha=90^\circ$ (3BL vs 12BL; 4BL vs 19BL). For $C/D=1$ tests, the increase was observed to be approximately 30% (10BL vs 13BL). These reductions are both lower than the corresponding reduction in deflection of the forepoles which was expected as 50%. A possible explanation for the difference with expectation is discussed below.

Soil deformations develop mainly as a result of ground movements towards the tunnel face and radial movement towards the tunnel centreline (components 1-a and 1-b depicted in **Figure 2.1**). **Section 5.5** showed that the area that benefited the most from having the FUS was near the installation area of the FUS which involved the radial soil displacement in the upper half of the tunnel. This is reflected in the marked reduction in the magnitude and extent of soil deformations. In contrast, the areas near the tunnel face and below the tunnel spring line have no forepoles and the effects that the FUS delivered were less significant. As a consequence, the overall reduction of the soil settlement is less than the reduction in the forepole deflection.

Interestingly, **Table 6.5** shows that replacing steel rods for brass rods in tests with forepoles arranged with the filling angle $\alpha=90^\circ$ for $C/D=3$ tunnels ([3BL vs 12BL]; [4BL

vs 19BL]) yielded an approximately 20% increase in settlement reduction which is about two times larger than the 10% increase observed in tests with $\alpha=75^\circ$ (2BL vs 20BL). This suggests the filling angle α also has influence on the relative effectiveness of the increase in the stiffness of the forepole. Therefore, it would be beneficial to find the appropriate filling angle in order to achieve the added effect of increasing the stiffness of the forepoles.

6.5.3 The effect of the filling angle in different tunnel depths

The effect of the filling angle has been shown to vary with the ratio C/D in **Section 5.5.2** and is emphasised in **Figures 6.1** and **6.2**. **Table 6.6** presents the different effectiveness of the FUS for the two filling angles $\alpha=75^\circ$ and $\alpha=90^\circ$ at two different tunnel depths $C/D=1$ and $C/D=3$. The results show that the filling angle $\alpha=75^\circ$ is better than $\alpha=90^\circ$ for tests with $C/D=1$ (8BL vs 10BL) but not for tests with $C/D=3$ (2BL vs 4BL; 20BL vs 19BL). The reason was explained in **Section 5.5.2**.

The implication from these observations is that for tunnels with small C/D ratio, the soil movements occur mainly near the tunnel crown hence having forepoles concentrated in that area proved to be better than spreading the forepoles evenly and extending to the tunnel spring line. For tunnels with large C/D ratio, the plastic collapse mechanism extends to the sides of the tunnel hence arranging forepoles near the tunnel spring line is important in making the FUS efficient in reducing the soil displacement. Therefore, the filling angle should extend to the areas most likely to have significant soil movement to improve the effectiveness of the FUS and maximise the added benefit offered by the increase in the stiffness of the forepole.

6.5.4 Effect of the embedded length with tunnel depth

Table 6.7 tabulates the effect of increasing the embedded length EL for different C/D ratios. It can be seen that increasing in the embedded length EL by 100% ($EL/D=0.5$ compared with $EL/D=1$) for the same positions of the forepoles ($\alpha=90^\circ$) delivered an increase in settlement reduction of an average of 10% for the $C/D=3$ tunnels (4BL vs 3BL – brass rods, 19BL vs 12BL – steel rods). It is noticed that the stiffness of the forepoles has little influence on the effectiveness of the increase in the embedded length.

Interestingly, for the $C/D=1$ tunnels the same amount of increase in EL/D yielded an additional 30% reduction in settlement which was three times larger than that for $C/D=3$ tunnels. This noticeable difference in the settlement reduction delivered by increasing EL/D for two different ratios $C/D=1$ and $C/D=3$ suggests that there were discrepancies in the quality of the foundation effect.

The concept of the foundation effect was introduced by Carrieri *et al.*, (2002) and Volkman & Schubert (2007) and refers to the tunnel lining and the soil beneath the FUS acting like foundations to support the forepoles (**Section 2.7.3**). Since the arrangements of the forepoles were the same (same α), the amount of the increase in the foundation length was identical to the increase in the embedded length EL . The tunnel lining was one of the two foundations for the forepoles and only provided the support when the lining deflection was small relative to the magnitude of the soil settlement.

Similarly, the “foundation effect” provided by the soil beneath the FUS only becomes efficient when the soil settlements in the foundation area was small relative to that above the tunnel crown and ideally, when the far end of the forepoles lies outside of the potential failure plane. **Figure 6.14** presents the shear planes in the soil mass post-test for the reference tests at both depths $C/D=1$ (test 9BL) and $C/D=3$ (test 5BL). The locations of the forepoles with $EL/D=1$ are also superimposed.

Generally, the extent of the shear plane for $C/D=3$ tunnel were larger than that for $C/D=1$ tunnel which both can be predicted by the upper bound failure mechanism proposed by Davis *et al.*, (1980) with a reasonable fit (**Section 5.5.1**). It is evident that for the same embedded length $EL/D=1$, the forepoles in $C/D=1$ tunnel extend beyond the shear plane which gained a better foundation effect compared with that for a $C/D=3$ tunnels where the forepoles would be inside the shear plane. This better foundation effect observed for $C/D=1$ tunnels resulted in the increase in settlement reduction of three times larger than that for $C/D=3$ tests when the embedded length was increased from $EL/D=0.5$ to $EL/D=1$.

Observations of the shear planes in the reinforced tunnel tests showed that using the FUS altered the shear plane in the soil mass compared with that for reference tests. **Figures 6.15-a, b** compare the shear planes in the reference and reinforced tests at both depths $C/D=1$ and $C/D=3$. For test 11BL, the forepoles extended beyond the potential shear

plane at the front of the tunnel, no failure plane was observed. In contrast, the extent of the shear plane in front of the tunnel face for the other reinforced tests were further from the tunnel face than for the reference tests for both depths. That implies, from an upper bound solution perspective, more external work (larger volume of the soil mass) was required to overcome the internal work and cause failure. That indicates that a stronger equivalent soil was achieved in the soil model reinforced by the FUS.

6.6 An assessment on the prediction of V_L using Load Factor approach

The available data from the centrifuge tests from this Chapter allows a Load Factor analysis to be carried out.

The load factor approach (Mair *et al.*, 1981; Macklin, 1999) has proved to be a useful method for predicting the volume loss due to tunnelling (Macklin, 1999; Dimmock, 2003; Divall, 2013). While other empirical methods require data from similar tunnelling projects to predict tunnelling-induced soil deformations, the Load Factor approach does not need the knowledge of a reference site. This makes the Load Factor method appear suitable at the preliminary design stage in tunnelling projects in areas that have not had a tunnel constructed before. An example is in Ho Chi Minh city, Vietnam where the first tunnel for an urban area metro transit system is about to be constructed.

The parameters needed for the prediction are the tunnel geometry including C/D , P/D , tunnel support pressure σ_T and the undrained shear strength S_u of the soil. From there, the Load Factor can be calculated and the corresponding volume loss can be estimated using the relationship proposed by Macklin (1999) which has been described in **Section 2.5.3**.

In **Section 2.5**, soil displacements induced by tunnelling were shown to be three-dimensional and accumulate with the advance of a tunnel which results in the symmetrical transverse soil settlement trough after the passage of the tunnel face. The volume of the transverse settlement trough (in 2D scenario, m^3/m) was shown to be related to the surface settlement profile or the load factor (Mair *et al.*, 1981; Macklin, 1999). On this basis, two-dimensional approaches have been established to predict the total soil settlement and

volume loss after the passage of the tunnel heading while disregarding the 3D nature of the tunnelling-induced soil movements in the vicinity of the tunnel heading.

It is of interest to check whether the Load Factor approach would apply to the 3D volume loss generated in this project. The newly developed 3DIS allows the volume of the whole surface settlement trough in 3D to be accurately measured in three tests: 18BL, 19BL and 20BL. The corresponding volume loss is calculated using the measured volume of the settlement trough relative to the volume of excavation of the unlined portion $P=25\text{mm}$;

$$V_L = \frac{V_S}{V_{ex}} (\%) \quad (6.10)$$

$$V_{ex} = \left(\frac{\pi D^2}{2 \times 4} \right) P \text{ (mm}^3\text{)} \quad (6.11)$$

Where V_S is the volume of the settlement trough in 3D measured by 3DIS (mm^3),

V_{ex} is the volume of the excavation in 3D (mm^3).

(Note: a half section is modelled, so V_S relates to surface settlement in the centrifuge model and V_{ex} relates to the structurally unlined tunnel heading, P , in the centrifuge model).

The calculated volume losses $V_L(\%)$ from these three tests are presented in **Figure 6.16**. There was no clear distinction in the magnitudes of the total volume loss between the three tests until the tunnel support pressure reduced to 140kPa. That supports the approach of assessing the soil deformation after the increase of the tunnel lining deflection became negligible to study the effect of FUS (**Section 5.4.2**).

The Load Factors in the three tests were calculated using **Equation 2.9** with the tunnel support pressure at collapse σ_{TC} determined from **Section 6.3** and tunnel stability using **Equation 2.1**.

$$LF = \frac{N}{N_{TC}} \quad (2.9 \text{ bis}) \quad (6.12)$$

$$N = \frac{\sigma_{ob} - \sigma_T}{S_u} \quad (2.1 \text{ bis}) \quad (6.13)$$

Figure 6.17 compares the profile of the calculated Load Factor and the corresponding measured volume loss with the relationship proposed by Macklin (1999) (For $LF \geq 0.2$). It is evident that most of the data points fit very well with the linear regression line (solid line) which lie within the upper and lower bounds suggested by Macklin (1999) and denoted by dashed lines. The data points also fit well for the value of $LF < 0.2$ which can be a useful addendum to Macklin (1999) that allows the volume loss V_L to be predicted at the early stage of tunnelling. The results are encouraging and add weight to the empirical approach to predicting ground response to tunnelling.

6.7 Summary

The key findings from the centrifuge test data have been correlated and discussed in this chapter. Having such highly accurate measurements of the soil deformations caused by the simulation of tunnel excavation offers an opportunity to review some aspects of the current frame-work in tunnelling. Most importantly, a clearer understanding into the relative effects of the parameters of the FUS have been gained. The following summarises the main findings.

6.7.1 The test results within the current frame work

The simplified ground deformation mechanisms due to tunnelling proposed by Davis *et al.*, (1980) were further ratified in the measured soil deformation magnitude and extent at different ratio C/D tunnels. This suggests that the Davis *et al.*, (1980) upper bound mechanisms can be useful to estimate the appropriate filling angle α and the embedded length EL depending on the tunnel geometry C/D ratio.

The Load Factor approach (Mair *et al.*, 1981; Macklin, 1999) provided predictions that closely agreed with the measured volume losses and the determined tunnel stability ratio in the centrifuge tests. This confirms the Load Factor approach is applicable to the 3D scenario though further data and analysis are needed to make use of this approach.

The analysis using the linear elastic-perfectly plastic model (Mair & Taylor, 1993) gave an indication of the soil stiffening effect delivered by the FUS. Although the determined soil stiffness was not verified by other sophisticated method, a trend of the change in soil stiffness was shown to be in line with the observed settlement reductions offered by the FUS.

6.7.2 The relative effects of the parameters of the FUS

The effectiveness of the FUS in various arrangements were analysed and the results showed that the maximum surface settlement was reduced by 35÷75% and tunnel stability was increased by 6÷21%. The influence of the parameters α , EL and the forepole stiffness to the FUS effectiveness were shown to relate to each other and to be dependent on the ratio C/D . The following summarises the main observations.

The effect of the filling angle α was shown to vary with the ratio C/D which dictates the appropriate soil mobilisation mechanism (Davis *et al.*, 1980). This implies that the tunnel depth is an important factor in choosing the filling angle α and the results show that the FUS coverage should extend to the plastic deformation area i.e. to tunnel centreline for large C/D tunnels or have more forepoles above the tunnel crown in small C/D tunnels to increase the reinforcement effect. For the same quantity and material of forepoles, positioning the forepoles in this optimal α yielded an additional increase in the settlement reduction of approximately 10% compared to non-optimal α (4BL vs 2BL; 8BL vs 10BL).

The benefit of using stiffer forepoles depends on the filling angle α . Observation on the increase in the settlement reduction benefited from the increase in the stiffness of the forepoles in an appropriate filling angle ($\alpha=90^\circ$ for $C/D=3$ tests) was two times larger than that for non-optimal filling angle ($\alpha=75^\circ$ for $C/D=3$ tests).

An increase in the embedded length EL of 100% yielded an improved settlement reduction of at least 10% depending on the tunnel depth. That suggests the foundation effect gained from the embedded length depends on the tunnel depth.

The foundation effects of the soil to the FUS depends on not only the embedded length EL but also on the extent and magnitude of the soil movements developed beneath the

FUS. A longer embedded length that extends into soil subjected to smaller soil displacements compared to those developments in the area above the tunnel are shown to deliver a better foundation effect. The extent of ground deformations in deep and shallow tunnels tests corroborate the upper bound mechanism proposed by Davis *et al.*, (1980).

In a shallow tunnel with $C/D=1$, the additional increase in settlement reduction offered by extending the embedded length (EL/D increased from 0.5 to 1) was three times greater than that for $C/D=3$ tests. The implication is that for a large C/D tunnel, a larger embedded length is required than for a small C/D tunnel to achieve an adequate foundation effect for the FUS that will lead to reduced soil settlement and increased tunnel stability.

CHAPTER 7 CONCLUSION

7.1 Introduction

The key findings of this research are presented along with concluding remarks on the influences of the parameters of the Forepoling Umbrella System (FUS) on its reinforcing effectiveness both in reducing soil deformations due to tunnelling and increasing tunnel stability. The conclusions are followed by some discussion on the limitations of the experimental apparatus and recommendations for future work. Finally, a digression on the implications of the research results is provided.

7.2 Development of the 3D measurement system

The ground response associated with a forepole supported tunnel heading cannot be simulated by a simple plane strain model. Instead, a 3D model is needed and that in turn requires a system capable of measuring surface deformations in 3D so that greater insights into the effects of the FUS can be obtained. In this research, a novel 3D Imaging System (3DIS) was developed to cope with this requirement. The system allowed soil deformations at the model surface to be measured to a precision of 50 μ m and 35 μ m over a region of interest of 200x400mm of the model surface in vertical and horizontal directions respectively. This enabled more detailed analysis of horizontal surface displacements and 3D volume loss than has previously been possible.

7.3 The centrifuge tests

The centrifuge modelling technique was chosen as the research methodology due to its advantageous capability in replicating soil-structure interaction in a model featuring a non-axisymmetric forepole supported tunnel heading.

A total of twenty centrifuge tests were carried out covering a wide range of the variables including the tunnel depth C/D , the filling angle α , the embedded length EL/D and the stiffness of the forepole which allowed their relative influence to be investigated. All the tests were conducted at $125g$. At this acceleration, the model tunnel represented a corresponding tunnel at equivalent prototype scale with diameter of 6.25m located at depths of approximately $z_0=9.5\text{m}$ ($C/D =1$) and $z_0=22\text{m}$ ($C/D =3$). At these two depths, different soil movement mechanisms developed which influenced the effectiveness of the parameters of the FUS. The dimensions of the corresponding prototype scale tunnel and the FUS are appropriate for tunnel situations encountered in practice.

7.4 The merit of appropriate simplification approaches in this research

Despite the simplifications adopted in the centrifuge model, the soil deformations due to the simulated tunnelling in the centrifuge tests showed similar responses to tunnelling-induced soil displacements observed in practice. These included vertical and horizontal soil displacements in transverse and longitudinal planes and settlements with depth. This gave confidence in the findings of the effects of the FUS that should be applicable in tunnelling practice.

The Load Factor analysis (Mair *et al.*, 1981; Macklin, 1999) revealed good agreement between the experimental and empirical relationship of the measured volume losses and Load Factor implying that the developing 3D volume loss can be predicted. The simple linear elastic-perfectly plastic model (Mair & Taylor, 1993) allowed the change of the soil stiffness in the centrifuge model to be determined which brought to light the soil stiffening effect offered by the FUS.

7.5 The reinforcing effectiveness of the FUS

The results showed that using the FUS offers significant benefits in controlling ground movements due to tunnelling which was reflected in the reduction of the extent and magnitude of surface and subsurface soil deformations. Displacements of the ground

surface measured by the 3DIS showed marked effects of the FUS in the area above the forepoles and in front of the tunnel face and negligible effects in the area behind the tunnel face.

A rather wide variation in the effectiveness of the FUS placed in different arrangements was reflected in reductions of maximum soil settlement $SR=35\div75\%$ and increases in tunnel stability $SI=6\div21\%$. This highlights the importance of selecting appropriate parameters of the FUS to achieve an optimal design.

The tunnel depth C/D is an influential parameter that governs the soil movement mechanisms. Consequently, the relative influence of the parameters of the FUS varied with the tunnel depth C/D . The forepoles were found to be more effective when they extend around the tunnel periphery into the areas of potential plastic deformation. In the centrifuge model, the information on patterns of zones of movements were revealed by the deformed forepoles recovered post-test which further supported the collapse mechanisms proposed by Davis *et al.*, (1980). For a shallow tunnel, extending the forepoles into the region around the tunnel spring line was found unnecessary and less effective than concentrating the forepoles near the tunnel crown where the major soil movements occurred. However, for a deeper tunnel, arranging forepoles near the tunnel spring line was shown to be beneficial in reducing soil displacements in that area. The test results showed that positioning the forepoles in an appropriate filling angle yielded an increase of approximately 10% in settlement reduction compared with a non-optimal filling angle.

The reinforcing effectiveness of the FUS was shown to rely significantly on the foundation effects provided by the tunnel lining and the soil beneath the forepoles. Assuming the foundation effect provided by the tunnel lining is constant, the FUS was found to be most effective when able to mobilise a foundation effect at the ends of the forepoles furthest from the tunnel face. This is demonstrated by a considerable increase in settlement reduction of up to 30% when the embedded length was increased from $EL/D=0.5$ to $EL/D=1$.

An important finding regarding the embedded length was that EL/D is not the only factor that dictates the foundation effect. The FUS gains better foundation effect if the soil settlements in this area are small compared with those above the tunnel crown. Ideally,

the embedded length should lie beyond the potential shear plane that might develop in front of the tunnel face. The extent of the potential shear plane for a shallow tunnel was shown to be less than that for a deeper tunnel and both can be reasonably predicted by the upper bound collapse mechanism proposed by Davis *et al.*, (1980). This means that for a deeper tunnel, in order to achieve a better foundation effect a larger EL/D is required to ensure the embedded length extends outside of the potential failure zone.

Based on the upper bound collapse mechanisms (Davis *et al.*, 1980) and the actual shear planes observed in the centrifuge tests, a chart (**Figure 7.1**) has been produced to aid selection of the embedded length such that it extends beyond the potential failure plane. The application of this chart can be checked against the actual shear planes observed in the clay model in **Section 6.5.4**. The key findings of the settlement reduction offered by the FUS with different settings of EL/D , C/D and bending stiffness of the forepoles are presented in **Figure 7.2**. The chart in **Figure 7.2** only covered two different tunnel depths $C/D=1$ and $C/D=3$; for tunnels at other depths interpolation/extrapolation may need to be carried out to estimate the corresponding SR with caution. Application of these charts are discussed along with the implications of the tests results in practice in **Section 7.7**.

7.6 Limitations of the result and recommendation for further work

7.6.1 Coverage of filling angle and number of forepoles

Only two filling angles α were used as test variables and the difference between the two were relatively small ($\alpha=90^\circ-75^\circ=15^\circ$). This small variation caused a difference of approximately 10% in settlement reduction. Having a wider range of the filling angle will be beneficial to give more detail on the influence of this variable to the effectiveness of the FUS.

7.6.2 Friction between clay model and Perspex windows

The inherent friction at the interface of the clay model and the Perspex windows was apparent in the centrifuge test and was confirmed in a simple series of shear box tests. The different friction induced by the choice of texture material/target associated with the

PIV and Visimet methods resulted in discrepancies in the magnitude of the measured soil displacements even though the mechanisms of soil displacement were found to be comparable. Nevertheless, acknowledging the significance of the friction is necessary in making an appropriate interpretation of the obtained soil deformations. More extensive shear box experiments are presently being conducted to find the appropriate texture material with low friction that can then be used when adopting the PIV measurement system.

7.6.3 Use of finite element analysis

With recent development in constitutive soil models and numerical software, behaviour of soil and its interaction with a FUS can be modelled. With the centrifuge test data as a benchmark, finite element analysis using a sophisticated soil model might reveal subsurface soil displacements in the transverse direction which would be useful in gaining a clearer insight into the effectiveness of the FUS.

7.6.4 Improvement in 3D Imaging System

The 3DIS has demonstrated its capability in measuring soil surface displacements to high precision. The performance of 3DIS is limited by the SfM-MVS algorithm and the resolution of the cameras (resolution of the current cameras are 2MP which can be considered relatively modest). Nowadays, higher resolution cameras are available but tend to be large in size and hence not suitable for the constrained environment of the centrifuge. In the future, with the availability of small size and high resolution cameras, an increase in the performance of the technique can be expected. The 3DIS was developed not only for this project but also with the applicability for other physical models where 3D soil displacements might be important.

7.7 Implications of results

The research was carried out to improve the understanding of the influence of the parameters of a FUS on its effectiveness in reducing tunnelling-induced soil deformations

and increasing tunnel stability. From this, a clearer insight into achieving an optimal design of a FUS has been gained.

In the centrifuge tests, the deformation of the model tunnel lining was observed when the tunnel support pressure reduced. That caused a delay in the effect of the FUS in reducing soil settlements as the FUS reinforcing capability relies on the foundation effect provided by the tunnel lining. Tunnel lining deformation in practice might not be similar to that in a centrifuge test. However, the main principle is to ensure that the “tunnel end” of the forepoles are in contact with the constructed lining and minimise any deformation in this area to maximise the potential foundation effect.

If the tunnel depth C/D is known, the required EL/D to ensure the forepoles extend outside of the potential shear plane can be determined by using the chart in **Figure 7.1**. An alternative to extending the embedded length to increase the reinforcing effectiveness of the FUS is to increase the bending stiffness of the forepoles. From **Figure 7.2**, it can be seen that the increase in the bending stiffness of the forepoles can deliver a reinforcing effectiveness equivalent to that offered by using a longer embedded length. An example is the tunnel in test 13BL which was reinforced by steel rods with $EL/D=0.5$ and the achieved SR was comparable with that for the tunnel reinforced by brass rods with $EL/D=1$ (test 11BL). This means that using stiffer forepoles can reduce the required embedded length EL/D and offer a saving in terms of time for FUS installation.

An extensive literature review has been provided in this research which presented several methods that can be used to predict maximum soil settlement due to tunnelling w_{max} . Analysis of the potential damage to surrounding structures can be carried out to determine an acceptable level of soil settlement due to tunnelling, $w_{threshold}$. From there, the required settlement reduction $SR = (w_{max} - w_{threshold})/w_{max}$ can be determined. Based on the tunnel geometry, the chart in **Figure 7.2** and key findings given in this thesis can be used at least as the first step in selecting the FUS parameters to achieve the desired settlement reduction.

REFERENCES

- Aksoy, C.O. and Onargan, T., 2010. The role of umbrella arch and face bolt as deformation preventing support system in preventing building damages. *Tunnelling and underground space technology*, 25(5), pp.553-559.
- Atkinson, J.H. (1981). *Foundation and Slopes - An introduction to applications of critical state soil mechanics*. McGraw-Hill, UK.
- Attewell, P.B. and Woodman, J.P. (1982). Predicting the dynamics of ground settlement and its derivatives caused by tunnelling in soil. *Ground Engineering*, Vol.15. No.8, 13-22 and 36.
- Attewell, P. B. and Yeates, J. (1984). *Ground movements and their effects on structures*. Blackie and Son Ltd, Attewell, P.B. and Taylor, R.K.
- Boonyarak, T. and Ng, C.W., 2014. Effects of construction sequence and cover depth on crossing-tunnel interaction. *Canadian Geotechnical Journal*, 52(7), pp.851-867.
- Broms, B.B. & Bennermark, H. (1967). Stability of clay in vertical openings. *J. Soil Mechanics and Foundation Division*. American Society of Civil Engineers, SM1, 71-94.
- Calvello, M. & Taylor, R.N. (1999). Centrifuge modelling of a spile-reinforced tunnel heading. Proc. 2nd Int. Symp. *Geotechnical Aspects of Underground Construction in Soft Ground*. Tokyo.
- Carrieri, G., Fiorotto, R., Grasso, P. & Pelizza, S. (2002) Twenty years of experience in the use of the umbrella-arch method of support for tunnelling. *Proc. 4th Int. Workshop on Micropiles*, Venice.
- Clough, G.W. and Schmidt, B. (1981). Design and performance of excavations and tunnels in soft clay. *Soft Clay Engineering*, 569-634. Elsevier.
- Craig, W.H. (1995). Chapter 1: Geotechnical centrifuges: past, present and future. In: Taylor, R.N., (Ed.), *Geotechnical centrifuge technology*. Blackie Academic and Professional, Glasgow.

- da Silva, T.S., Elshafie, M.Z.E. and Sun, T., 2016. Fibre optic instrumentation and calibration in the geotechnical centrifuge. *Proceeding of the 3rd European Conference on Physical Modelling in Geotechnics, Eurofuge2016*. Nantes, France.
- Date, K., Mair, R.J. & Soga, K. (2008). Reinforcing effects of forepoling and facebolts in tunnelling. *Geotechnical Aspects of Underground Construction in Soft Ground – Ng, Huang & Liu (eds)*. Taylor & Francis Group, London
- Davis, E.H., Gunn, M.J., Mair, R.J. and Seneviratne, H.N., 1980. The stability of shallow tunnels and underground openings in cohesive material. *Geotechnique*, 30(4), pp.397-416.
- Dimmock, P.S., 2003. *Tunnelling-induced ground and building movement on the Jubilee Line Extension*. PhD thesis, University of Cambridge.
- Divall, S., 2013. *Ground movements associated with twin-tunnel construction in clay*. PhD Thesis, City University London.
- Divall, S., Taylor, R. N. & Xu, M. Centrifuge modelling of tunnelling with forepoling. *International Journal of Physical Modelling in Geotechnics*, doi: 10.1680/jphmg.15.00019
- Gall Zeidler Consultants, L.L.C. and Ashburn, V., 2008. Pre-Support Measures for Shallow NATM Tunneling in Urban Settings. *North American Tunneling 2008 Proceedings*, p.152.
- Gorasia, R.J., 2013. *Behaviour of ribbed piles in clay*. PhD thesis, City University London.
- Grant, R.J., (1998). *Movements around tunnel in two-layer ground*. PhD Thesis, City University London.
- Garnier, J. (2002). Properties of soil samples used in centrifuge models. *Physical Modelling in Geotechnics: ICPMG '02*, Phillips, Guo & Popescu (eds.).
- Gunn, M.J. (1993). The prediction of surface settlement profiles due to tunnelling. Predictive Soil Mechanics. *Proc. Wroth Memorial Symp.*, Oxford, July 1992 (ed. G.T. Houlsby and A.N. Schofield), 304-316. Thomas Telford, London.
- Harris, D.I., 2001. 11 Protective measures. *Building response to tunnelling: Case studies from construction of the Jubilee Line Extension, London, 200 (2001)*, p.135.

- Hisatake, M. and Ohno, S., 2008. Effects of pipe roof supports and the excavation method on the displacements above a tunnel face. *Tunnelling and Underground Space Technology*, 23(2), pp.120-127.
- Hong, S.W. and Bae, G.J., 1995. Ground movements associated with subway tunnelling in Korea. *Proceedings of Underground Construction in Soft Ground*. Rotterdam: AA Balkema, pp.229-232.
- James, M.R. and Robson, S., 2012. Straightforward reconstruction of 3D surfaces and topography with a camera: Accuracy and geoscience application. *Journal of Geophysical Research: Earth Surface*, 117(F3).
- James, M.R. and Robson, S., 2014. Sequential digital elevation models of active lava flows from ground-based stereo time-lapse imagery. *ISPRS Journal of Photogrammetry and Remote Sensing*, 97, pp.160-170.
- Jones, B. and Clayton, C., 2013. Guidelines for Gaussian curve-fitting to settlement data. In *Underground-The Way to the Future: Proceedings of the World Tunnel Congress, WTC 2013* (pp. 645-652). CRC Press.
- Juneja, A., Hedge, A., Lee, F.H. & Yeo, C.H. (2010). Centrifuge modelling of tunnel face reinforcement using forepoling. *Tunnelling and Underground Space Technology* 25, 377-381.
- Kimura, T. and Mair, R.J., 1981, June. Centrifugal testing of model tunnels in soft clay. In *Proceedings of the 10th international conference on soil mechanics and foundation engineering* (pp. 319-322). ISSMFE: International Society for Soil Mechanics and Foundation Engineering.
- Le, B.T., Nadimi, S., Goodey, R.J. and Taylor, R.N., 2016. System to measure three-dimensional movements in physical models. *Géotechnique Letters*, 6(4), pp.1-7.
- Leca, E. and New, B. (2007). Settlements induced by tunnelling in Soft Ground. *Tunnelling and Underground Space Technology* 22, 119-149.
- Lunardi, P., 2008. *Design and construction of tunnels: Analysis of Controlled Deformations in Rock and Soils (ADECO-RS)*. Springer Science & Business Media.
- Macklin, S.R., 1999. The prediction of volume loss due to tunnelling in overconsolidated clay based on heading geometry and stability number. *Ground engineering*, 32(4), pp.30-33.

- Maidl, B., Thewes, M., Maidl, U. (2013). *Handbook of Tunnel Engineering* (Two volumes). Wiley Ernst & Sohn, Germany.
- Mair, R.J. (1979). *Centrifugal modelling of tunnelling construction in soft clay*. PhD Thesis, University of Cambridge.
- Mair, R.J., 2008. Tunnelling and geotechnics: new horizons. *Géotechnique*, 58(9), pp.695-736.
- Mair, R.J., Gunn, M.J. and O'Reilly, M.P., 1982. Ground movement around shallow tunnels in soft clay. *Tunnels & Tunnelling International*, 14(5).
- Mair, R. J., Taylor, R. N. & Bracegirdle, A. (1993). Subsurface settlement profiles above tunnels in clays. *Geotechnique* 43, No. 2, 315-320.
- Mair, R.J. & Taylor, R.N., 1993. Prediction of clay behaviour around tunnels using plasticity solutions. In *Predictive Soil Mechanics: Proceedings of the Wroth Memorial Symposium* Held at St. Catherine's College, Oxford, 27–29 July 1992 (p. 449). Thomas Telford.
- Mair, R.J. & Taylor, R.N. (1997). Theme lecture: Bored tunnelling in the urban environment. *Proc. 14th Int. Conf. Soil Mechanics and Foundation Engineering*, Hamburg. Balkema, Rotterdam.
- McNamara, A.M. (2001). *Influence of heave reducing piles on ground movements around excavations*. PhD thesis, City, University of London.
- Martos, F. (1958). Concerning an approximate equation of subsidence trough and its time factors. *Int. strata control congress*, Leipzig (Berlin: Deutsche Akademie der Wissenschaften zu Berlin, Sektion für Bergbau, 1958), 191-205.
- Nadimi, S., Divall, S., Fonseca, J., Goodey, R. & Taylor, R.N. (2016). An addendum for particle image velocimetry in centrifuge modelling. *Proceeding of the 3rd European Conference on Physical Modelling in Geotechnics, Eurofuge2016*. Nantes, France.
- Nyren, R. (1998). *Field measurements above twin tunnels in London Clay*. Ph.D. Thesis, Imperial College.
- Ocak, I., 2008. Control of surface settlements with umbrella arch method in second stage excavations of Istanbul Metro. *Tunnelling and Underground Space Technology*, 23(6), pp.674-681.

- Oke, J.D.S.H., 2016. *Determination of nomenclature, mechanistic behaviour, and numerical modelling optimization of umbrella arch systems*. PhD Thesis, Queen's University, Canada.
- O'Reilly, M.P. & New, B.M. (1982). Settlements above tunnels in the United Kingdom - their magnitude and prediction. *Proc. Tunnelling '82 Symp., Institution of Mining and Metallurgy*, London (ed. MJ. Jones), 173-181.
- Peck, R.B. (1969). Deep excavations and tunnelling in soft ground. *Proc. 7th Int. Conf. Soil Mechanics and Foundation Engineering*, Mexico, State of the Art Volume, 225-290.
- Pokrovsky, G.I. & Fyodorov, I.S. (1968). Centrifugal modelling in the construction industry. Moscow: Stroiiedat. In draft translation, *Building Research Establishment Library*, Vol. 1.
- Pokrovsky, G.I. & Fyodorov, I.S. (1968). Centrifugal modelling in the construction industry. Moscow: Niedra. In draft translation, *Building Research Establishment Library*, Vol. 2.
- Robertson, D.P., Cipolla, R. (2009). Structure from motion. In: Varga, M., (Ed.), *Practical Image Processing and Computer Vision*. John Wiley and Sons Ltd., New York.
- Schmidt, B. (1969). *Settlements and ground movements associated with tunnelling in soil*. Ph.D. thesis, University of Illinois.
- Schofield, A.N. and Wroth, C.P. (1968). *Critical State Soil Mechanics*. McGraw-Hill, London.
- Shirlaw, J.N., Ong, J.C.W., Rosser, H.B., Tan, C.G., Osborne, N.H. and Heslop, P.E., 2003. Local settlements and sinkholes due to EPB tunnelling. *Proceedings of the Institution of Civil Engineers-Geotechnical Engineering*, 156(4), pp.193-211.
- Smith, MW, Carrivick, J and Quincey, D (2015) Structure from Motion Photogrammetry in Physical Geography. *Progress in Physical Geography*. ISSN 0309-1333 (In Press).
- Specification for tunnelling Third edition (2012). British Tunnelling Society (BTS) & Institution of Civil Engineers (ICE).

- Stanier, S.A. Blaber, J., Take, W.A. & White, D.J. 2015. Improved image based deformation measurement for geotechnical applications. *Canadian Geotechnical Journal*.
- Stanier, S., Dijkstra, J., Leśniewska, D., Hambleton, J., White, D. and Wood, D.M., 2016. Vermiculate artefacts in image analysis of granular materials. *Computers and Geotechnics*, 72, pp.100-113.
- Sugiyama, T., Hagiwara, T., Nomoto, T., Nomoto, M., Ano, Y., Mair, R.J., Bolton, M.D. and Soga, K., 1999. Observations of ground movements during tunnel construction by slurry shield method at the Docklands Light Railway Lewisham extension-East London. *Soils and Foundations*, 39(3), pp.99-112.
- Taylor, R.N. (1984). *Ground movements associated with tunnels and trenches*. Ph.D. thesis, University of Cambridge.
- Taylor, R.N. (ed.) (1995a). *Geotechnical Centrifuge Technology*. Blackie Academic and Professional, Glasgow.
- Taylor, R.N., Robson, S., Grant, R.J. and Kuwano, J. (1998). An image analysis system for determining plane and 3-D displacements in centrifuge models. *Proc. Int.Conf. Centrifuge 98*, Tokyo. Balkema, Rotterdam.
- Triggs, B., McLauchlan, P.F., Hartley, R.I. and Fitzgibbon, A.W., 1999, September. Bundle adjustment - a modern synthesis. In *International workshop on vision algorithms* (pp. 298-372). Springer Berlin Heidelberg.
- Volkman G.M., Button E.A. & Schubert W. 2006. A Contribution to the Design of Tunnels Supported by a Pipe Roof. *Proc. 41st U.S. Rock Mechanics Symp.*, American Rock Mech. Assoc., June 17-21, Golden, CO.
- Volkman, G.M. and Schubert, W., 2007, May. Geotechnical model for pipe roof supports in tunneling. In *Proceeding of the 33rd ITA-AITES World tunneling congress, underground spaced the 4th dimension of metropolises*. London: Taylor & Francis Group (pp. 755-760).
- Vrba, V. & J. Barták (2007). Model analysis of pre-lining methods used in tunnel construction. In *Proceedings of the World Tunnel Congress 2007 and 33rd ITA/AITES Annual General Assembly*, Prague, May 2007.

- White, D.J., 2002. *Investigation into the behaviour of pressed-in piles*. PhD thesis, University of Cambridge.
- White, D. J., Take, W. A. & Bolton, M. D. (2003). Soil deformation measurement using particle image velocimetry (PIV) and photogrammetry. *Geotechnique* 53, No. 7, 619–631.
- Yeo, C.H. (2011). *Stability and collapse mechanisms of unreinforced and forepole-reinforced tunnel headings*. PhD Thesis, National University of Singapore.
- Zeidler, K. and Yeo, C.H. 2007. FE modelling for the shallow Fort Canning Tunnel. In *Proceedings of EURO TUN 2007*. Vienna, Austria. Aug 27-29, 2007.

TABLES

Parameter	Unit	Value
Steel pipe diameter and wall thickness	mm mm	70-200 4-8
Steel pipe length, L	m	12-18
Embedded length, EL	m	3-6
Insertion angle, β	°	5-7
Filling angle, α	°	60-75

Table 1.1: Typical parameters of a FUS (Volkman & Schubert, 2007).

C/D	1	2	3	4	5
$\tan(\theta_1) = \tan(\theta_2)$	2.2	3.0	3.6	4.1	4.6
$\theta_1 = \theta_2$ (°)	65.6	71.6	74.5	76.3	77.7

Table 2.1: θ_1 and θ_2 calculated by **Equation 2.2** proposed by Davis *et al.*, (1980).

Reference	Range of Values for V_L (%)	Type of Tunnelling
O'Reilly & New (1982)	1.0 - 1.4	Open Face
New & Bowers (1994)	1.0 - 1.3	Heathrow Trial Tunnels
Barakat (1996)	0.7 - 1.6	Open Face
Broms & Shirlaw (1989)	< 1.0	Closed Face (EPBM)
Mair & Taylor (1997)	1.0 - 2.0	Open Face
Mair & Taylor (1997)	0.5 - 1.5	NATM
Mair & Taylor (1997)	1.0 - 2.0	EPBM or slurry shields
Shirlaw <i>et al.</i> , (2003)	0 - 6	EPBM
Hover <i>et al.</i> , (2015)	1-1.3	Open Face

Table 2.2: Typical values of volume loss, V_L .

Parameter	Metric unit	Scaling law (model/prototype)
Gravity	m/s^2	n
Length	m	$1/n$
Area	m^2	$1/n^2$
Volume	m^3	$1/n^3$
Weight, force	$kg\ m/s^2$	$1/n^2$
Density	kg/m^3	1
Unit weight	kN/m^3	n
Stress and pressure	kPa (kN/m^2)	1
Strain	-	1
Bending stiffness, EI	Nm^2	$1/n^4$
Axial stiffness, EA	N	$1/n^2$

Table 3.1: Centrifuge scaling laws (Marshall, 2009).

Series	Date	No	C/D	EL/D	$\alpha(^{\circ})$	FUS	σ'_{v0} (kPa)	Comment
CD3B	17/06/2014	1BL	3	0.5	90	Brass	175	Preliminary test to check the functionalities of the apparatus.
	20/08/2014	2BL	3	0.5	75	Brass	175	Model was spun down to replace the burst bag. Useable results.
	27/08/2014	3BL	3	1	90	Brass	175	Useable results.
	02/09/2014	4BL	3	1	90	Brass	175	LVDTs extensions bent, surface settlement from Visimet. Useable results.
	09/09/2014	5BL	3	-	-	-		Reference test. Useable results.
T-CD2	04/11/2014	6BL	2				175	PXI computer crashed in flight. No useable results.
	22/01/2015	7BL	2				175	Model clay was visibly softer. Unreliable results.
CD1B	05/02/2015	8BL	1	0.5	75	Brass	175	Model rods were concentrated more at the crown. Useable results.
	19/02/2015	9BL	1	-	-	-	175	Reference test. Useable results.
	19/03/2015	10BL	1	0.5	90	Brass	175	Useable results.
	30/03/2015	11BL	1	1	90	Brass	175	Useable results.
S	16/06/2015	12BL	3	1	90	Steel	175	Useable results.
	07/07/2015	13BL	1	0.5	90	Steel	175	Useable results.
T-CD3	10/02/2016	14BL	3	-	-	-	350	Test 3D imaging system (3DIS) in flight. Bad lighting.
	14/03/2016	15BL	3	-	-	-	250	Test 3DIS in flight. Good lighting. Completed
	21/03/2016	16BL	3	-	-	-	175	Test 3DIS in flight. Front face was not fully greased. Unreliable results.
	07/04/2016	17BL	3	1	90	Steel	175	Test 3DIS in flight. Model clay was visibly softer. Unreliable results.
CD3S	14/04/2016	18BL	3	-	-	-	175	Reference test - PIV & 3D system. Useable results.
	26/04/2016	19BL	3	0.5	90	Steel	175	Useable results.
	06/05/2016	20BL	3	0.5	75	Steel	175	Useable results.

Table 4.1: Undertaken centrifuge tests.

Symbol	Parameter	Value
κ	average gradient of swelling line in $v: \ln p'$ space	0.05
λ	gradient of compression line in $v: \ln p'$ space	0.19
M	stress ratio at critical state ($q': p'$)	0.89
Γ	specific volume at critical state when $p'=1\text{kPa}$	3.23
N	specific volume on INCL when $p'=1\text{kPa}$	3.29
φ'_c	critical state angle of shearing resistance	23°
γ	unit weight of soil (saturated for clay)	16.5 (kN/m ³)
γ_w	unit weight of water	9.81 (kN/m ³)

Table 4.2: Speswhite kaolin clay properties.

Test	C/D	EL/D	α ($^{\circ}$)	Material of model forepole	Young's moduli (GPa)	SR (%)
2BL	3	0.5	75	Brass	110	35
3BL	3	1	90	Brass	110	50
4BL	3	0.5	90	Brass	110	42
12BL	3	1	90	Steel	210	73
19BL	3	0.5	90	Steel	210	62
20BL	3	0.5	75	Steel	210	47
8BL	1	0.5	75	Brass	110	53
10BL	1	0.5	90	Brass	110	44
11BL	1	1	90	Brass	110	75
13BL	1	0.5	90	Steel	210	72

Table 6.1: Average of reduction of maximum surface settlement SR offered by FUS.

Series	Test	Average S_u from surface to tunnel CL			S_u at Tunnel CL		
		Shear vane reading	S_u (kPa)	Difference to mean (kPa)	Shear vane reading	S_u (kPa)	Difference to mean (kPa)
<i>C/D=3</i>	2BL	14.0	18.8	0.0	17.0	22.9	0.2
	3BL	14.8	19.9	1.0	18.0	24.2	1.5
	4BL	14.7	19.8	0.9	16.5	22.2	-0.5
	5BL	13.5	18.2	-0.7	17.0	22.9	0.2
	12BL	13.7	18.4	-0.4	15.9	21.4	-1.3
	18BL	14.0	18.8	0.0	17.5	23.6	0.9
	19BL	13.2	17.7	-1.1	16.0	21.5	-1.2
	20BL	14.2	19.1	0.2	17.0	22.9	0.2
	Mean		18.8			22.7	
<i>C/D=1</i>	8BL				11.3	15.2	-0.9
	9BL				11.7	15.7	-0.3
	10BL				12.7	17.1	1.0
	11BL				12.7	17.1	1.0
	13BL				11.3	15.2	-0.9
	Mean					16.1	

(*) Shear strength = Shear vane reading \times calibration factor (kPa).
Calibration factor = 1.346.

Table 6.2: Undrained shear strength of model clay post-test.

Test	C/D	S_u (kPa)	EL/D	α ($^\circ$)	Material of model forepole	σ_{TC} (kPa)	N_{TC}	SI (%)
2BL	3	31.5	0.5	75	Brass	112	7.9	6.0
3BL	3	31.5	1	90	Brass	98	8.3	12.0
4BL	3	31.5	0.5	90	Brass	107	8.0	8.1
5BL	3	31.5	-	-	-	126	7.4	-
12BL	3	31.5	1	90	Steel	88	8.6	16.2
18BL	3	31.5	-	-	-	108	8.0	-
19BL	3	31.5	0.5	90	Steel	74	9.1	13.5
20BL	3	31.5	0.5	75	Steel	87	8.7	8.3
8BL	1	28	0.5	75	Brass	15	5.0	13.8
9BL	1	28	-	-	-	32	4.4	-
10BL	1	28	0.5	90	Brass	22	4.8	8.1
11BL	1	28	1	90	Brass	6	5.3	21.1
13BL	1	28	0.5	90	Steel	10	5.2	17.9

Table 6.3: Tunnel stability ratio at collapse N_{TC} and stability increase SI .

Tests	α (°)	EL/D	Model rod	SR (%)		SI (%)		$SR_{C/D=1} - SR_{C/D=3}$ (%)	$SI_{C/D=1} - SI_{C/D=3}$ (%)
				$C/D=3$	$C/D=1$	$C/D=3$	$C/D=1$		
2BL vs 8BL	75	0.5	Brass	35	53	6	13.5	18	7.5
4BL vs 10BL	90	0.5	Brass	42	44	8.1	8.1	2	0
3BL vs 11BL	90	1	Brass	50	75	12	21.1	25	9.1
19BL vs 13BL	90	0.5	Steel	62	72	13.5	17.9	10	4.4

Table 6.4: Effectiveness of the FUS for different ratios C/D .

Tests	C/D	α (°)	EL/D	SR (%)		SI (%)		$SR_{steel} - SR_{brass}$ (%)	$SI_{steel} - SI_{brass}$ (%)
				Brass	Steel	Brass	Steel		
2BL vs 20BL	3	75	0.5	35	47	6	8.3	12	2.3
3BL vs 12BL	3	90	1	50	73	12	16.2	23	4.2
4BL vs 19BL	3	90	0.5	42	62	8.1	13.5	20	5.4
10BL vs 13BL	1	90	0.5	44	72	8.1	17.9	28	9.8

Table 6.5: Relative effect of filling angle to increase in stiffness of the forepole.

Tests	C/D	EL/D	Model rod	SR (%)		SI (%)		$SR_{\alpha=90^\circ} - SR_{\alpha=75^\circ}$ (%)	$SI_{\alpha=90^\circ} - SI_{\alpha=75^\circ}$ (%)
				$\alpha=75^\circ$	$\alpha=90^\circ$	$\alpha=75^\circ$	$\alpha=90^\circ$		
2BL vs 4BL	3	0.5	Brass	35	42	6	8.1	7	2.1
20BL vs 19BL		0.5	Steel	47	62	8.3	13.5	15	5.2
8BL vs 10BL	1	0.5	Brass	53	44	13.8	8.1	-9	-5.7

Table 6.6: Relative effect of filling angle in different ratios C/D .

Tests	C/D	α (°)	Model rod	SR (%)		SI (%)		$SR_{EL/D=1} - SR_{EL/D=0.5}$ (%)	$SI_{EL/D=1} - SI_{EL/D=0.5}$ (%)
				$EL/D=0.5$	$EL/D=1$	$EL/D=0.5$	$EL/D=1$		
4BL vs 3BL	3	90	Brass	42	50	8.1	12	8	3.9
19BL vs 12BL	3	90	Steel	62	73	13.5	16.2	11	2.7
10BL vs 11BL	1	90	Brass	44	73	8.1	21.1	29	13

Table 6.7: Relative effect of embedded length EL/D in different ratios C/D .

FIGURES

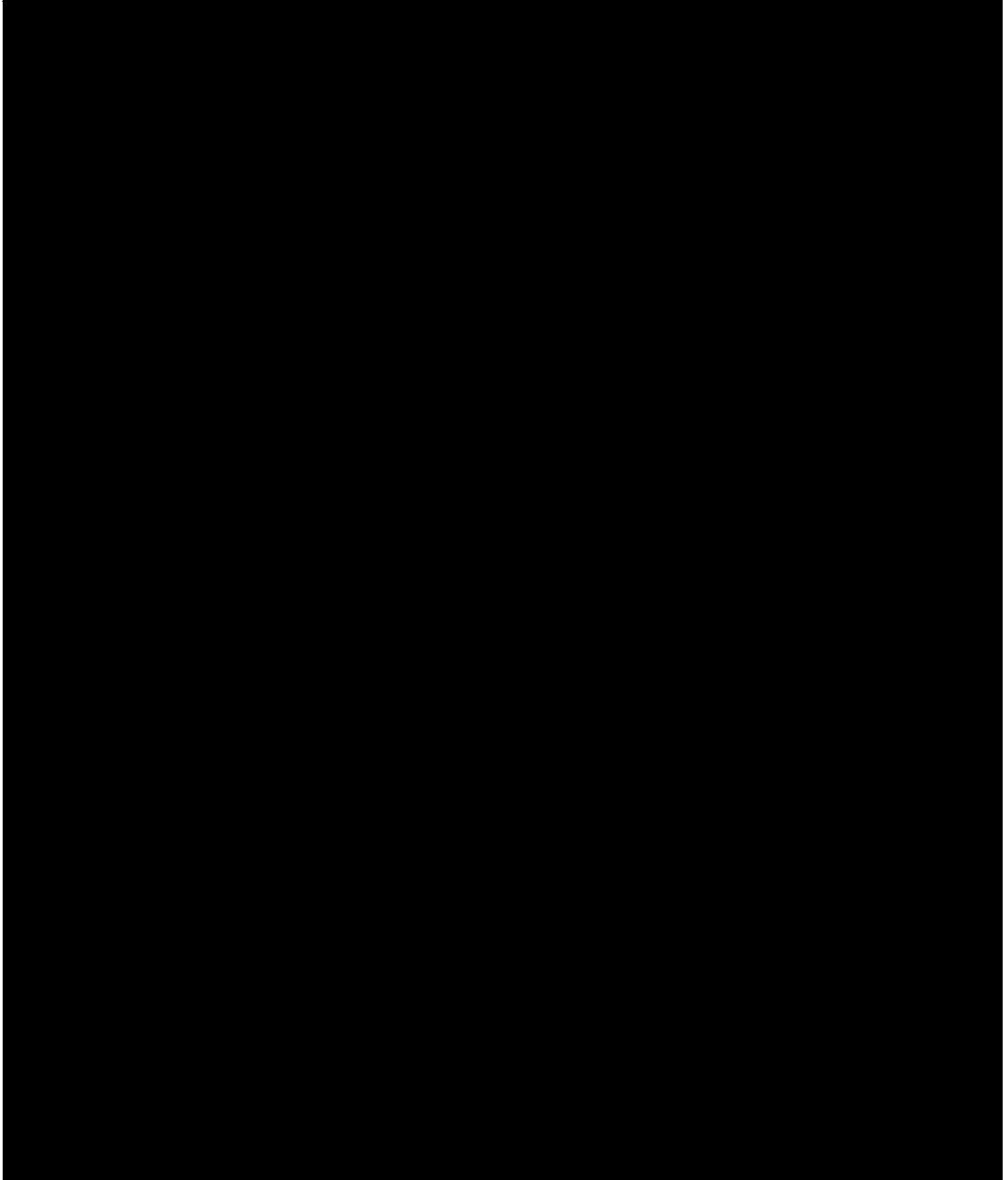


Figure 1.1: Congestion in underground space (courtesy Keller).

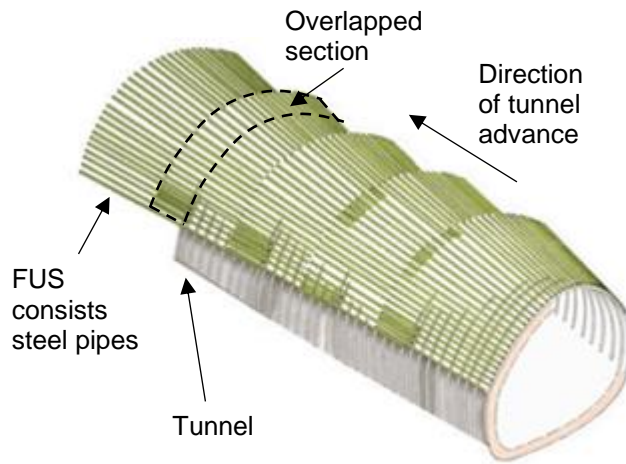
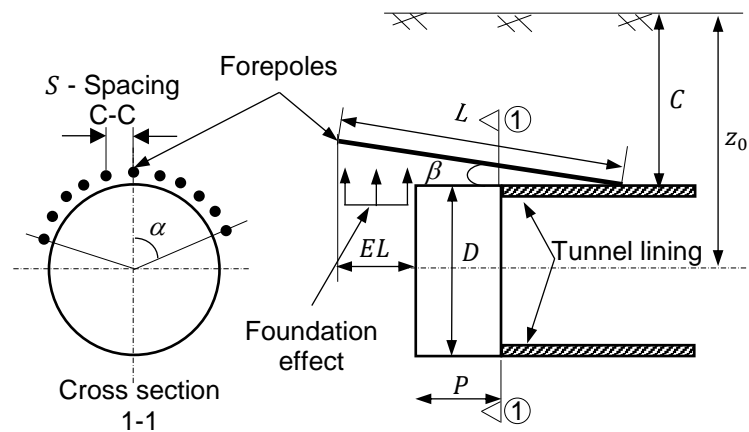


Figure 1.2: Forepoling Umbrella System (after Carrieri *et al.*, 2002).



D : tunnel diameter; C : cover depth;
 P : unlined portion; EL : embedded length;
 L : forepoles length; z_0 : tunnel depth
 S : centre to centre spacing between forepoles;
 β : insertion angle; α : filling angle.

Figure 1.3: Forepoling Umbrella System schematic diagram.

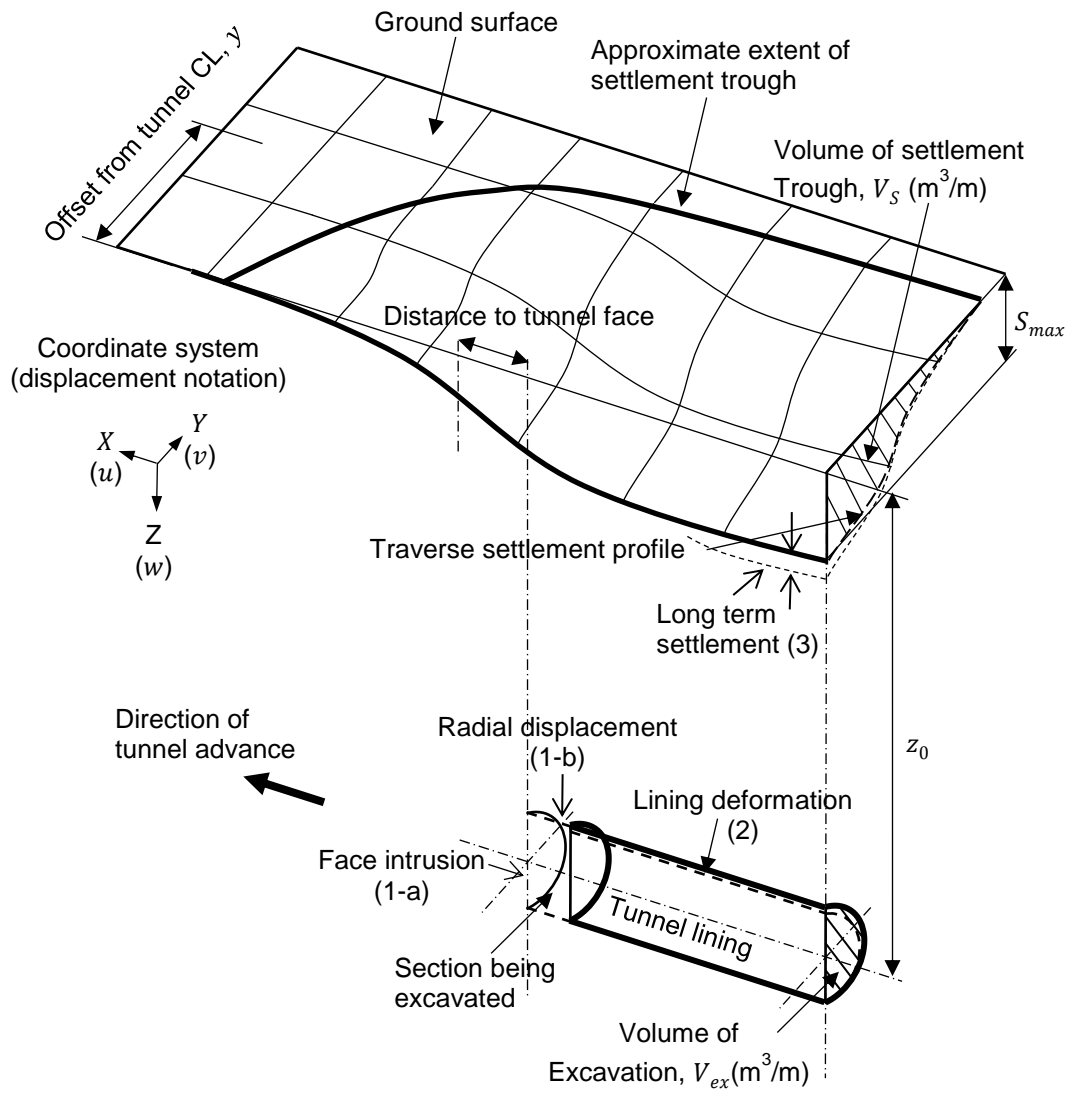


Figure 2.1: Idealised 3D tunnel advance and related soil deformations.

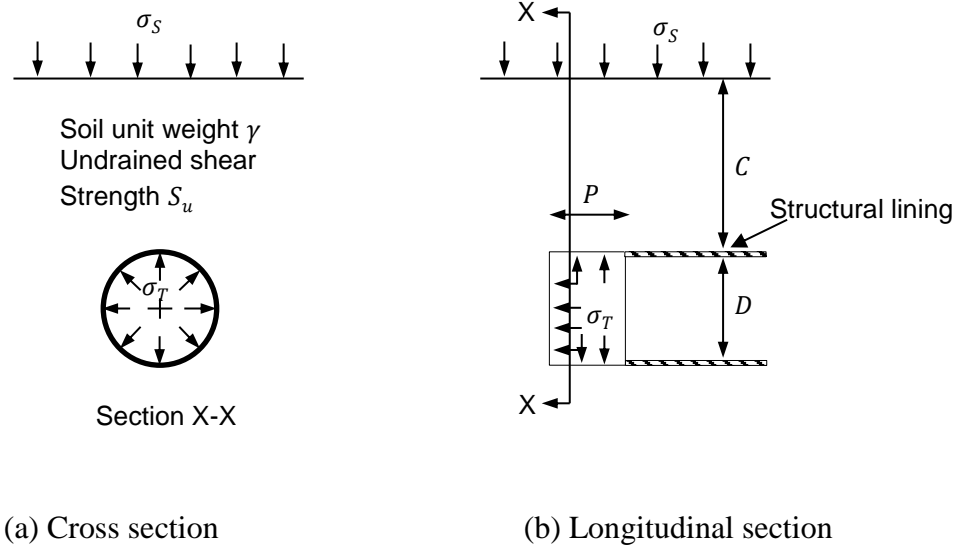


Figure 2.2: An idealisation of shield tunnelling (after Davis *et al.*, 1980).

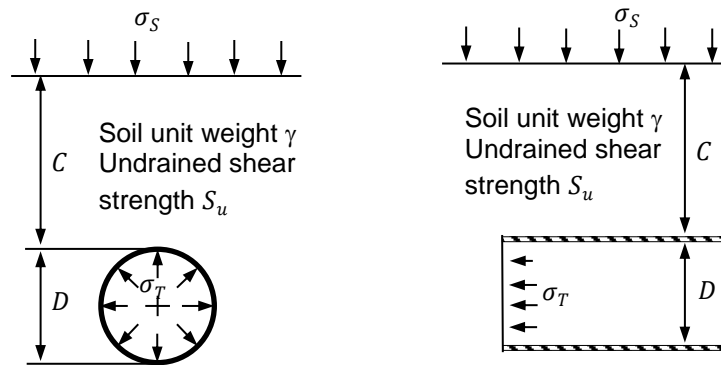
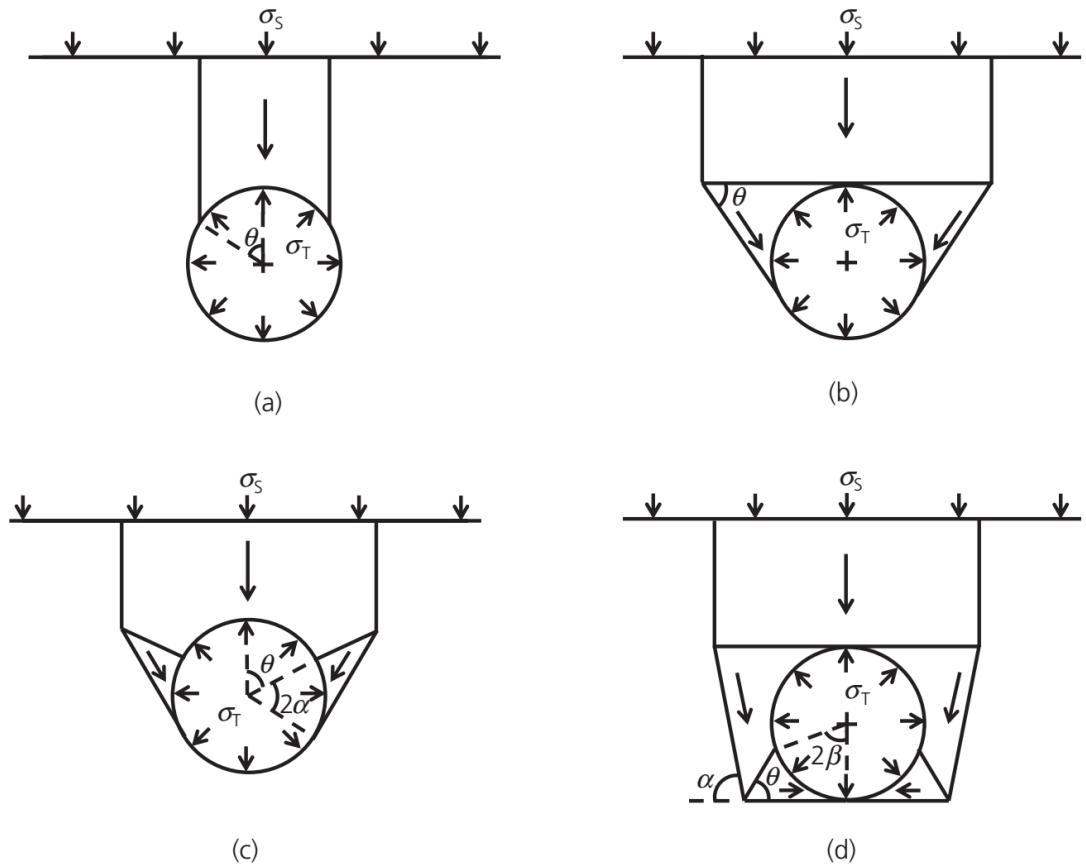


Figure 2.3: Cases of tunnel heading (after Davis *et al.*, 1980).



(a) Upper bound mechanism A; (b) Upper bound mechanism B; (c) Upper bound mechanism C; d) Upper bound mechanism D.

Figure 2.4: Four upper bound collapse mechanisms for the transverse plane strain section of a circular tunnel (After Davis *et al.*, 1980).

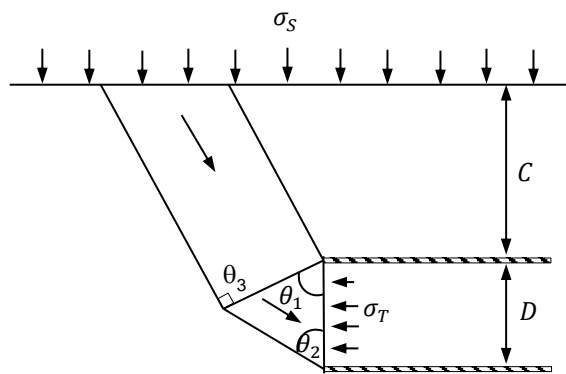


Figure 2.5: Upper bound mechanisms for a plane strain heading (after Davis *et al.*, 1980).

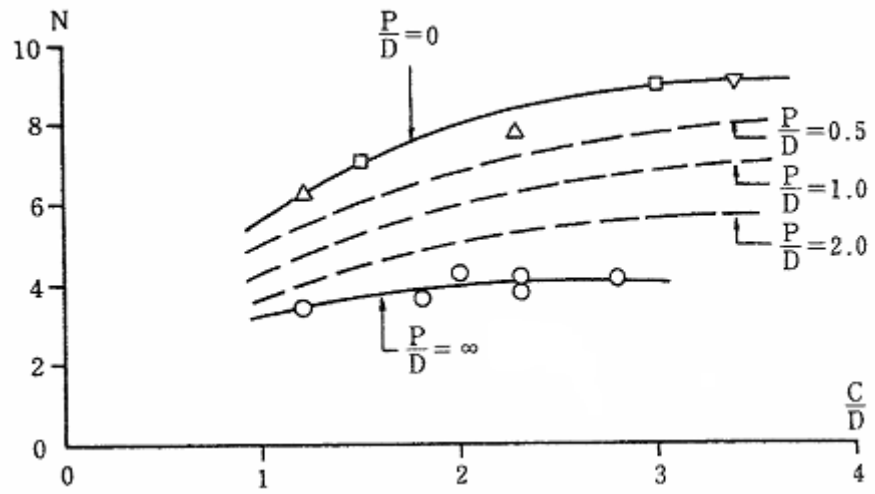


Figure 2.6: Influence of heading geometry on stability ratio at failure (after Kimura & Mair, 1981).

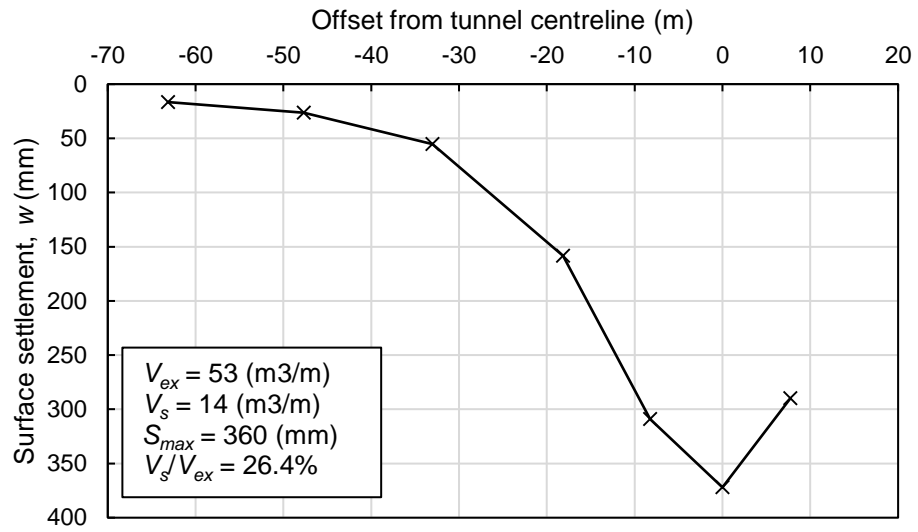


Figure 2.7: Surface settlement at a British coal mine tunnel project (after Schmidt, 1969).

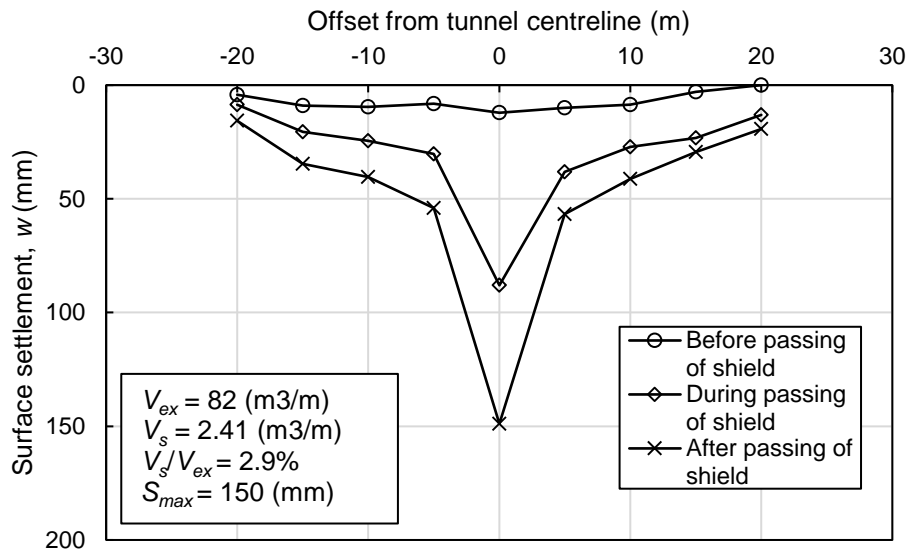


Figure 2.8: Bruxelles Metro tunnel, 1968 (after Schmidt, 1969).

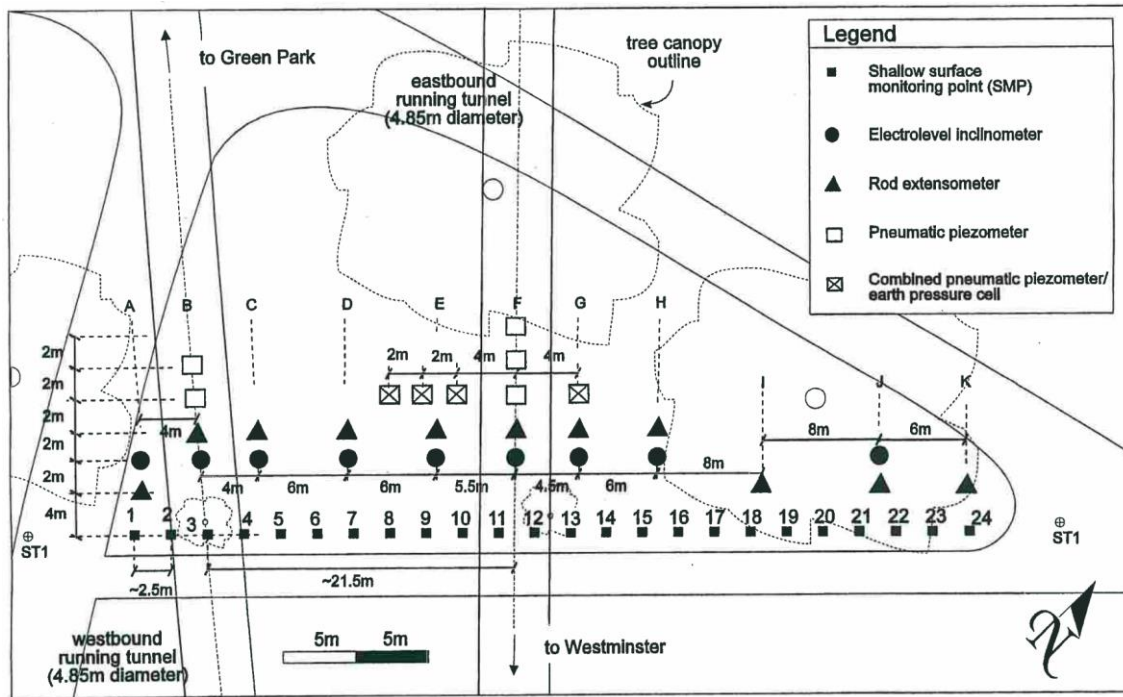


Figure 2.9: Instrumentation layout plan at St James' Park (Nyren, 1998).

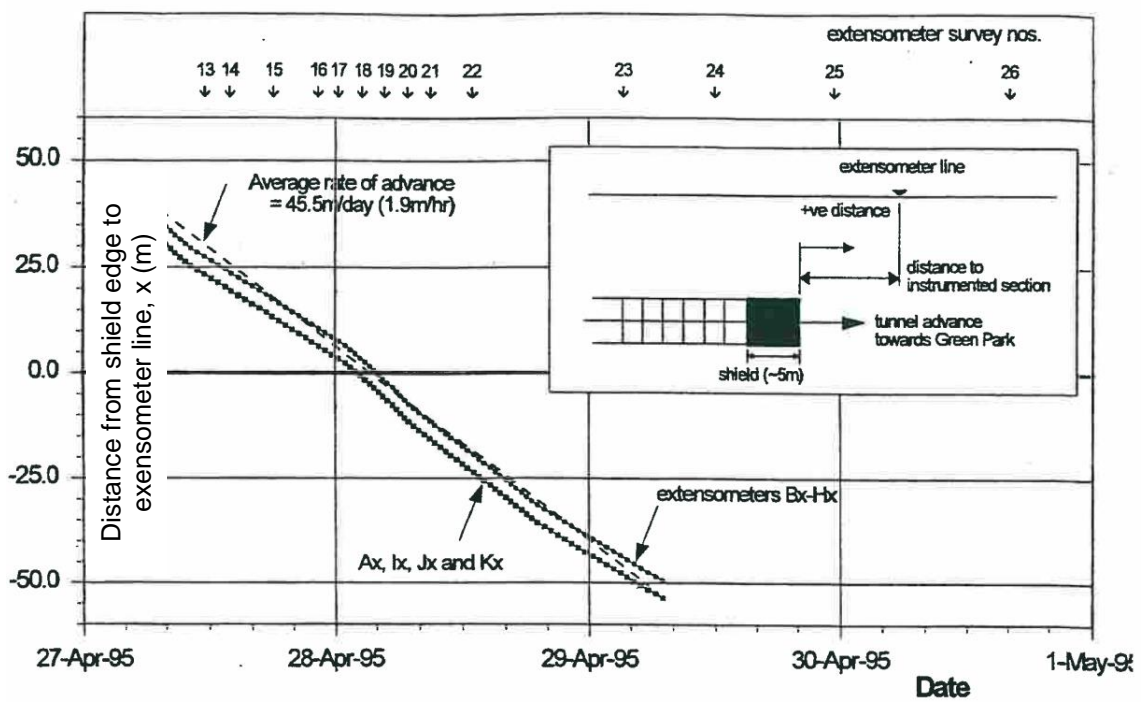


Figure 2.10: Time line of the surveys in relation to the advance of the tunnel (Nyren, 1998).

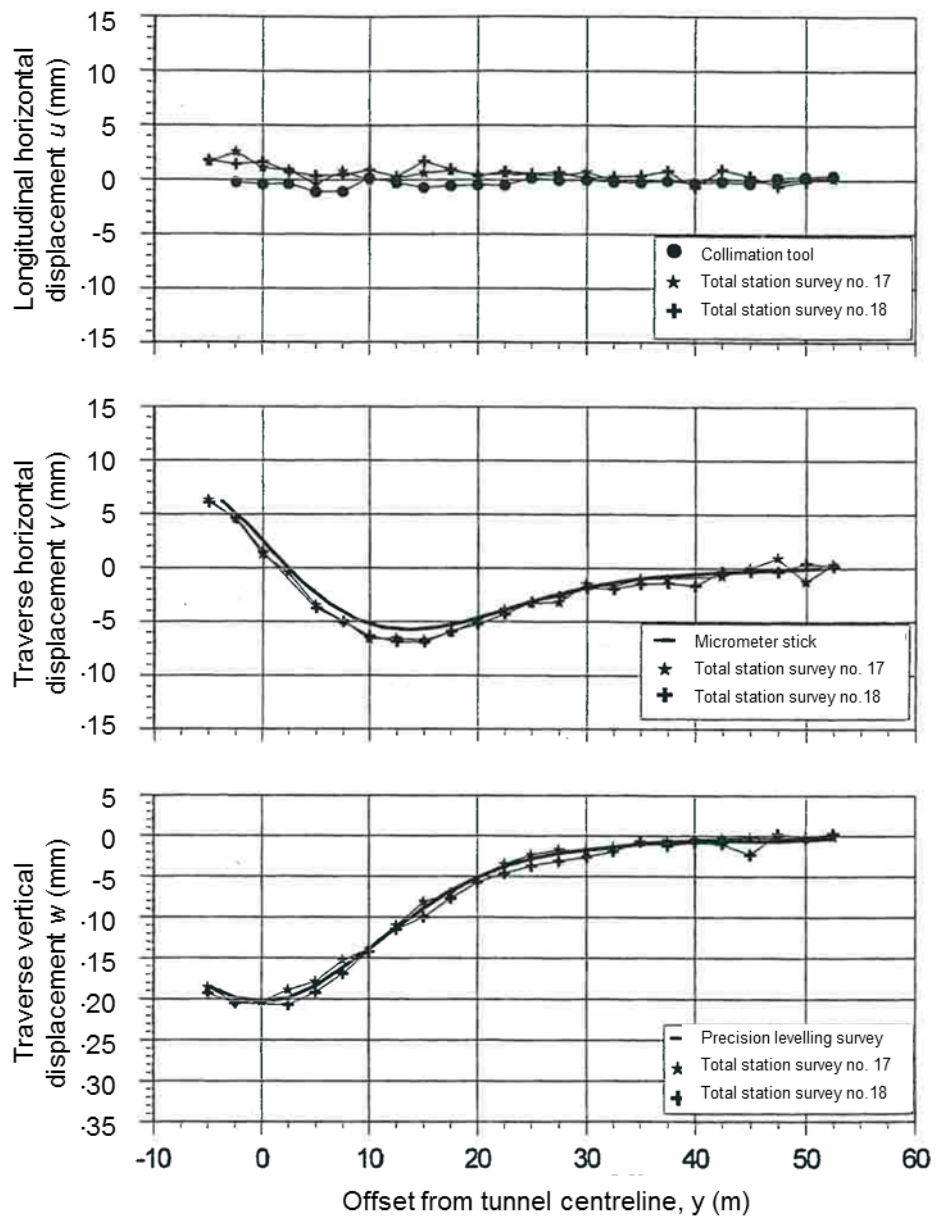


Figure 2.11: Comparison of final displacement profiles determined from independent measurements immediately after westbound tunnel construction (After Nyren, 1998).

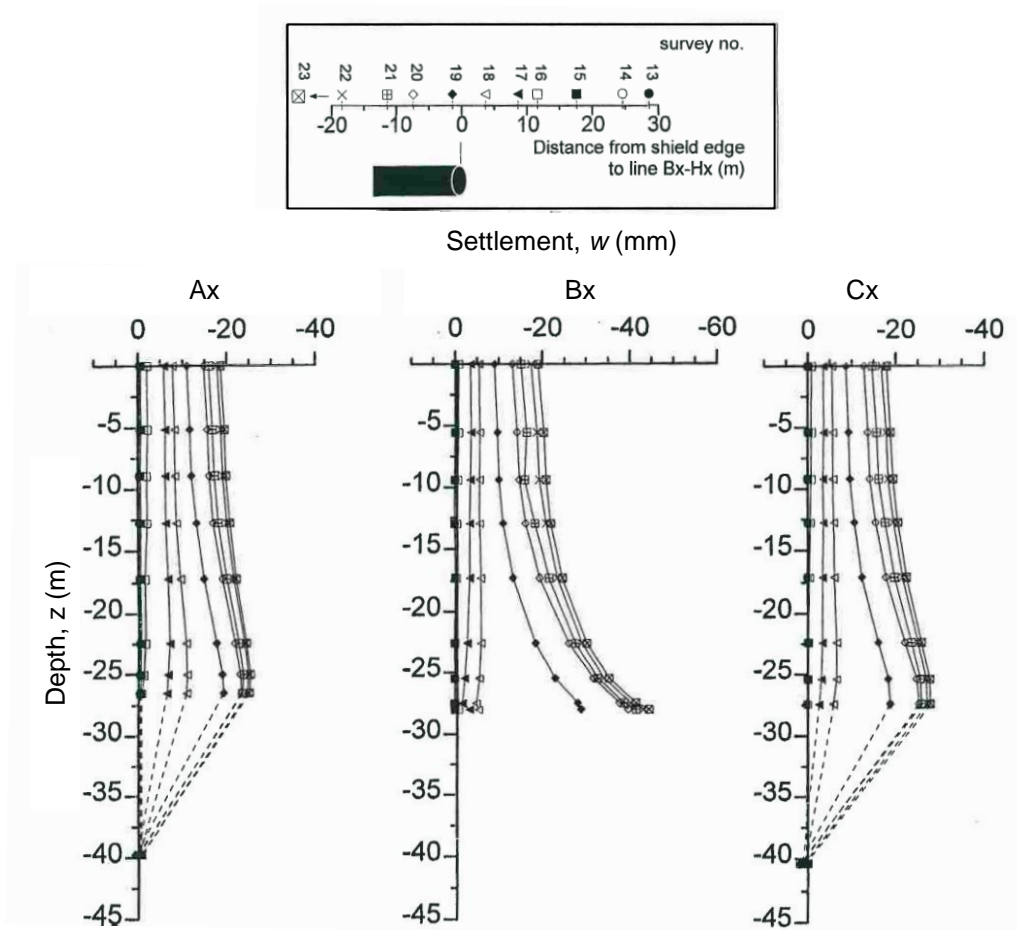


Figure 2.12: Vertical subsurface settlement with westbound tunnel face position for extensometer (positions of the extensometers are depicted in **Figure 2.9**) (after Nyren, 1998).

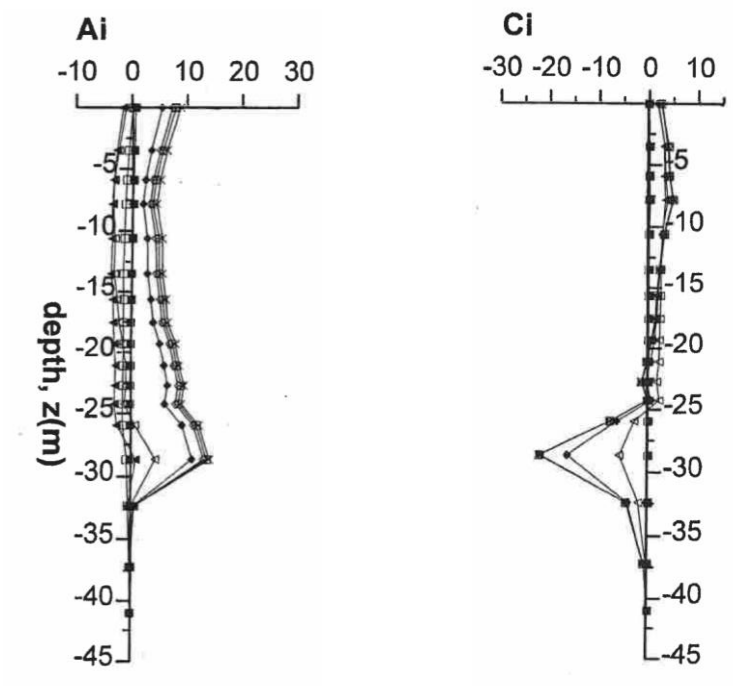
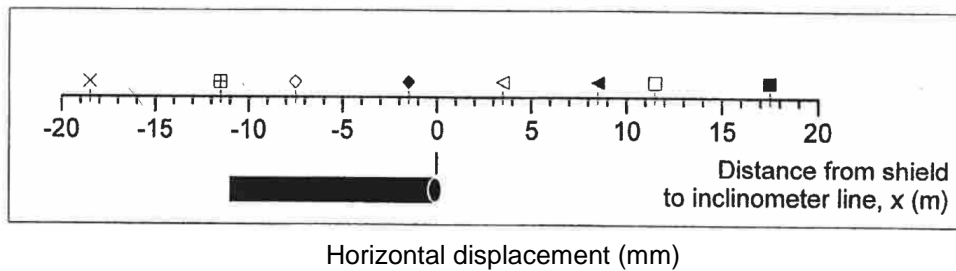


Figure 2.13: Vertical profile of horizontal displacements from electrolevel inclinometers (after Nyren, 1998).

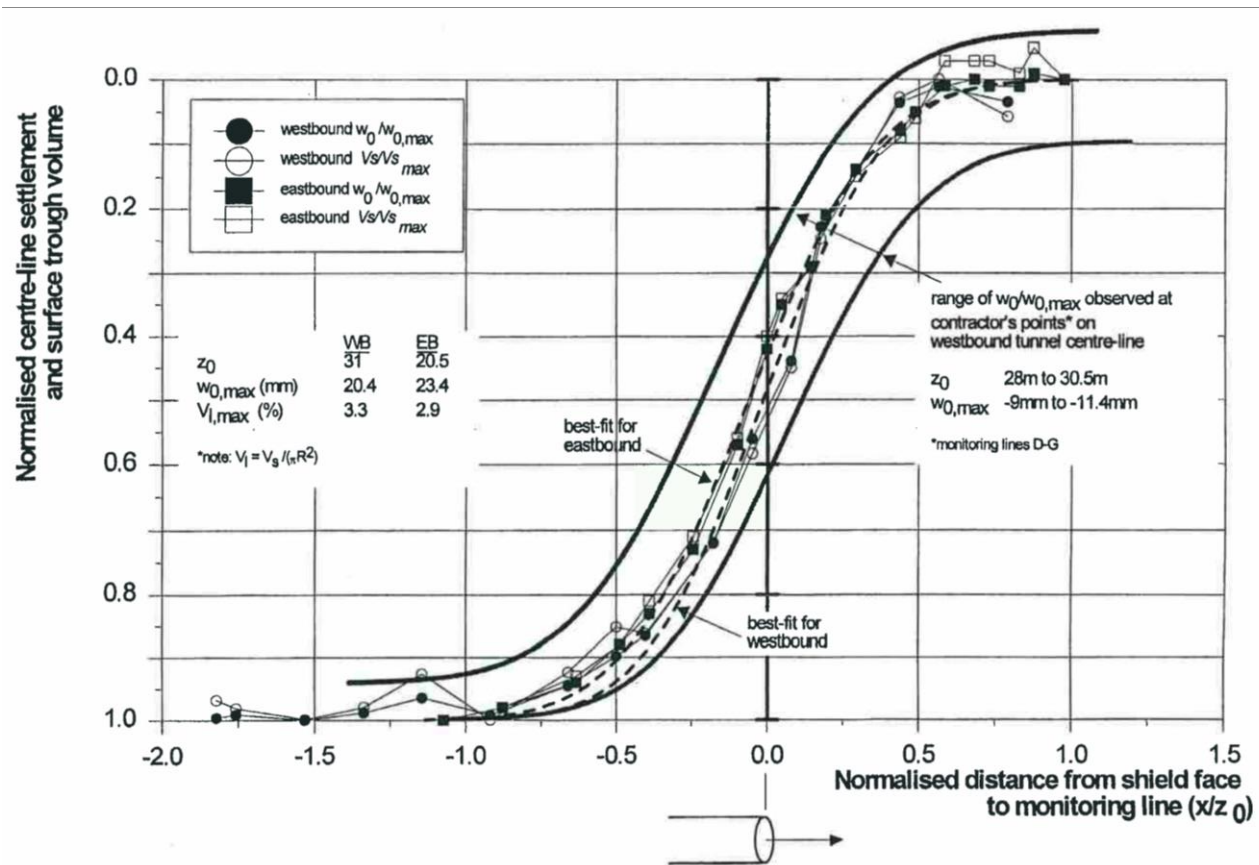


Figure 2.14: Parallel profiles of normalised centreline settlement and surface trough volume with tunnel face position for both tunnels at St. James's Park, and comparisons with other field data (Nyren, 1998).

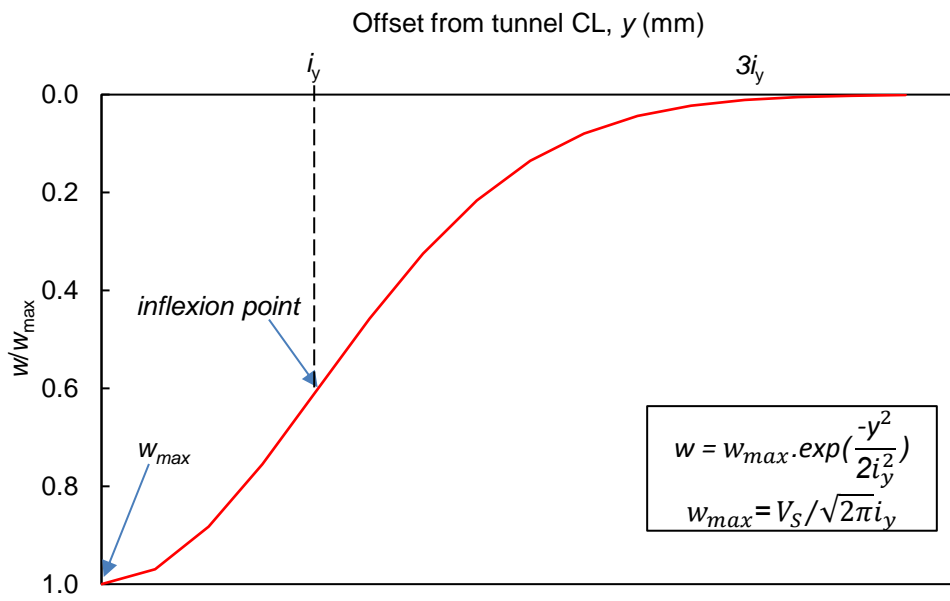


Figure 2.15: Usage of Gaussian curve to represent settlement trough (after O'Reilly & New, 1982).

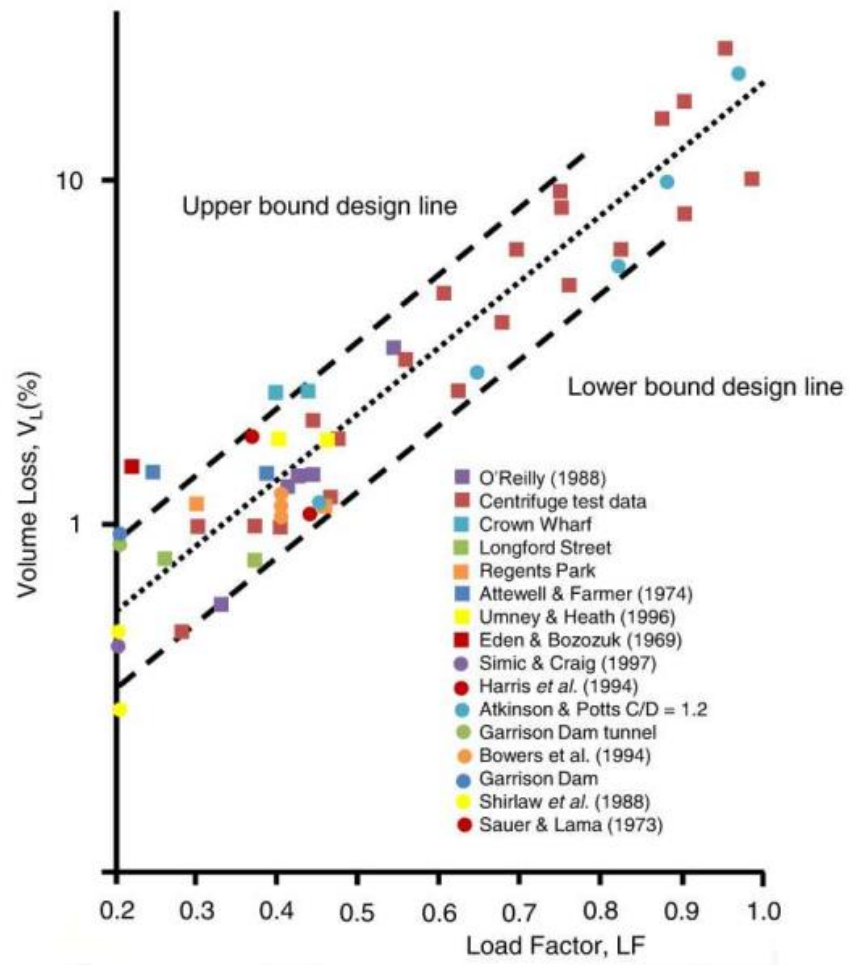
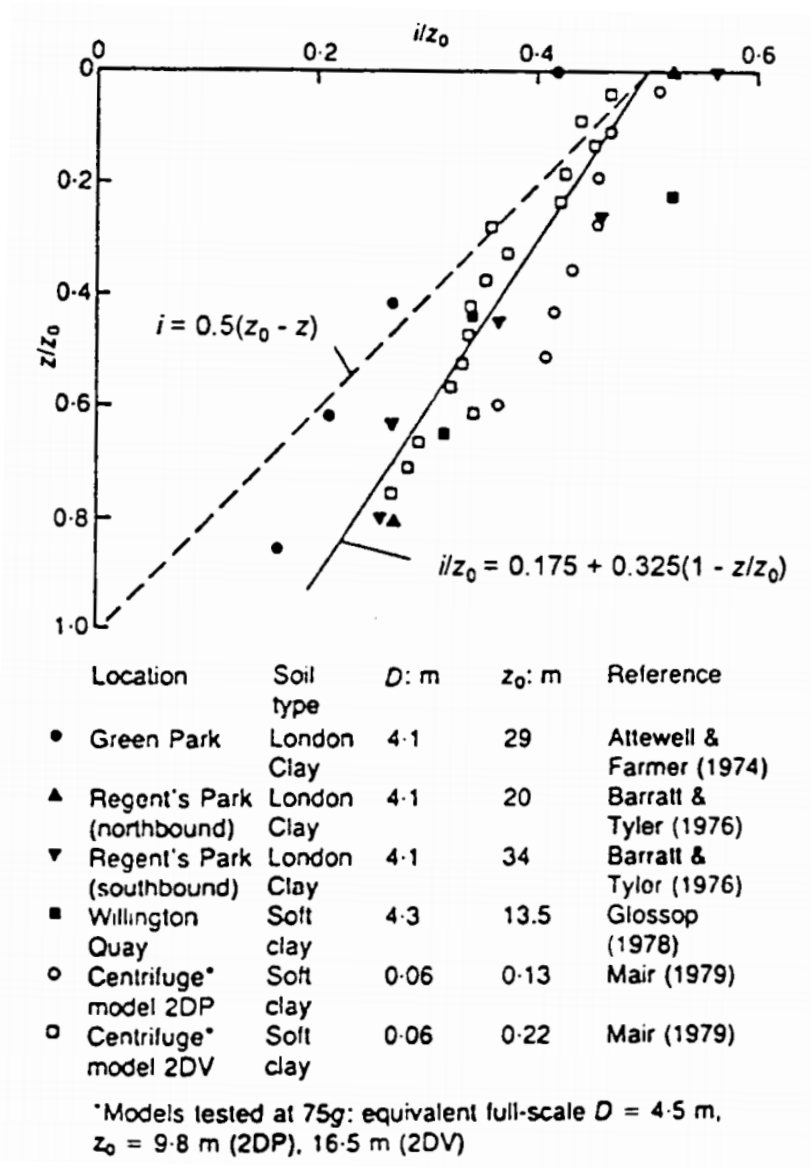
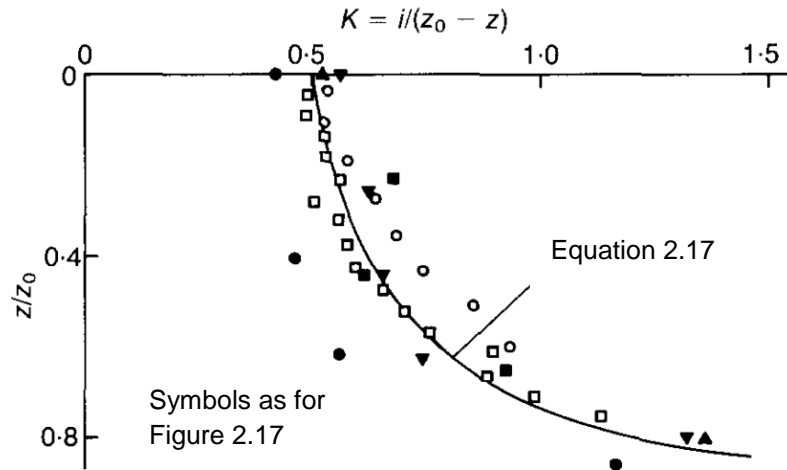


Figure 2.16: Relationship between volume loss and load factor (after Macklin, 1999).



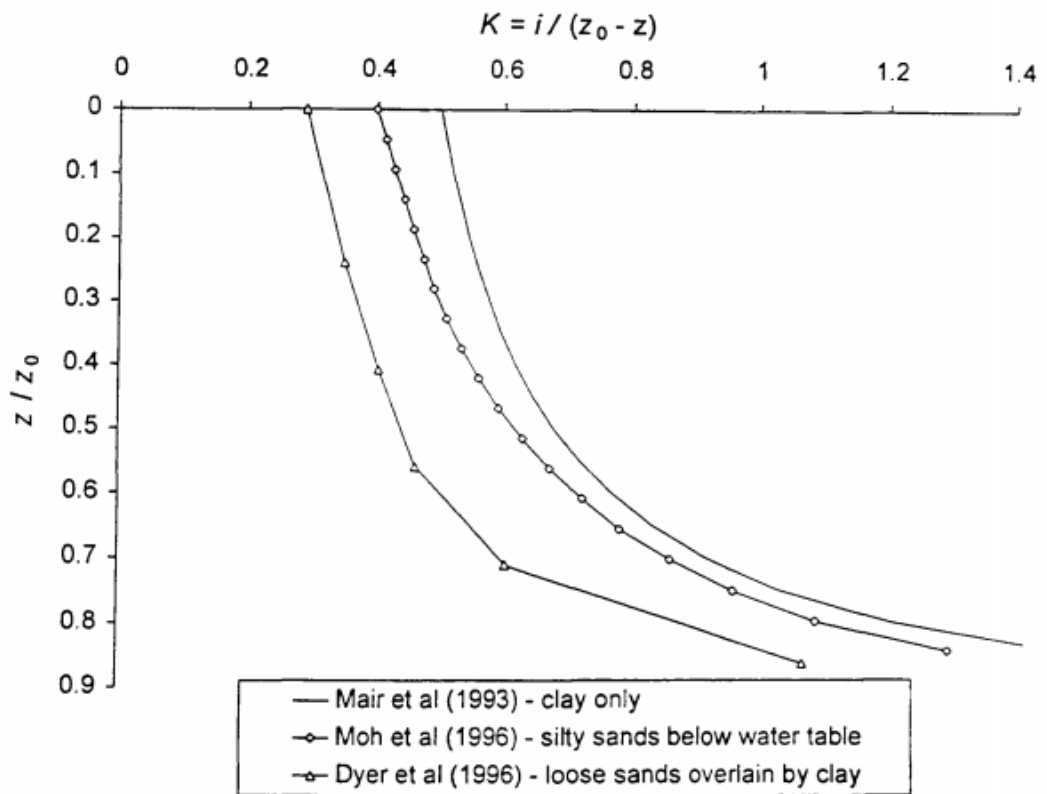
*i in this Figure is i_y

Figure 2.17: Variation of subsurface settlement trough width parameter with depth for tunnels in clays (after Mair *et al.*, 1993).



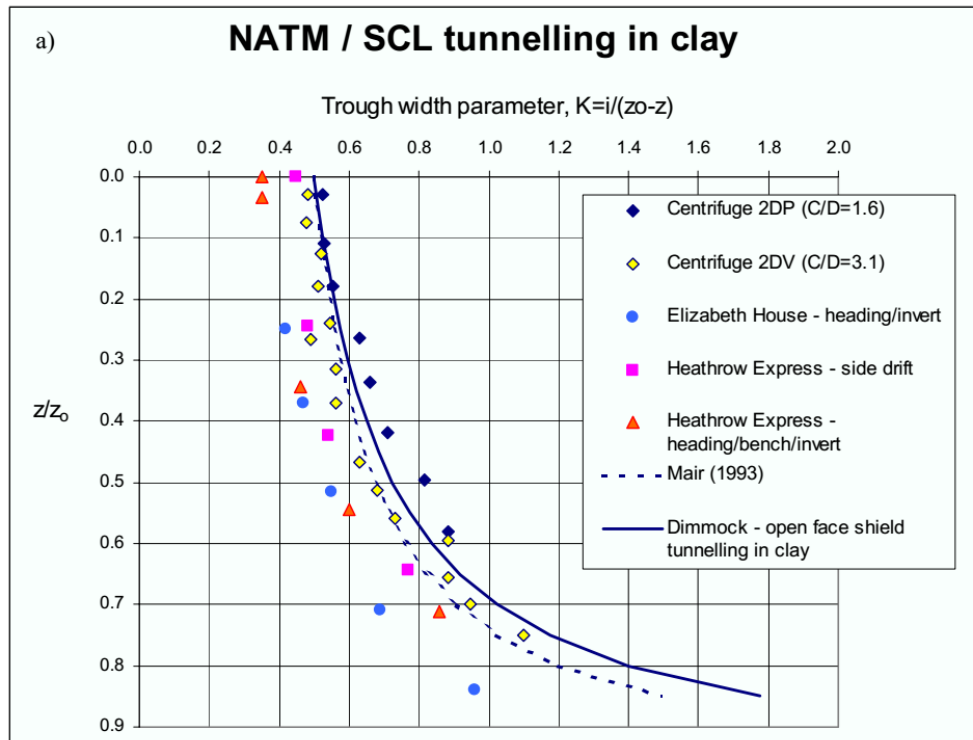
* i in this Figure is i_y

Figure 2.18: Variation of K with depth for subsurface settlement profiles above tunnels in clays. (Mair *et al.*, 1993).



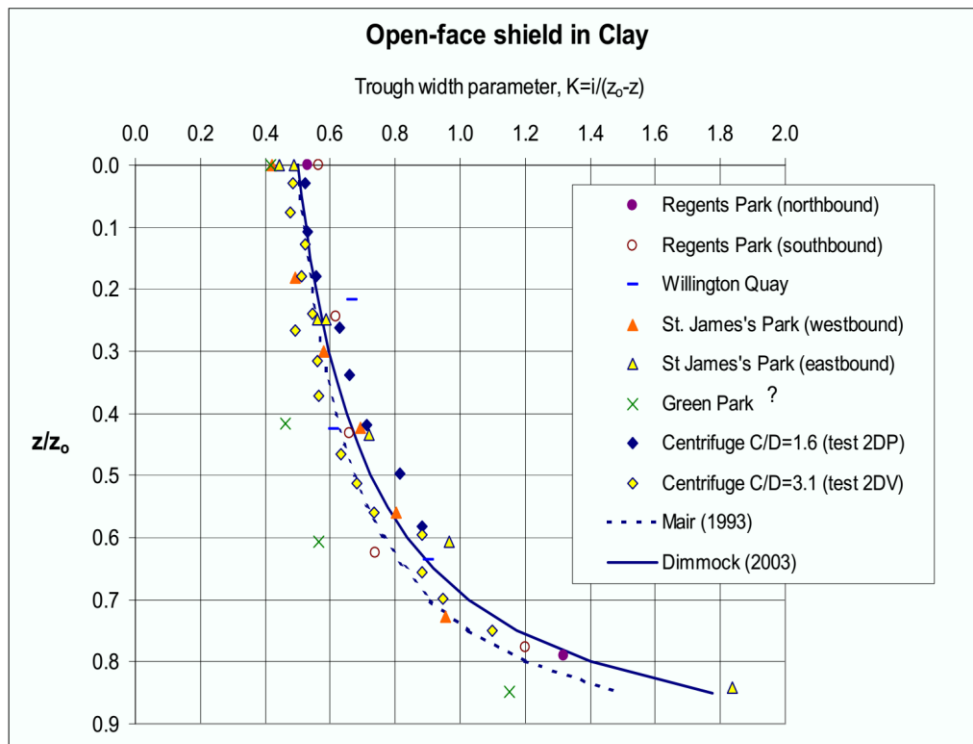
* i in this Figure is i_y

Figure 2.19: Variation of trough width parameter K with depth in different soil types (Grant, 1998).



* i in this Figure is i_y

Figure 2.20: The variation of trough width with depth for NATM/SCL tunnelling in clay (Dimmock, 2003).



* i in this Figure is i_y

Figure 2.21: Variation of trough width with depth for open-face shield tunnelling in clay (Dimmock, 2003).

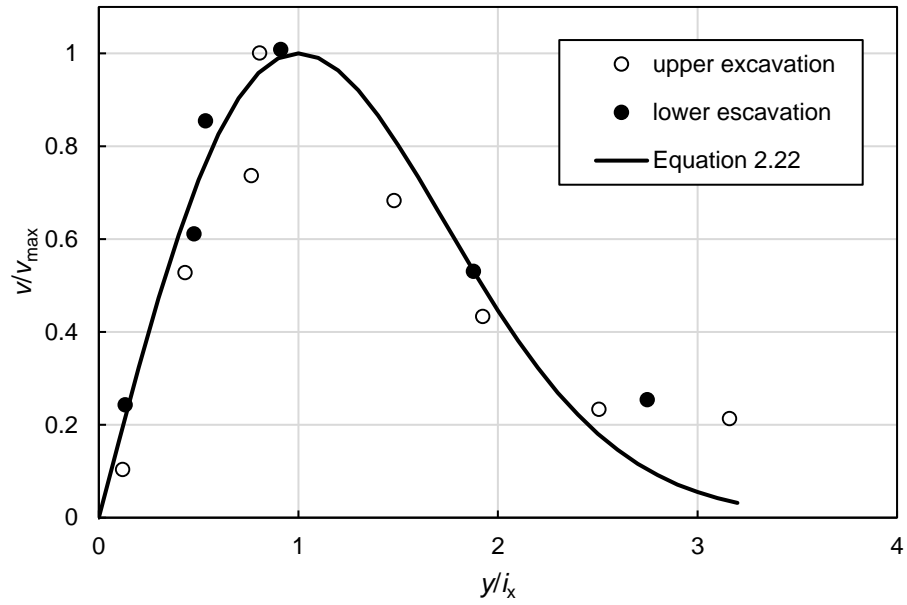


Figure 2.22: Distribution of horizontal ground surface displacement above a tunnel (after Hong & Bae, 1995).

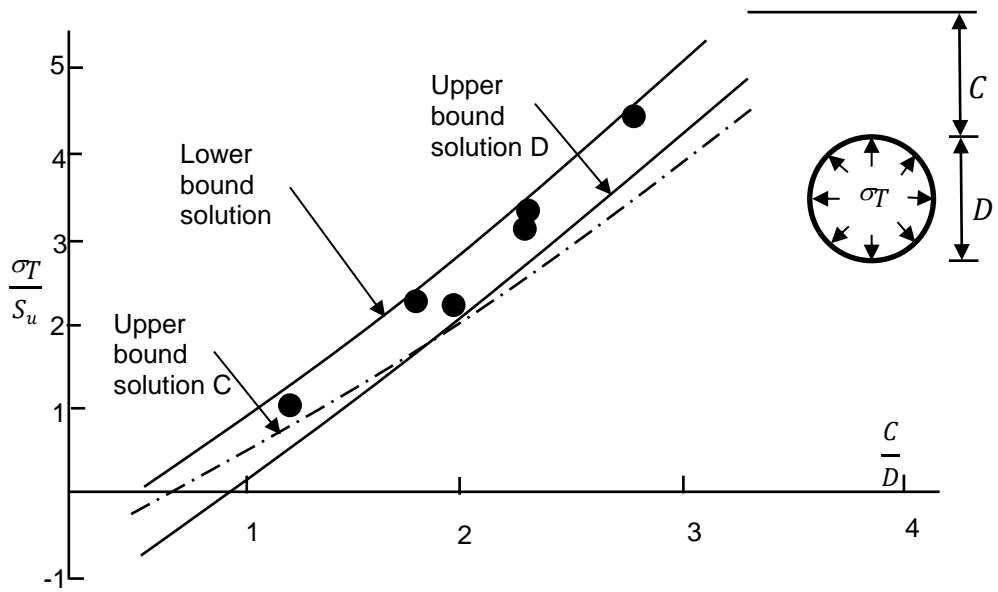
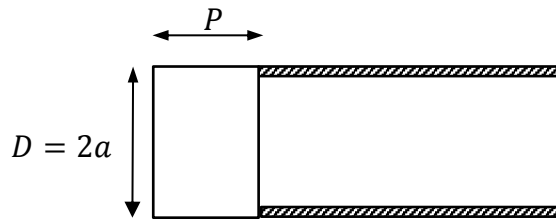
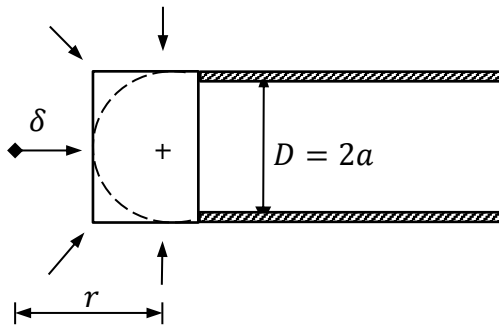


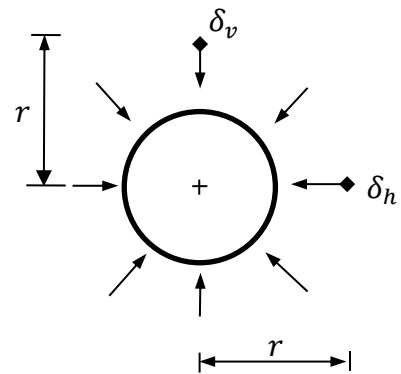
Figure 2.23: Predicted and observed tunnel support pressure at collapse (after Kimura & Mair, 1981).



a) Idealised tunnel heading.

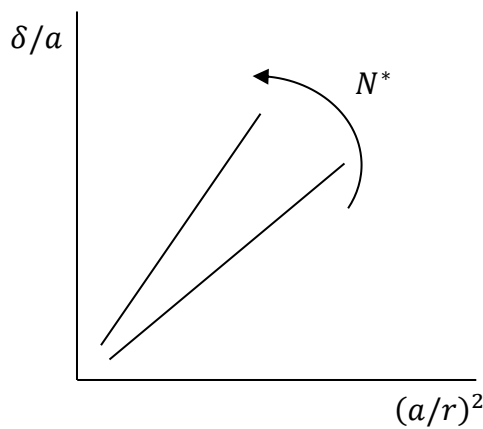


b) Spherical

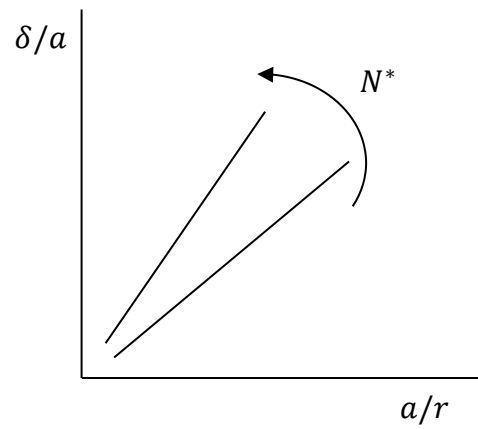


c) Cylindrical

Figure 2.24: Idealisation of tunnel heading and ground behaviours around tunnel heading (after Mair & Taylor, 1993).



a) Spherical



b) Cylindrical

Figure 2.25: Radial deformation associated with unloading a cavity in an elastic-perfectly plastic continuum (after Mair & Taylor, 1993).

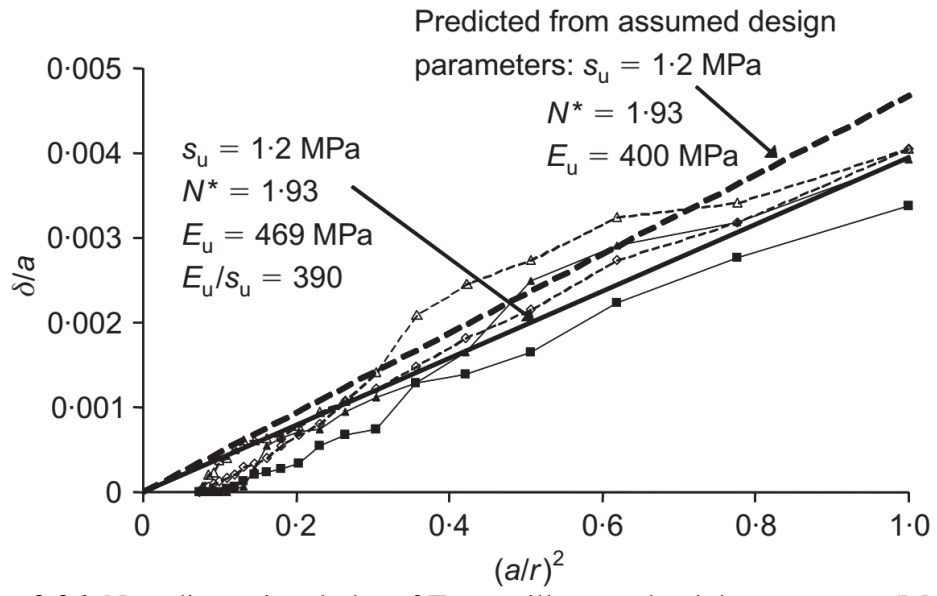


Figure 2.26: Non-dimensional plot of Tartaguille tunnel axial movements (Mair, 2008).

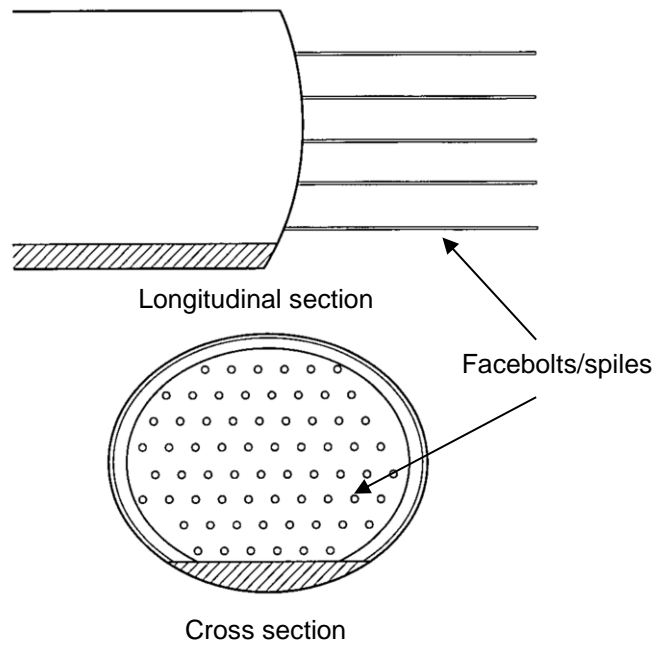
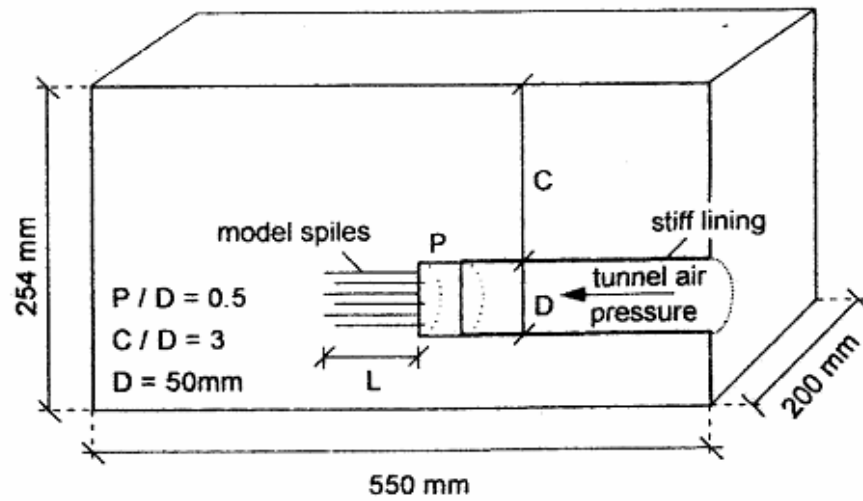
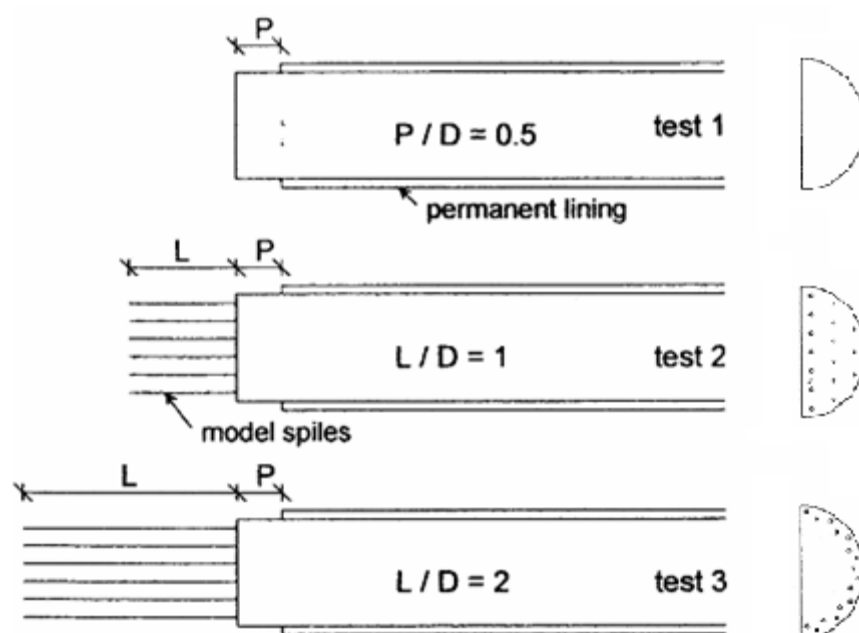


Figure 2.27: Schematic of tunnel reinforced by spiles (After Harris, 2001).



a. Schematic of the model



b. Spile patterns: length and spacing

Figure 2.28: Testing arrangement of spiles in centrifuge modelling (after Calvello & Taylor, 1999).

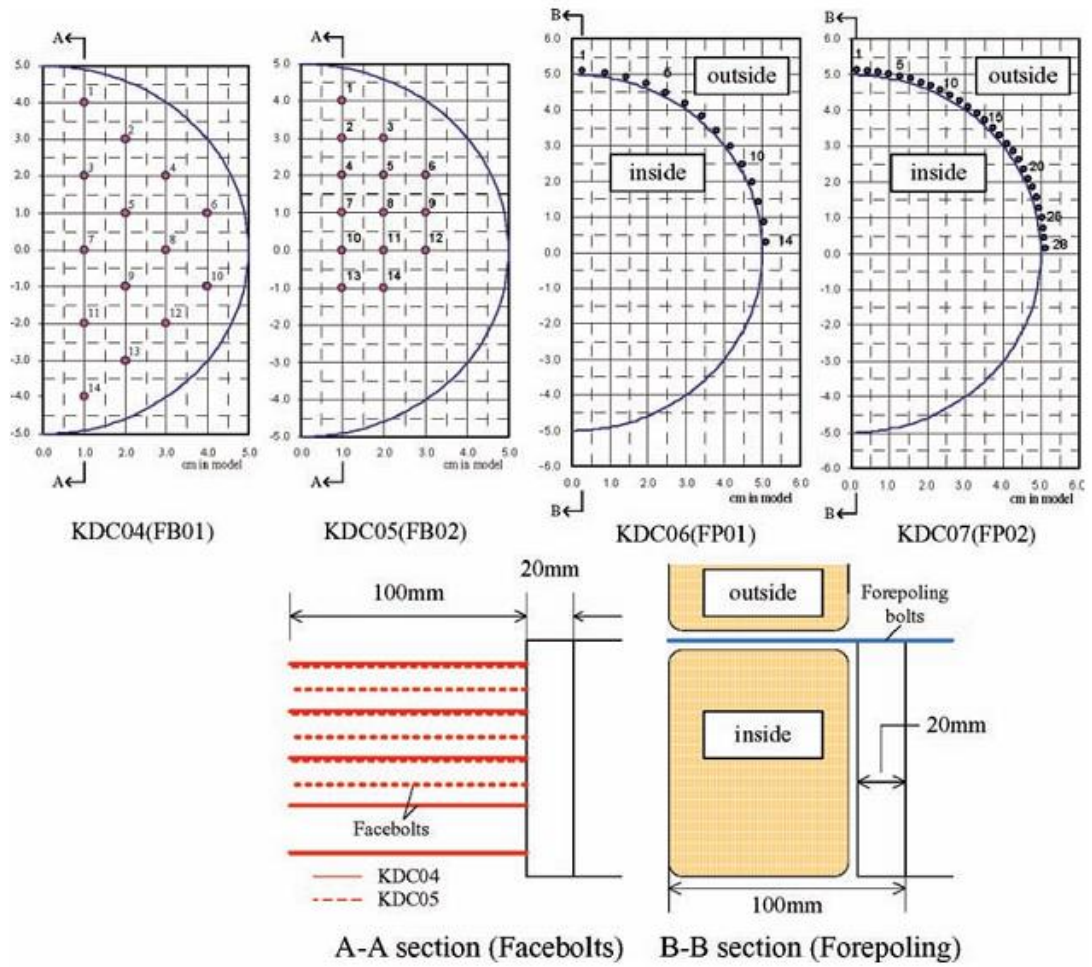
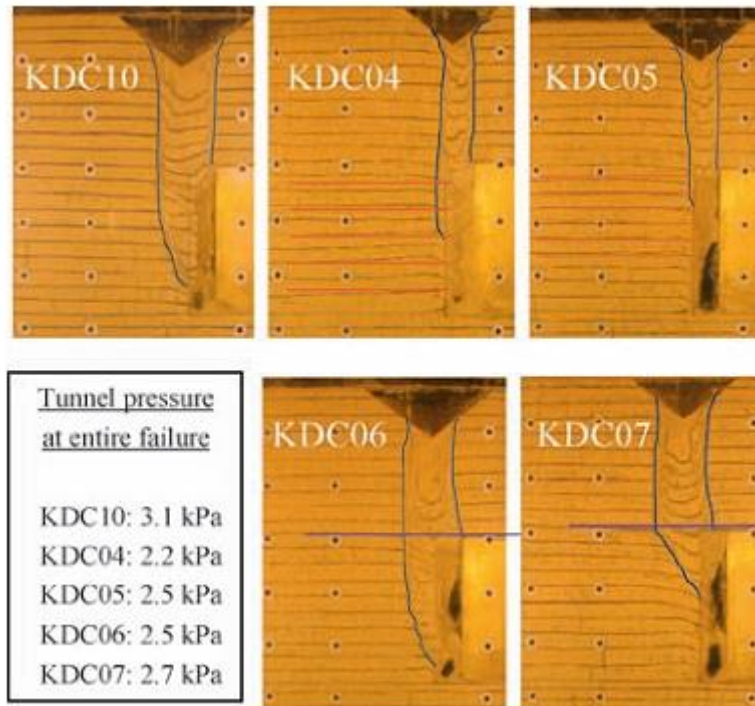


Figure 2.29: The arrangement patterns of bolts (Date *et al.*, 2008).

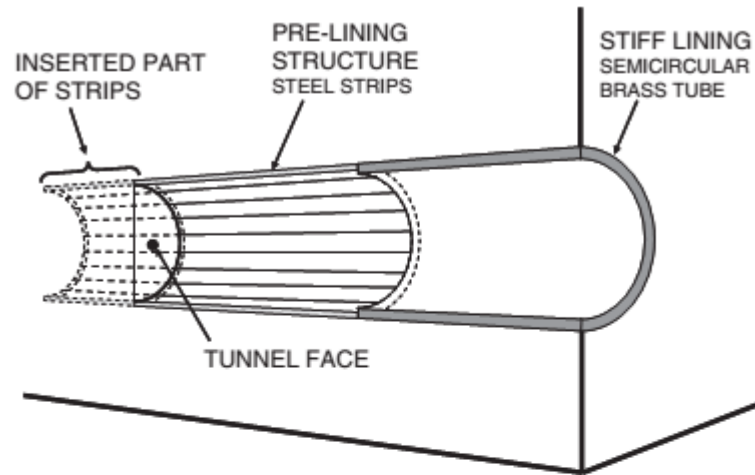


KDC10 is the reference test; Parameters of the tests are shown in Figure 2.29.

Figure 2.30: Tunnel failure patterns on the longitudinal section (Date *et al.*, 2008).



Figure 2.31: Installation of steel pipes into tunnel crown (DSI website).



Pre-lining structure model.

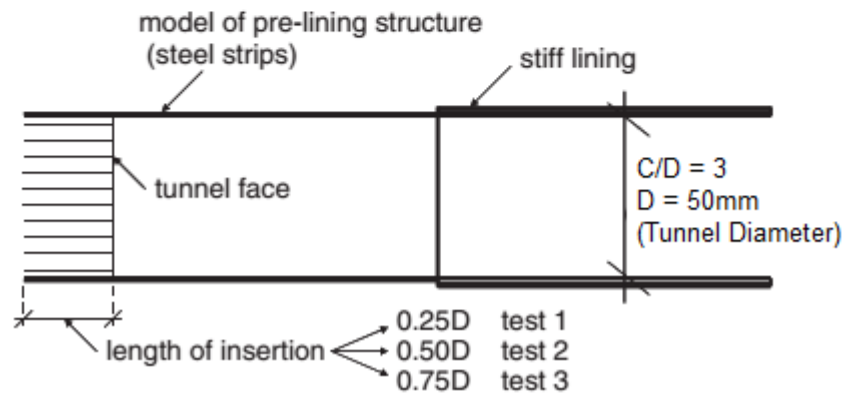


Figure 2.32: Testing arrangement of forepoling roof in centrifuge modelling (Vrba & Bartak, 2007).

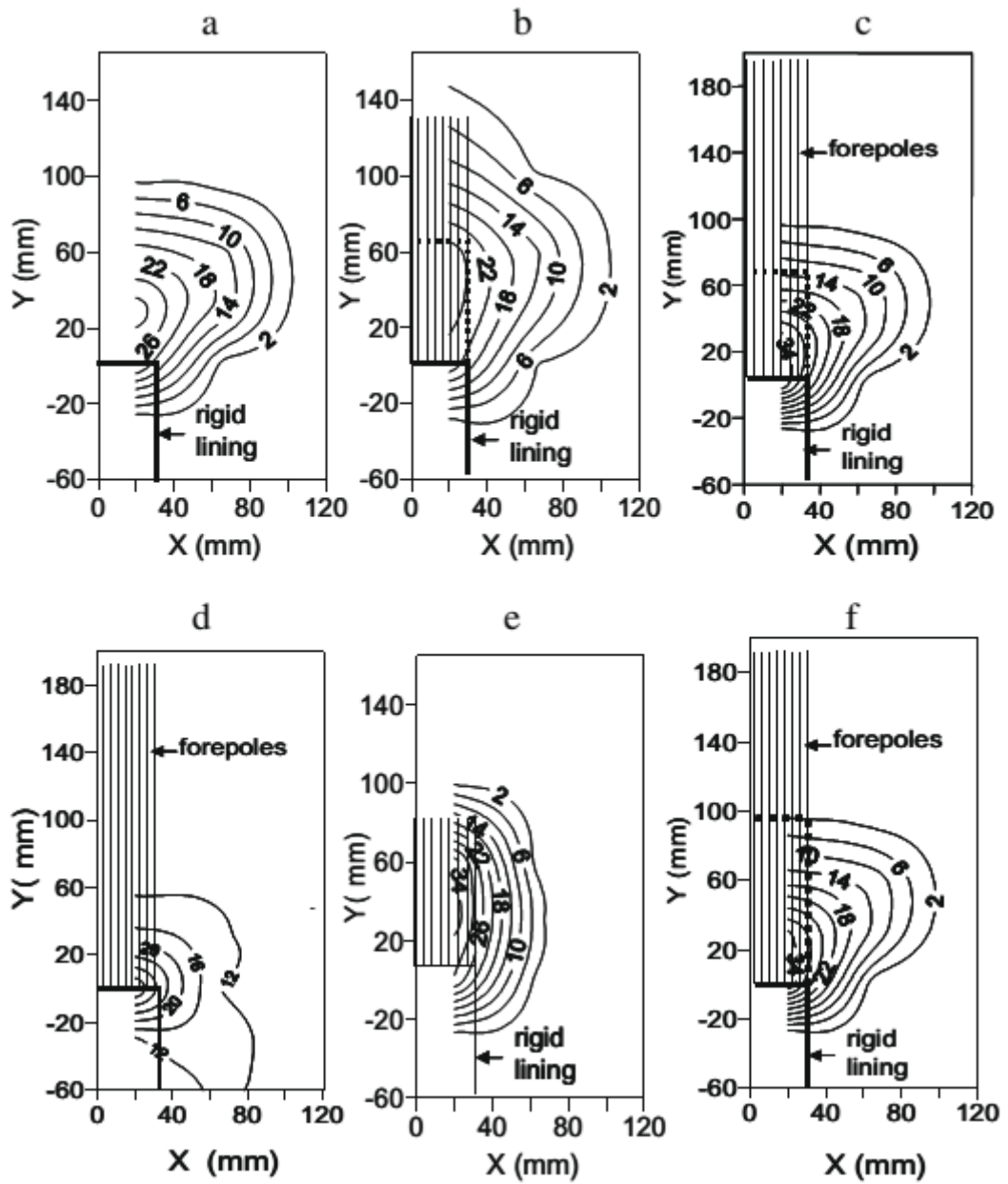


Figure 2.33: Surface settlement contours after tunnel excavation (Juneja *et al.*, 2010).

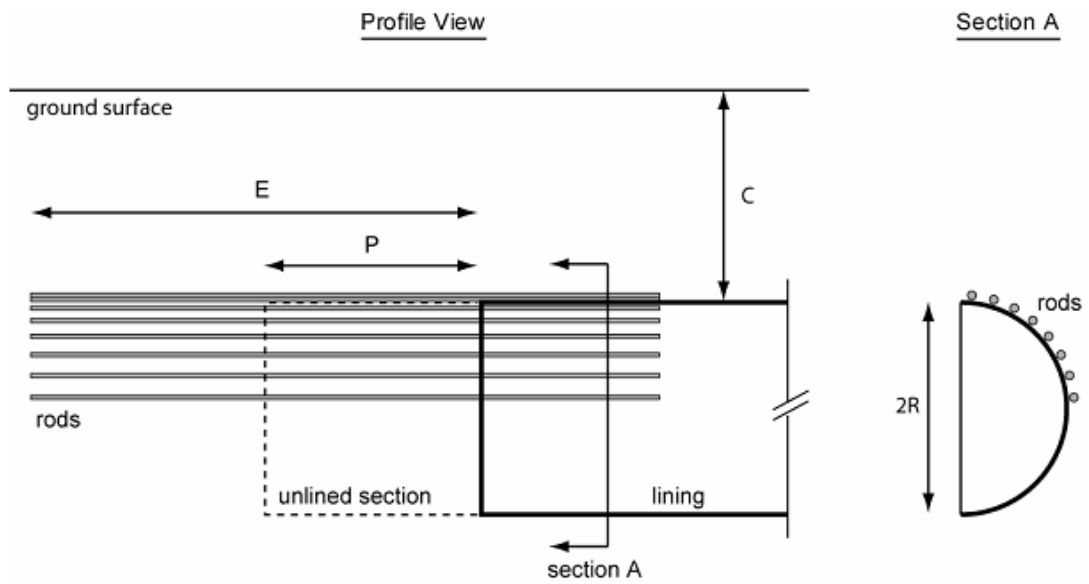


Figure 2.34: Model heading configuration (Yeo, 2011).

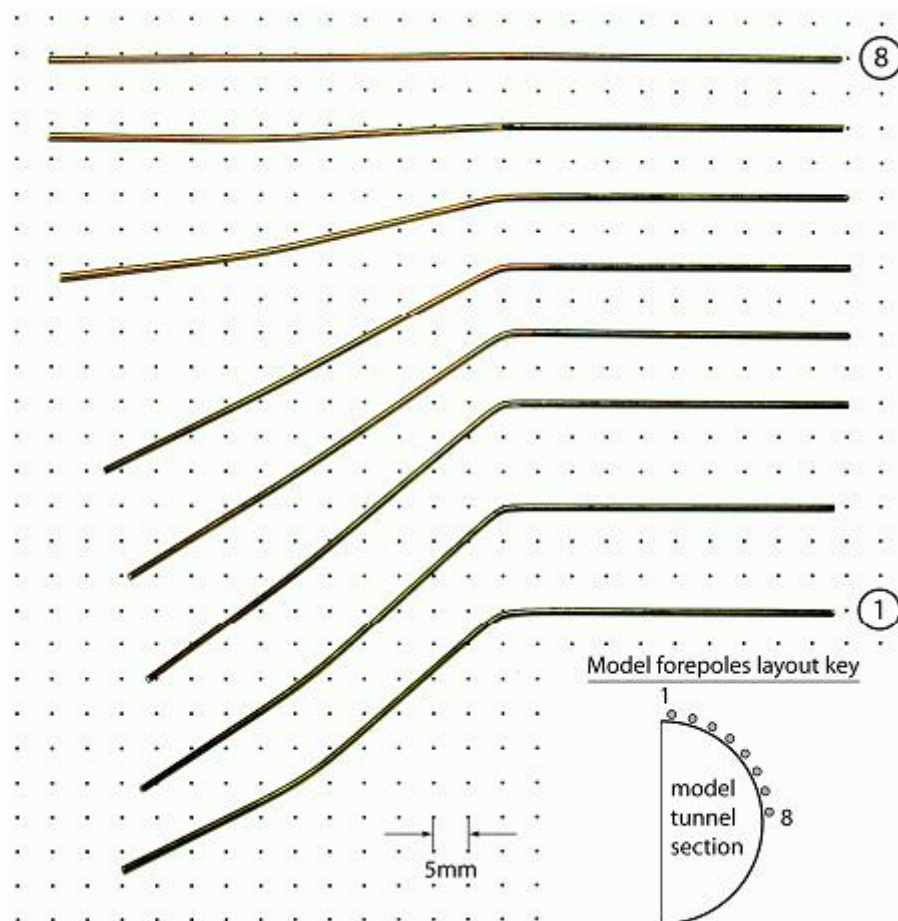


Figure 2.35: Model forepoles after testing (Yeo, 2011).

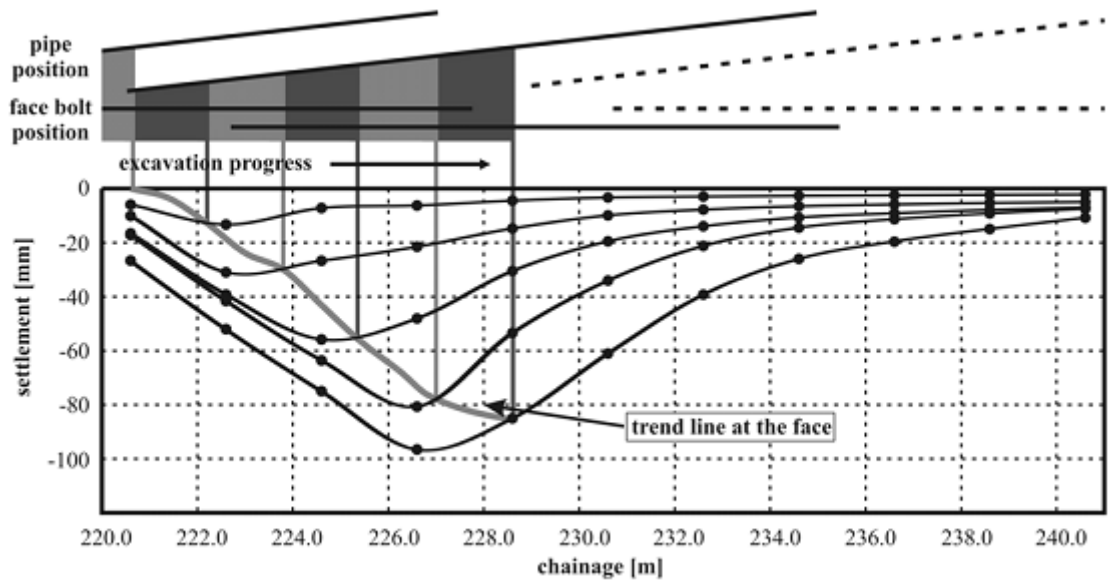


Figure 2.36: Deflection curve diagrams displaying measured settlement values from the Trojane tunnel (Volkman & Schubert, 2007).

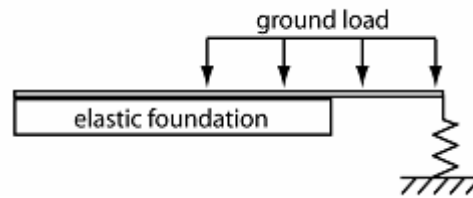
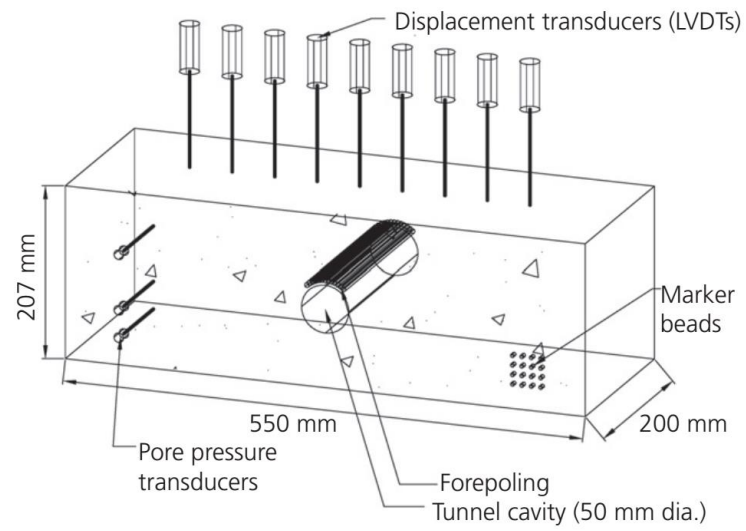
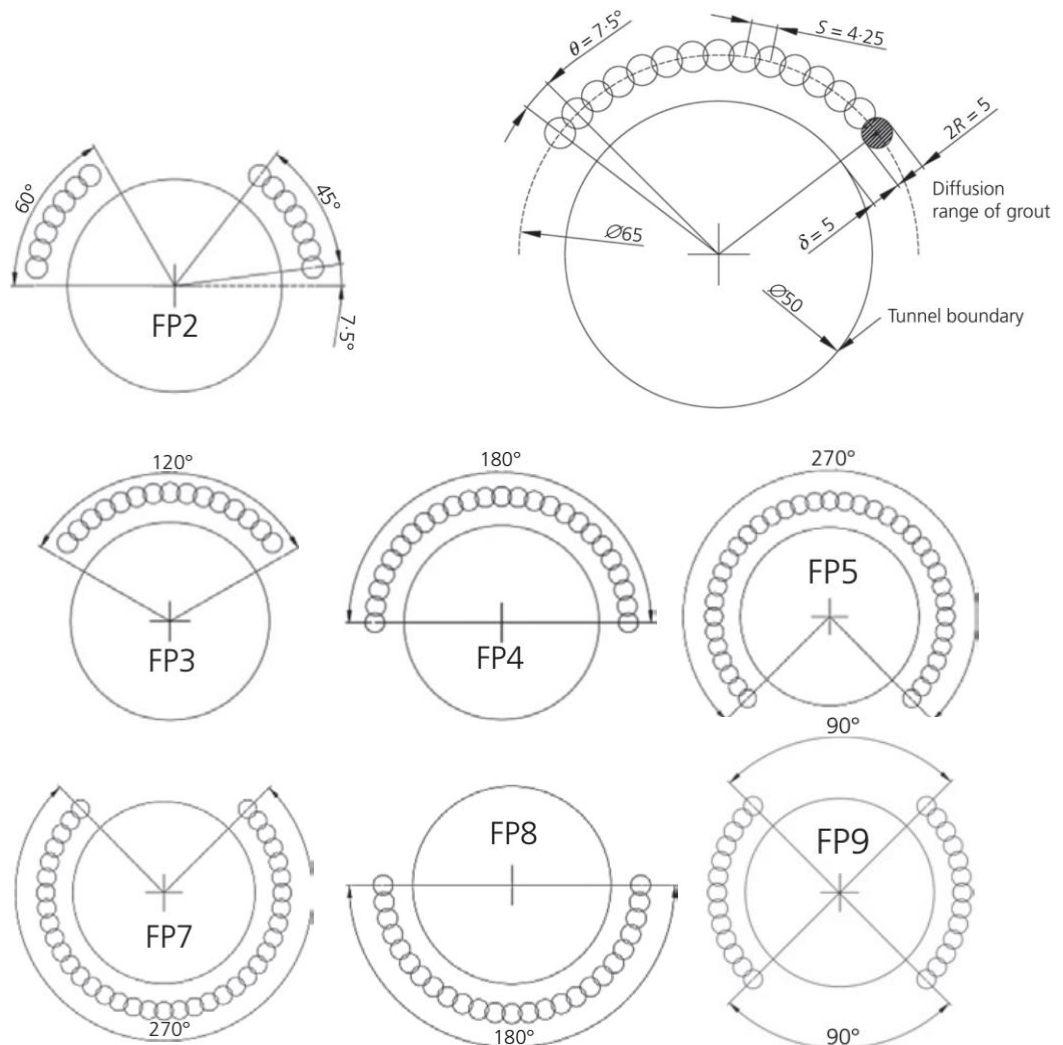


Figure 2.37: Foundation model for pipe roof (Carrieri *et al.*, 2002).



a) Centrifuge test diagram.



b) Illustration of testing variables and details of model steel pipe.

Figure 2.38: Centrifuge test conducted by Divall *et al.*, (2016).

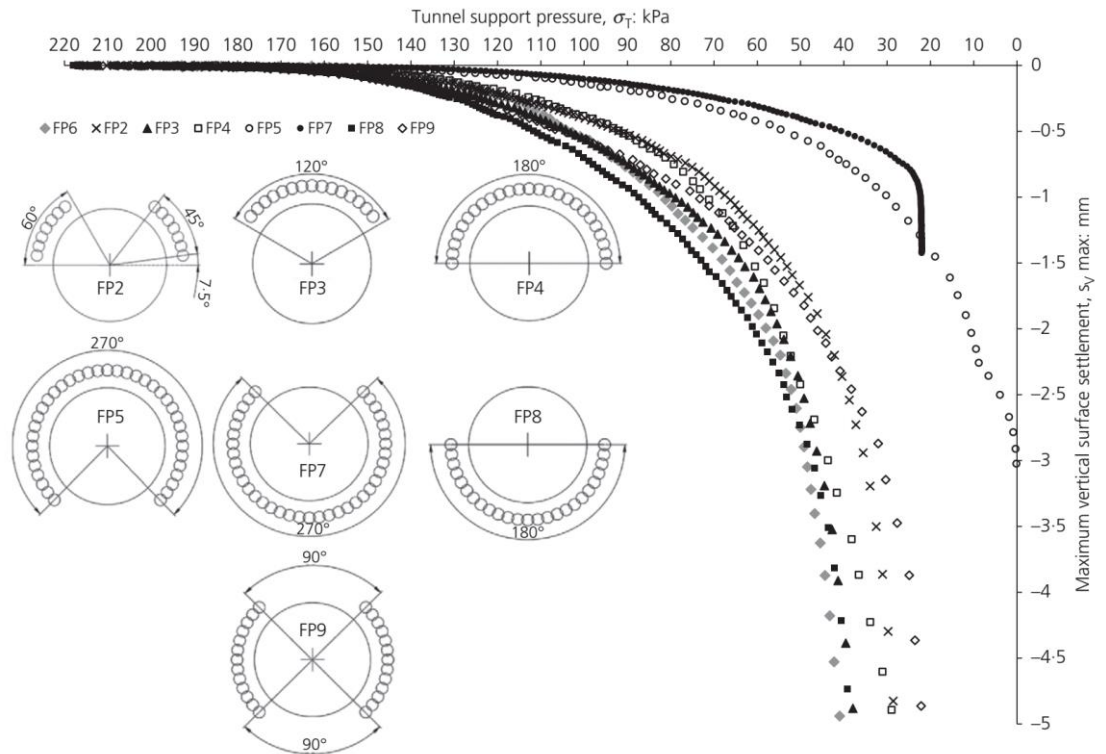


Figure 2.39: Tunnel support pressure against maximum vertical surface settlement for all forepoiling arrangements (Divall *et al.*, 2016).

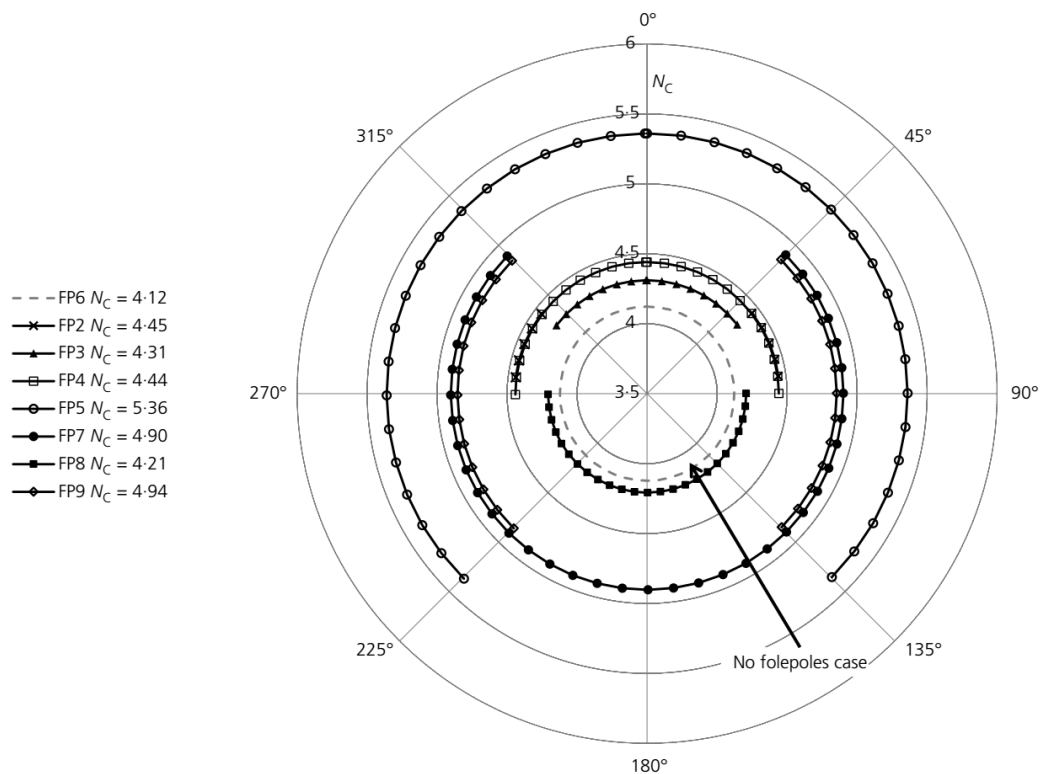


Figure 2.40: Stability ratio against forepoiling position (Divall *et al.*, 2016).

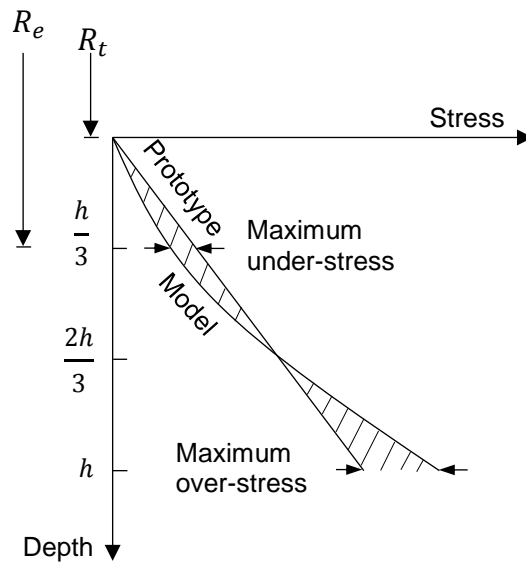


Figure 3.1: Comparison of stress variation with depth in a centrifuge model and its corresponding prototype (after Taylor, 1995).

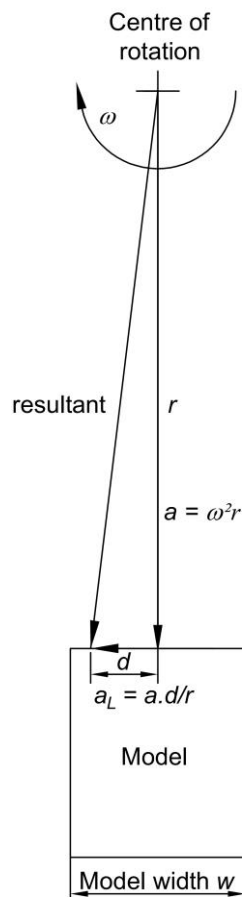


Figure 3.2: Lateral acceleration component a_L created within the model during spinning.

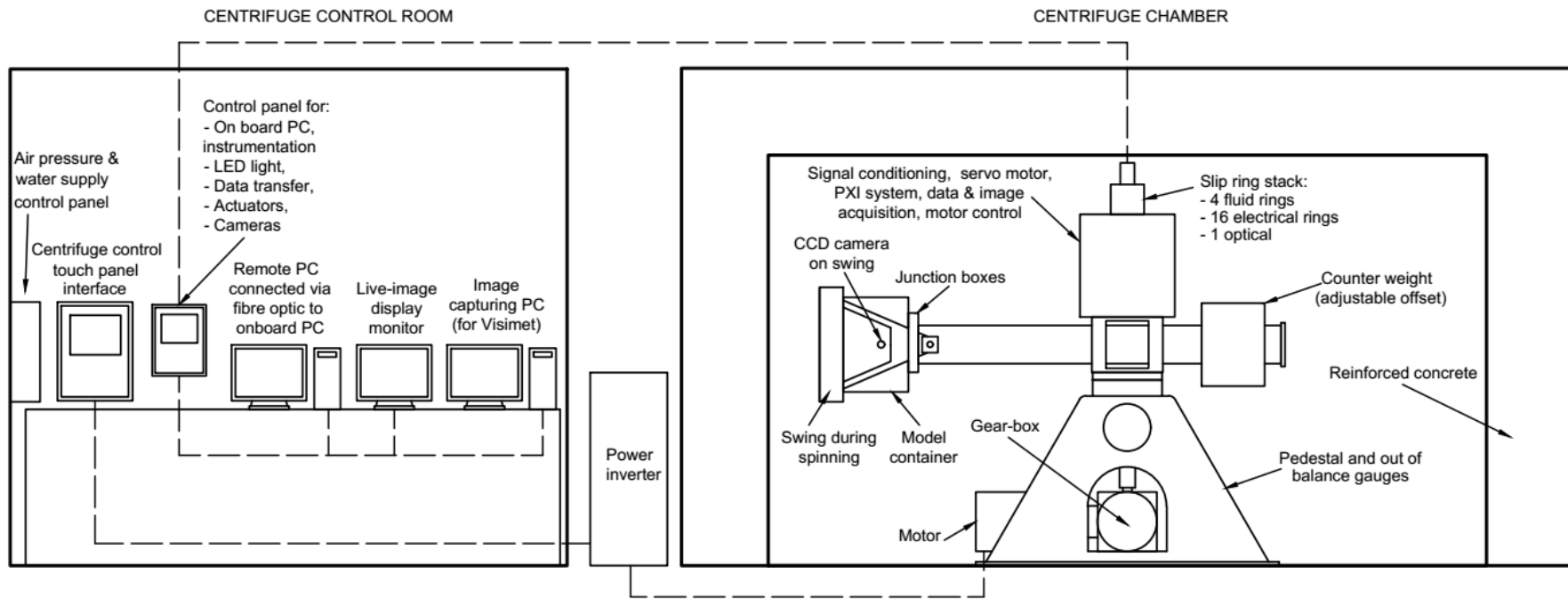


Figure 3.3: General arrangement of the Acutronic 661 at City, University of London.

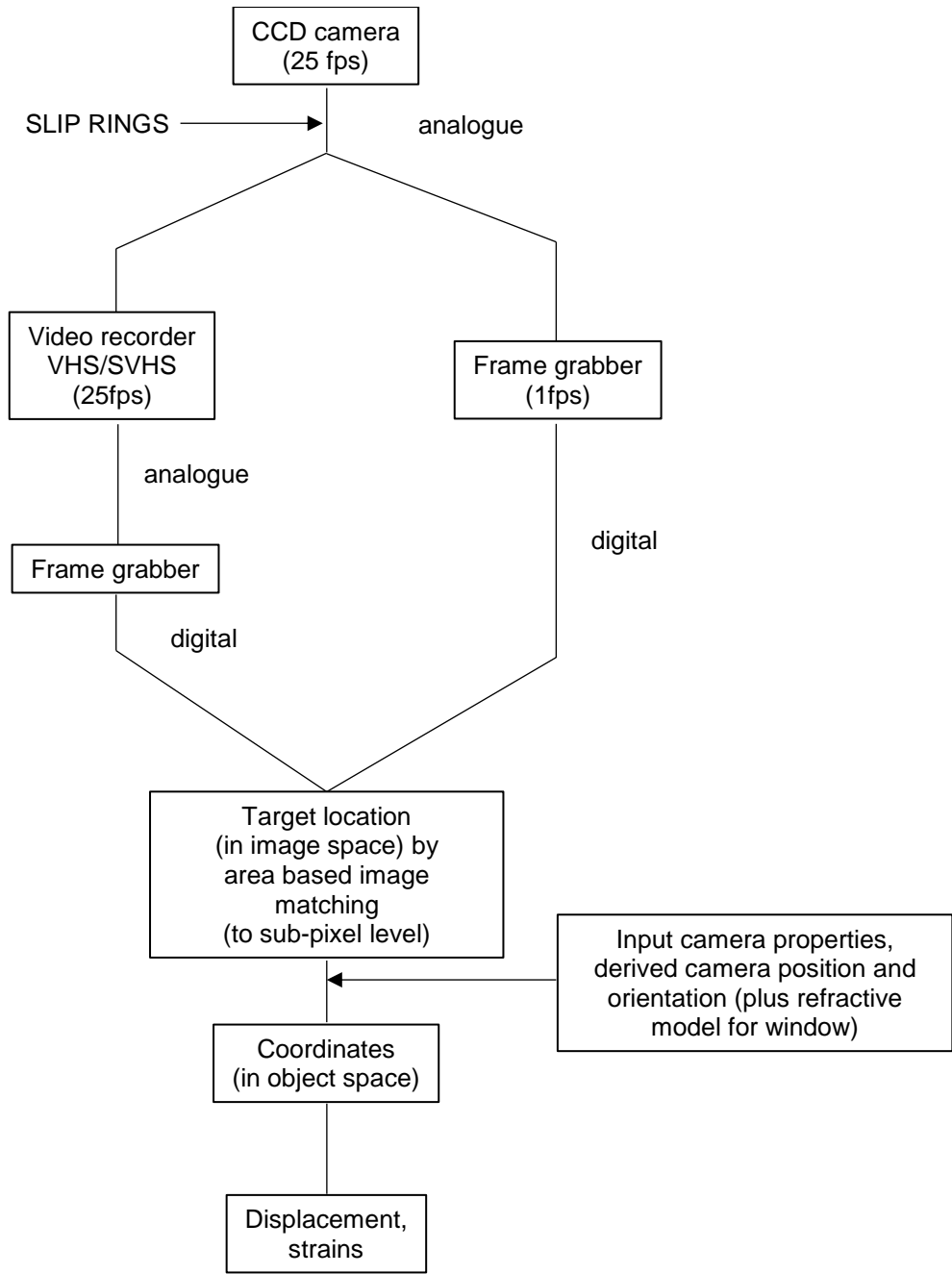


Figure 3.4: Flow chart for Visimet image processing procedure (after Grant, 1998).

PIV

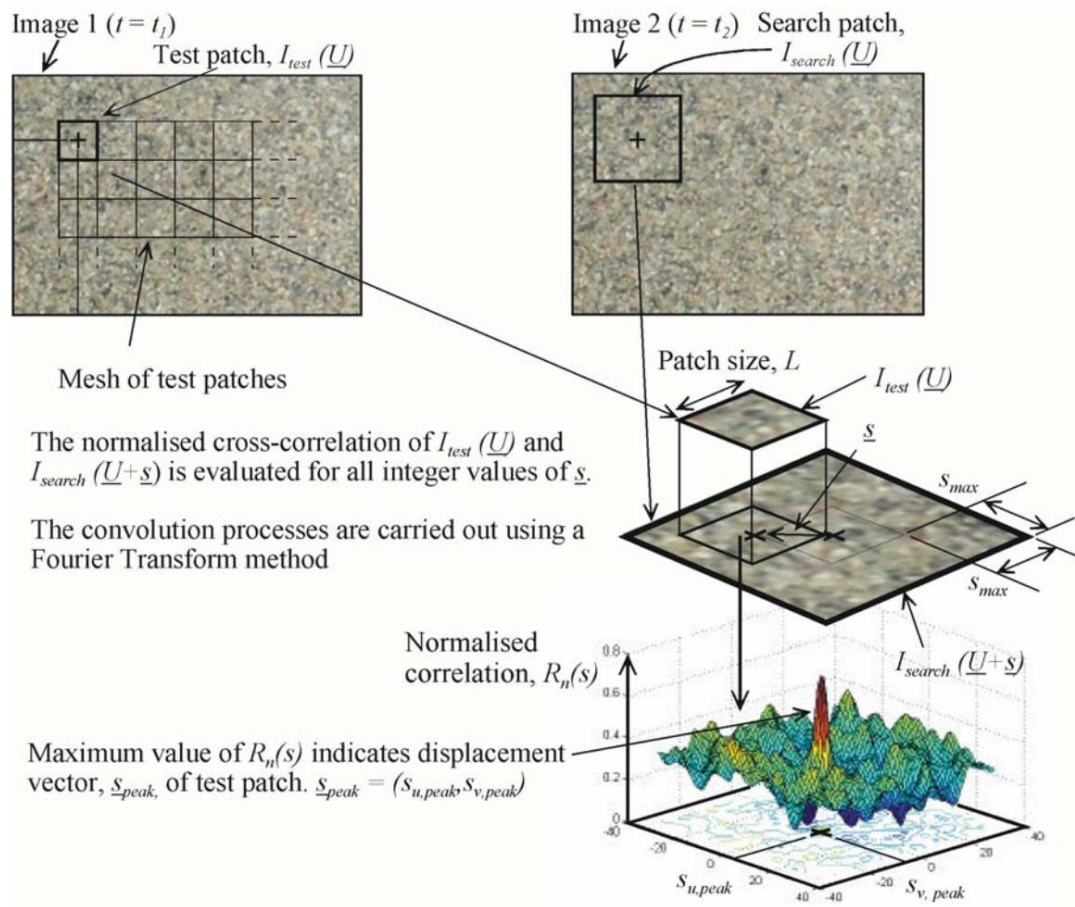


Figure 3.5: Image manipulation during PIV analysis (White, 2002).

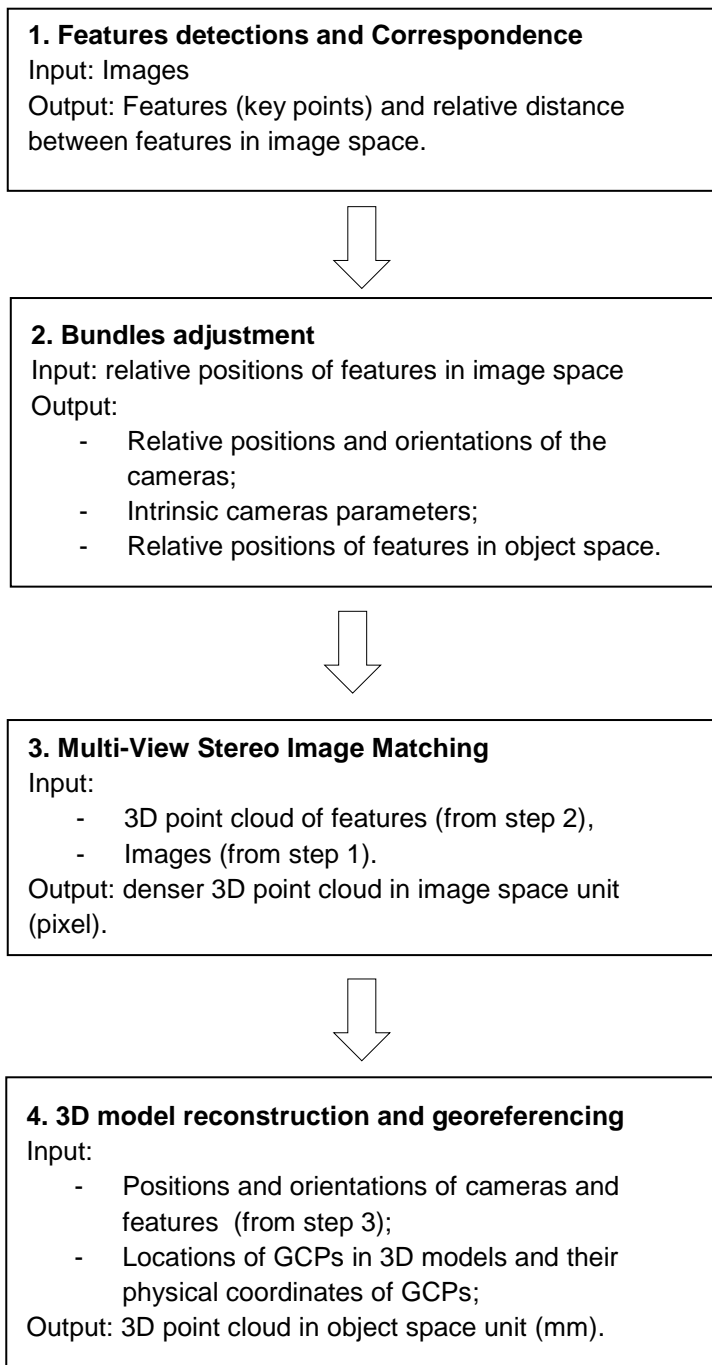


Figure 3.6: Workflow of Structure from Motion and Multi-View Stereo.

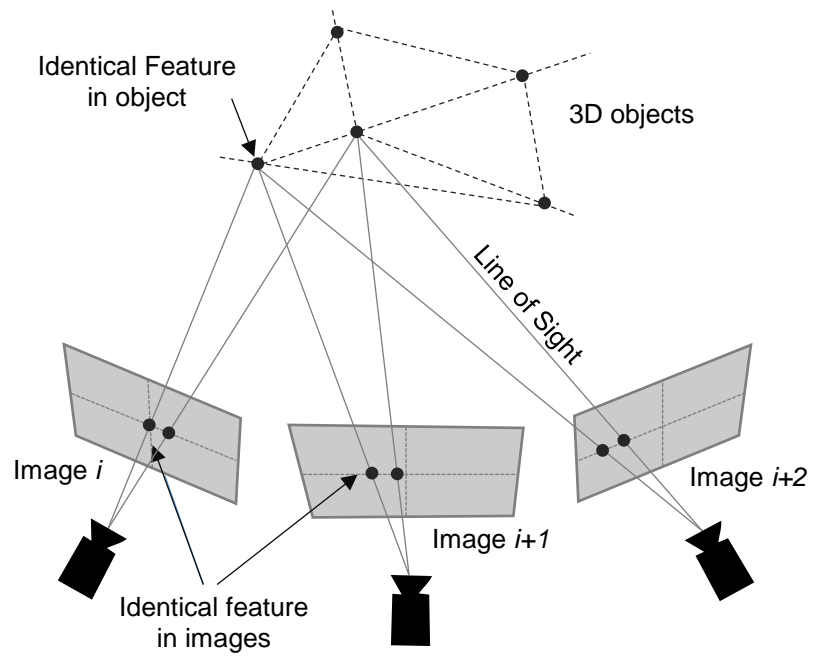


Figure 3.7: Feature detection and correspondence of SfM (after Le *et al.*, 2016).

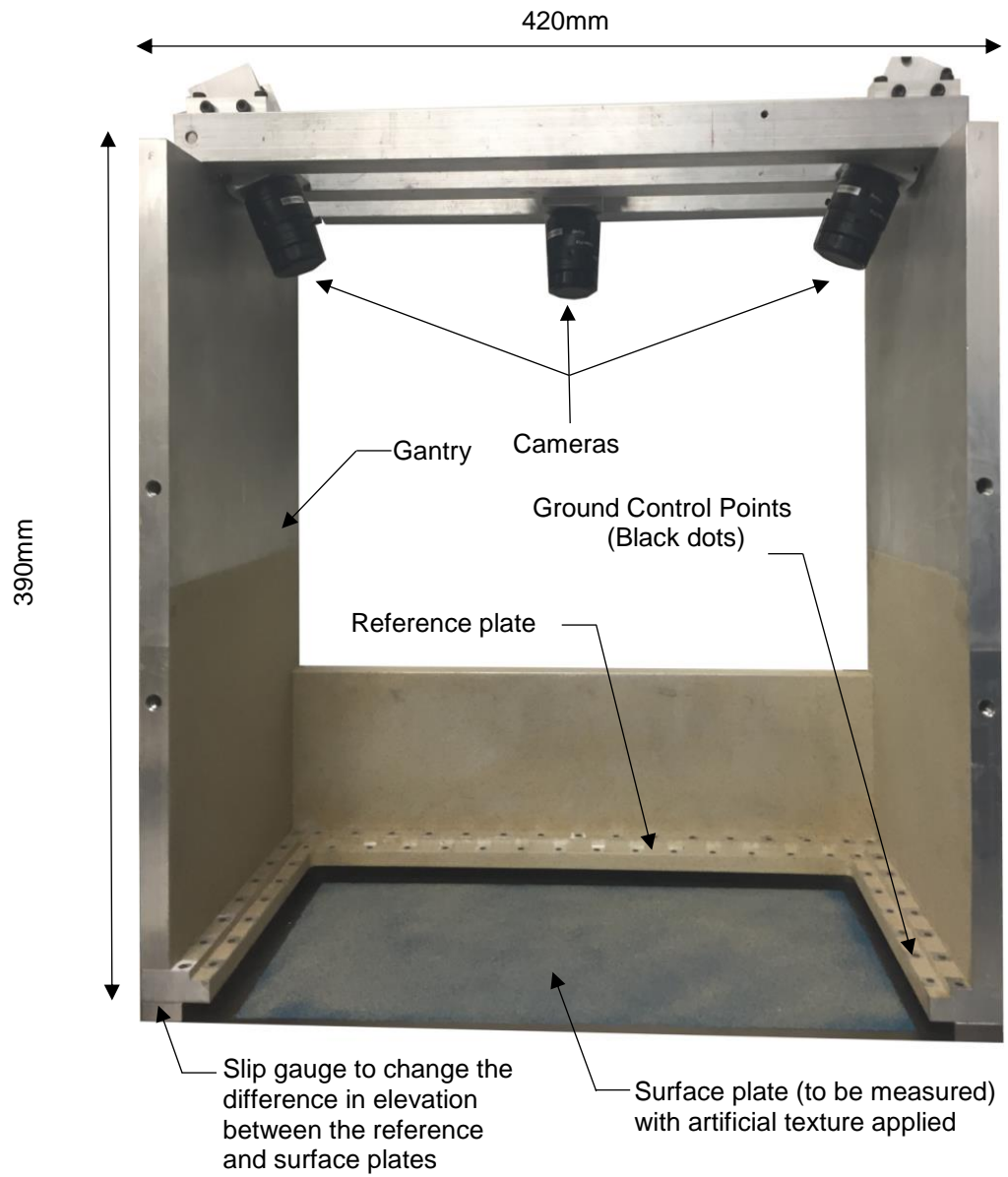


Figure 3.8: Complete 3D Imaging system apparatus (after Le *et al.*, 2016).

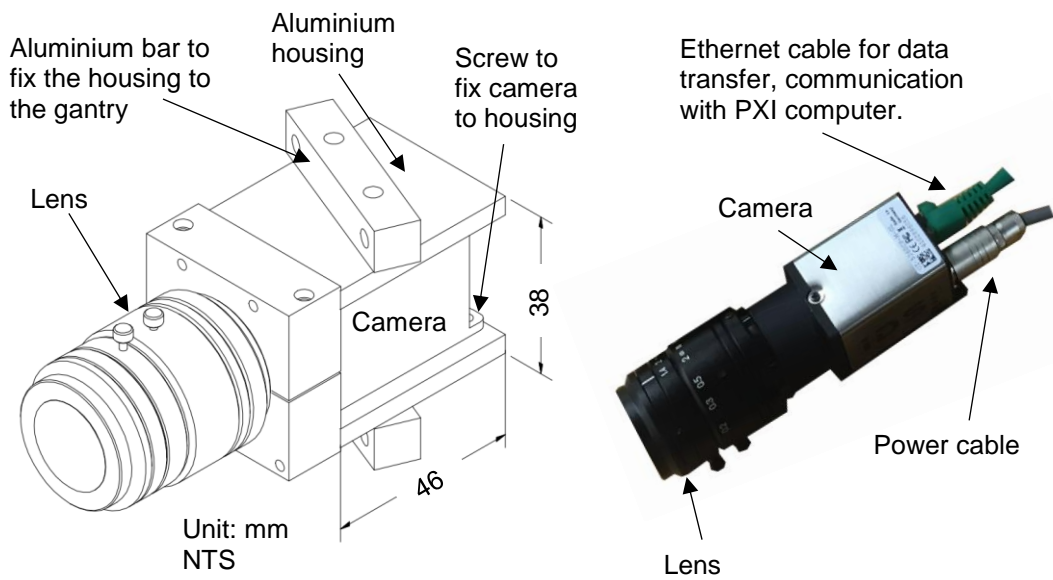


Figure 3.9: Details on camera and housing.

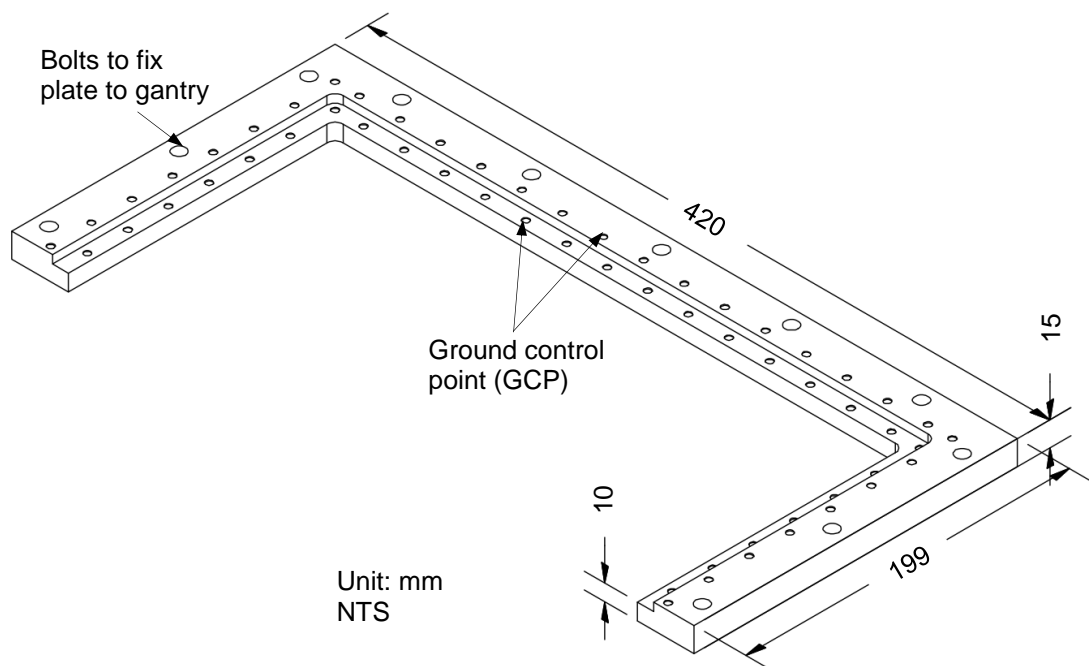


Figure 3.10: Details of reference plate.

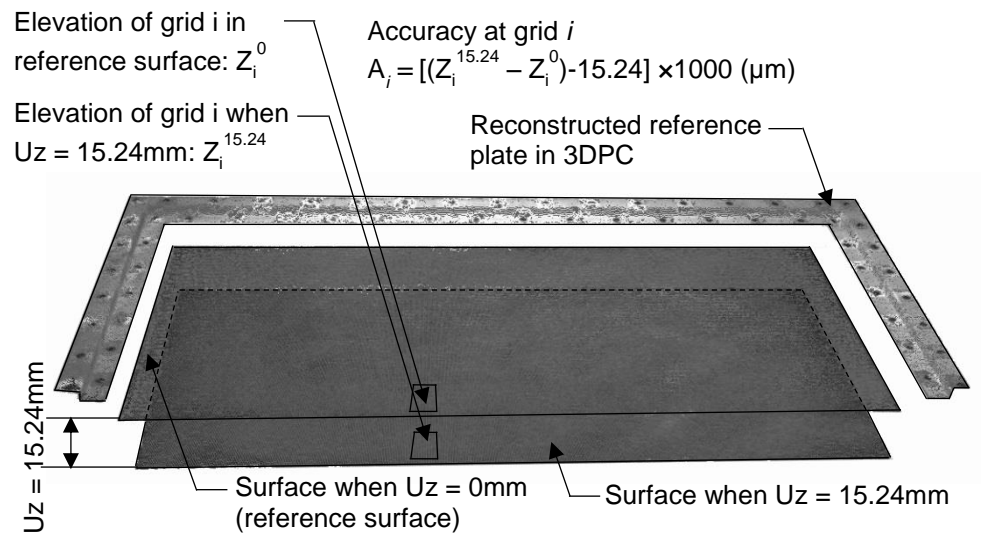
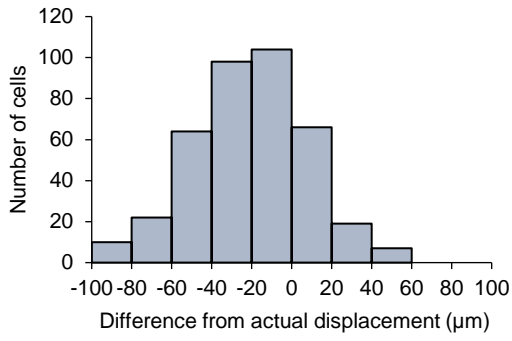
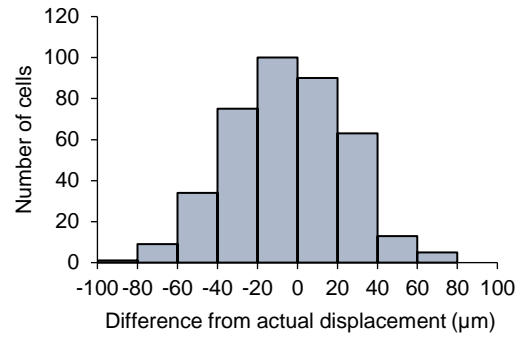


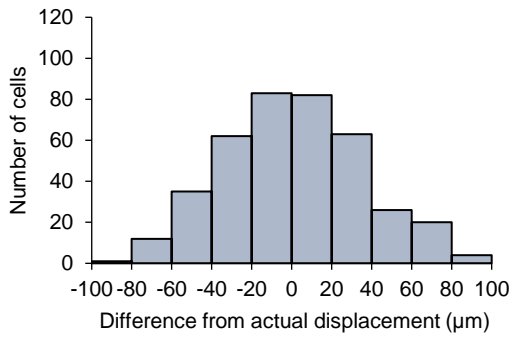
Figure 3.11: Determination of vertical displacement accuracy on reconstructed 3DPC of measured surfaces when $U_z = 0\text{mm}$ (reference surface) and $U_z = 15.24\text{mm}$ (after Le *et al.*, 2016).



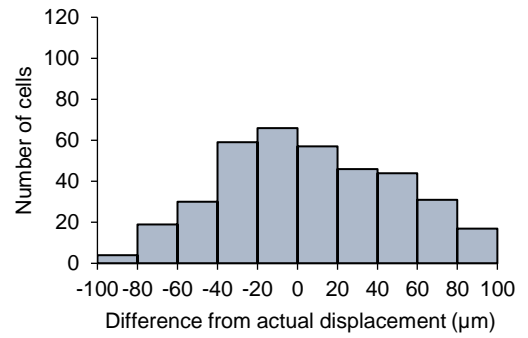
a) $U_z=2.540\text{mm}$, $SD=28\mu\text{m}$



b) $U_z=5.105\text{mm}$, $SD=28\mu\text{m}$



c) $U_z=10.160\text{mm}$, $SD=32\mu\text{m}$



d) $U_z=15.240\text{mm}$, $SD=48\mu\text{m}$

Figure 3.12: Accuracy histograms in four elevation increments. The total number of cells is 390 (after Le *et al.*, 2016).

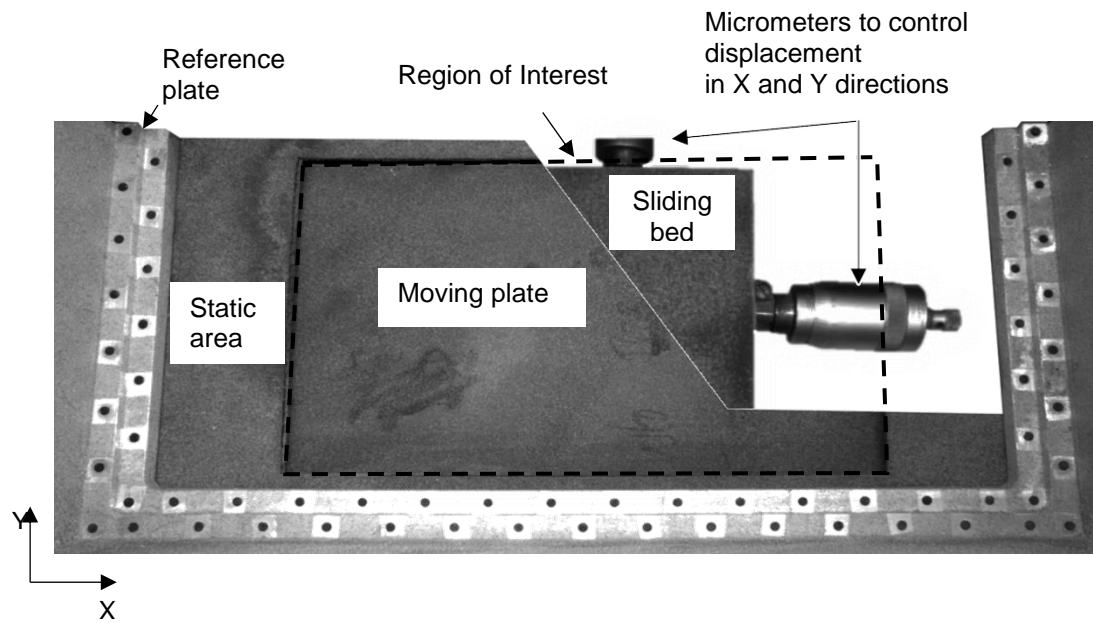


Figure 3.13: Experiment set up to quantify horizontal displacement measurement accuracy (after Le *et al.*, 2016).

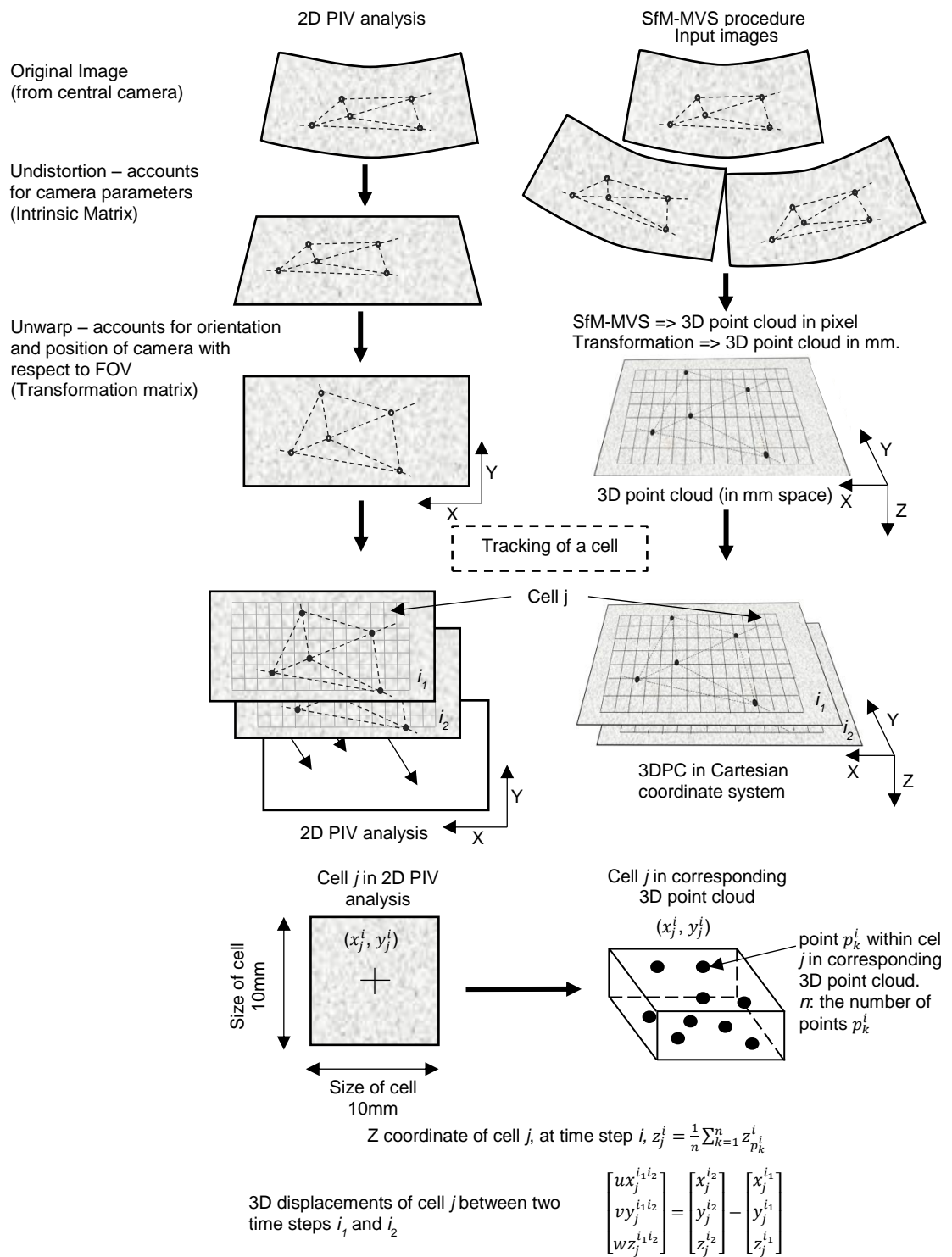
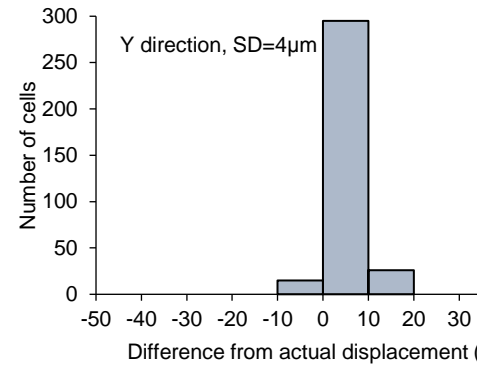
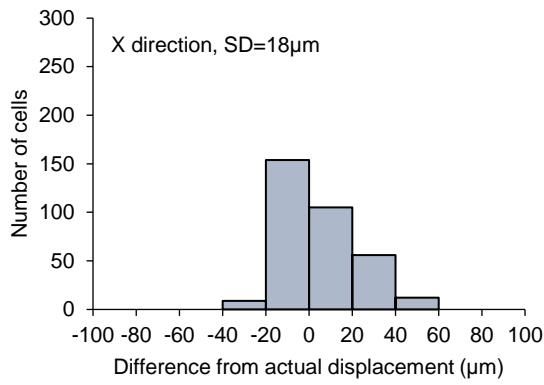
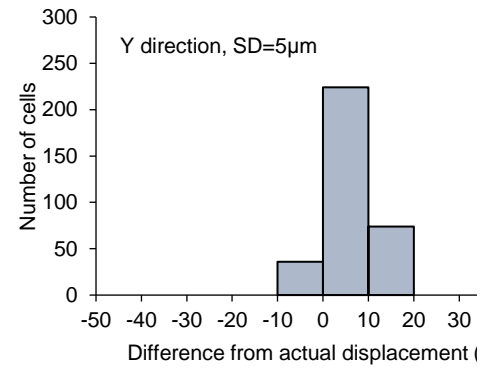
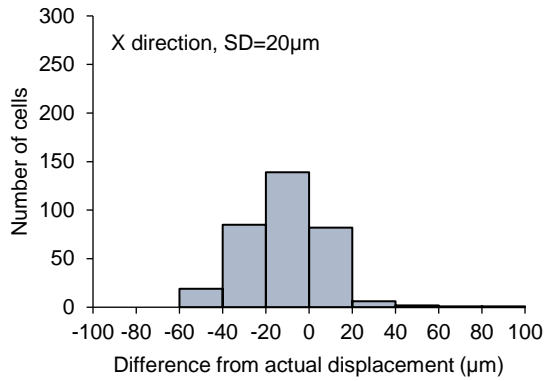


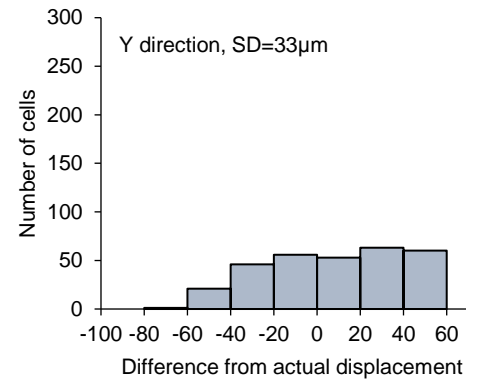
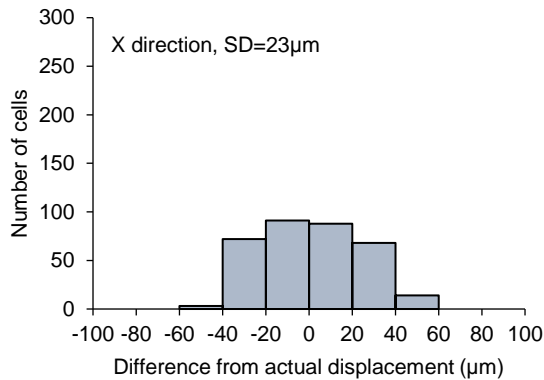
Figure 3.14: Schematic of horizontal tracking procedure.



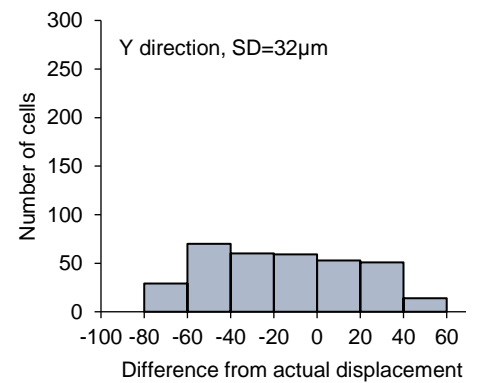
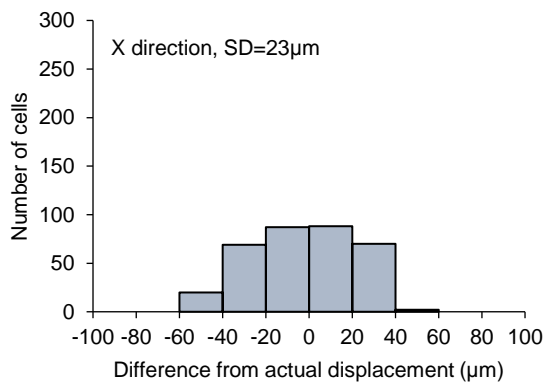
a) Increment 1: $U_x=1\text{mm}$, $U_y=0\text{mm}$



b) Increment 2: $U_x=2\text{mm}$, $U_y=0\text{mm}$



c) Increment 3: $U_x=2\text{mm}$, $U_y=1\text{mm}$



d) Increment 4: $U_x=2\text{mm}$, $U_y=2\text{mm}$

Figure 3.15: Accuracy histograms in four horizontal displacements. The total number of cells is 336. (after Le *et al.*, 2016).

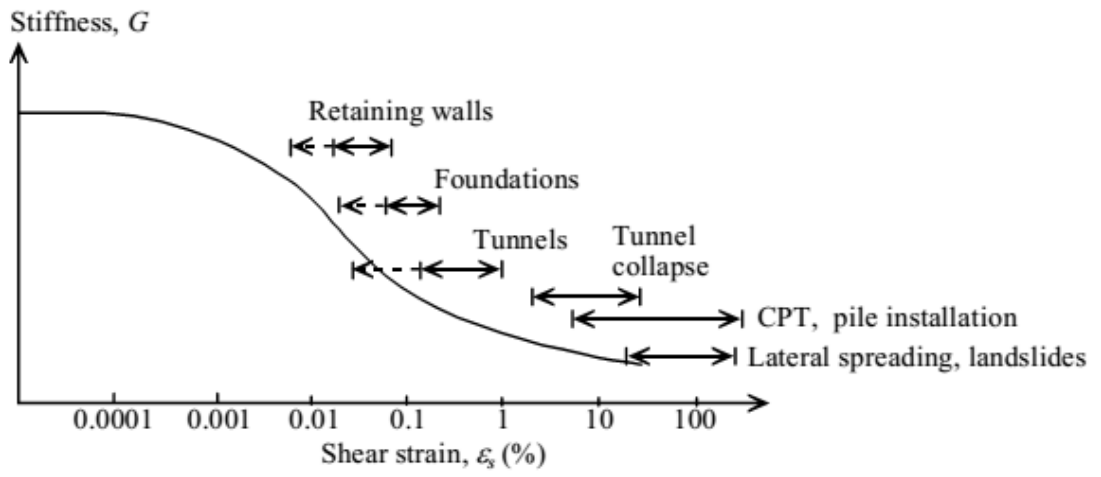


Figure 3.16: Typical strain levels for reliable measurement in geotechnical events (after Mair, 1993).

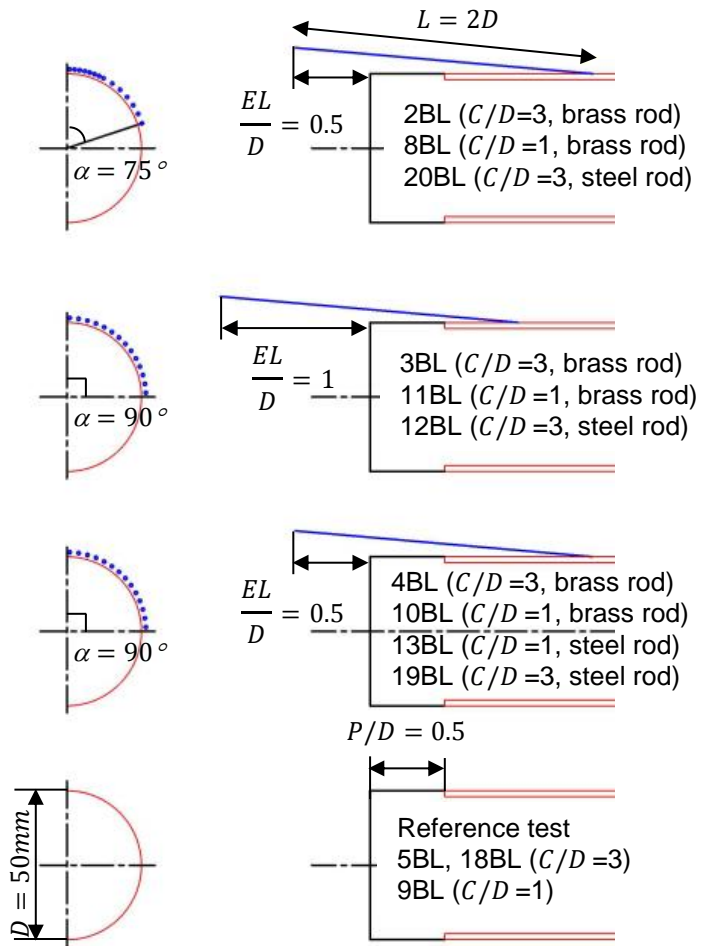


Figure 4.1: Schematic of Forepoling Umbrella System arrangements.

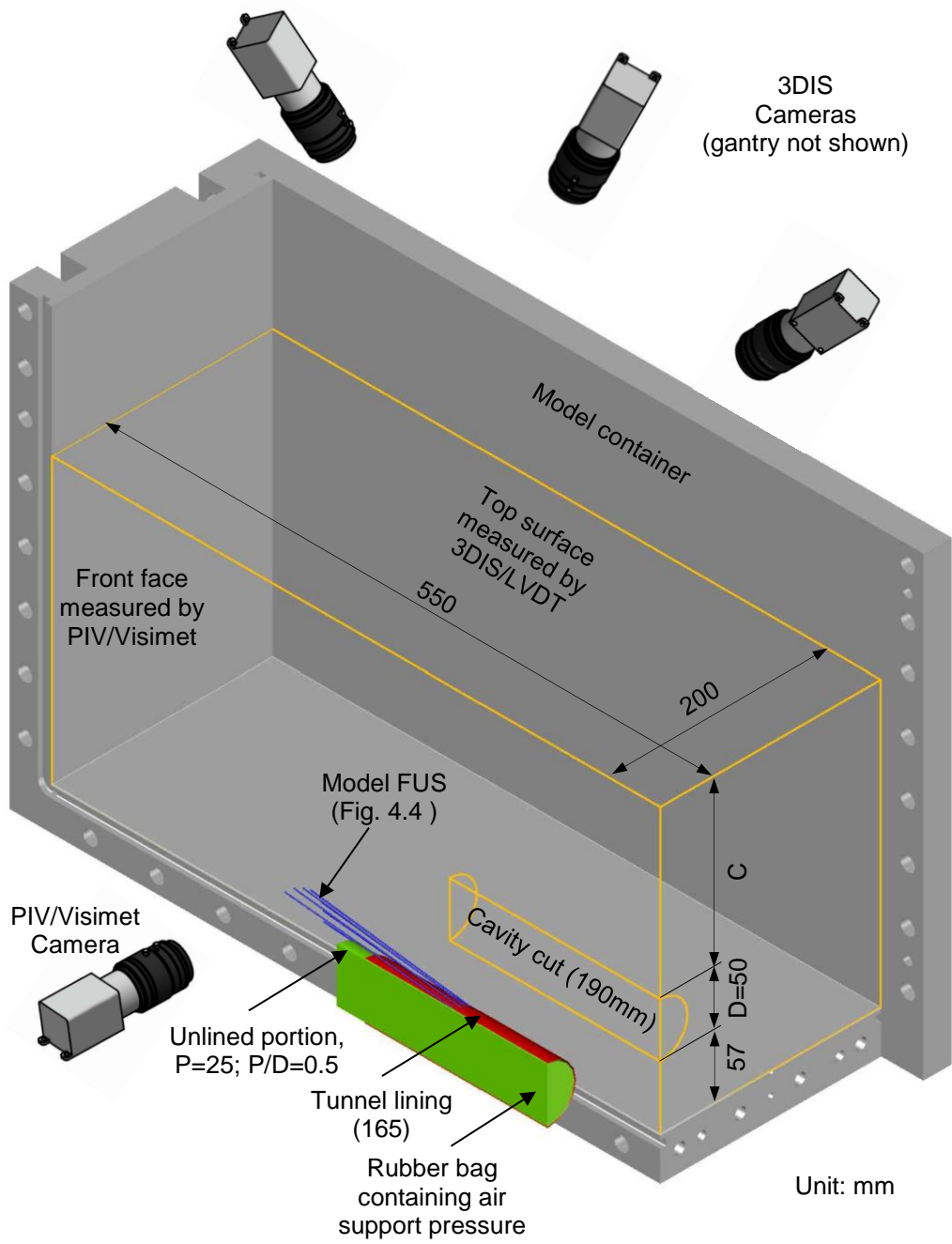
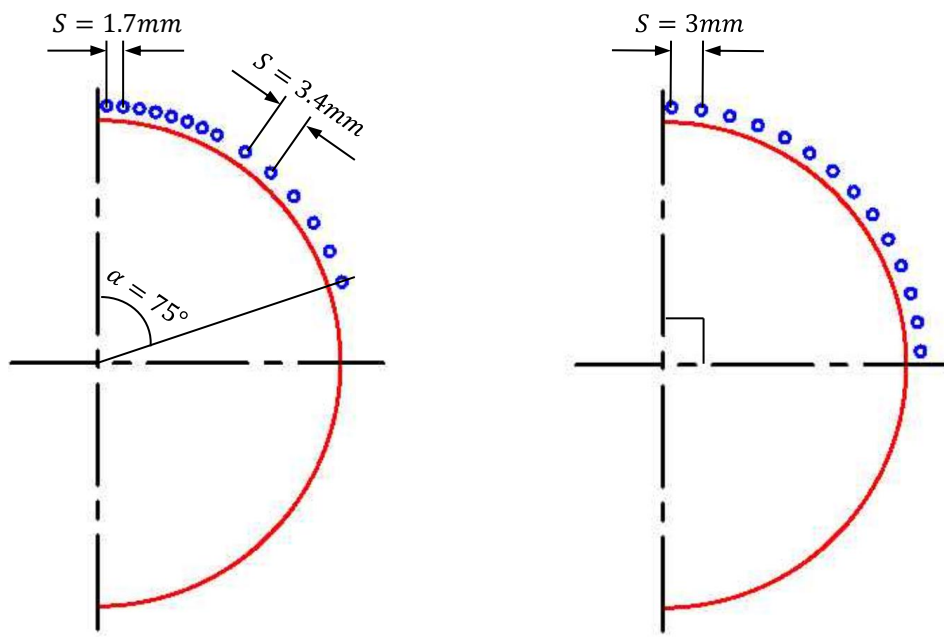


Figure 4.2: The complete model apparatus illustration.



a) Spacing S for $\alpha = 75^\circ$

b) Spacing S for $\alpha = 90^\circ$

Figure 4.3: Spacing S of the model forepoles.

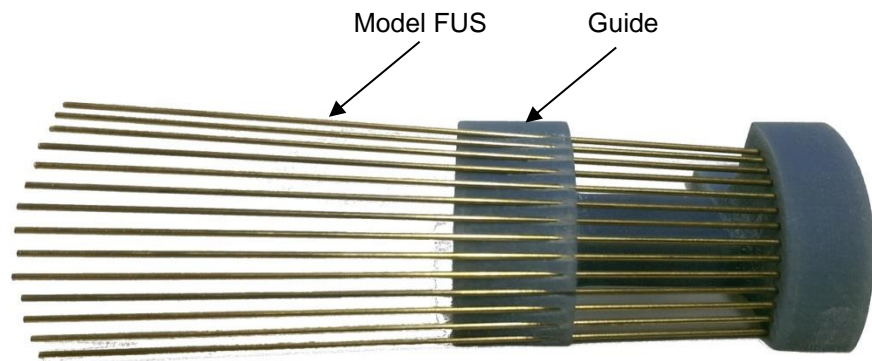
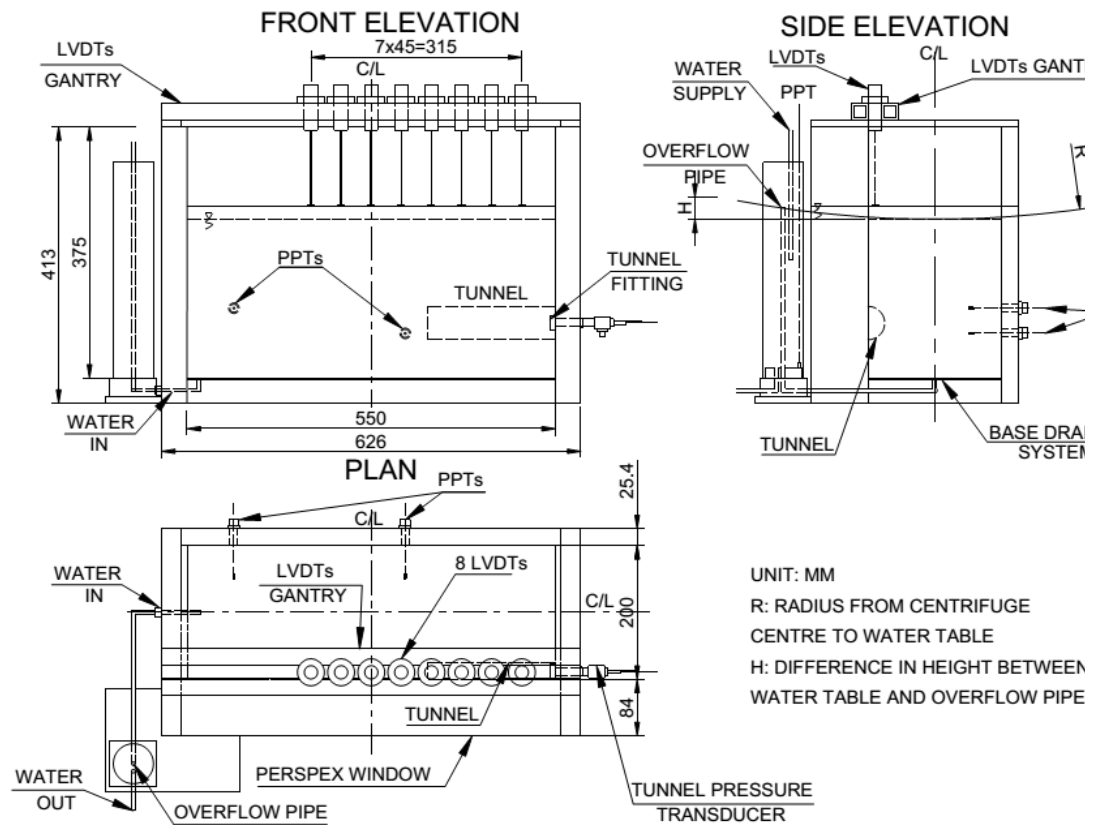


Figure 4.4: Guide produced by high-resolution 3D printer for precise installation of rods.



Unit: mm.

Figure 4.5: Locations and fixing details of instrumentation.

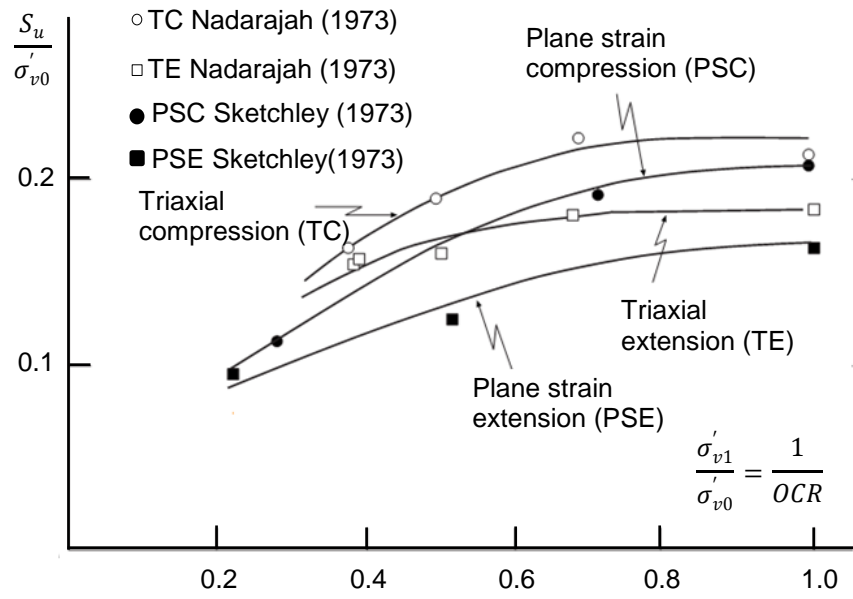


Figure 4.6: Relationship of the undrained shear strength with OCR and consolidation pressure (after Mair, 1979).

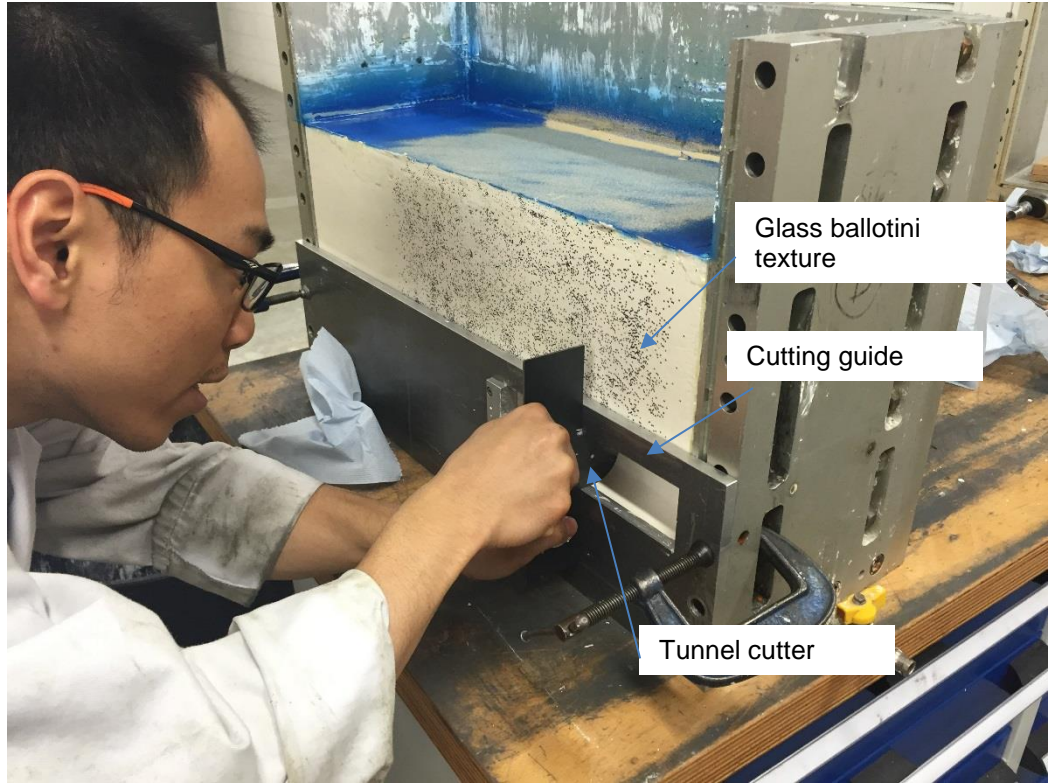


Figure 4.7: Create semi-circular tunnel cavity.

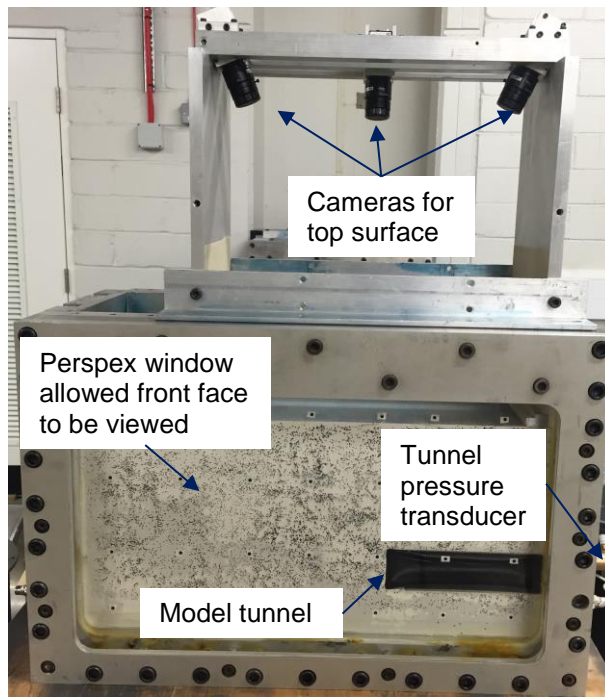


Figure 4.8: Model ready to load on to the centrifuge swing.

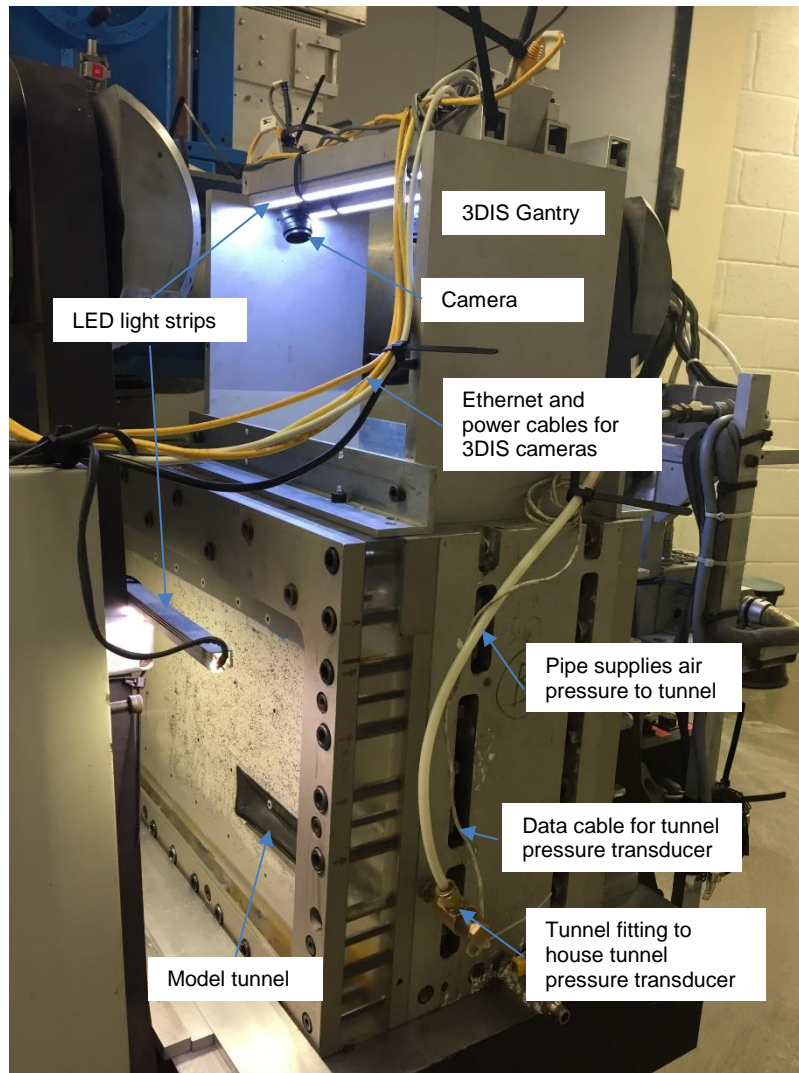


Figure 4.9: Model on swing before spin-up.

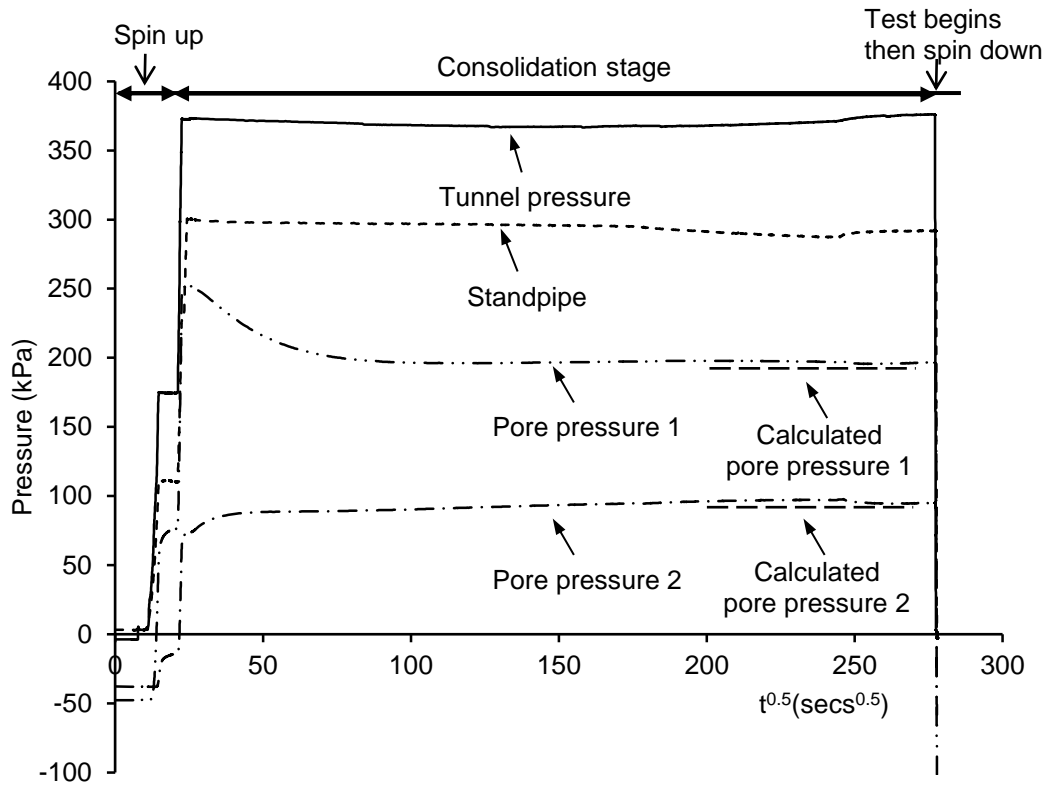


Figure 4.10: Pressure transducers responses from spin up to spin down in test 5BL.

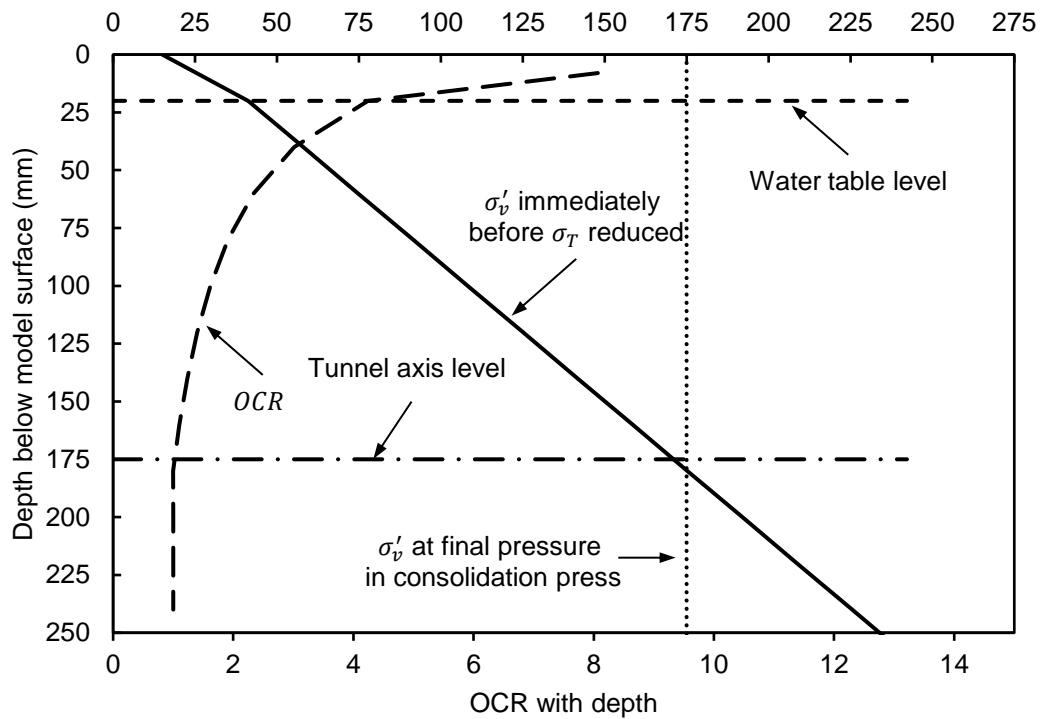
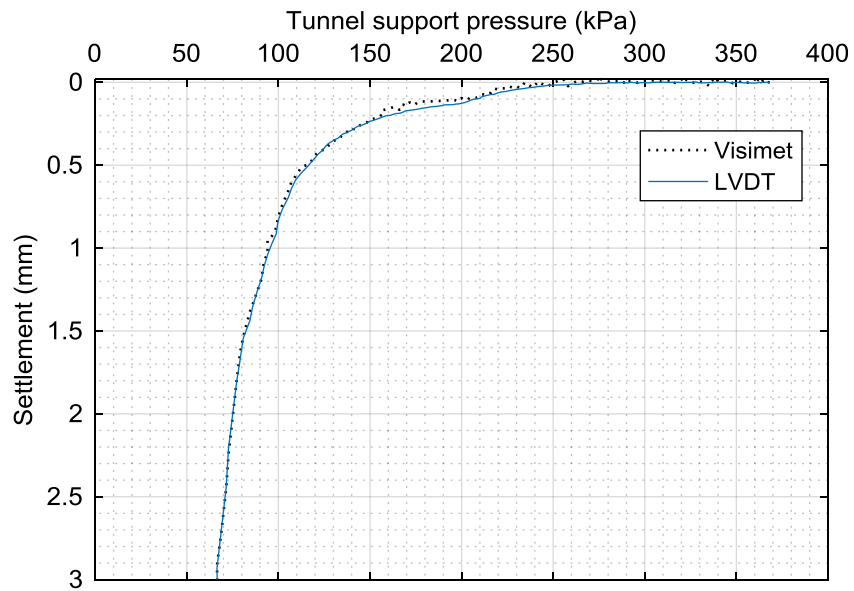
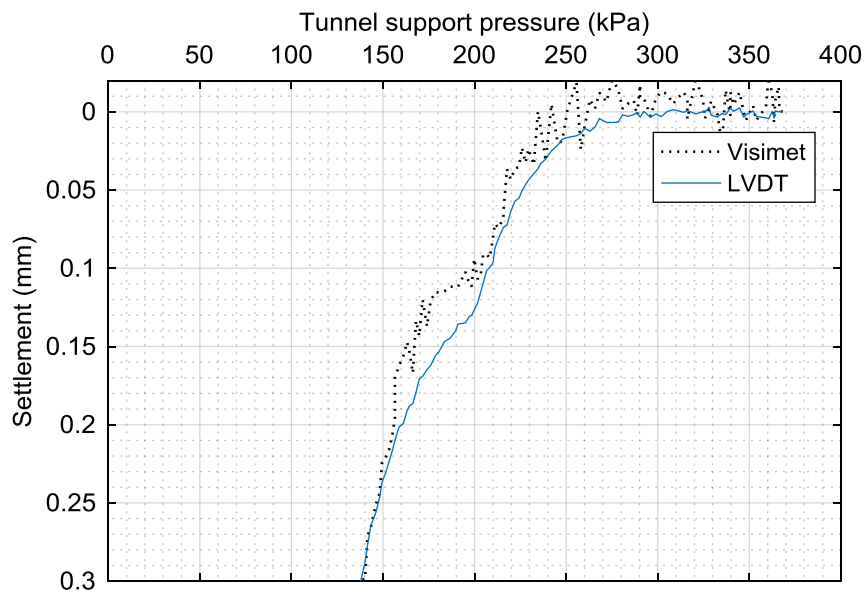


Figure 4.11: Stress history of model clay in $C/D=3$ tests.



a) Test data.



b) Settlement at early stages of test.

Figure 5.1: Comparison on the measurements on surface settlement made by LVDT and Visimet (Test 5BL).

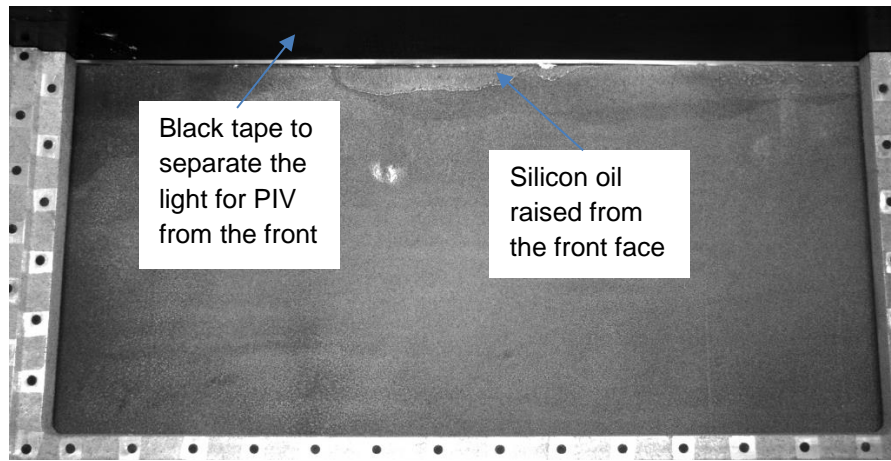


Figure 5.2: Top surface of the model captured by the middle camera during the test.

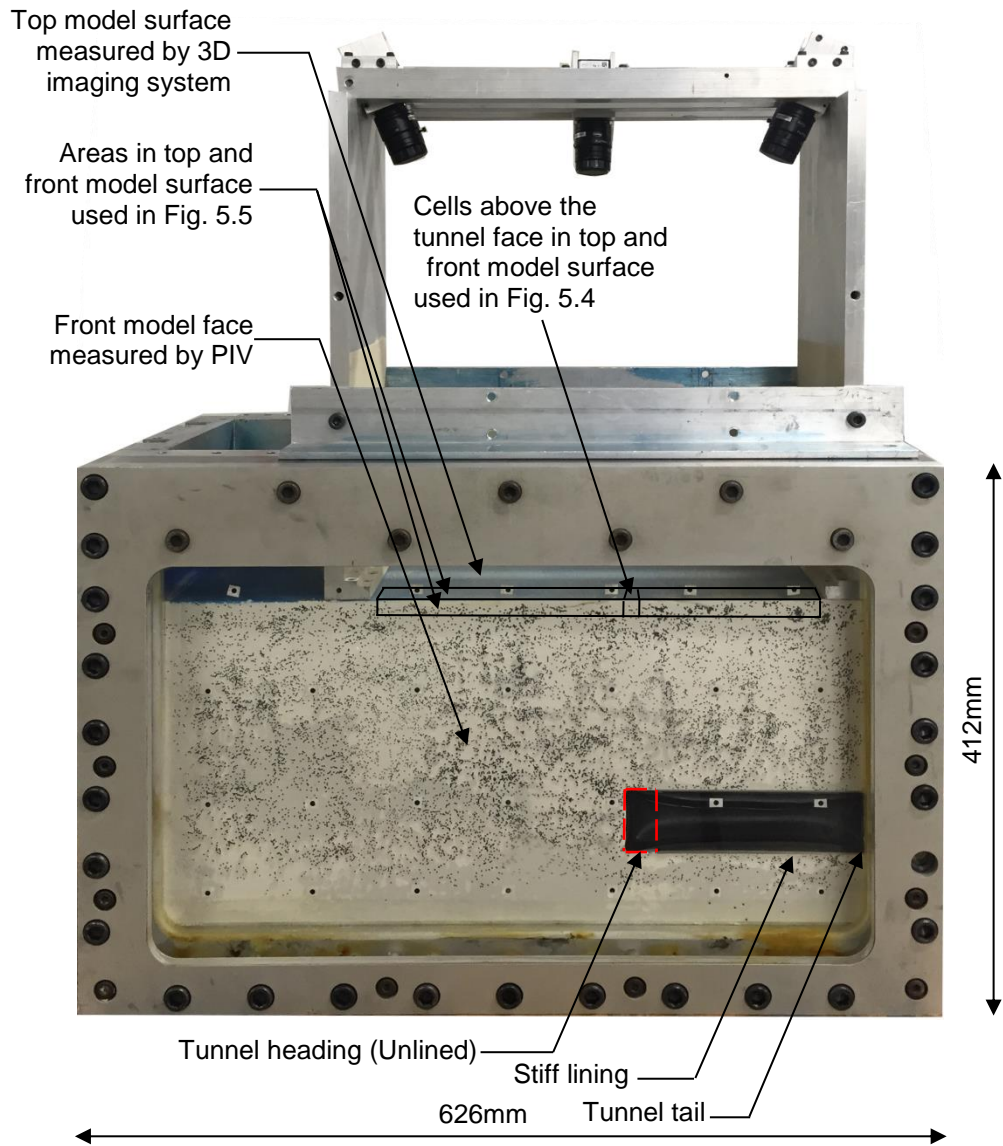
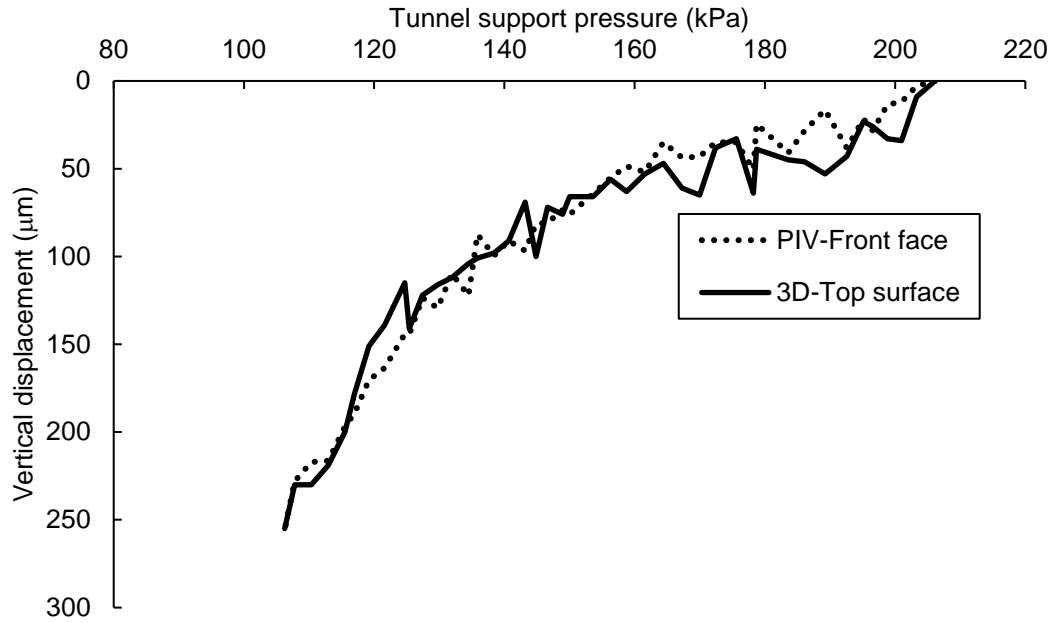
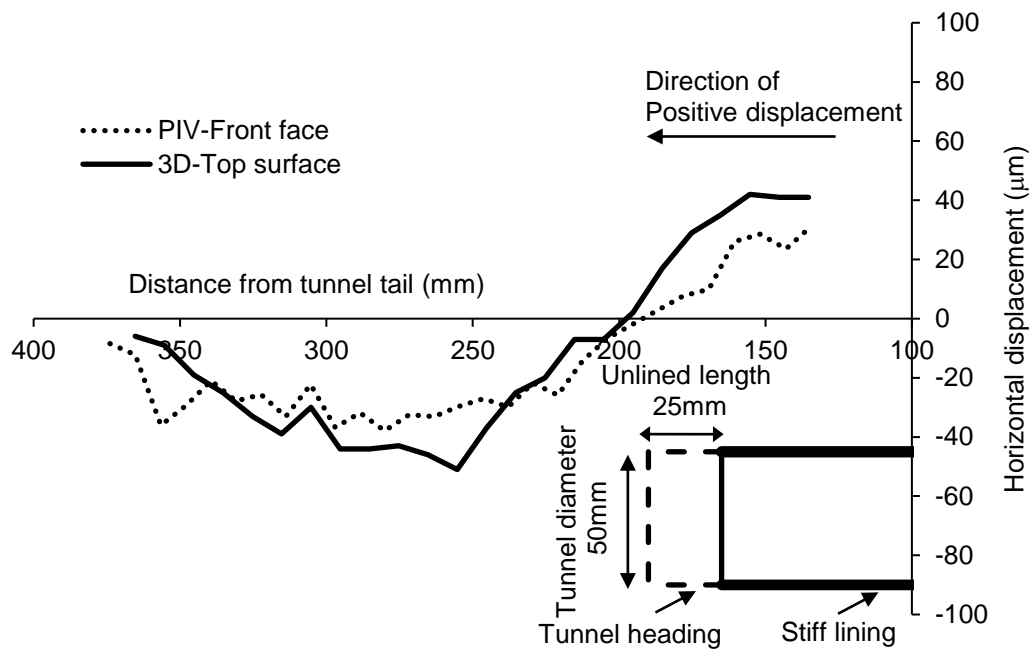


Figure 5.3: Three-dimensional centrifuge model simulating tunnel construction.



(The measured locations are depicted in **Figure 5.3**).

Figure 5.4: Comparison of the vertical surface settlement above the tunnel face measured by 3D imaging system and 2D PIV.



(The measured areas are depicted in **Figure 5.3**).

Figure 5.5: Comparison of horizontal displacements measured by 3D imaging system and 2D PIV when σ_T reduced from 206 to 106kPa.

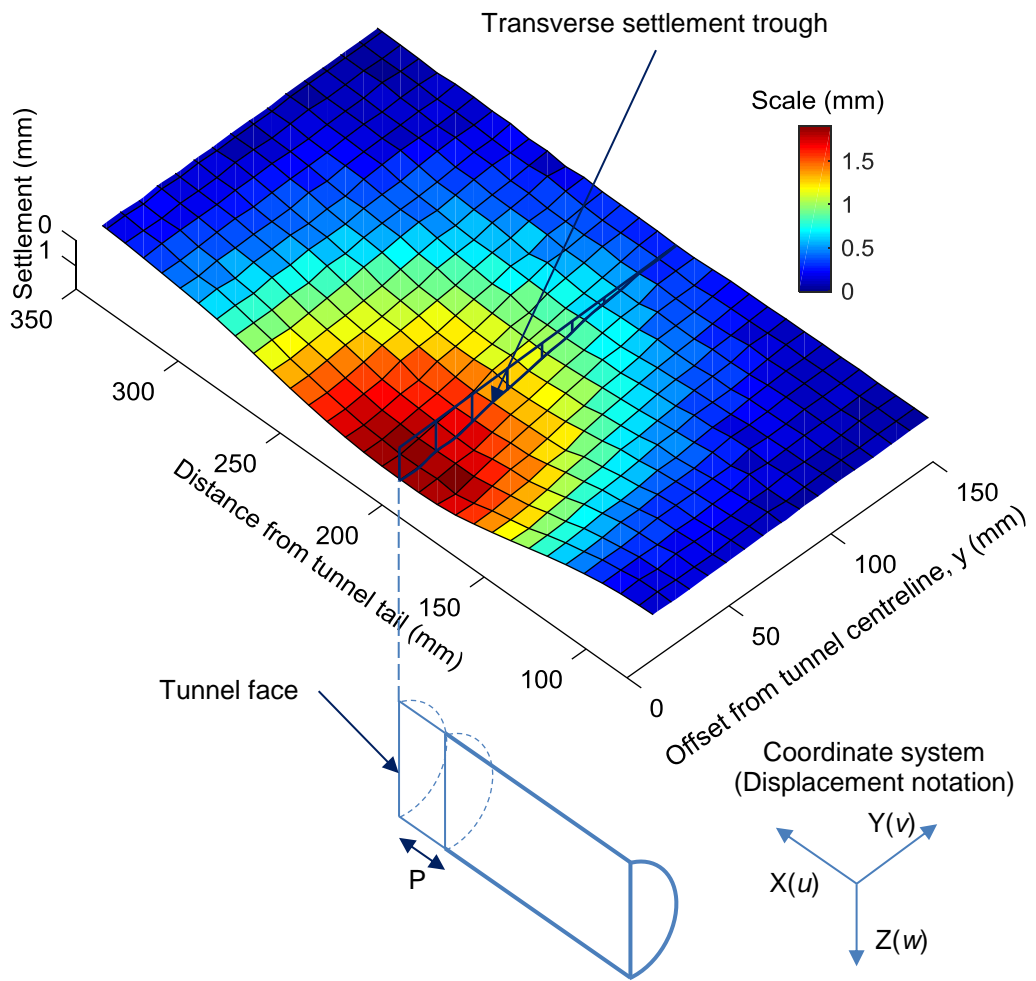
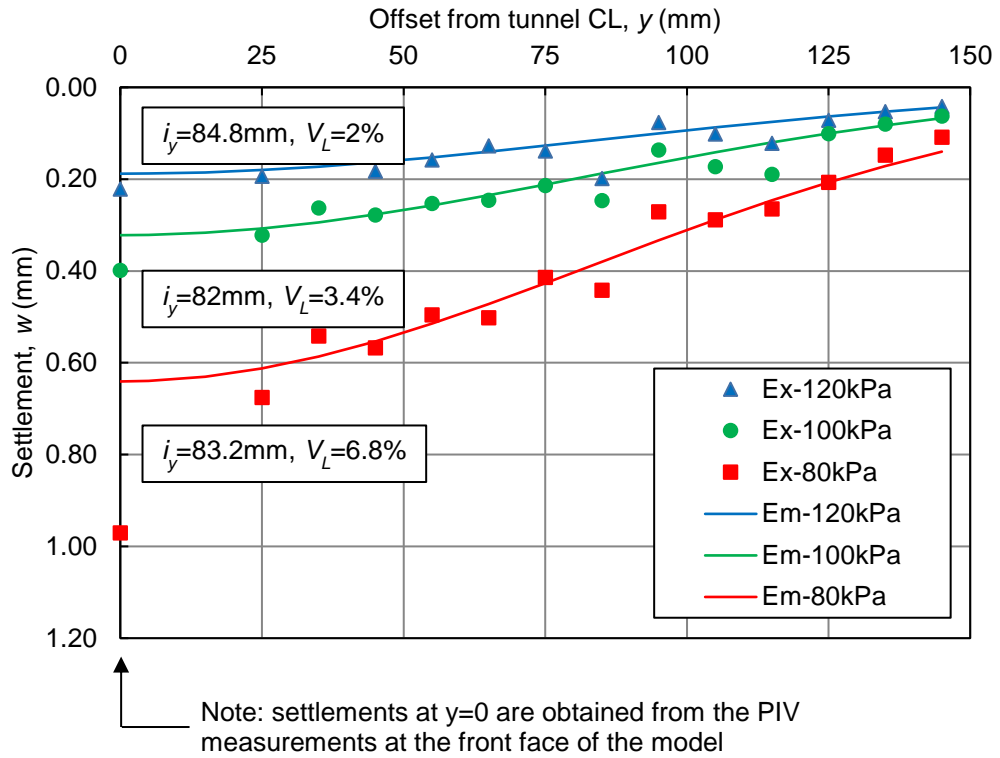


Figure 5.6: A typical 3D Settlement trough in test 18BL ($\sigma_T=60\text{kPa}$).



Ex: Experimental data; Em: Empirical Gaussian curve.

Figure 5.7: Transverse surface settlement profile above tunnel face in test 18BL.

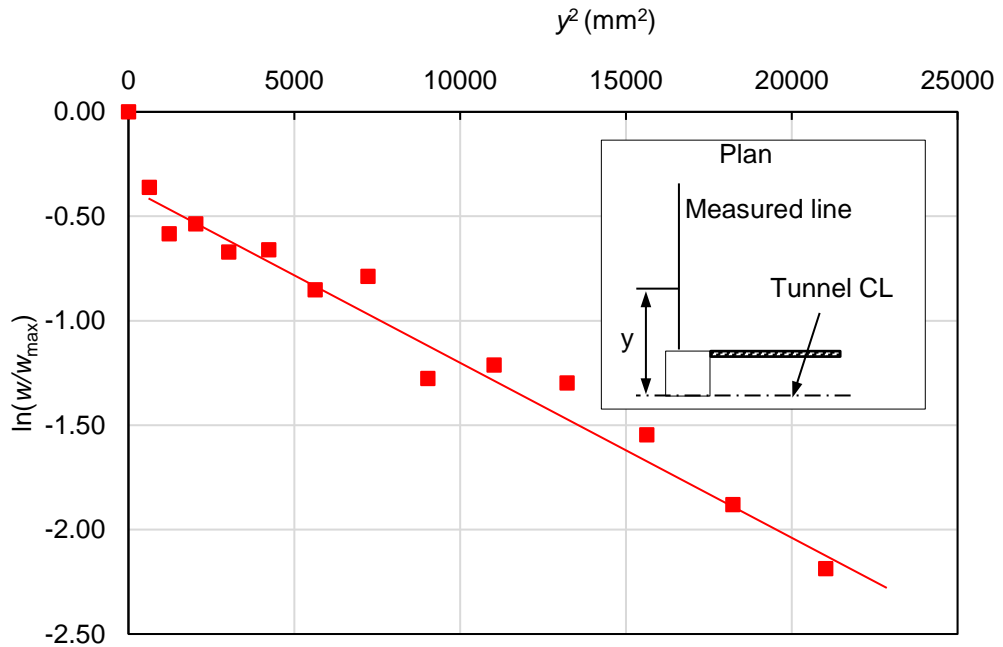


Figure 5.8: The fitting of the measured settlement trough with Gaussian curve ($\sigma_T = 80\text{kPa}$).

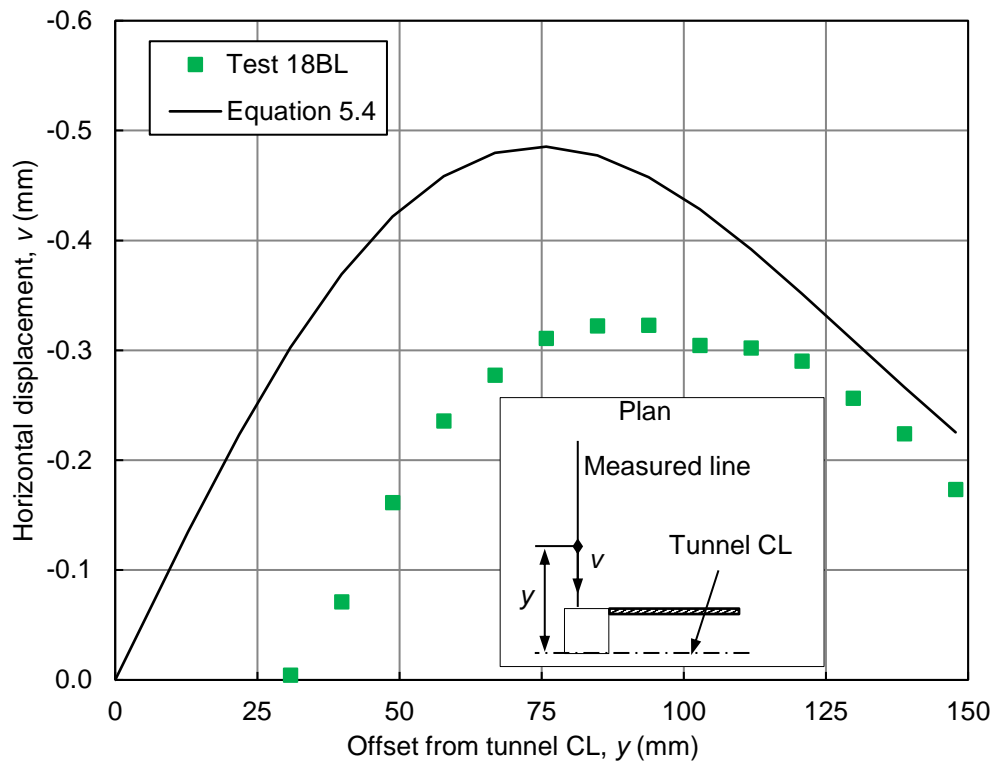


Figure 5.9: Horizontal displacement at the surface in test 18BL when σ_T reduced to 60kPa.

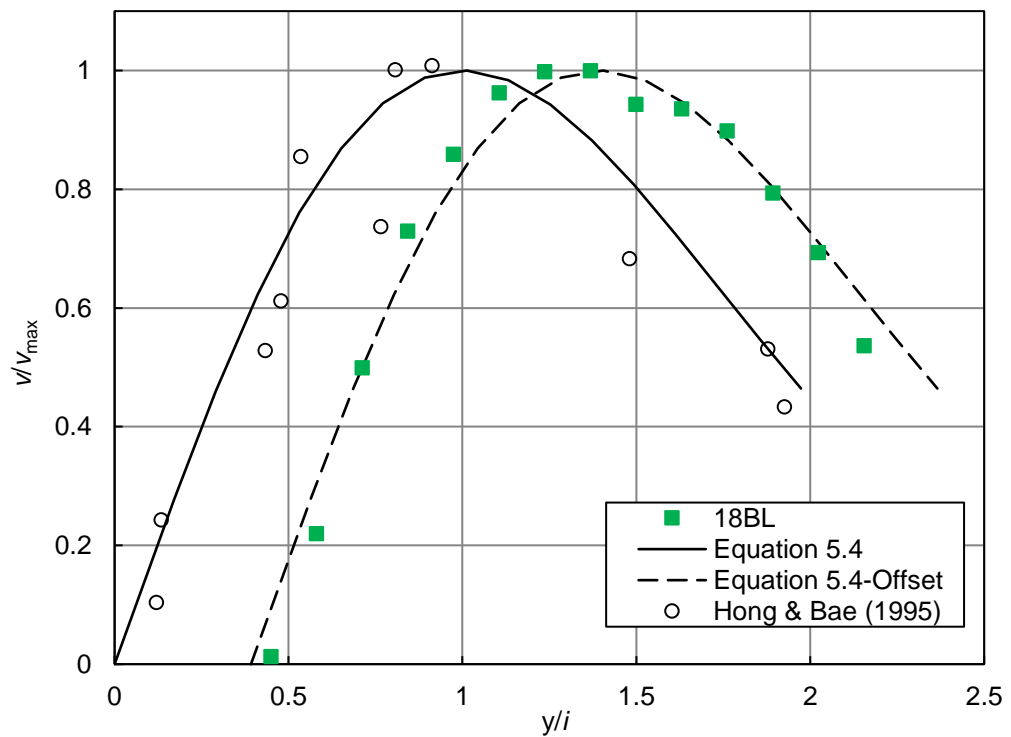


Figure 5.10: Trend of horizontal soil displacement.

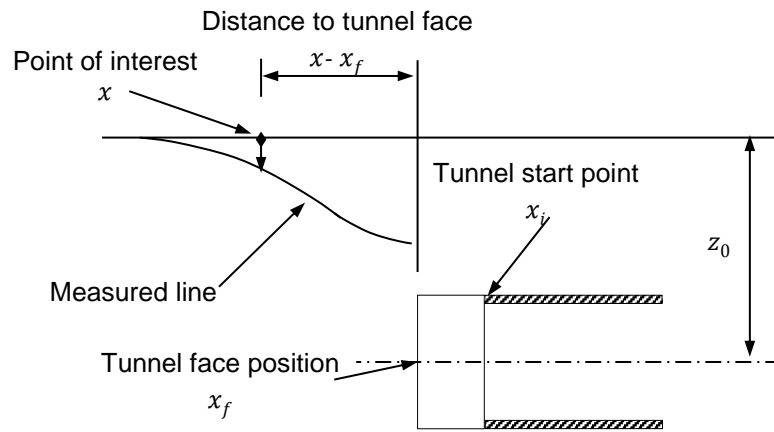


Figure 5.11: Illustration of parameters in **Equation 5.5**.

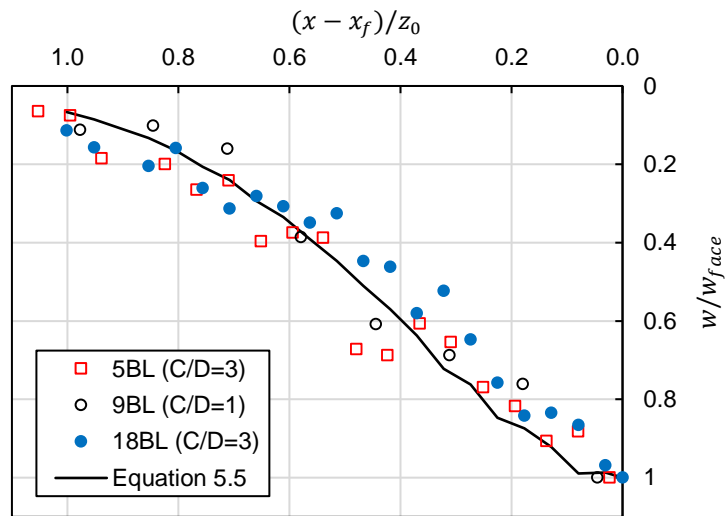
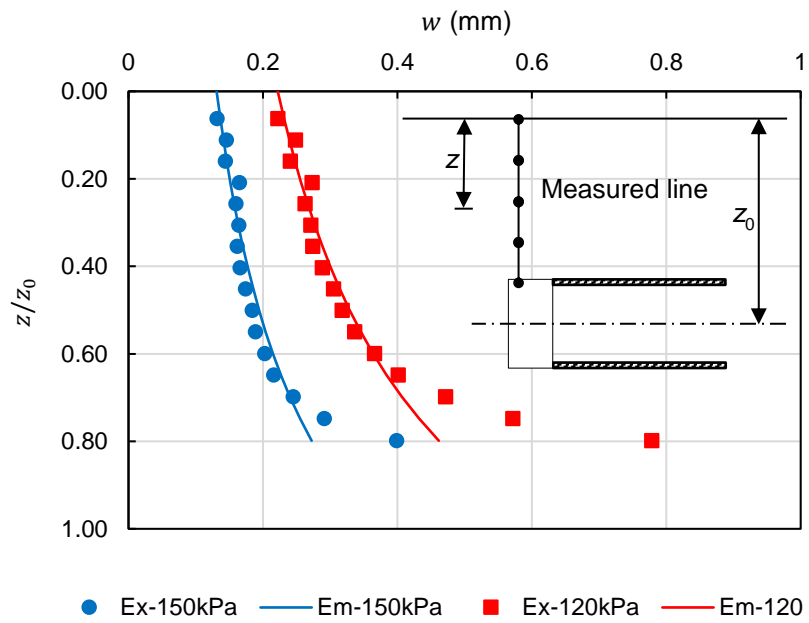


Figure 5.12: The trend of longitudinal settlement above tunnel centreline in reference tests.



Ex: experimental data; Em: empirical data.

Figure 5.13: Subsurface settlement with depth in test 18BL at $\sigma_T=150\text{kPa}$ and 120kPa.

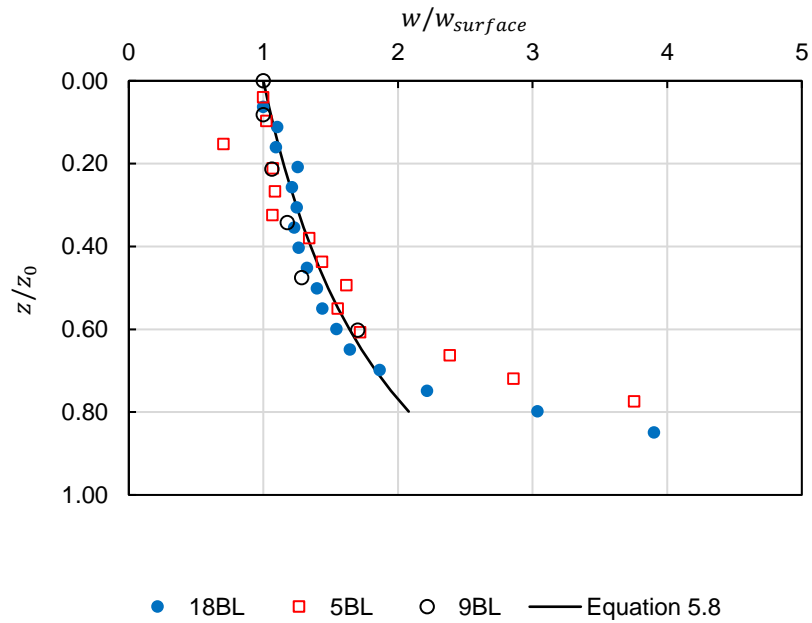


Figure 5.14: Typical profiles of subsurface settlement with depth in reference tests.

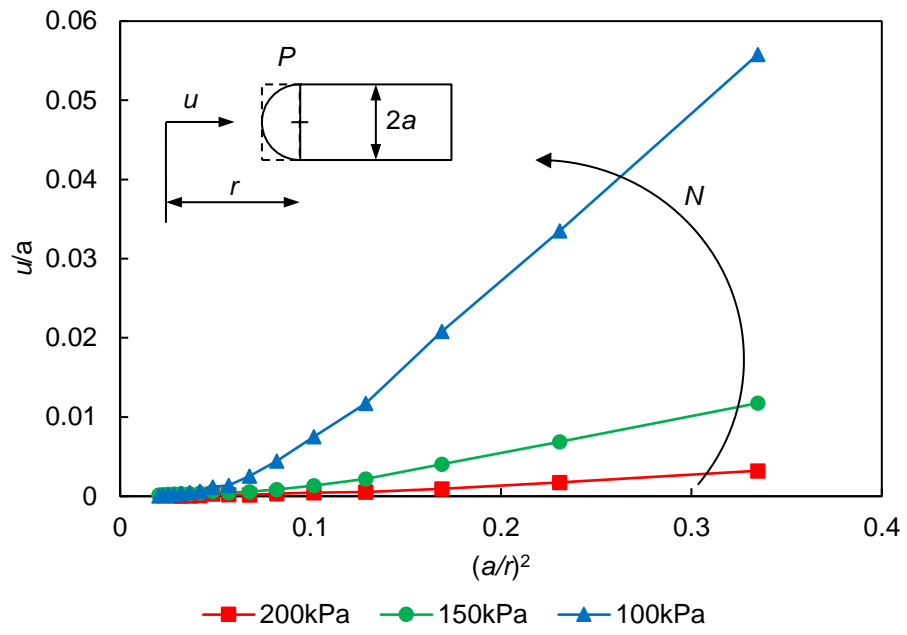


Figure 5.15: Typical longitudinal horizontal soil displacements ahead of the tunnel face in test 18BL.

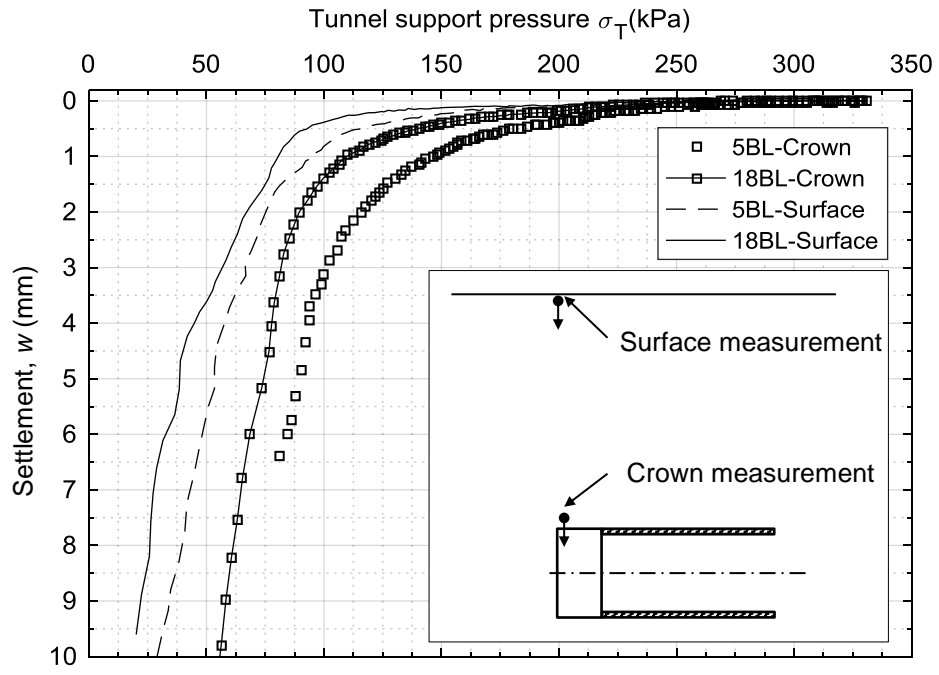


Figure 5.16: Comparison on the crown and surface settlements in reference tests 5BL and 18BL.

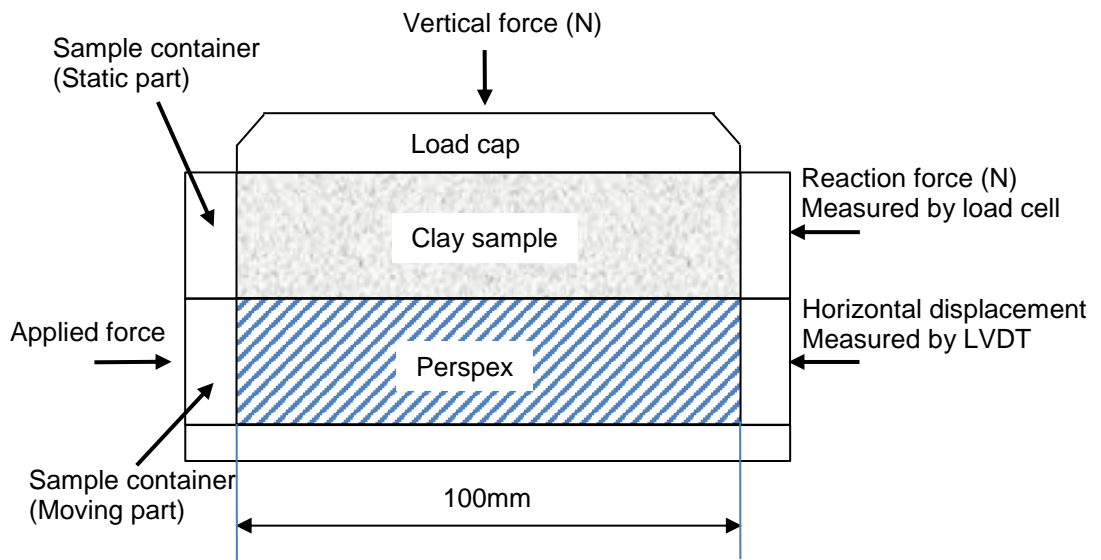


Figure 5.17: Shear box apparatus for friction determination.

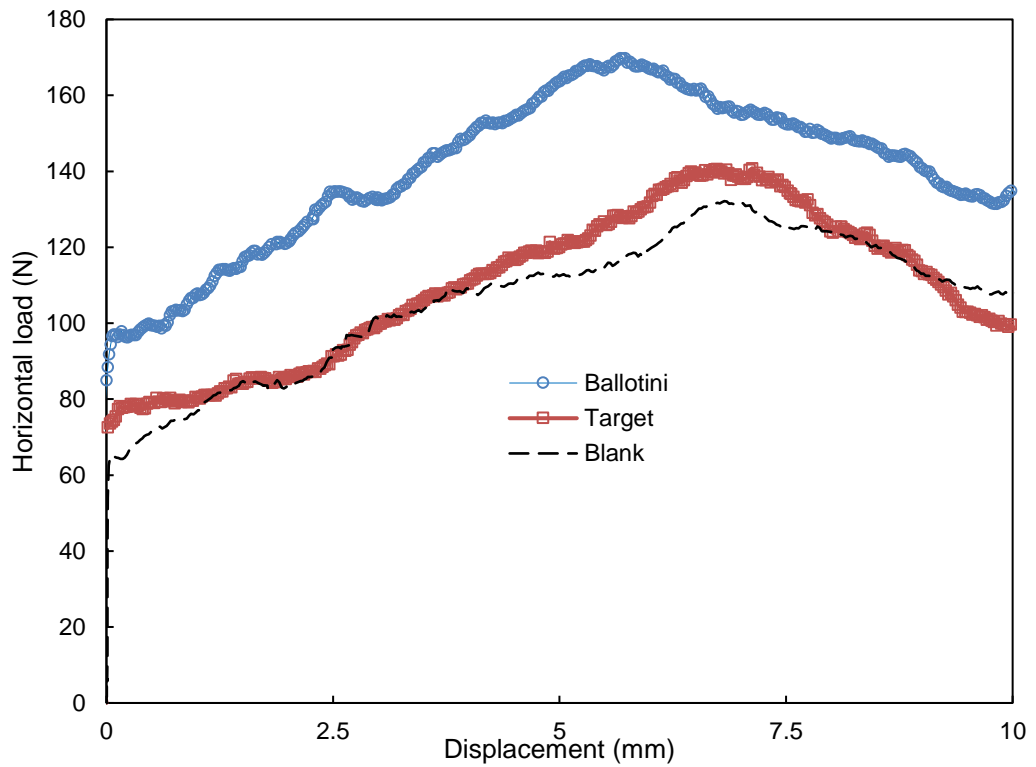
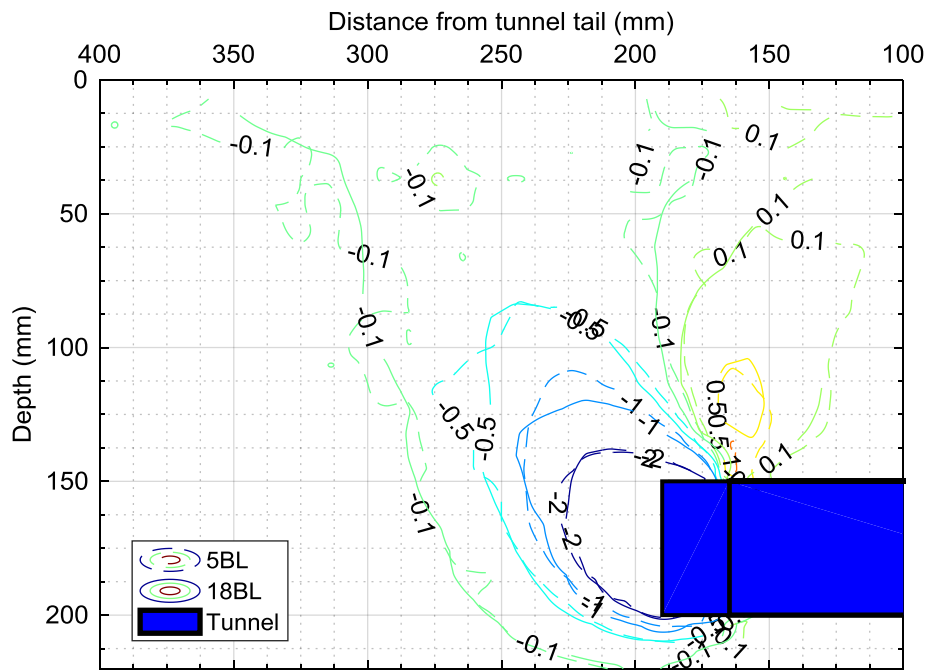
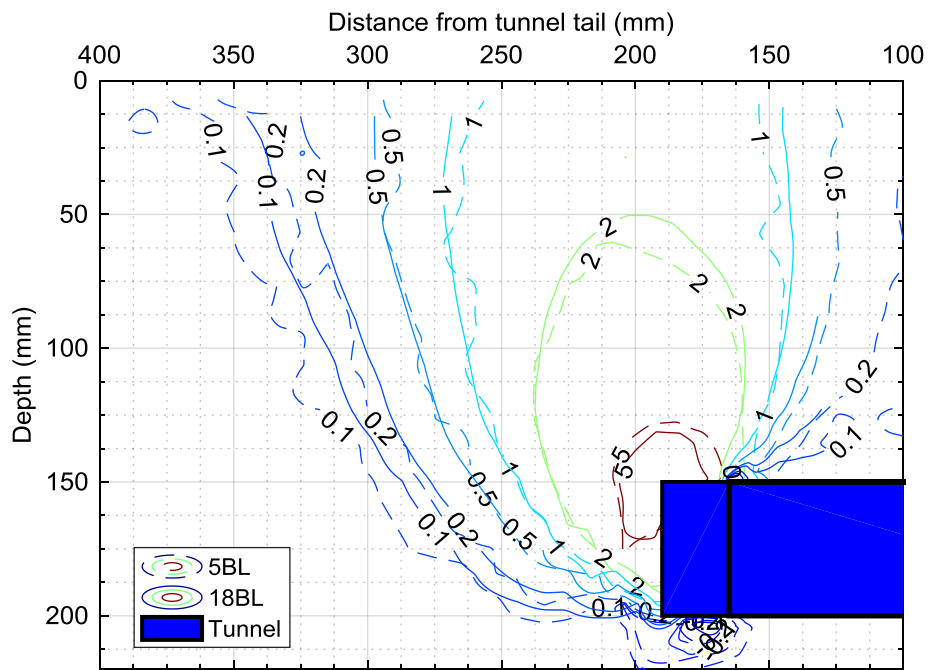


Figure 5.18: Shear box experiments results.

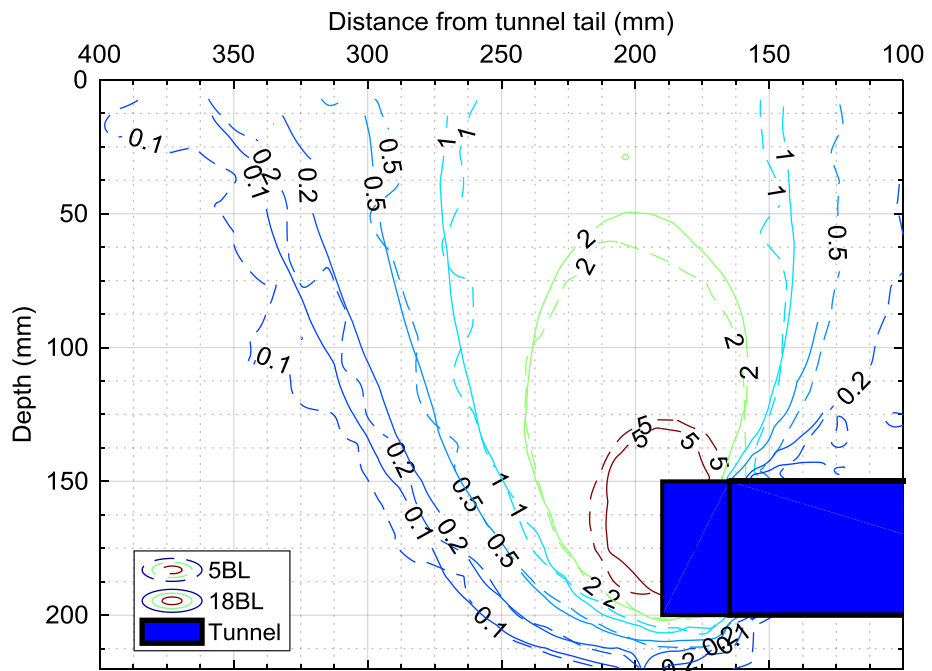


a) Horizontal displacements contour (mm).

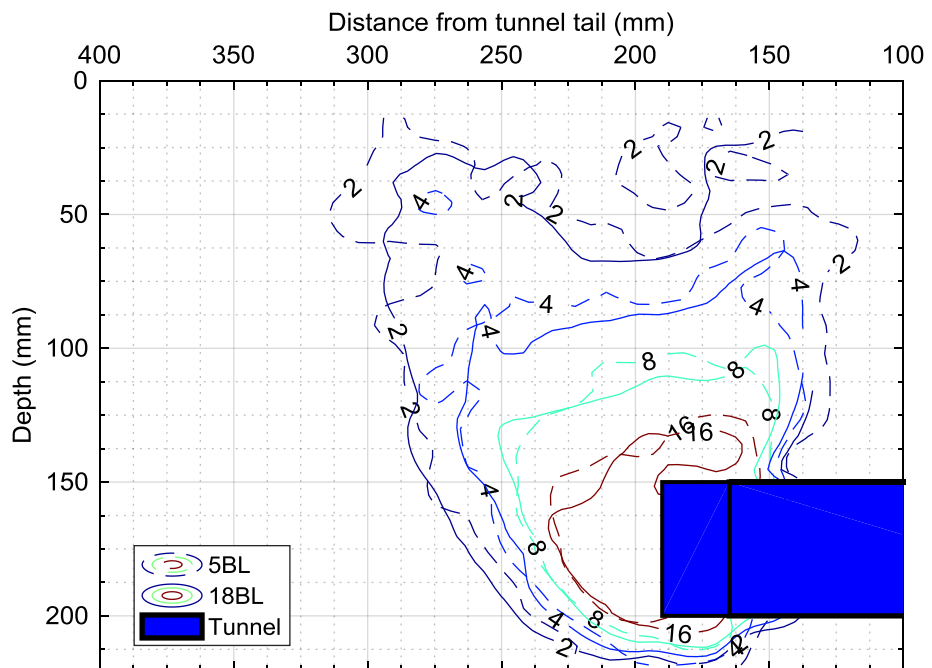


b) Vertical displacements contour (mm).

Figure 5.19: Comparison on the subsurface soil deformations in tests 5BL ($\sigma_T=80\text{kPa}$) and 18BL ($\sigma_T=68.5\text{kPa}$).



c) Resultant displacements contour (mm).



d) Engineering shear strains contours (%).

Figure 5.19: Comparison on the subsurface soil deformations in tests 5BL ($\sigma_T=80\text{kPa}$) and 18BL ($\sigma_T=68.5\text{kPa}$).

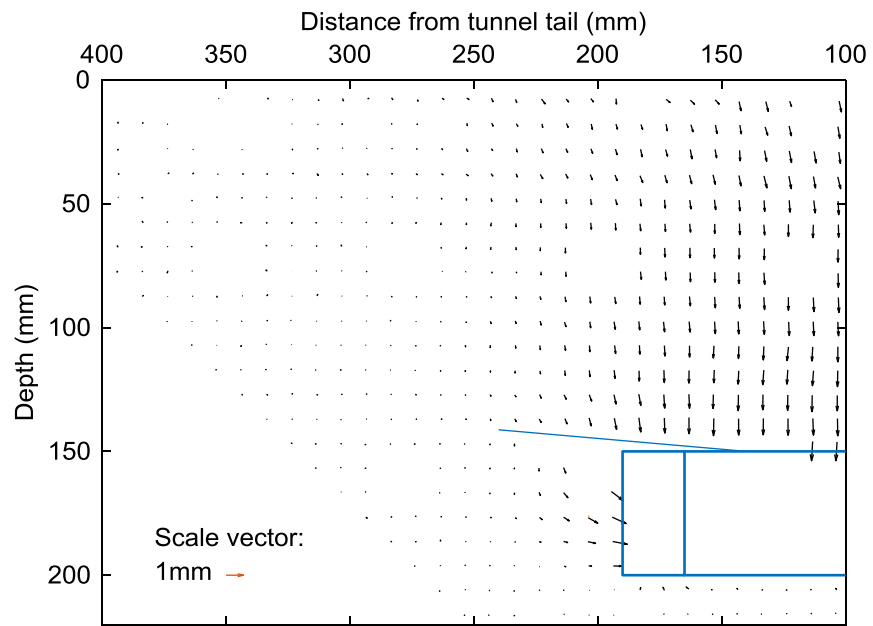


Figure 5.20: Subsurface soil displacements in test 3BL when σ_T reduced from 381kPa to 200kPa.

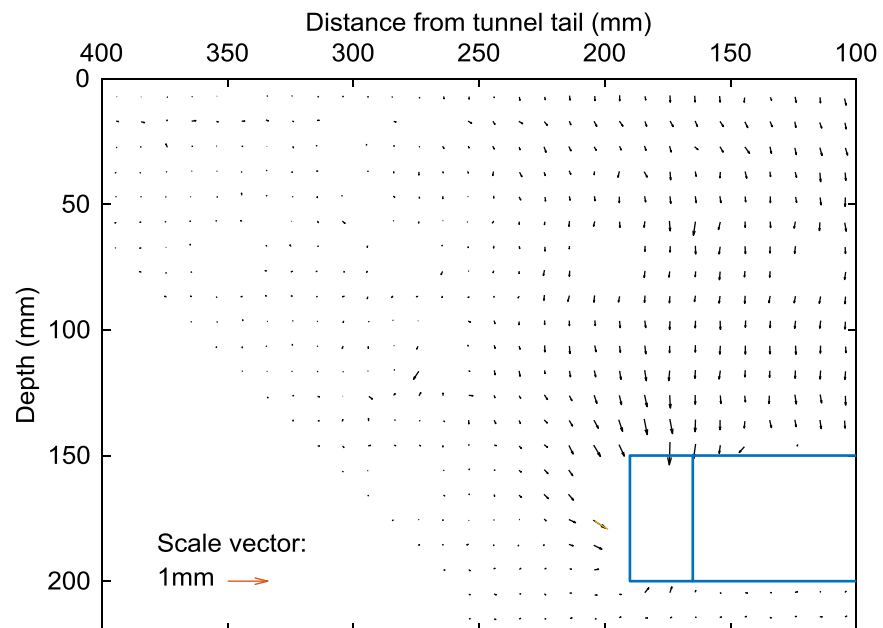


Figure 5.21: Subsurface soil displacements in test 5BL when σ_T reduced from 365kPa to 200kPa.

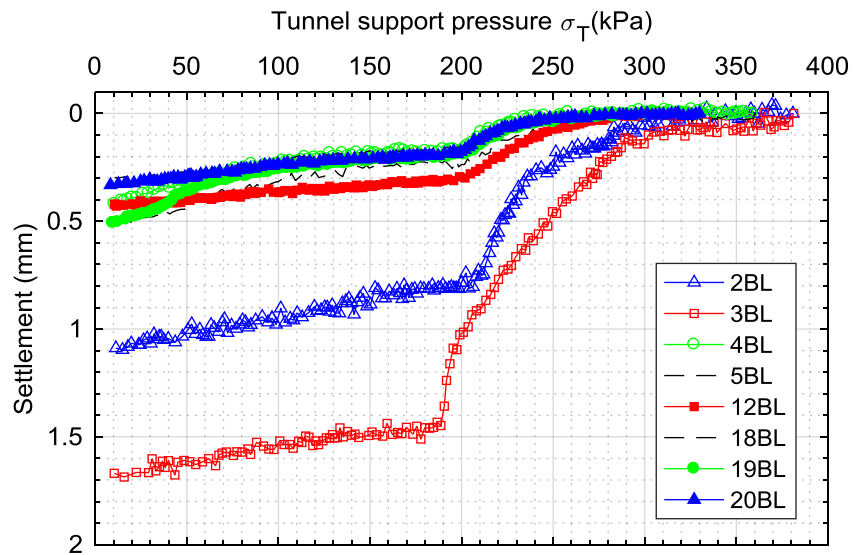


Figure 5.22: Vertical settlement of a point above the tunnel lining in $C/D=3$ tests.

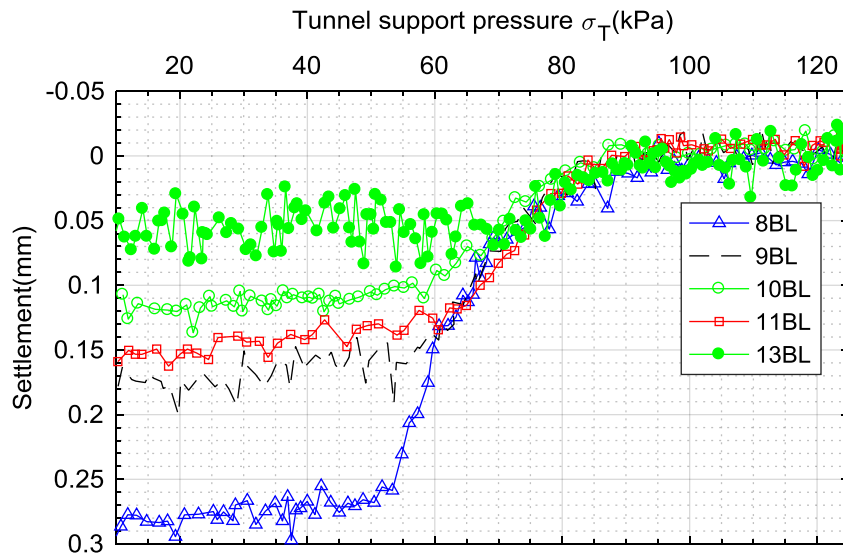


Figure 5.23: Vertical settlement of a point above the tunnel lining in $C/D=1$ tests.

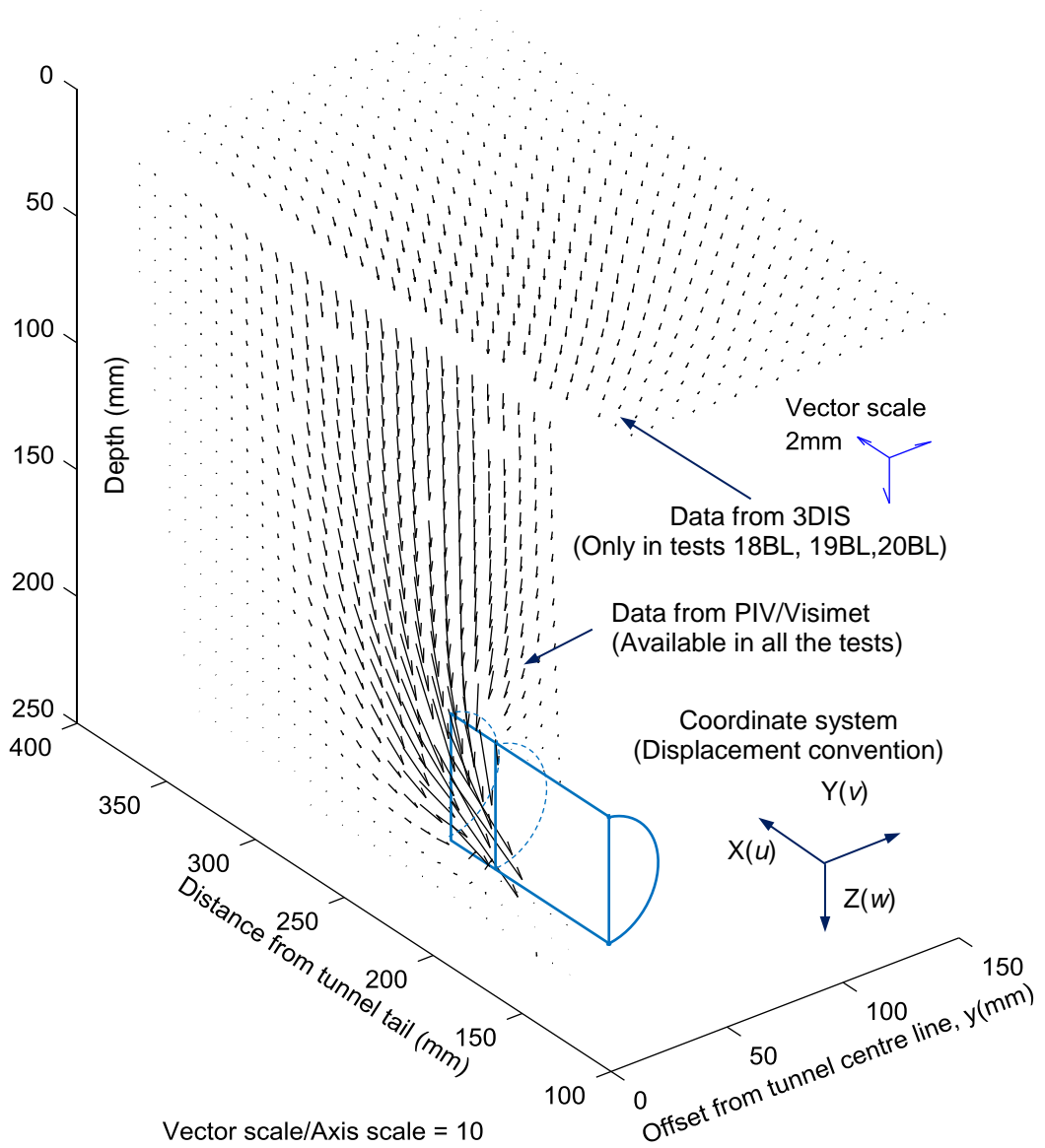
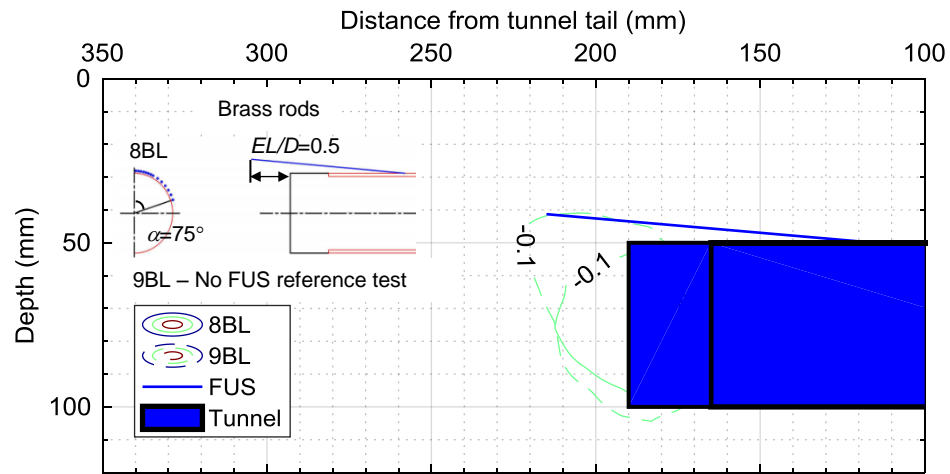
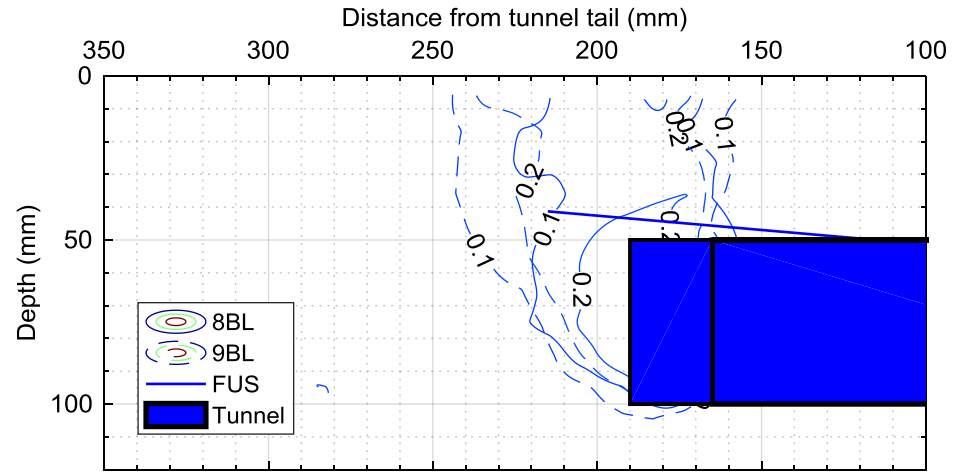


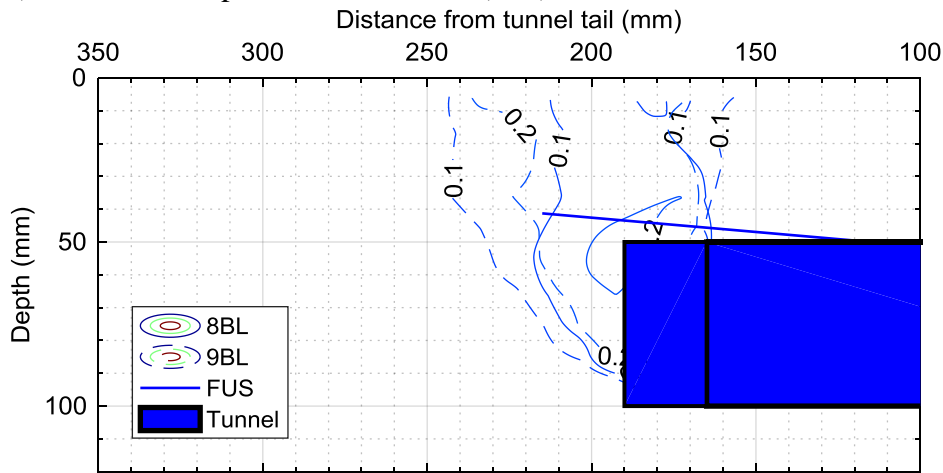
Figure 5.24: Typical data set from centrifuge tests (From test 18BL).



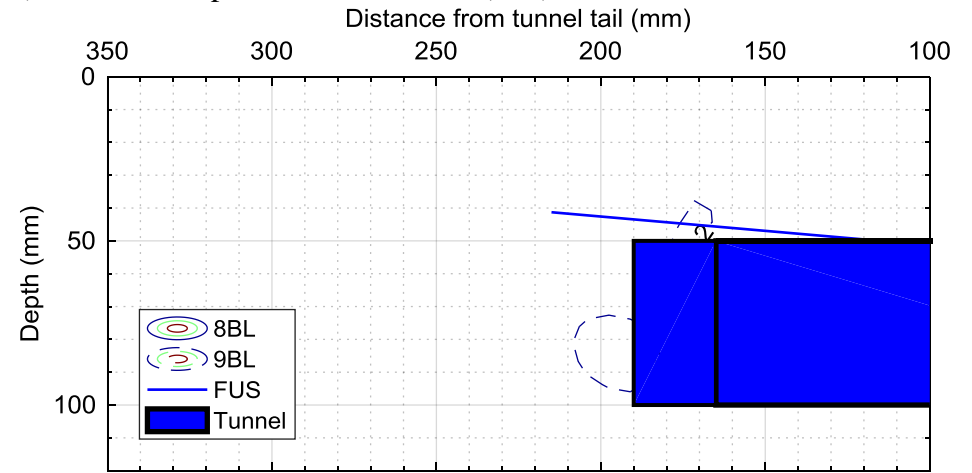
a) Horizontal displacements contour (mm).



c) Resultant displacements contours (mm).

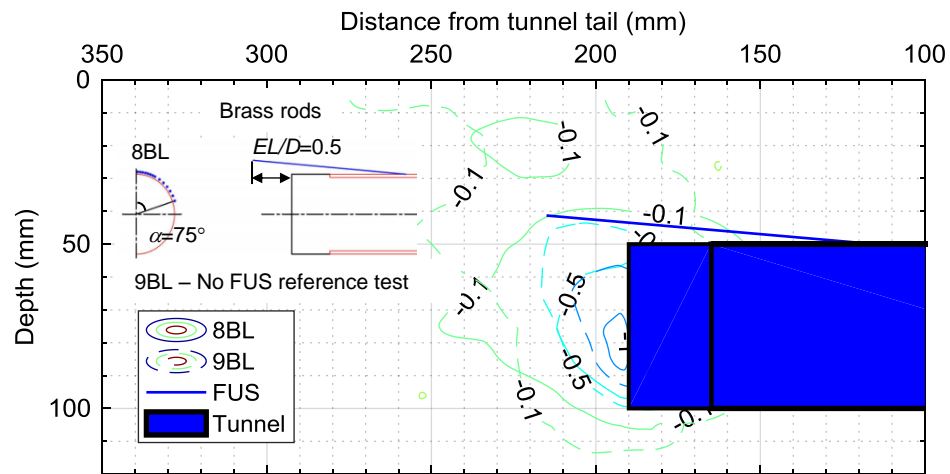


b) Vertical displacements contours (mm).

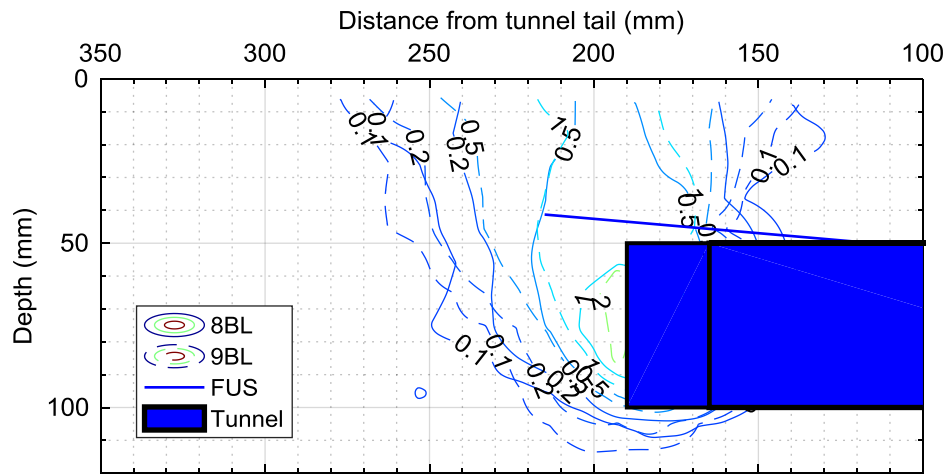


d) Engineering shear strains contour (%).

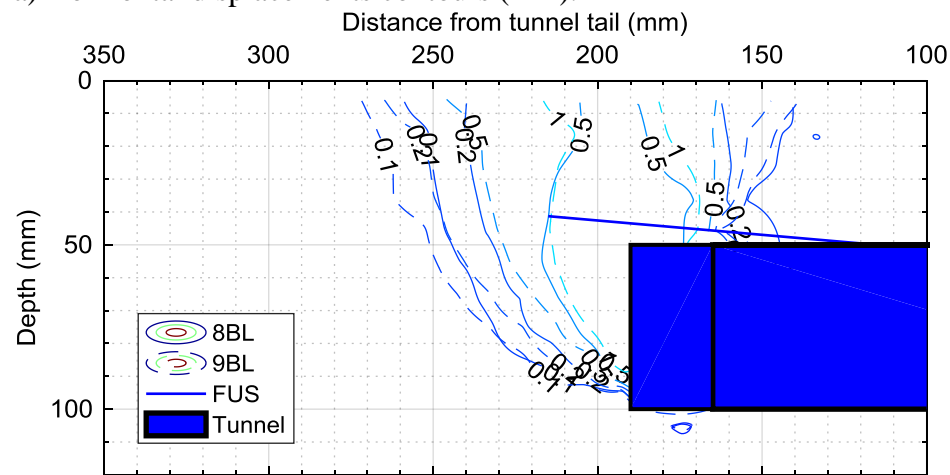
Figure 5.25: Subsurface soil deformations in test 8BL & 9BL when σ_T reduced from 55kPa to 40kPa.



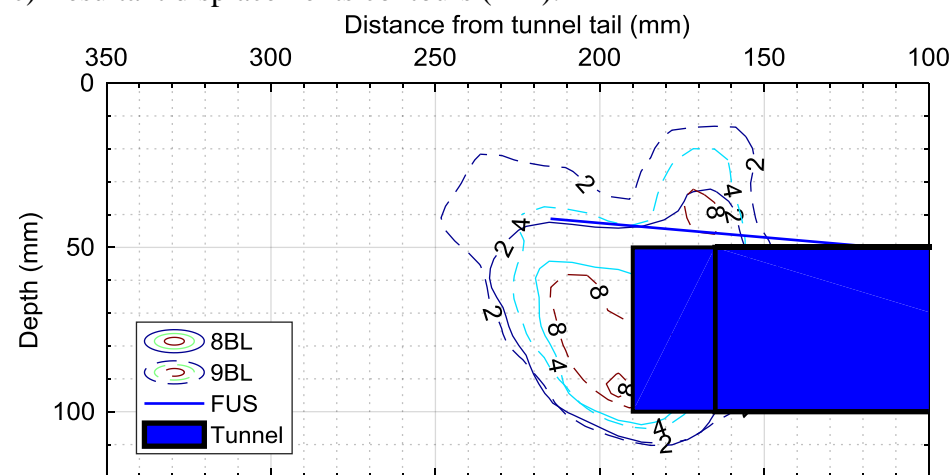
a) Horizontal displacements contours (mm).



c) Resultant displacements contours (mm).

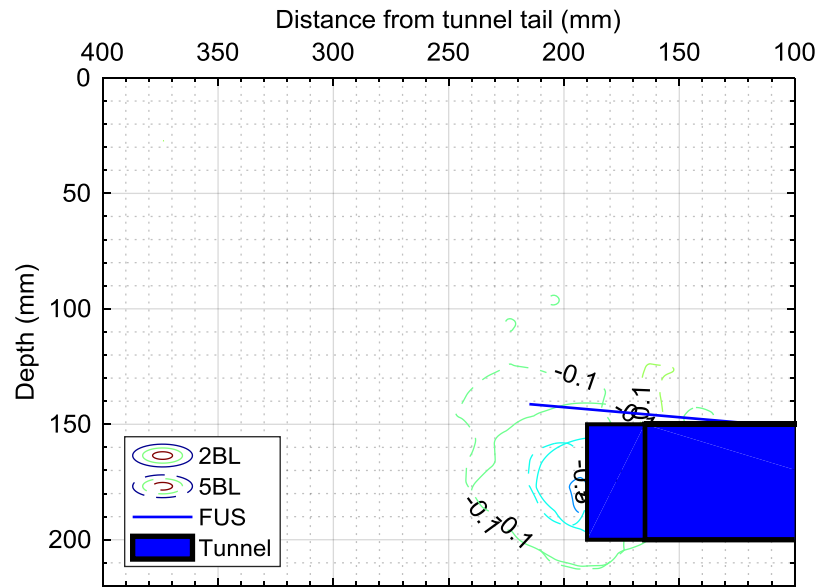


b) Vertical displacements contours (mm).

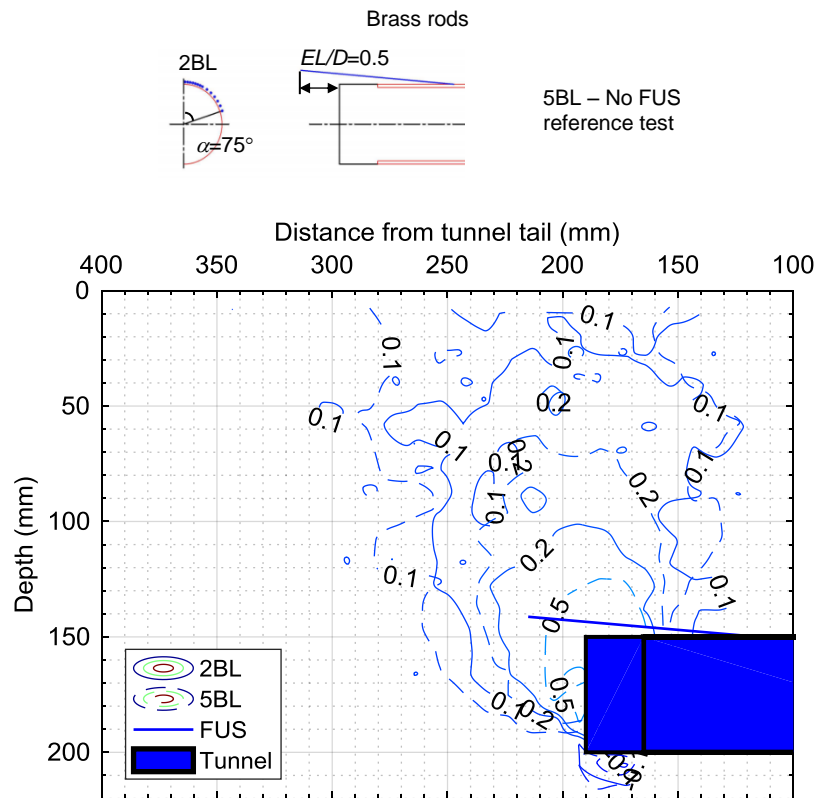


d) Engineering shear strains contour.

Figure 5.26: Subsurface soil deformations in test 8BL & 9BL when σ_T reduced from 55kPa to 20kPa.

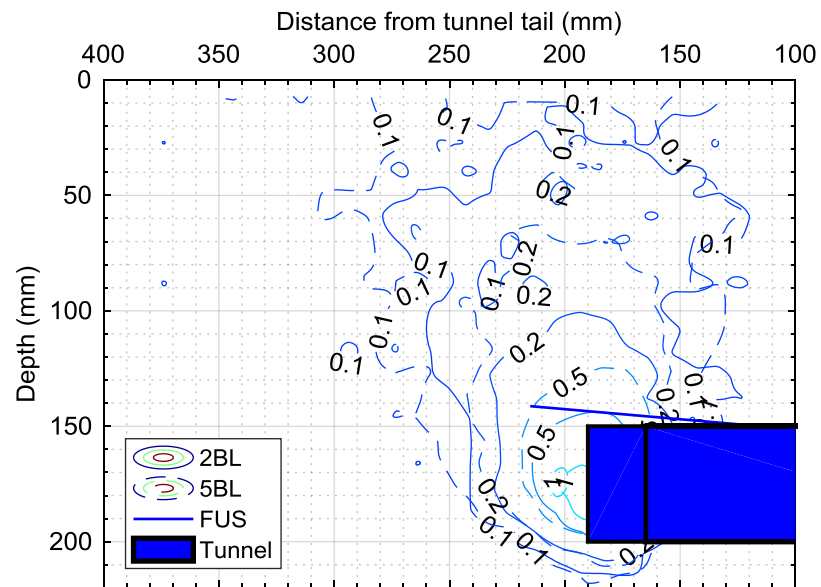


a) Horizontal displacements contours (mm).

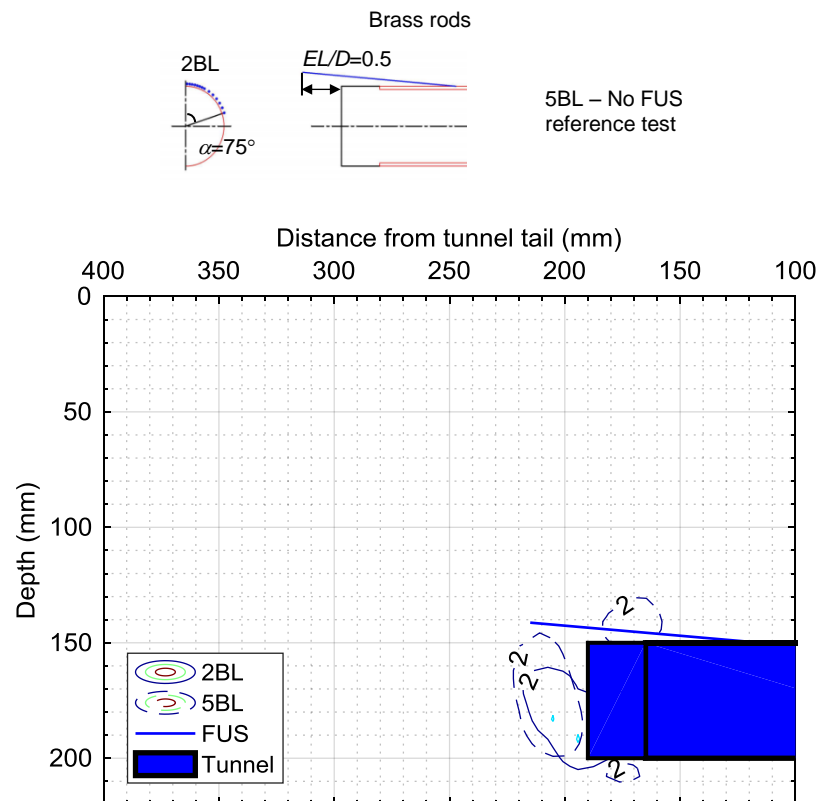


b) Vertical displacements contours (mm).

Figure 5.27: Subsurface soil deformations in tests 2BL and 5BL when σ_T reduced from 180kPa to 140kPa.

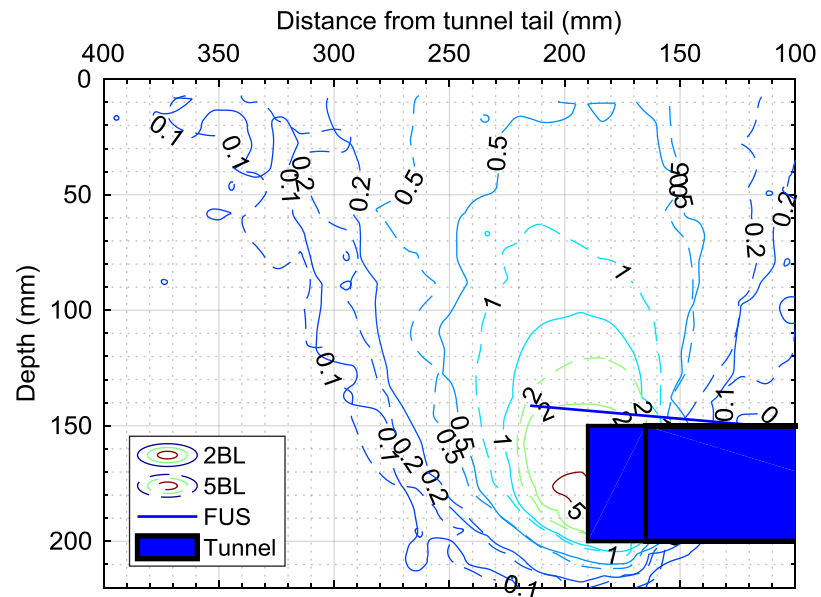


c) Resultant displacements contours (mm).

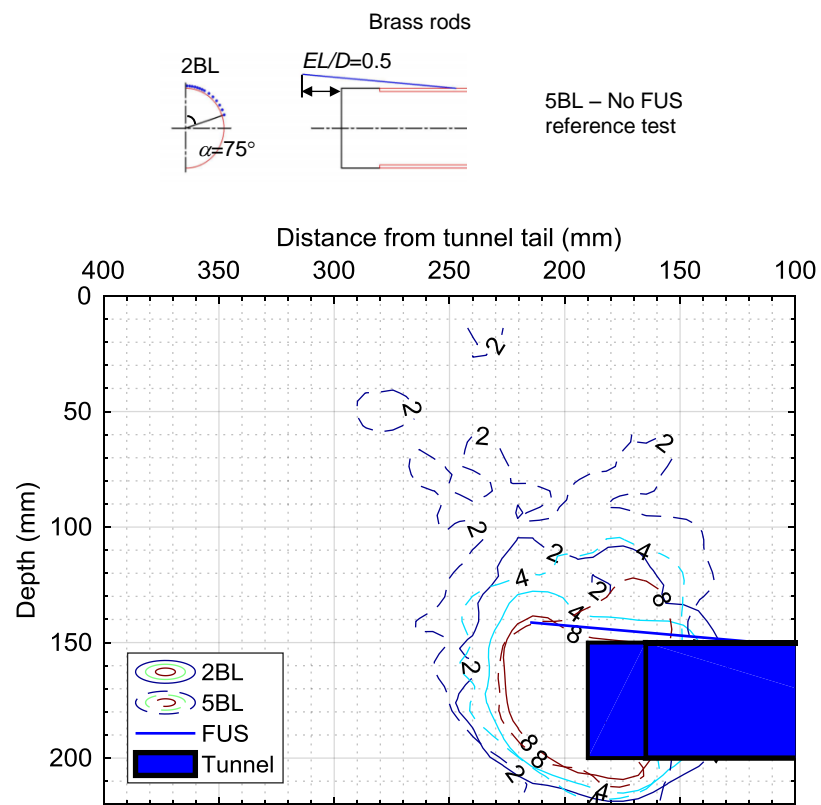


d) Engineering shear strains contour.

Figure 5.27: Subsurface soil deformations in tests 2BL and 5BL when σ_T reduced from 180kPa to 140kPa.

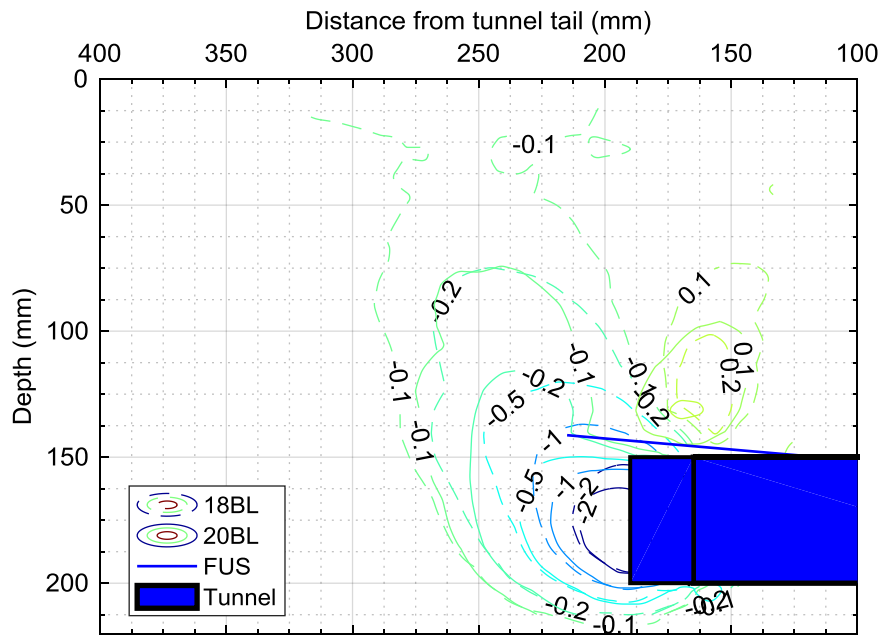


c) Resultant displacements contours (mm).

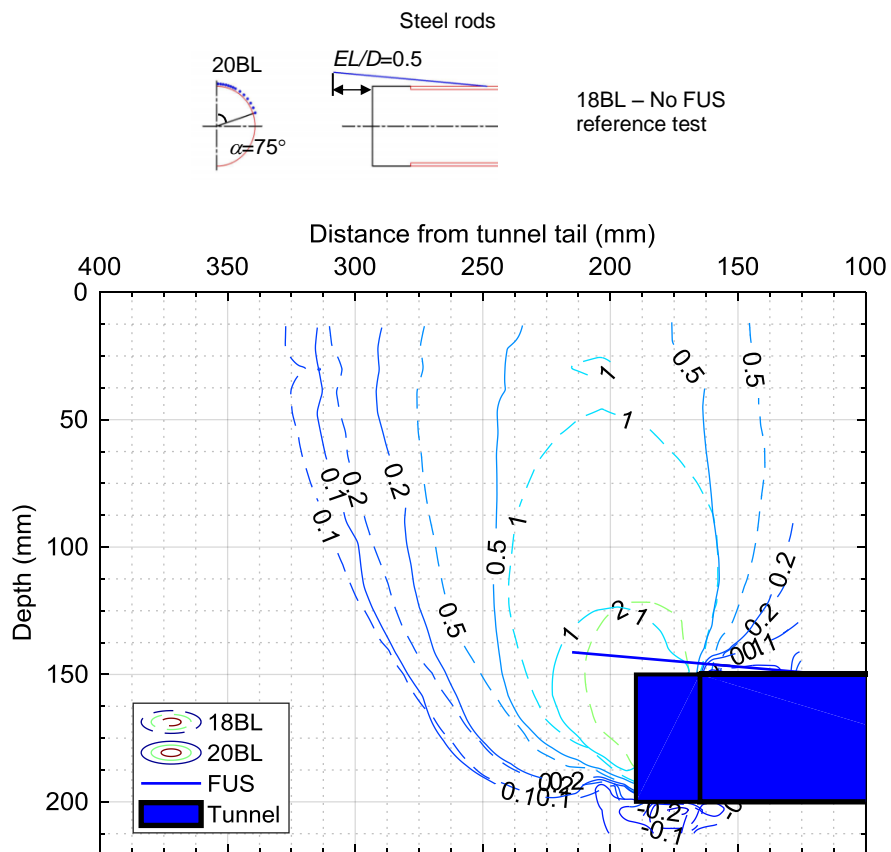


d) Engineering shear strains contour.

Figure 5.28: Subsurface soil deformations in tests 2BL and 5BL when σ_T reduced from 180kPa to 100kPa.

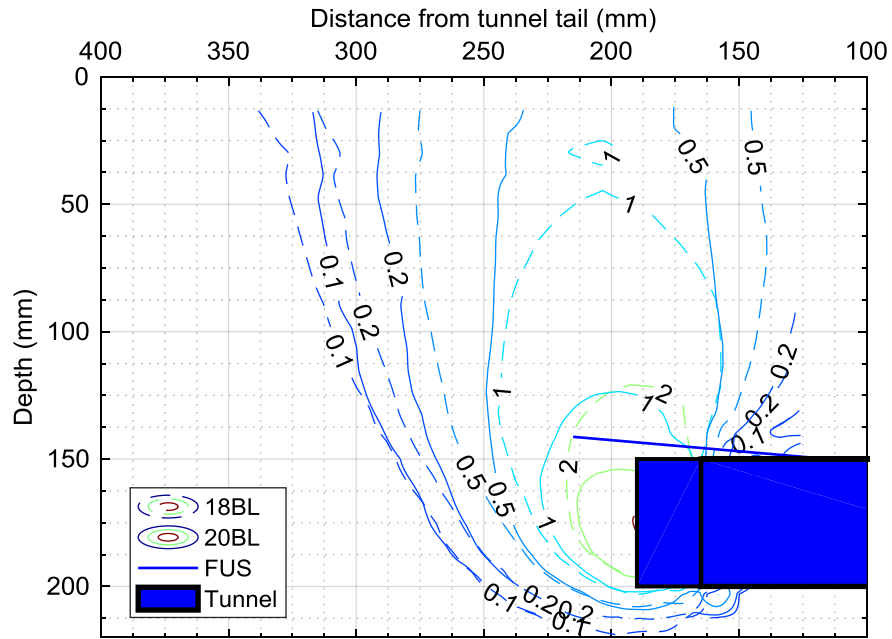


a) Horizontal displacements contours (mm).

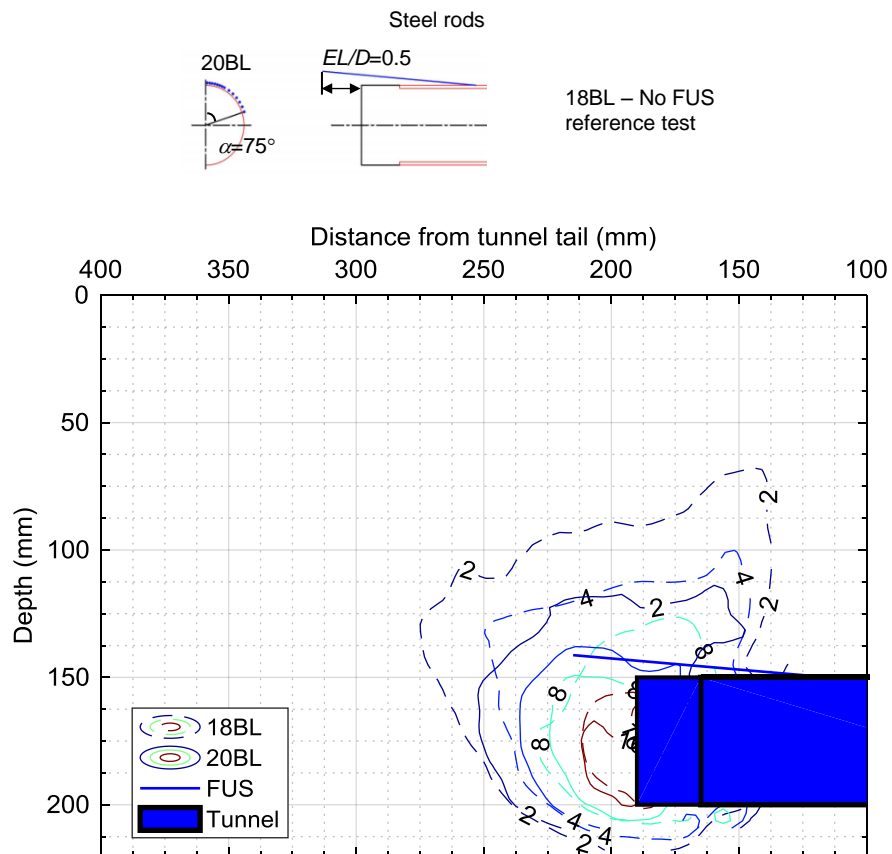


b) Vertical displacements contours (mm).

Figure 5.29: Subsurface soil deformations in tests 18BL and 20BL when σ_T reduced from 180kPa to 80kPa.

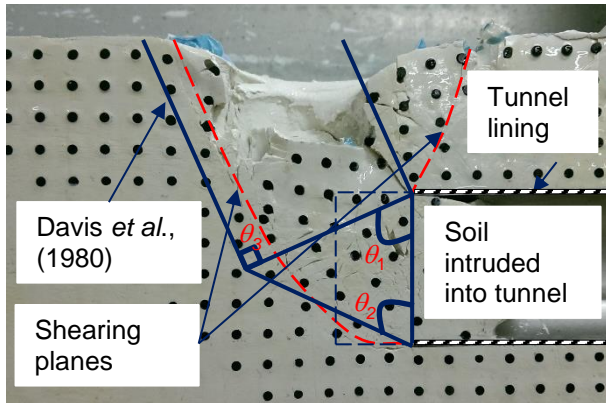


c) Resultant displacements contours (mm).



d) Engineering shear strains contour.

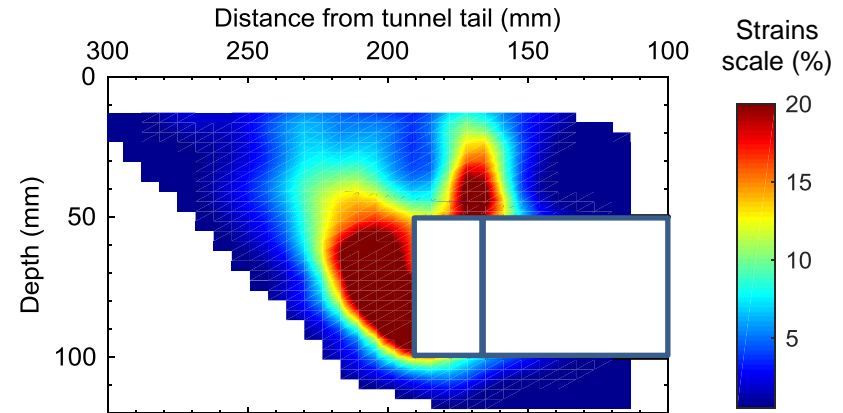
Figure 5.29: Subsurface soil deformations in tests 18BL and 20BL when σ_T reduced from 180kPa to 80kPa.



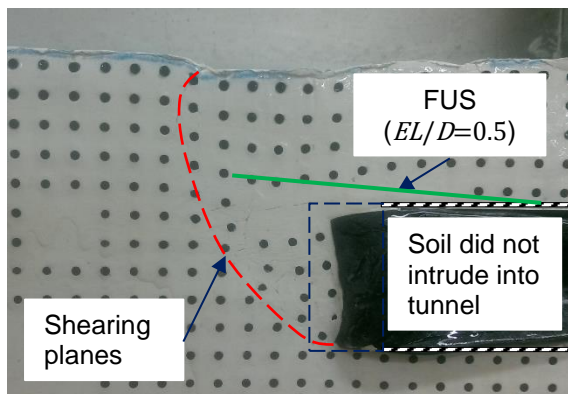
Note: The drawn shearing planes were visible.

a) Model post-test

Figure 5.30: Model post-test in reference test 9BL.



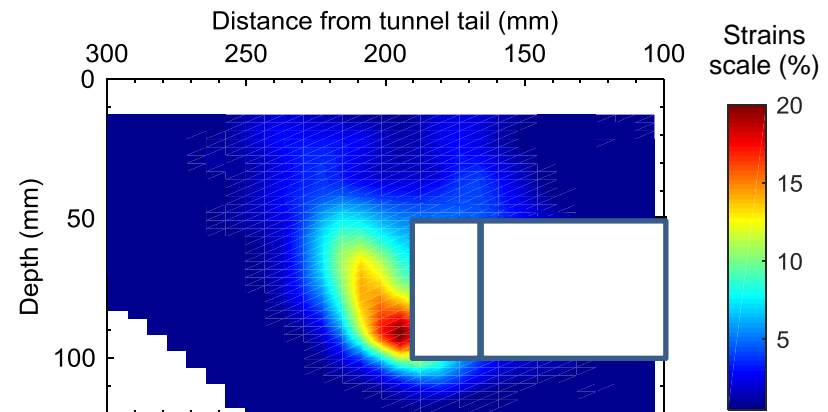
b) Engineering shear strains field at the end of test



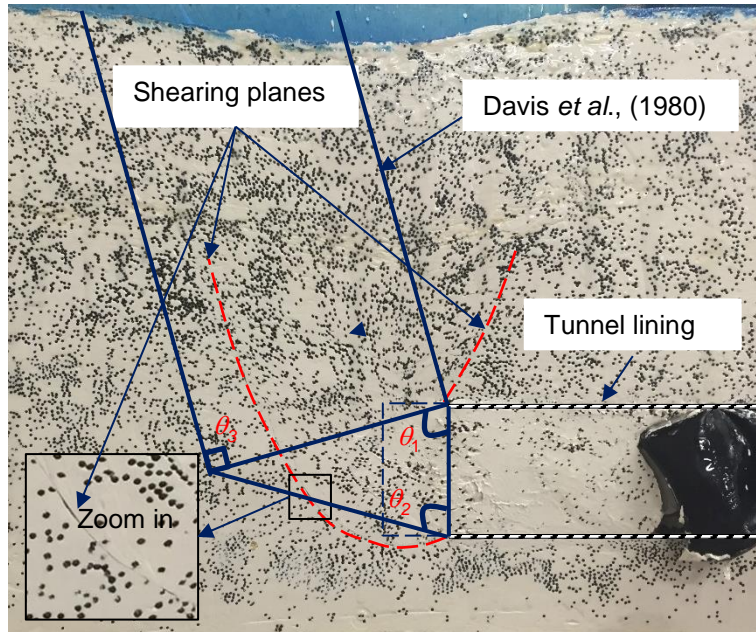
Note: The drawn shearing plane was visible.

a) Model post-test

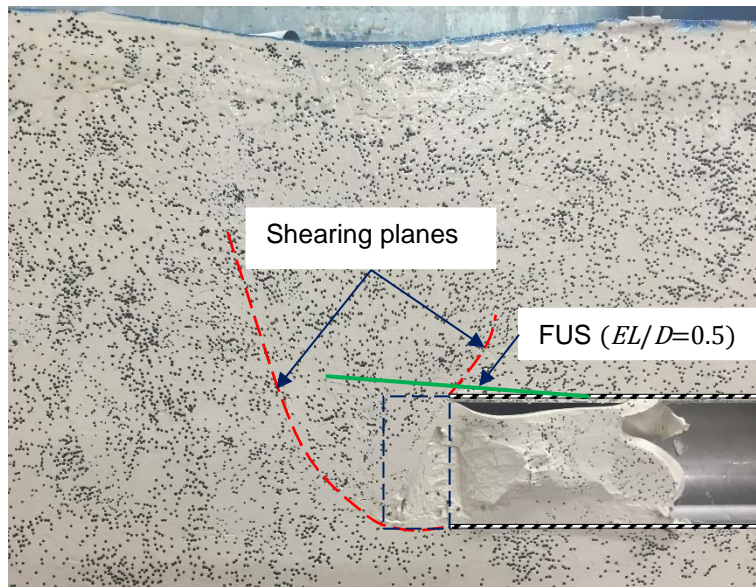
Figure 5.31: Model post-test in reinforced test 8BL.



b) Engineering shear strains field at the end of test

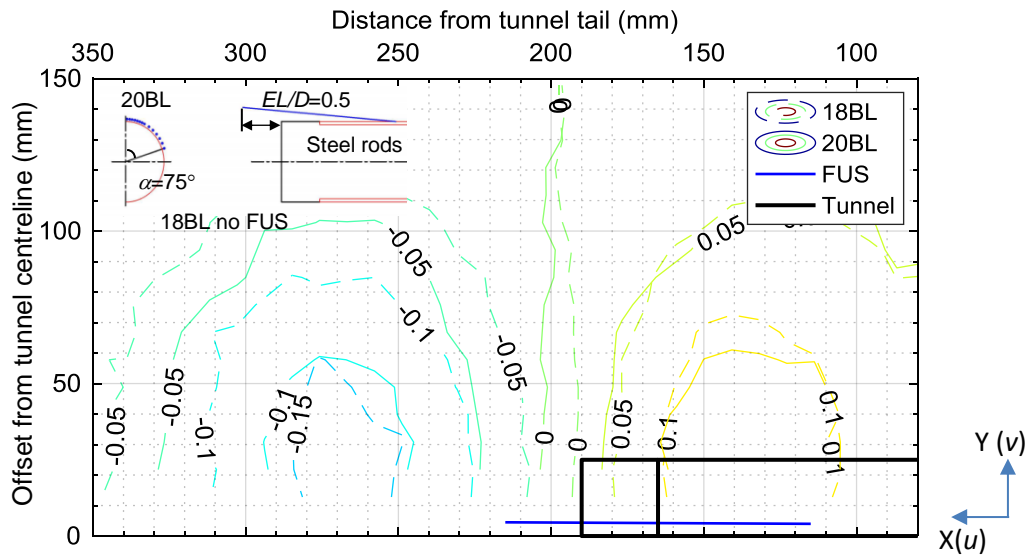


Note: The drawn shearing planes were visible.
 a) Reference test 18BL.

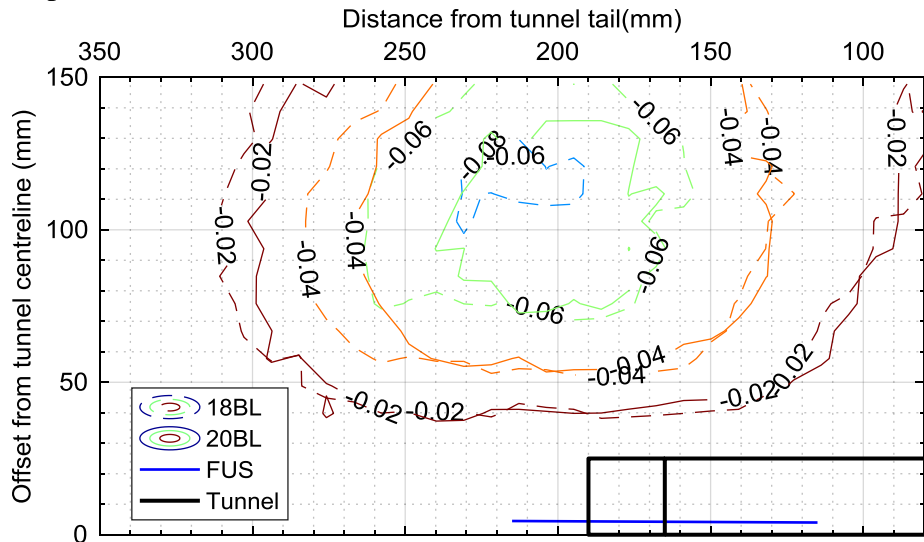


Note: The drawn shearing planes were visible.
 b) Reinforced test 20BL.

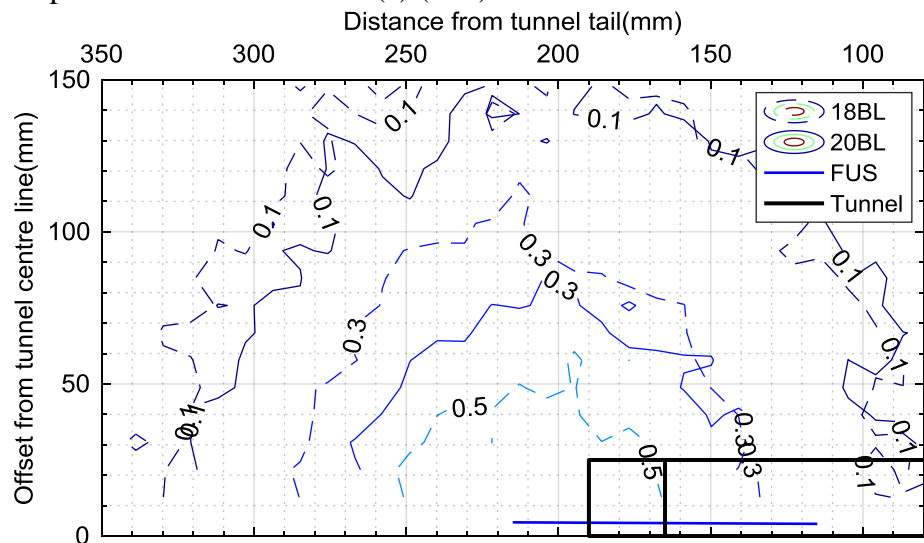
Figure 5.32: $C/D=3$ models post tests.



a) Soil displacement in X direction (u) (mm).

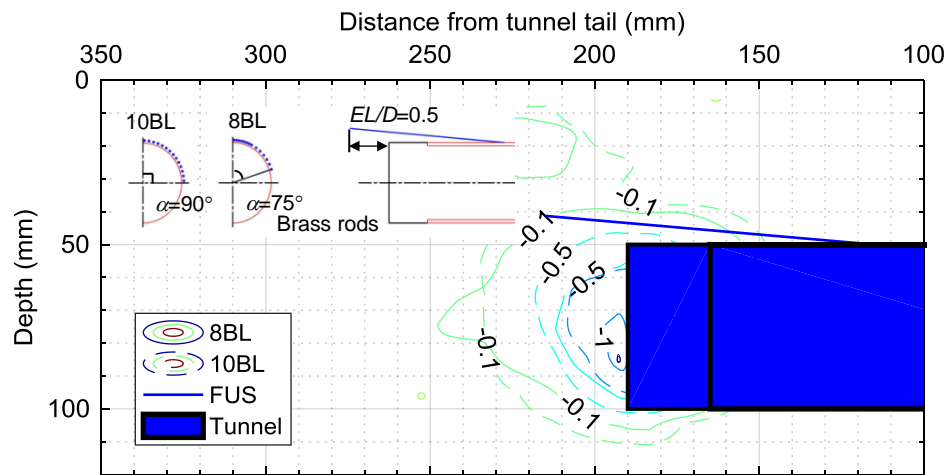


b) Soil displacement in Y direction (v) (mm).

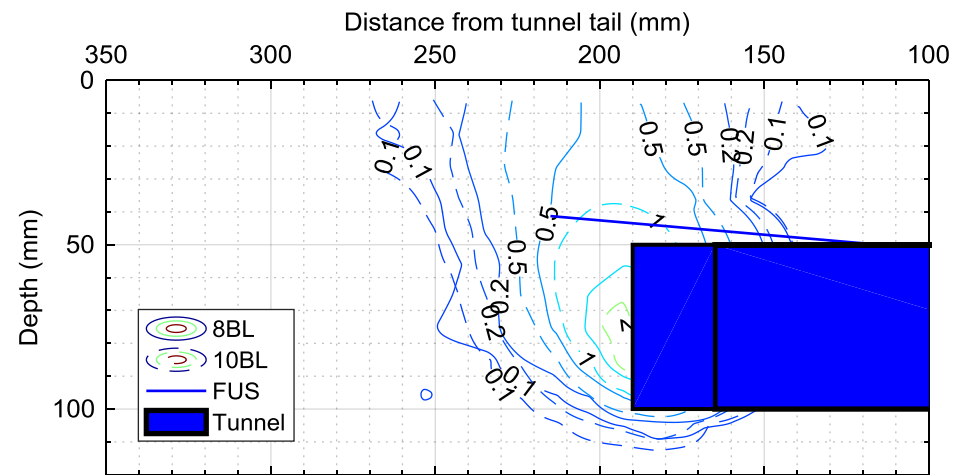


c) Soil displacement in Z direction (w) (mm).

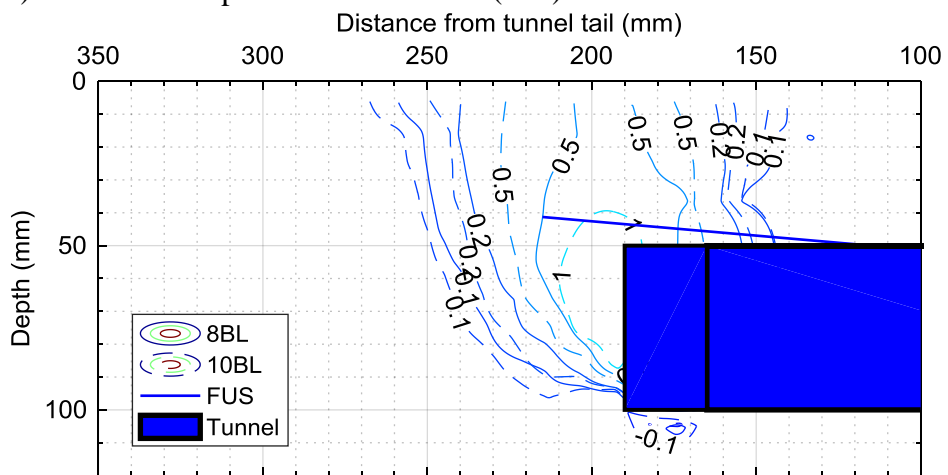
Figure 5.33: Soil displacements in tests 18BL and 20BL when σ_T reduced from 180 to 80kPa.



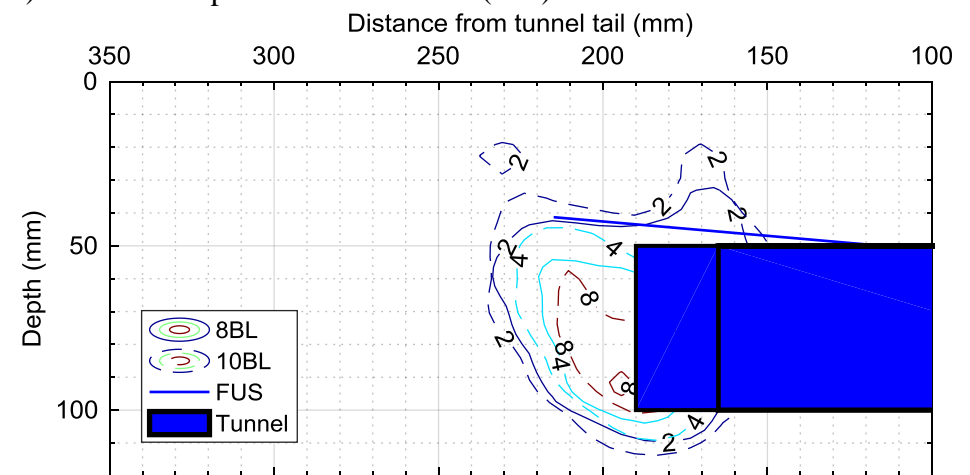
a) Horizontal displacements contours (mm).



c) Resultant displacements contours (mm).

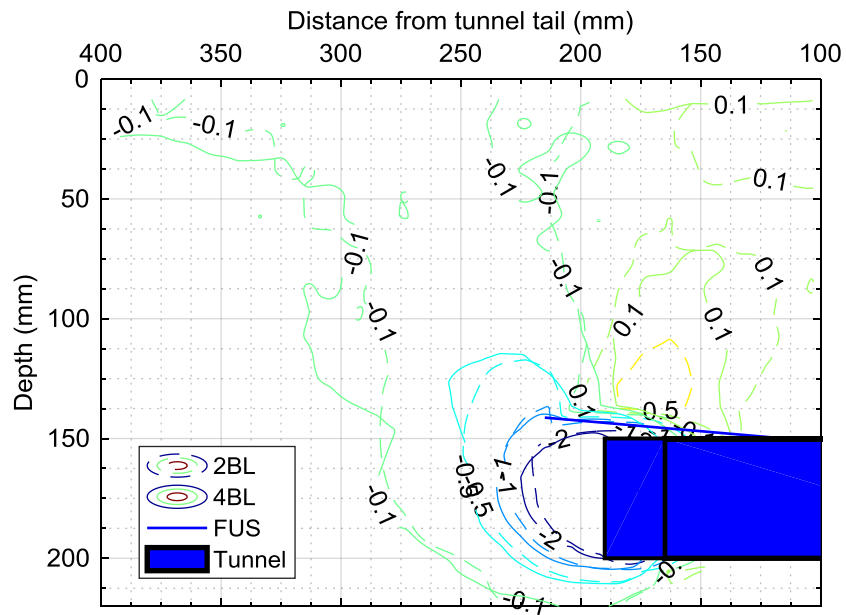


b) Vertical displacements contours (mm).

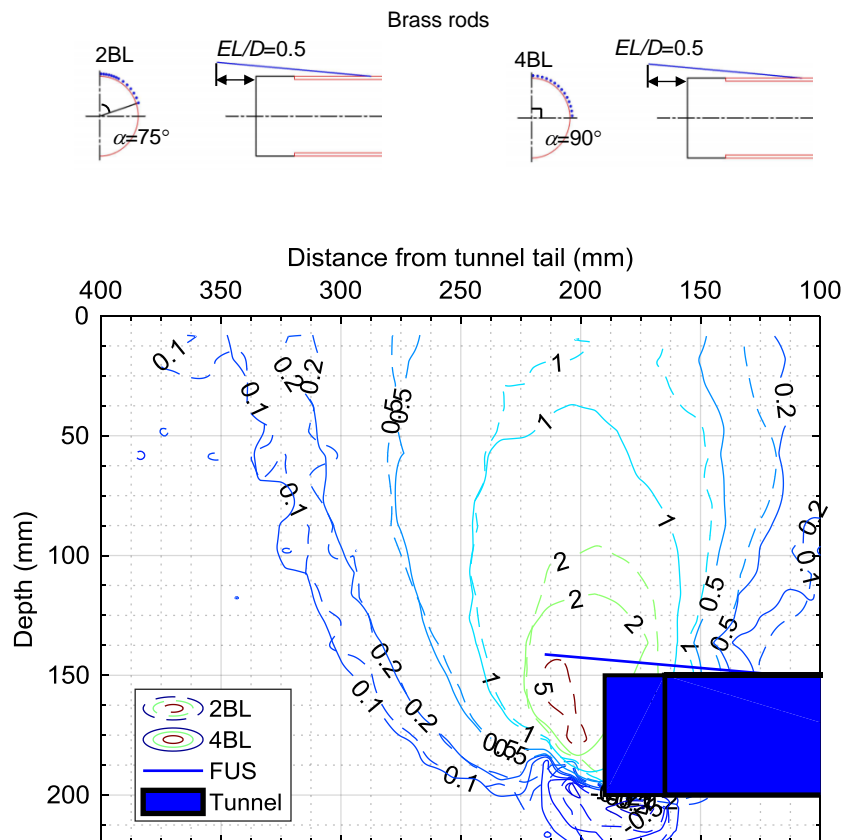


d) Engineering shear strains contour (%).

Figure 5.34: Effect of filling angle - Subsurface soil deformations in tests 8BL and 10BL when σ_T reduced from 55kPa to 20kPa.

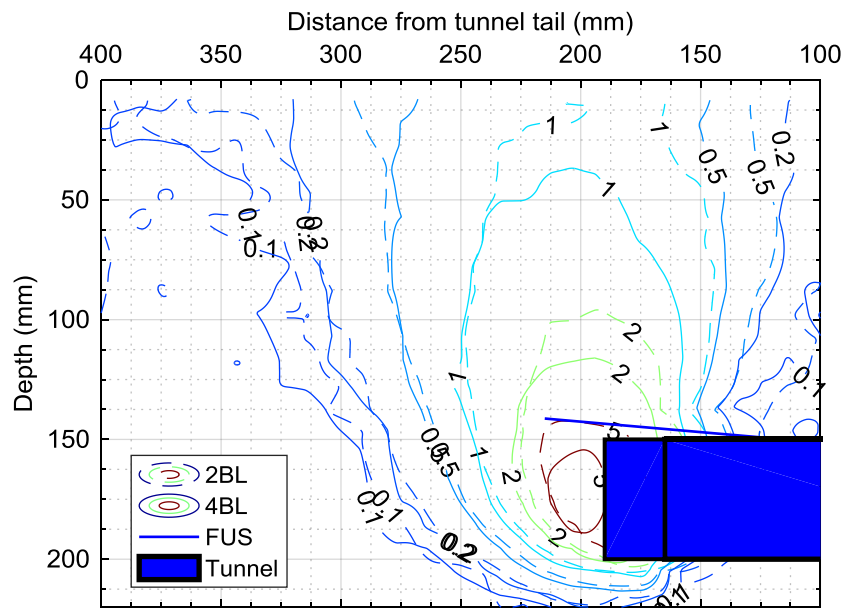


a) Horizontal displacements contours (mm).

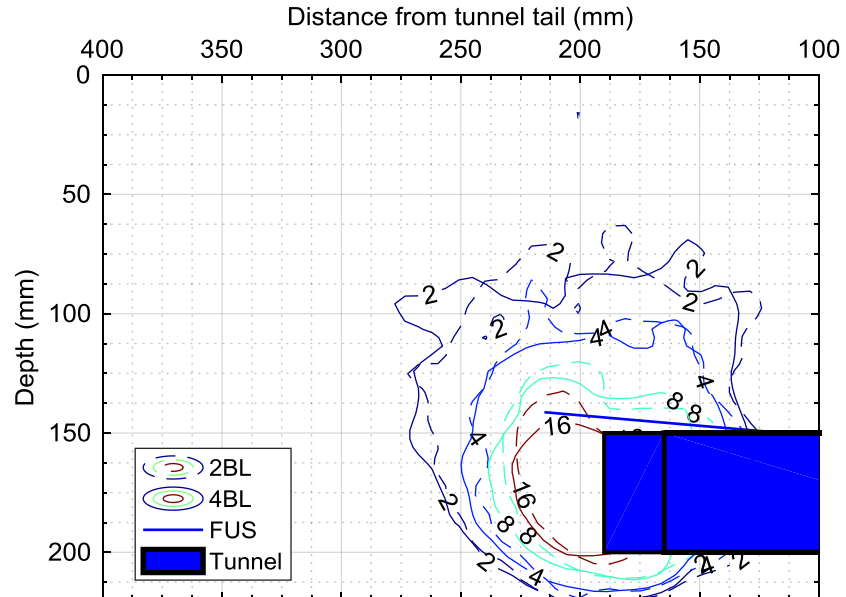
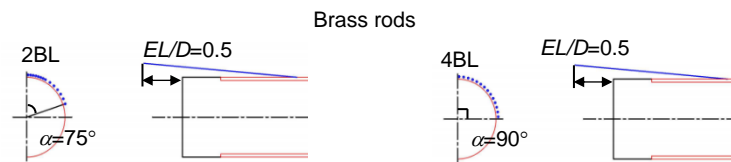


b) Vertical displacements contours (mm).

Figure 5.35: Effect of filling angle - Subsurface soil deformations in tests 2BL and 4BL when σ_T reduced from 180kPa to 80kPa.

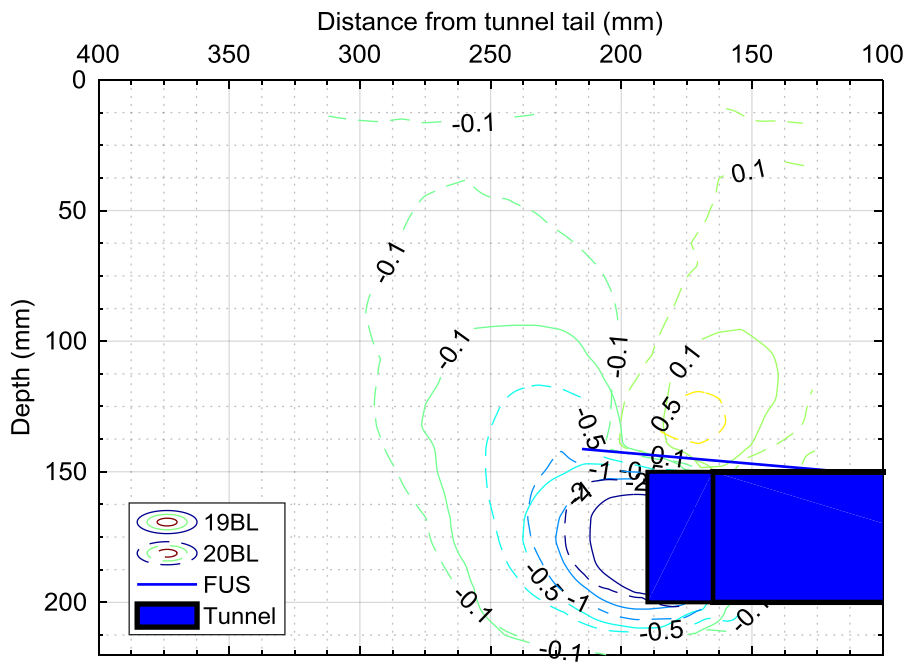


c) Resultant displacements contours (mm).

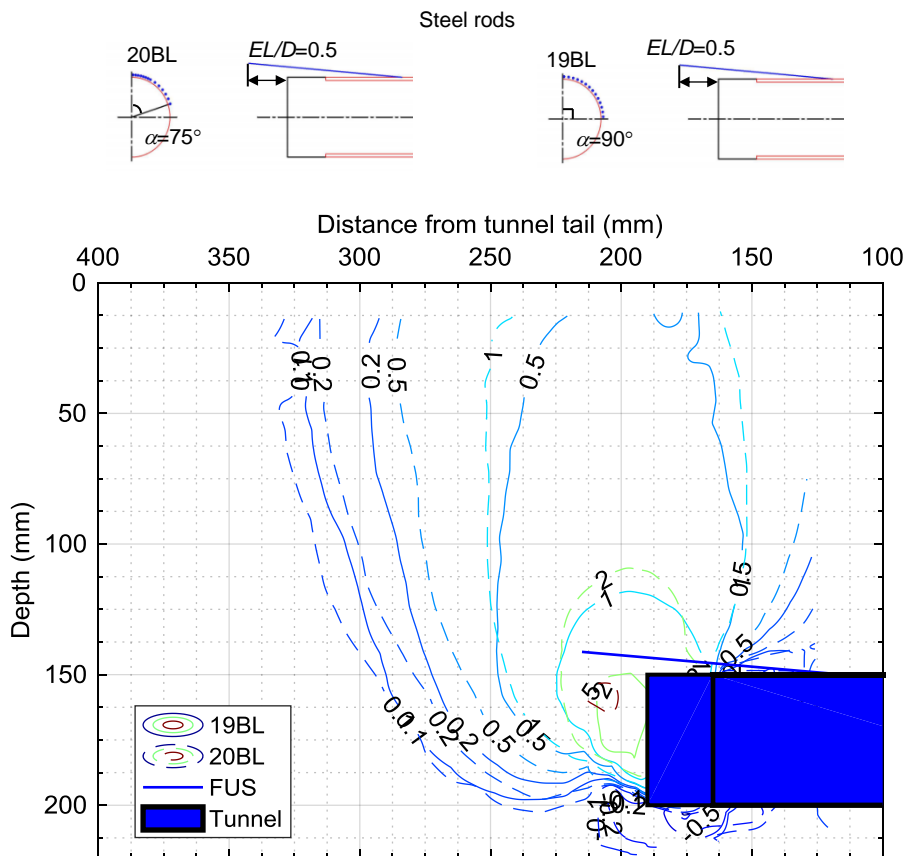


d) Engineering shear strains contours (%).

Figure 5.35: Effect of filling angle - Subsurface soil deformations in tests 2BL and 4BL when σ_T reduced from 180kPa to 80kPa.

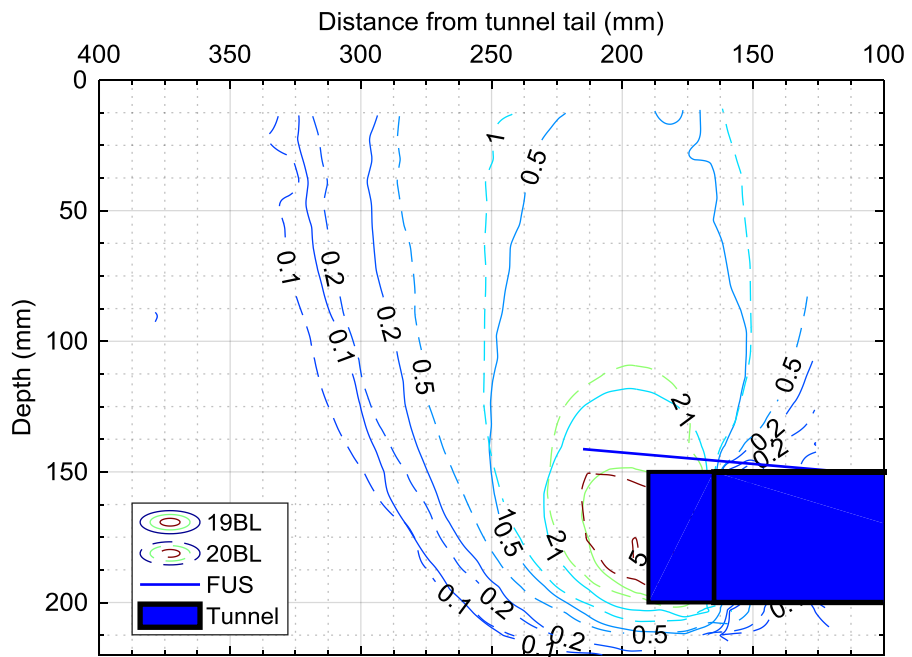


a) Horizontal displacements contours (mm).

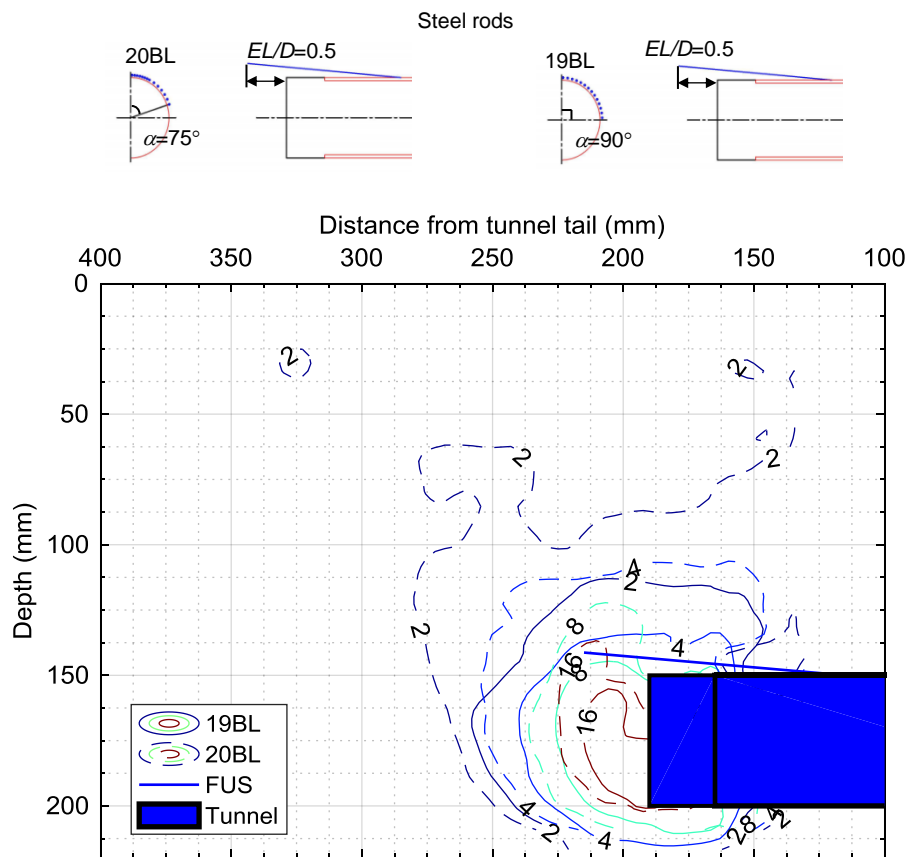


b) Vertical displacements contours (mm).

Figure 5.36: Effect of filling angle - Subsurface soil deformations in tests 19BL and 20BL when σ_T reduced from 180kPa to 60kPa.

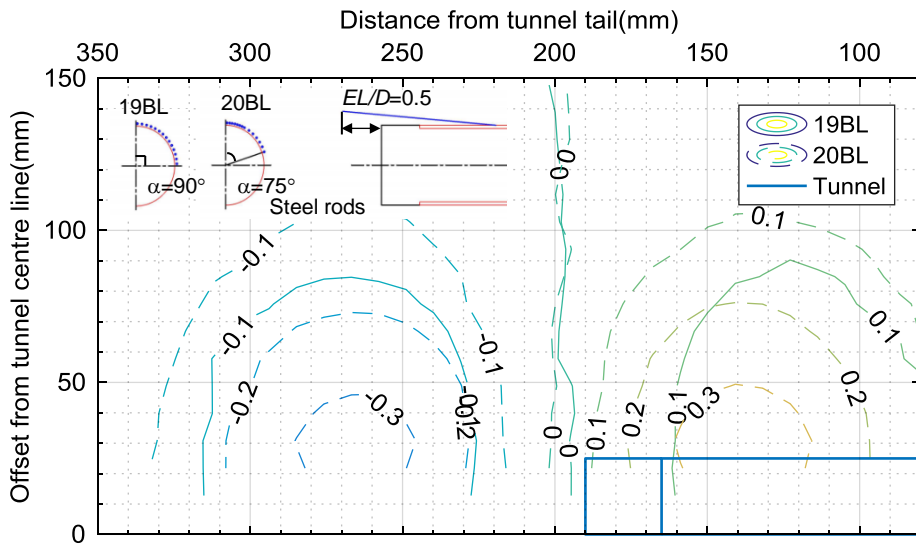


c) Resultant displacements contours (mm).

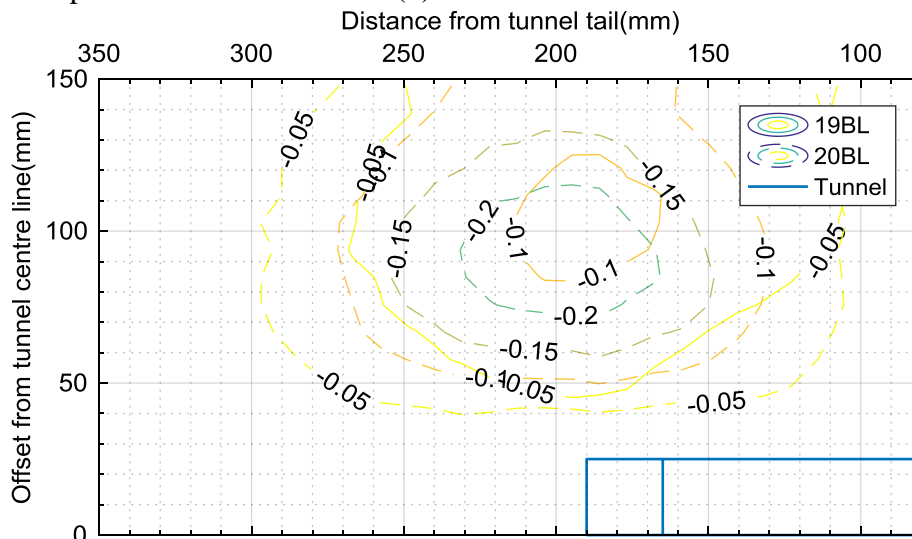


d) Engineering shear strains contours (%).

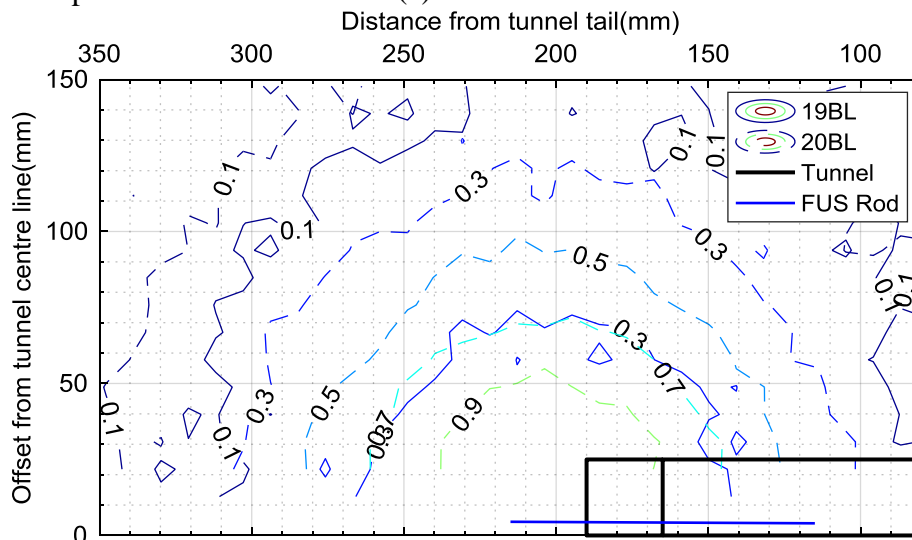
Figure 5.36: Effect of filling angle - Subsurface soil deformations in tests 19BL and 20BL when σ_T reduced from 180kPa to 60kPa.



a) Soil displacement in X direction (u).

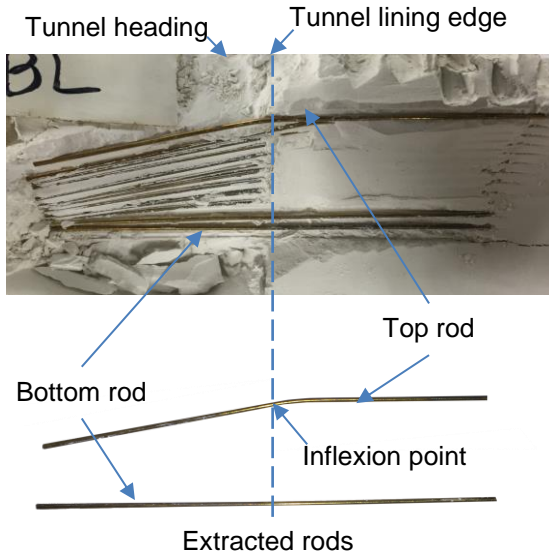


b) Soil displacement in Y direction (v).

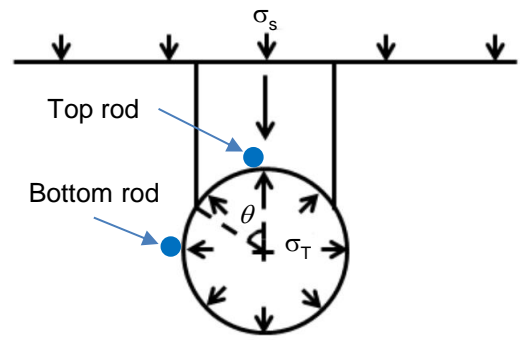


c) Soil displacement in Z direction (w).

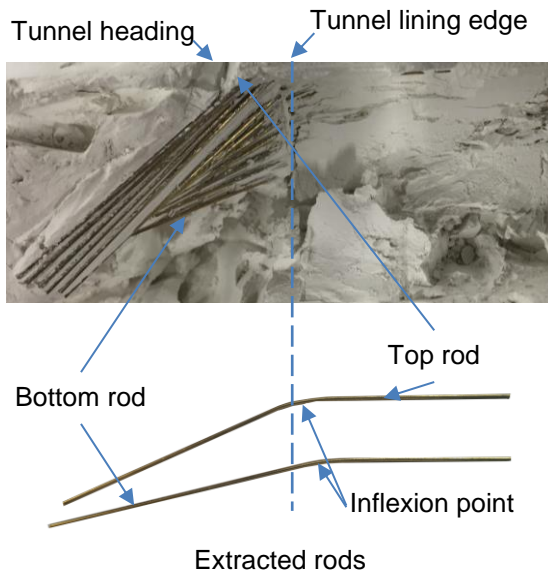
Figure 5.37: Effect of filling angle - Soil displacement in tests 19BL and 20BL when σ_T reduced from 180 to 60kPa.



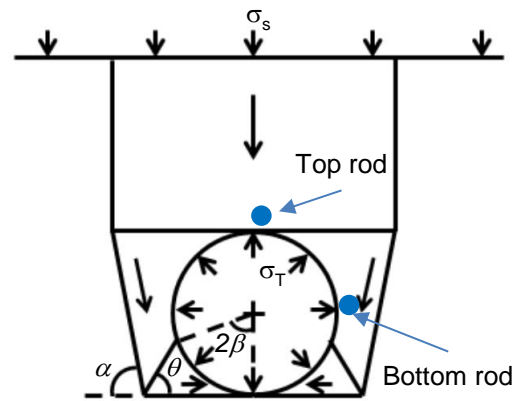
a) Post-test tunnel heading in test 10BL ($\alpha = 90^\circ$).



b) Collapse mechanism A (after Davis *et al.*, 1980)

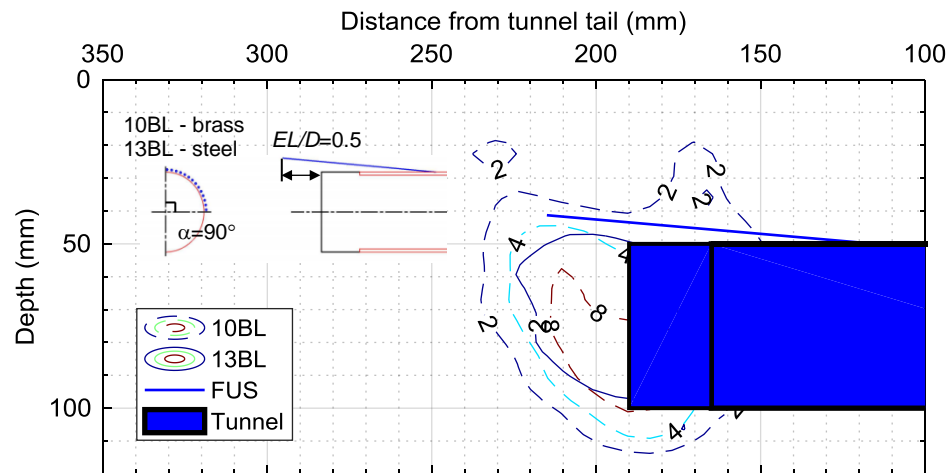


c) Post-test tunnel heading in test 4BL ($\alpha = 90^\circ$).

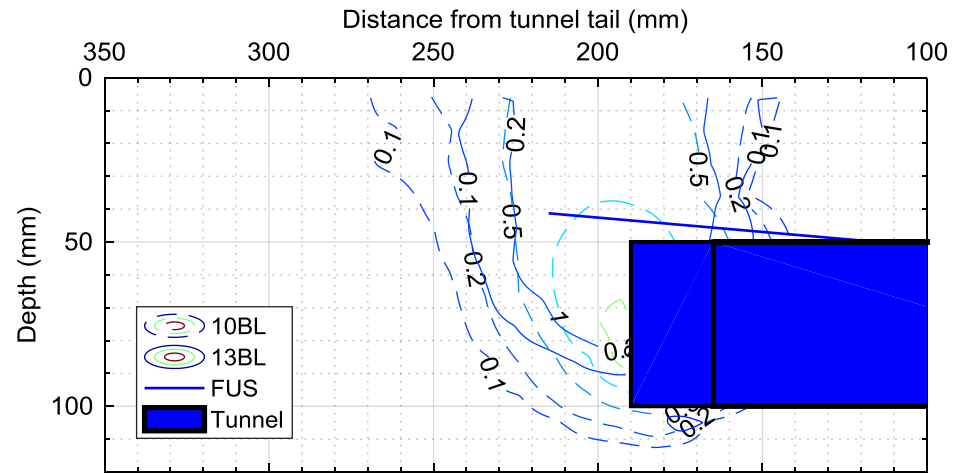


d) Collapse mechanism D (after Davis *et al.*, 1980).

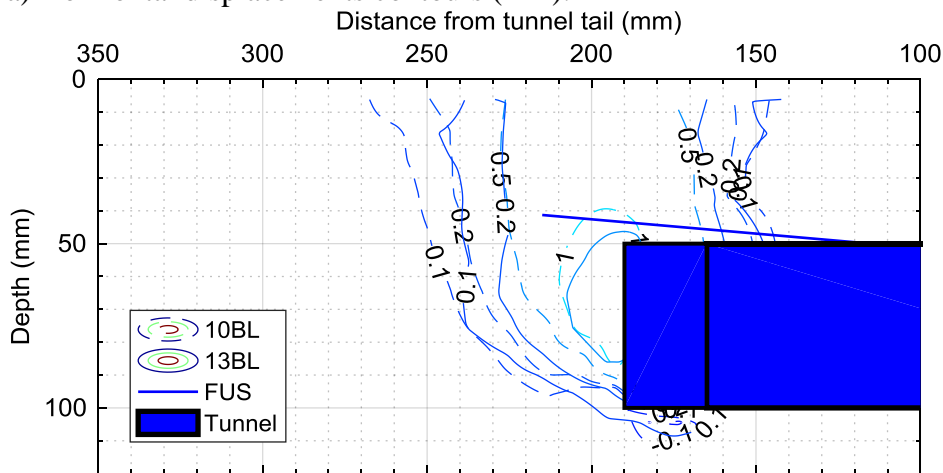
Figure 5.38: The tunnel headings and the model forepoles post-test.



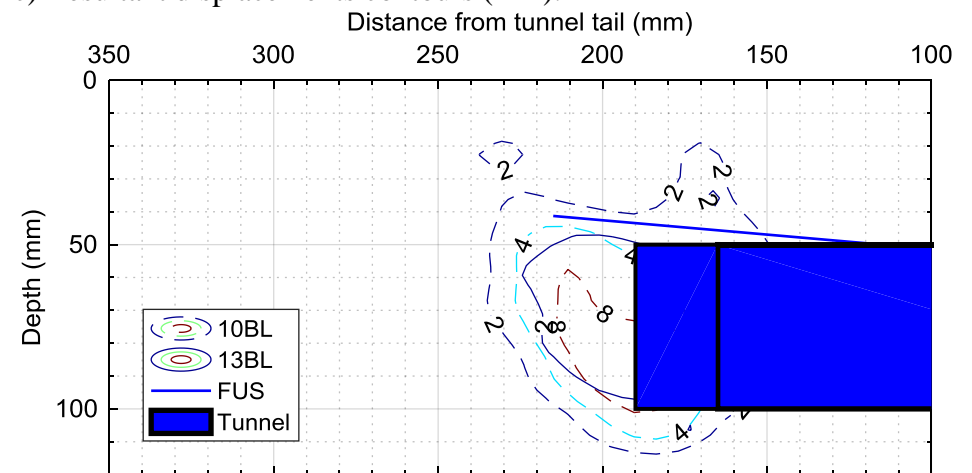
a) Horizontal displacements contours (mm).



c) Resultant displacements contours (mm).

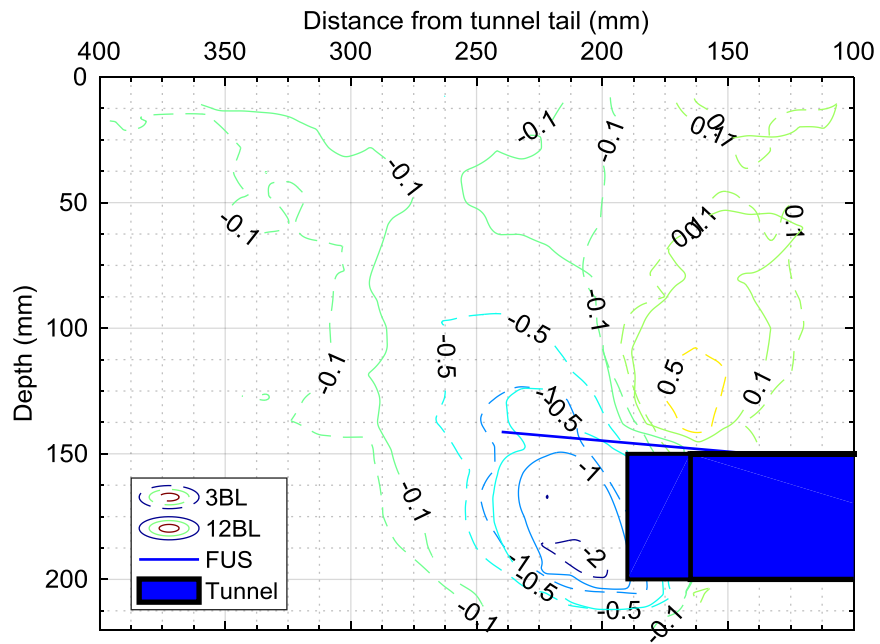


b) Vertical displacements contours (mm).

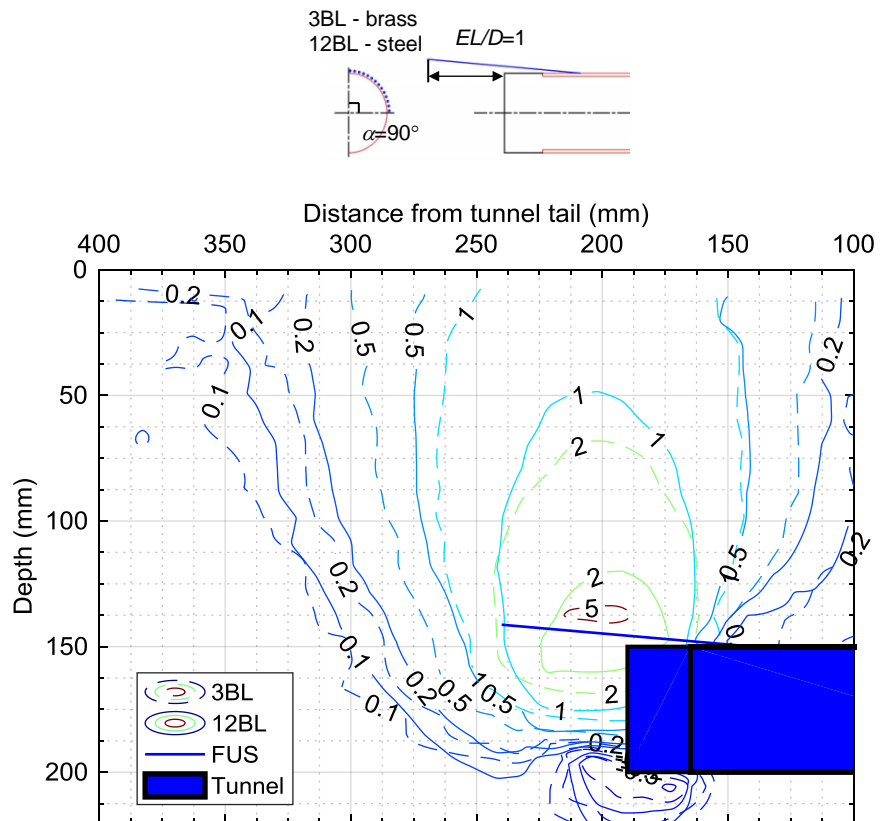


d) Engineering shear strains contour.

Figure 5.39: Effect of FUS stiffness - Subsurface soil deformations in tests 10BL and 13BL when σ_T reduced from 55kPa to 20kPa.

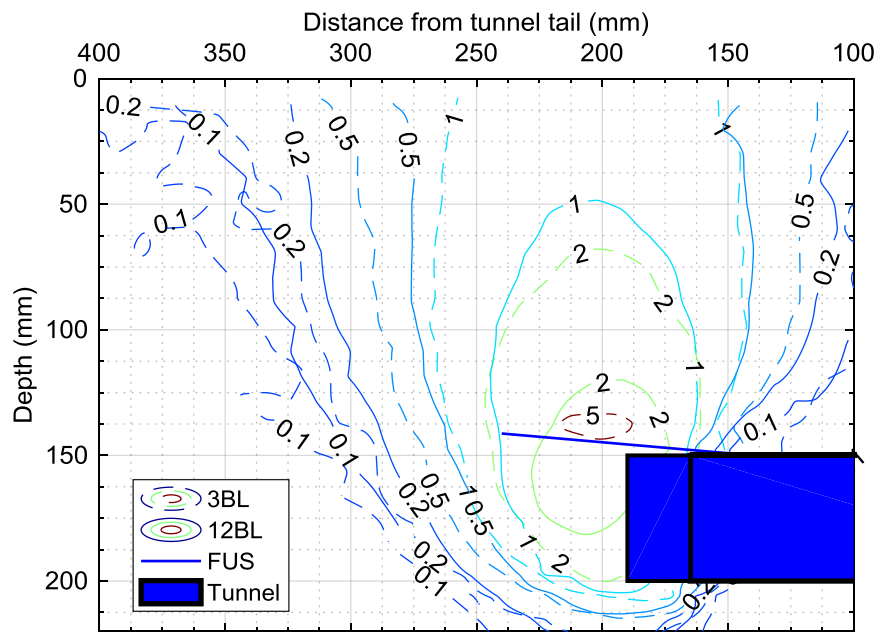


a) Horizontal displacements contours (mm).

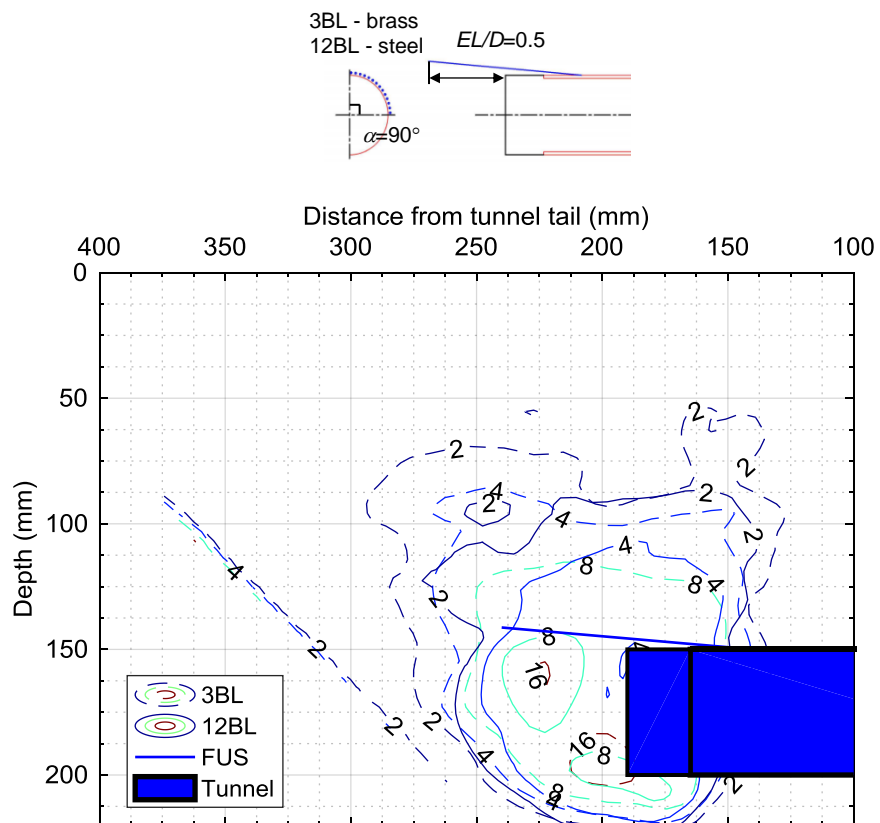


b) Vertical displacements contours (mm).

Figure 5.40: Effect of FUS stiffness - Subsurface soil deformations in tests 3BL and 12BL when σ_T reduced from 180kPa to 60kPa.

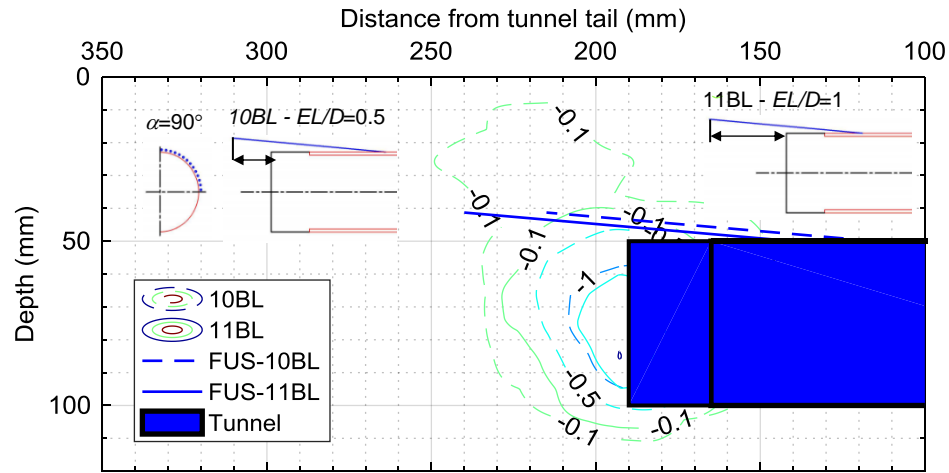


c) Resultant displacements contours (mm).

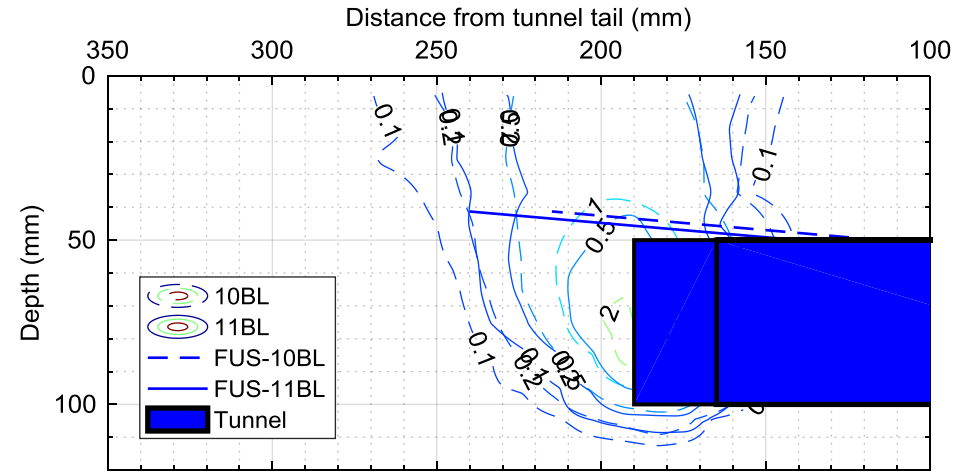


d) Engineering shear strains contours (%).

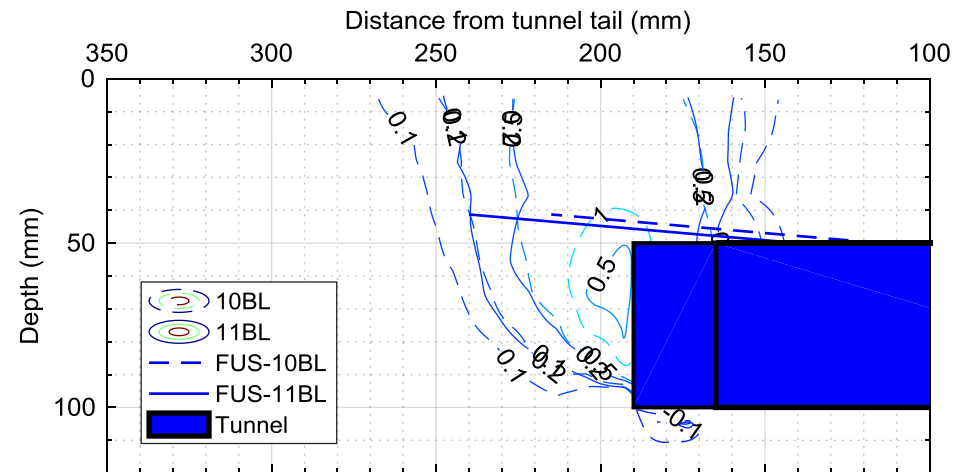
Figure 5.40: Effect of FUS stiffness - Subsurface soil deformations in tests 3BL and 12BL when σ_T reduced from 180kPa to 60kPa.



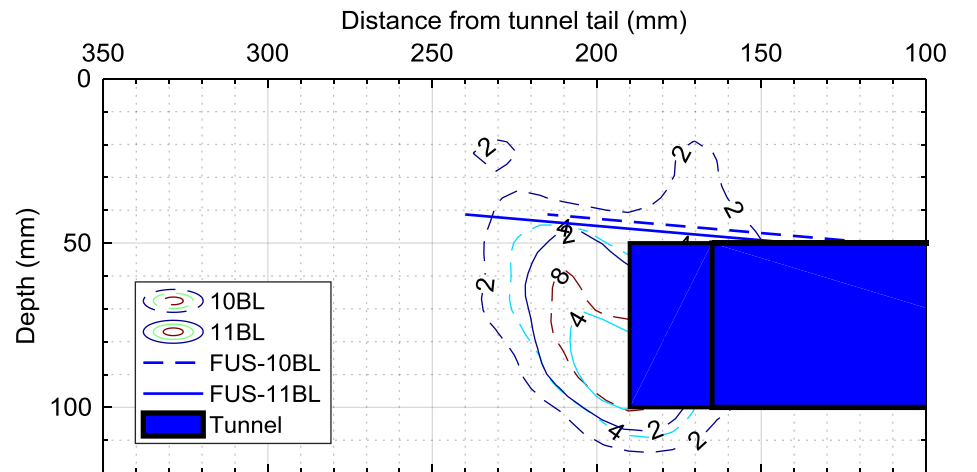
a) Horizontal displacements contours (mm).



c) Resultant displacements contours (mm).

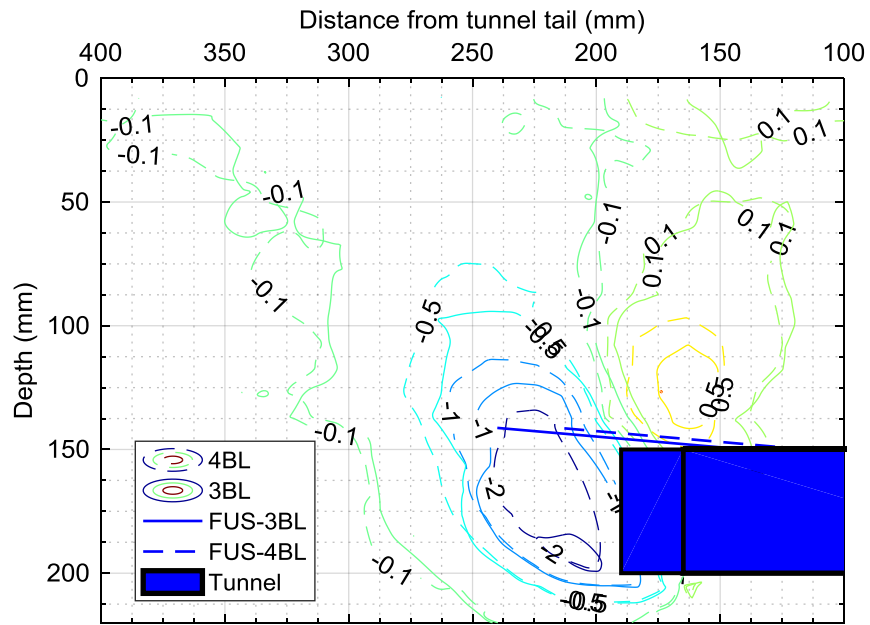


b) Vertical displacements contours (mm).

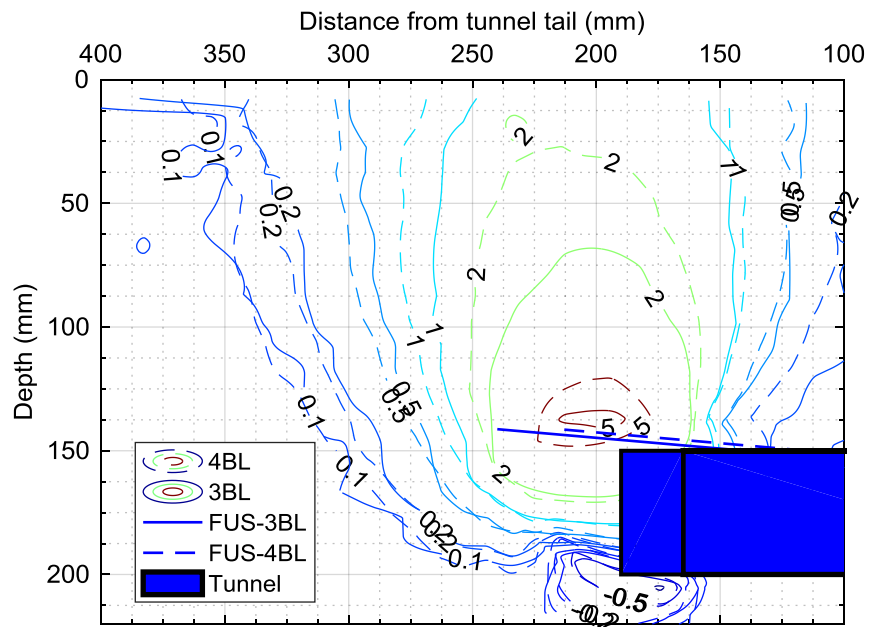
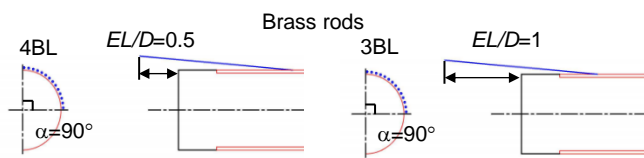


d) Engineering shear strains contour (%).

Figure 5.41: Effect of EL - Subsurface soil deformations in tests 10BL and 11BL when σ_T reduced from 55kPa to 20kPa.

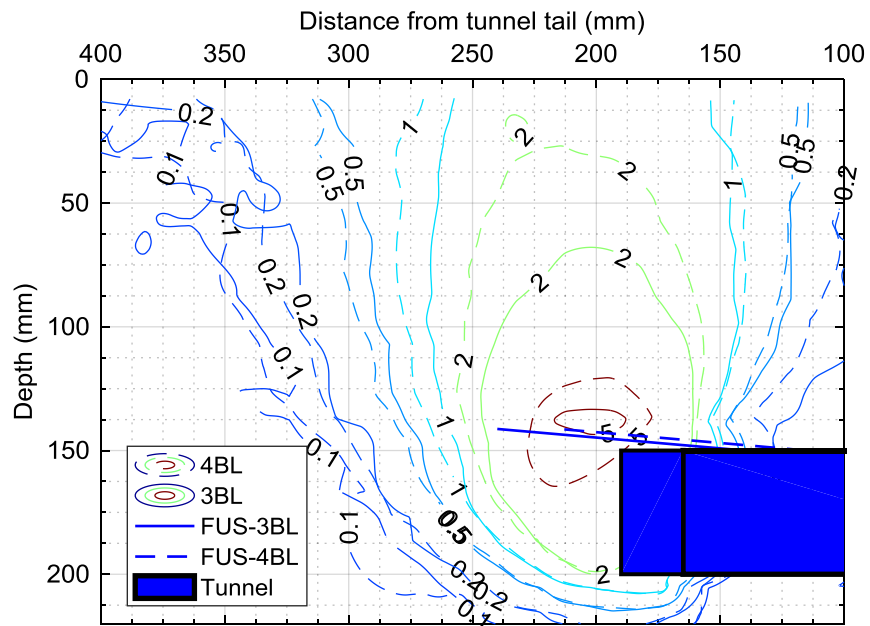


a) Horizontal displacements contours (mm).

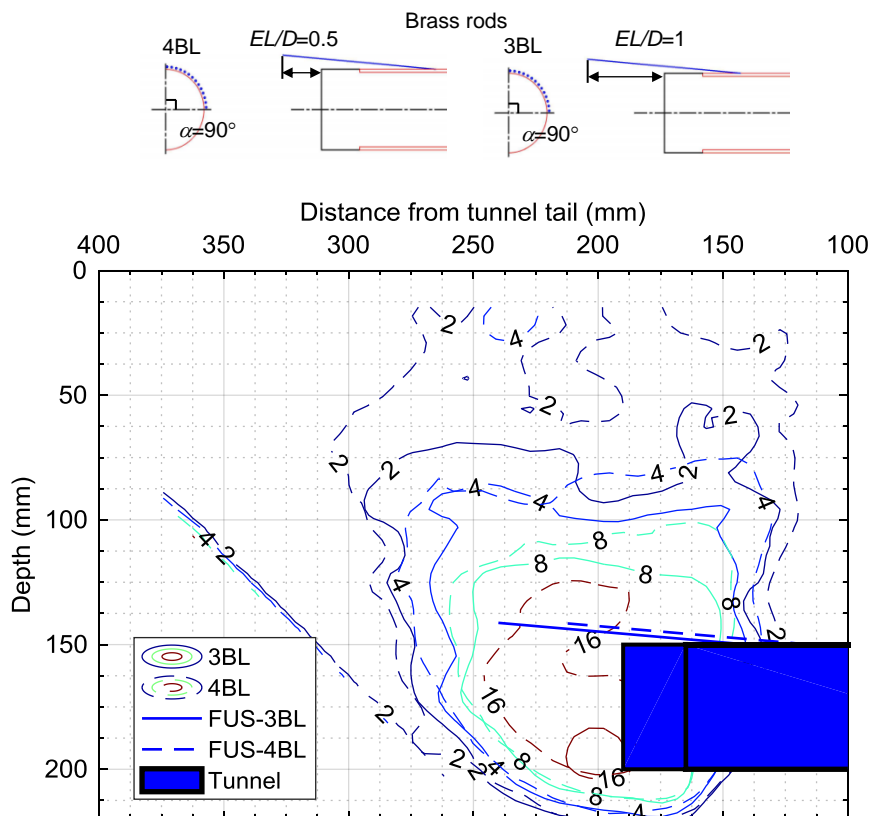


b) Vertical displacements contours (mm).

Figure 5.42: Effect of EL - Subsurface soil deformations in tests 3BL and 4BL when σ_T reduced from 180kPa to 60kPa.

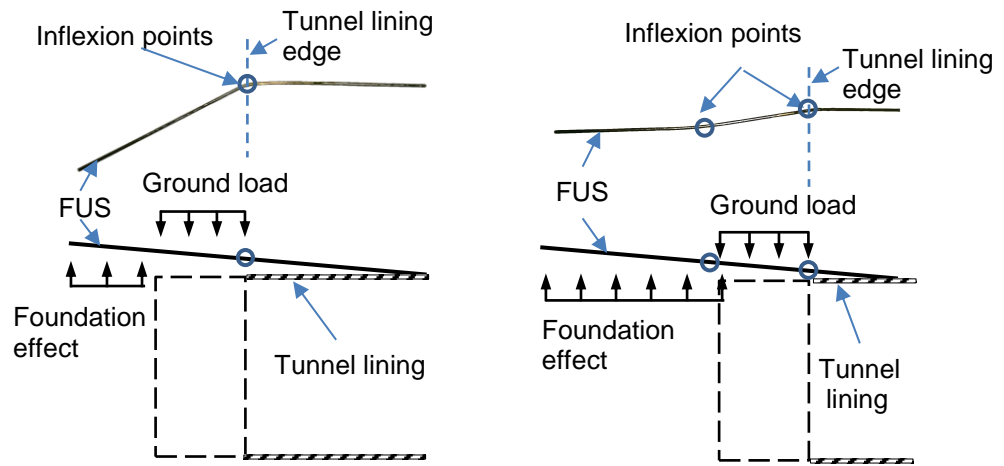


c) Resultant displacements contours (mm).



d) Engineering shear strains contours (%).

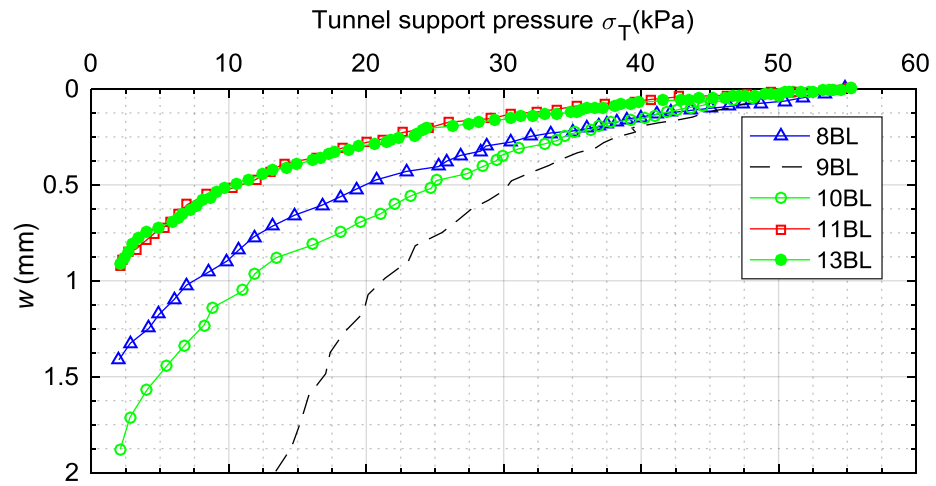
Figure 5.42: Effect of EL - Subsurface soil deformations in tests 3BL and 4BL when σ_T reduced from 180kPa to 60kPa.



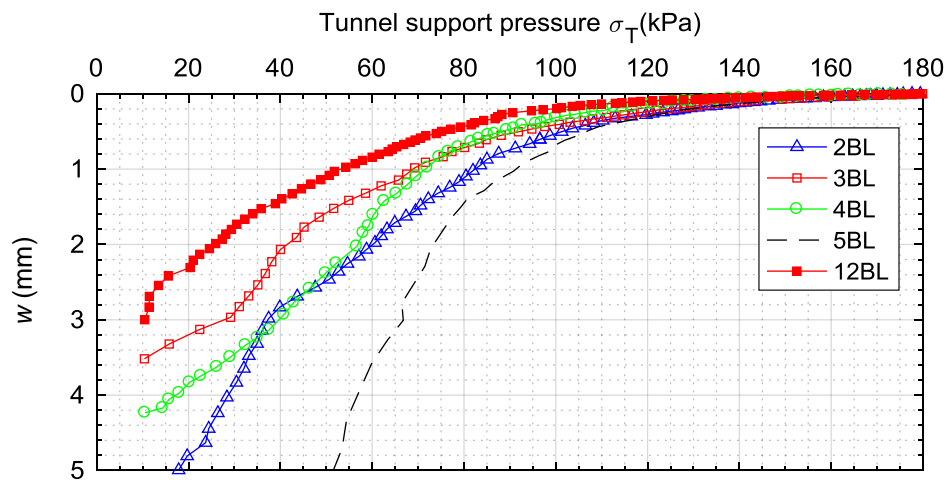
a) $4BL$ ($EL/D = 0.5$)

b) $3BL$ ($EL/D = 1$).

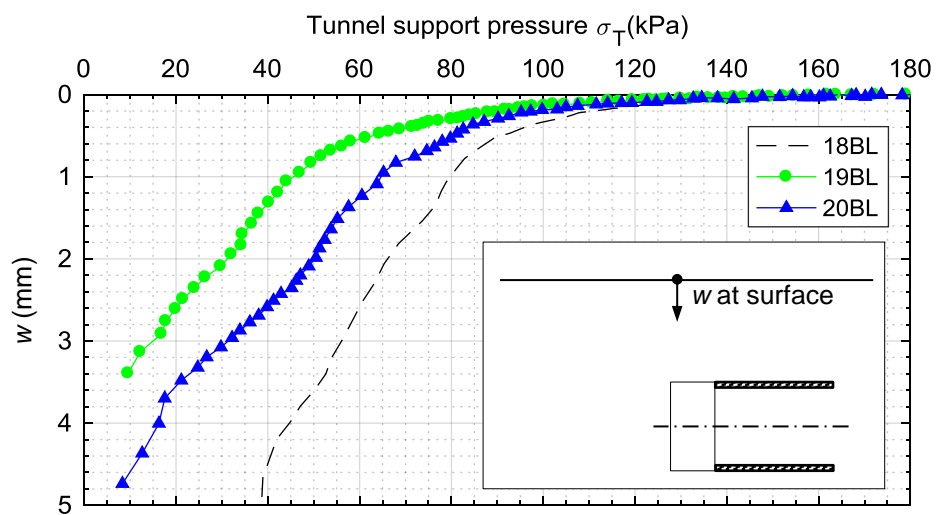
Figure 5.43: Schematic representation of rod post-test.



a) $C/D=1$ tests.

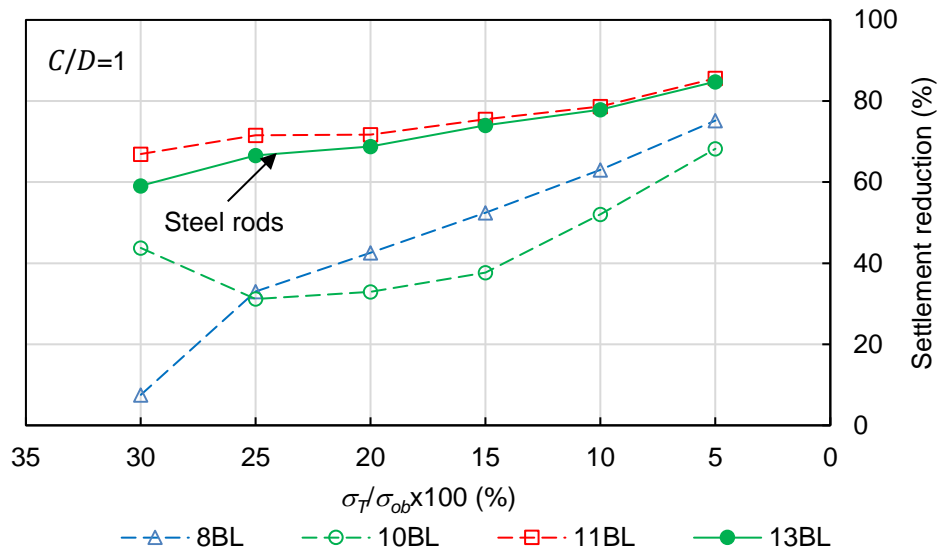


b) $C/D=3$ test (measured by LVDT/Visimet)



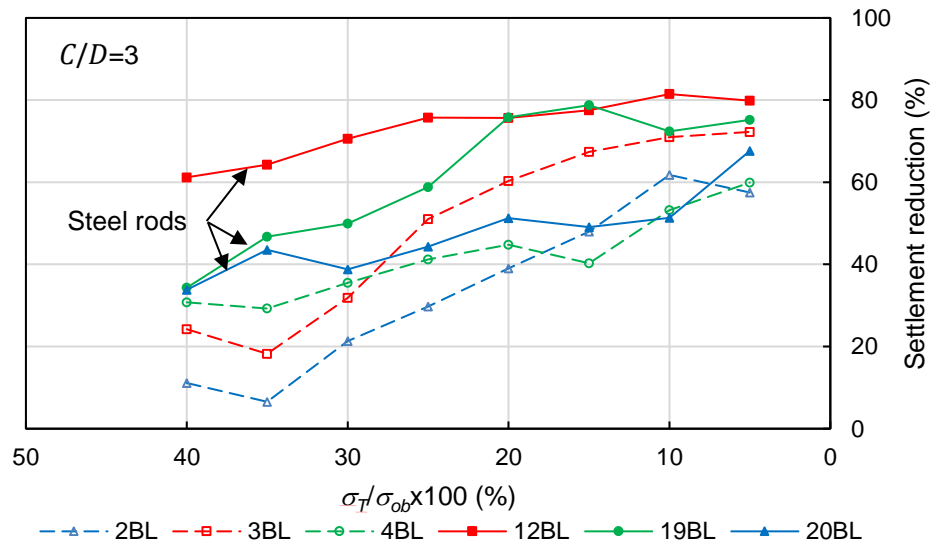
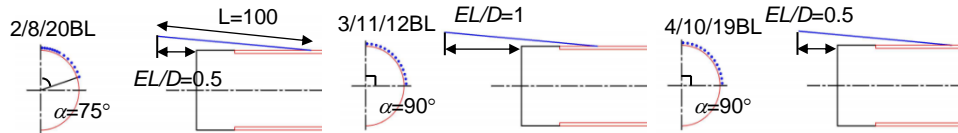
c) $C/D=3$ (measured by GeoPIV_RG)

Figure 6.1: Maximum surface settlement above tunnel face.



a) *C/D=1* tests.

Diagram of the FUS arrangement



b) *C/D=3* tests.

Figure 6.2: Settlement reduction delivered by the FUS.

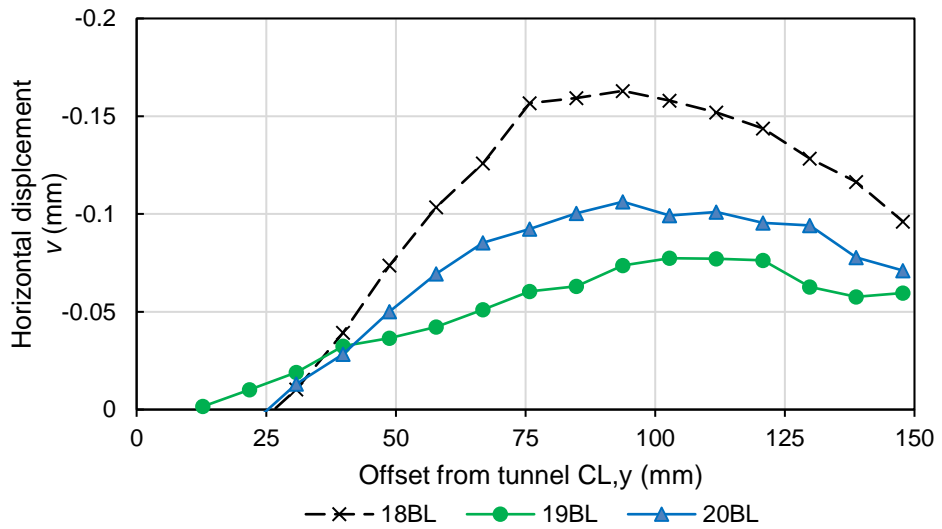


Figure 6.3: Horizontal displacement in transverse direction when σ_T reduced from 180kPa to 72kPa ($0.2\sigma_{ob}$).

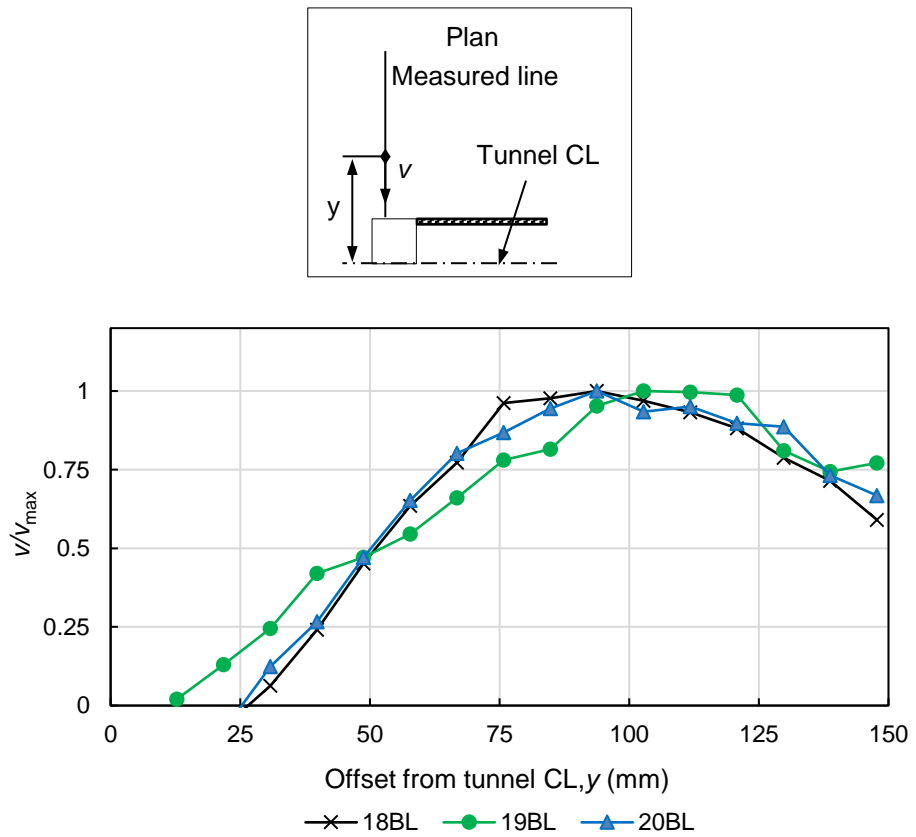
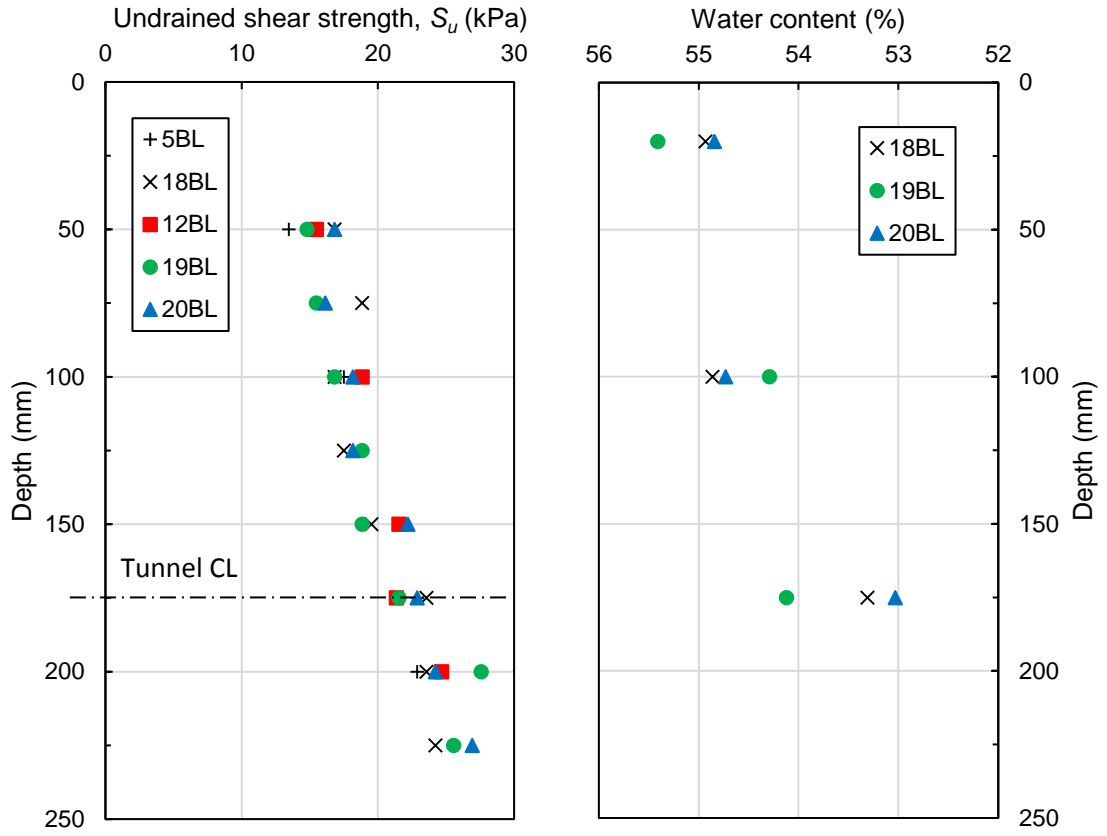


Figure 6.4: Horizontal displacement in transverse direction when σ_T reduced from 180kPa to 72kPa ($0.2\sigma_{ob}$).



a) Undrained shear strength profile.

b) Water content profile.

Figure 6.5: Undrained shear strength and water content of centrifuge model clay post-test at various depth.

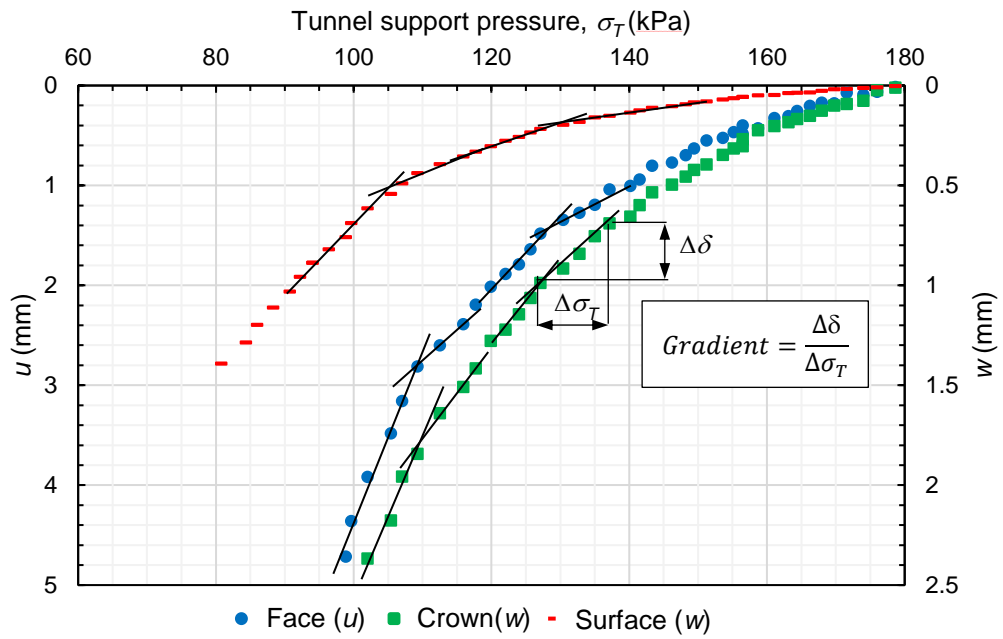


Figure 6.6: Soil displacements in test 5BL.

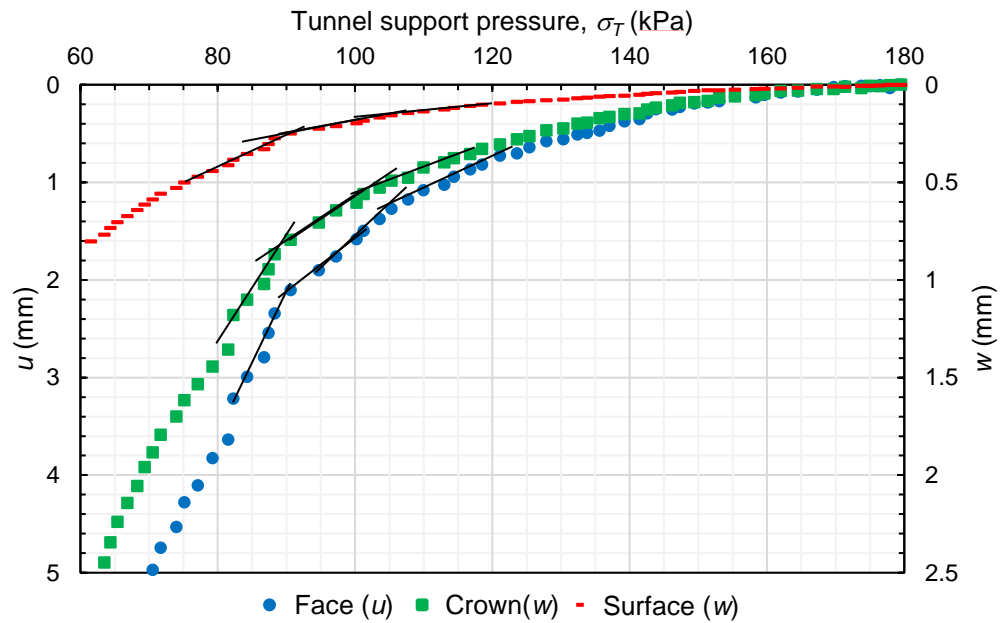


Figure 6.7: Soil displacements in test 12BL.

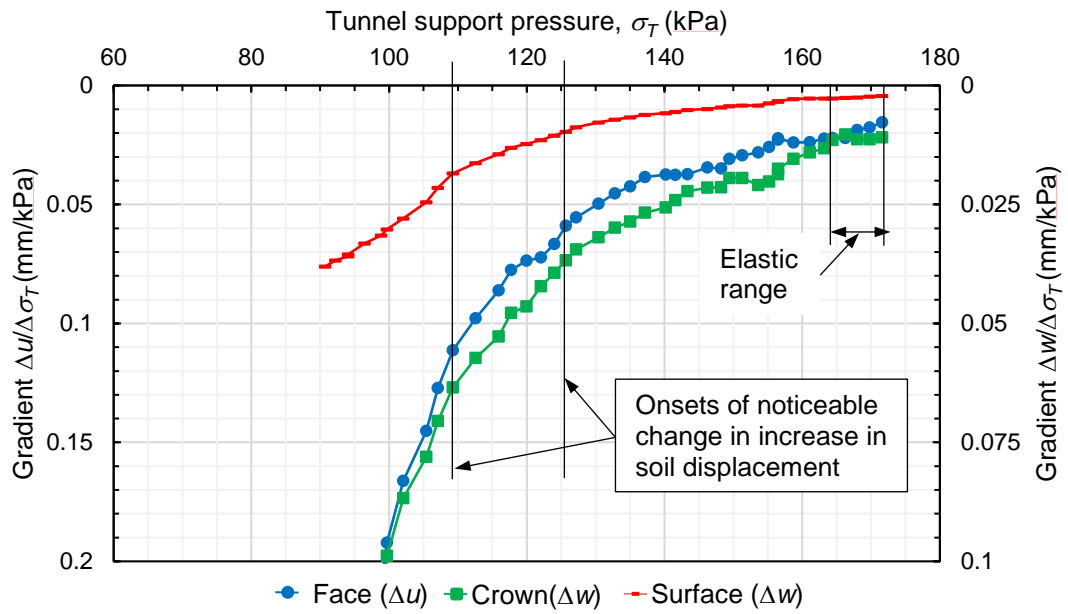


Figure 6.8: Gradient of soil displacement in test 5BL.

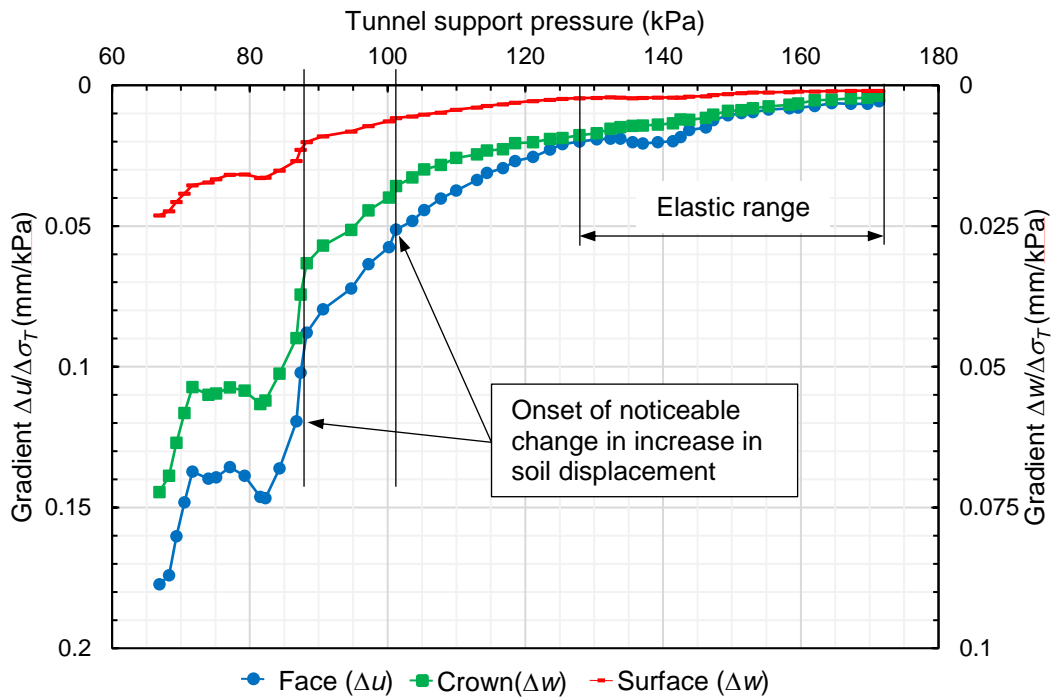


Figure 6.9: Gradient of soil displacement in test 12BL.

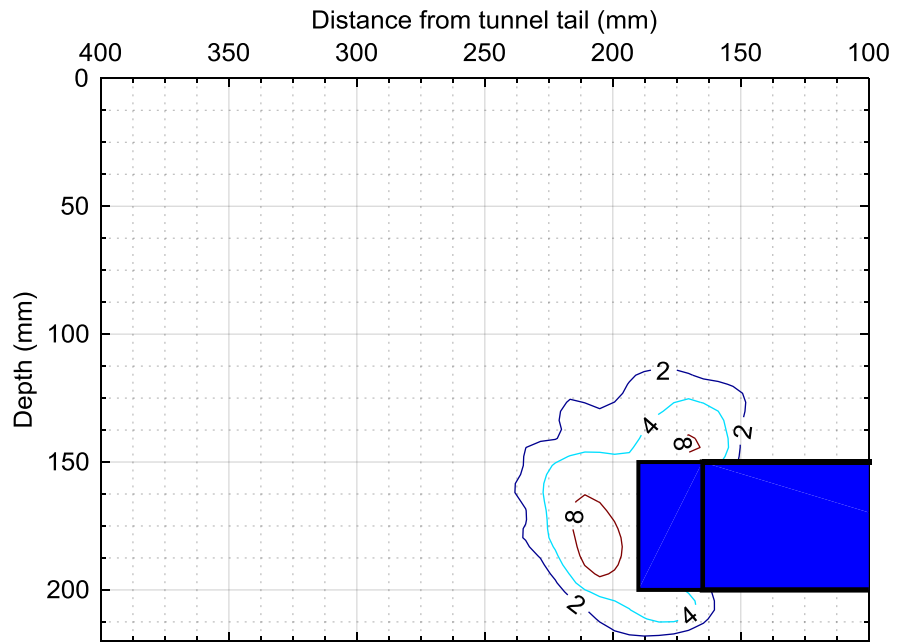


Figure 6.10: Engineering shear strains in soil in test 5BL at $\sigma_{TC}=126\text{kPa}$.

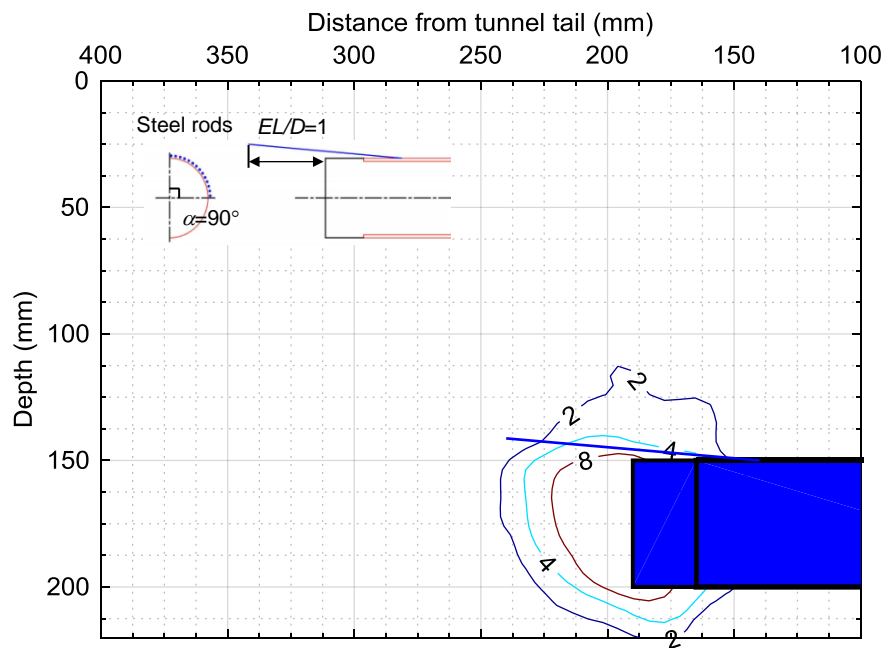


Figure 6.11: Engineering shear strains in soil in test 12BL at $\sigma_{TC}=88\text{kPa}$.

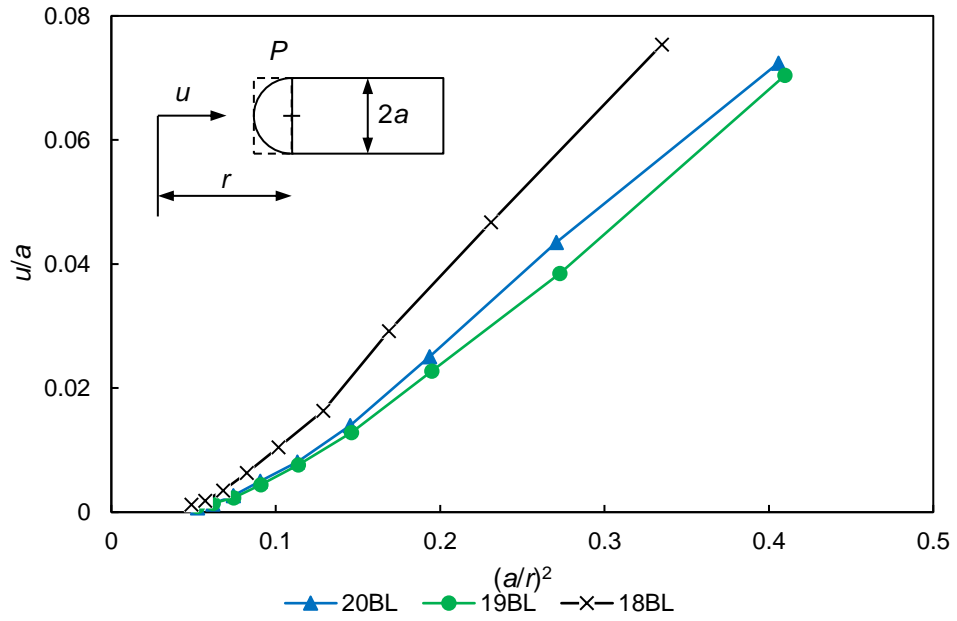


Figure 6.12: Longitudinal horizontal soil displacement ahead of the tunnel face in tests 18BL, 19BL and 20BL ($\sigma_T=90\text{kPa}$).

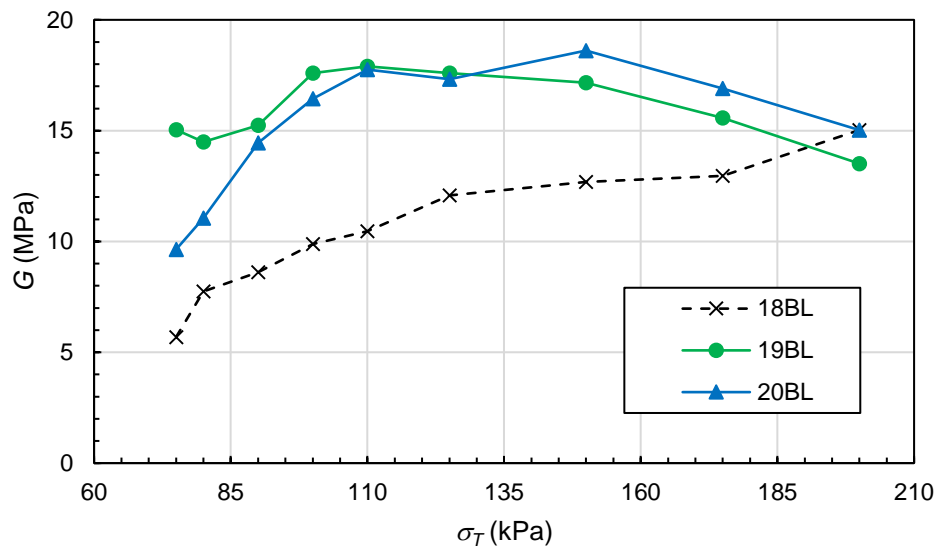


Figure 6.13: Change in stiffness of soil during the centrifuge tests.

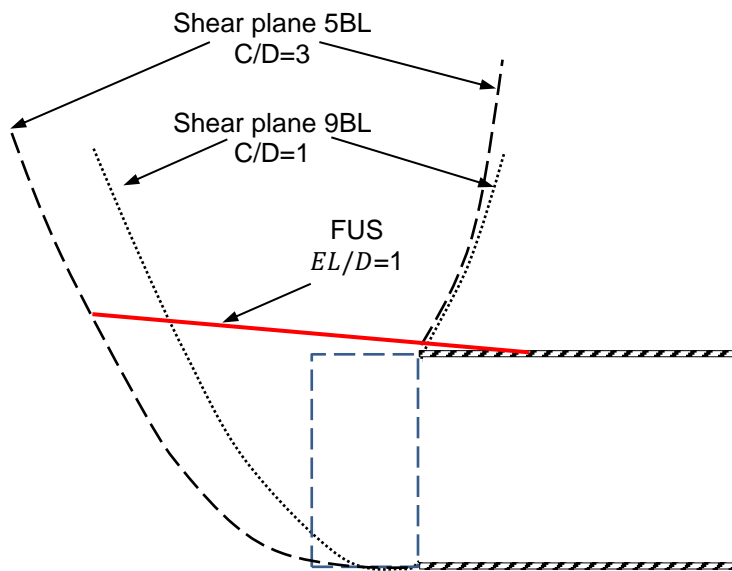
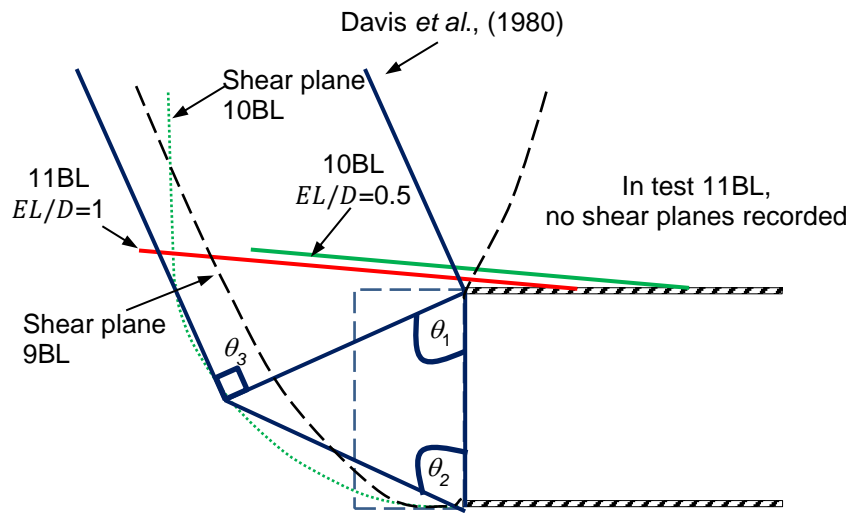
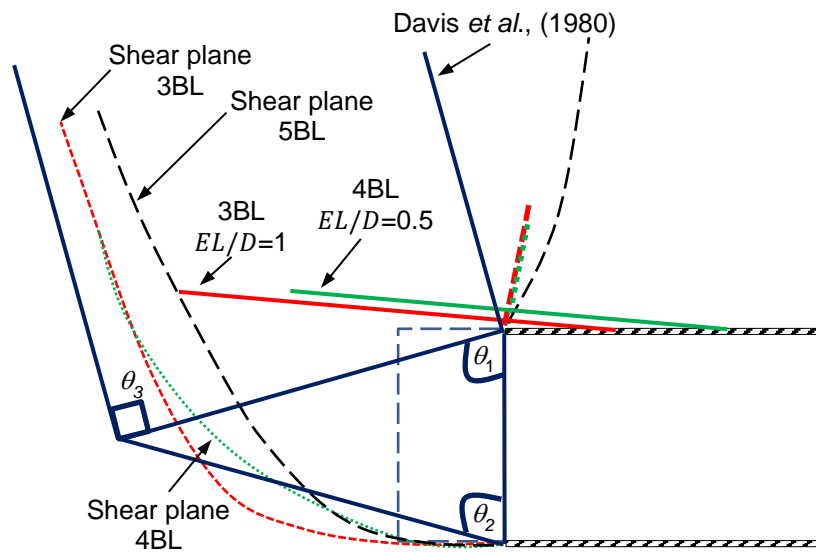


Figure 6.14: Relative locations of the shear planes and the FUS with $EL/D=1$ in the reference tests and reinforced tests.



a) Shear planes for $C/D=1$ tunnels



a) Shear planes for $C/D=3$ tunnels

Figure 6.15: Comparison of the shear planes for the reinforced and reference tests.

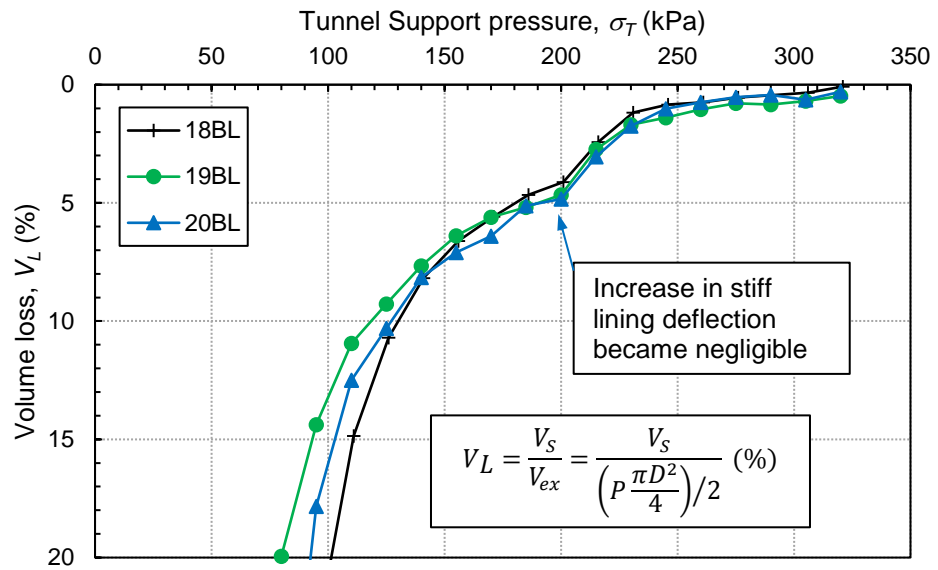


Figure 6.16: The measured volume loss when σ_T reduced.

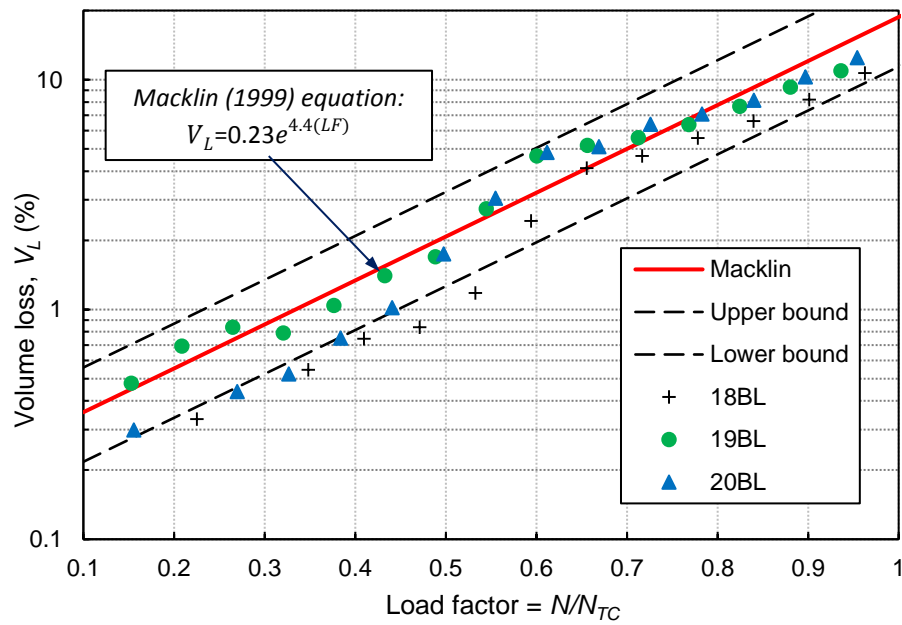


Figure 6.17: Comparison of the Load Factor-Volume loss relationship with Macklin (1999).

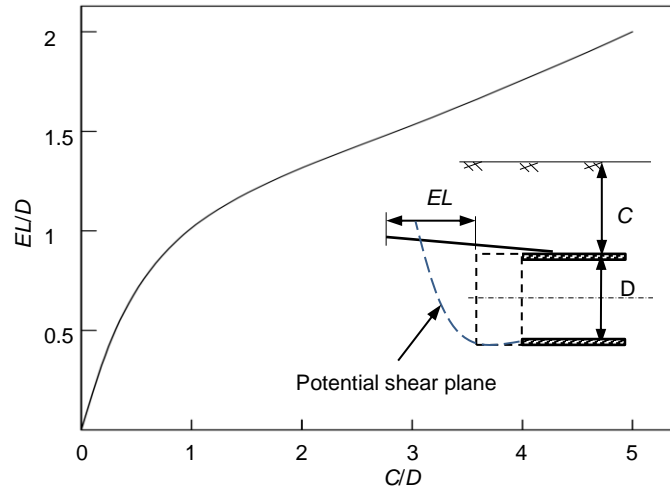
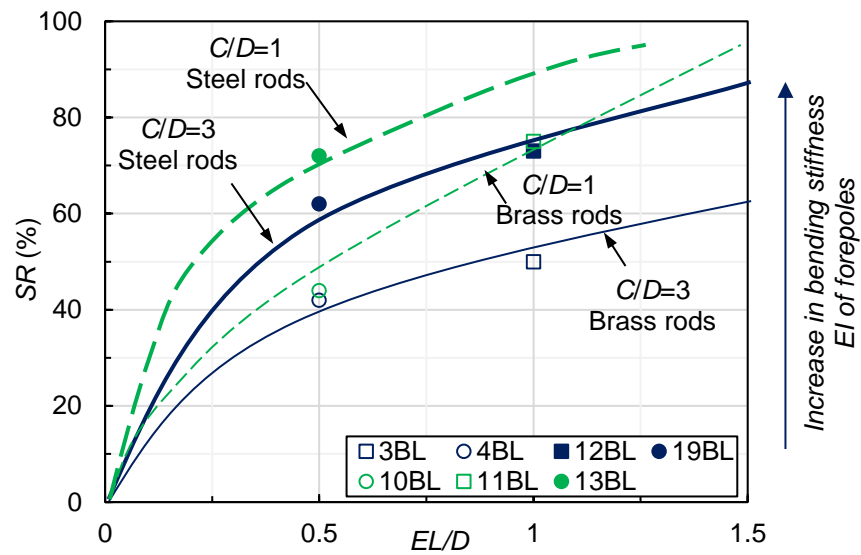


Figure 7.1: Recommended embedded length EL/D for different tunnel depth C/D .



Bending stiffness equivalence:

Brass rod: steel pipes with diameter of 135mm and wall thickness of 8mm

Steel rod: steel pipes with diameter of 165mm and wall thickness of 8mm.

Figure 7.2: Relationship between settlement reduction SR and EL/D for different tunnel depths C/D .

APPENDIX 1 BENDING STIFFNESS OF THE MODEL FOREPOLES

Bending stiffness EI

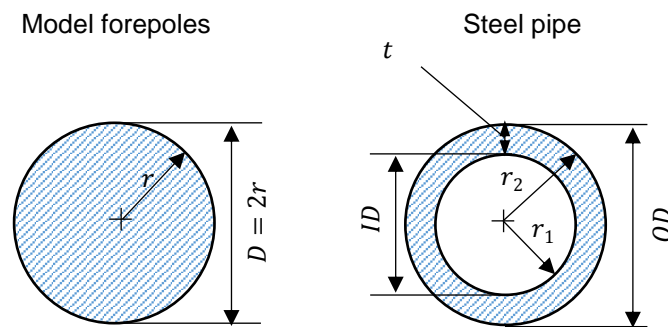
where E is Young's modulus,

I is area of moment of inertia.

Young's modulus of steel $E_s = 210 \text{ GPa} = 210 \times 10^9 \text{ Pa}$

Young's modulus of brass $E_b = 110 \text{ GPa} = 110 \times 10^9 \text{ Pa}$

Figure A illustrates cross sections of a model forepole and a steel pipe.



NTS

D : diameter of model rod; r : radius of model rod

OD : outer diameter of steel pipe; ID : inner diameter of steel pipe;

r_1 : inner radius of steel pipe; r_2 : outer radius of steel pipe.

t : wall thickness of steel pipe

Figure A: Cross section of model forepoles and steel pipes.

Second moment of area of a rod of radius r

$$I = \frac{\pi}{4} r^4$$

Second moment of area of a pipe of inner radius r_1 and outer radius r_2

$$I = \frac{\pi}{4} (r_2^4 - r_1^4)$$

The centrifuge scaling law for bending stiffness EI is $EI_m/EI_p = 1/n^4$. All the tests were conducted at $n = 125g$.

Table A tabulates the bending stiffness of the model rods under $125g$ and the corresponding prototype steel pipes.

Model at 125g				Prototype		
Steel rod 1mm D				Steel pipe 165mm OD , 8mm t		
Dimension	Value	Unit		Dimension	Value	Unit
D	1.0	mm		OD	165	mm
r	0.5	Mm		WT	8	mm
I	4.91E-14	m ⁴		ID	149	mm
				r_2	82.5	mm
				r_1	74.5	mm
				I	1.22E-05	m ⁴
EI	2.52E+06	Nm ²		EI	2.56E+06	Nm ²
Brass rod 1mm D				Steep pipe 135mm OD , 8mm t		
Dimension	Value	Unit		Dimension	Value	Unit
D	1.0	Mm		OD	135	mm
r	0.5	Mm		WT	8	mm
I	4.91E-14	m ⁴		ID	119	mm
				r_2	67.5	m
				r_1	59.5	m
				I	6.46E-06	m ⁴
EI	1.32E+06	Nm ²		EI	1.36E+06	Nm ²

Table A: Bending stiffness calculation.

Therefore, at $125g$ the 1mm diameter brass and steel rods under $125g$ have a bending stiffness equivalent to steel pipes of respectively approximately 135mm and 165mm outer diameter with 8mm wall thickness at prototype scale.